UNIVERSITÀ
DEGLI STUDI
DI PADOVA

INRS
Centre - Eau Terre Environnement

NUMERICAL MODELING OF FLOW AND SOLUTE TRANSPORT PHENOMENA IN SUBSURFACE AND COUPLED SURFACE–SUBSURFACE HYDROLOGY

Thesis presented for the degree of Doctor of Philosophy to:
Institut National de la Recherche Scientifique, Centre Eau Terre Environnement, Québec
University of Padua, School of Civil and Environmental Engineering, Italy

Advisors: Prof. Claudio Paniconi
Prof. Mario Putti

PhD student: Carlotta Scudeler

Abstract

The overall aim of the work described in this thesis is to bring a number of contributions to hydrology and hydrological modeling in the framework of a specific physically-based numerical model for integrated surface–subsurface and flow–transport processes, the CATchment-HYdrology Flow-Transport (CATHY_FT) model. These contributions revolve around three main themes: the enhancement of the numerical performance of hydrological models for flow and transport phenomena, the improvement of our current understanding of complex boundary conditions in order to reduce the errors associated with their modeling, and the testing and benchmarking of distributed physically-based models for groundwater flow and transport processes. The work to achieve the general objective is elaborated into four stages. First, the Larson-Niklasson post-processing algorithm is implemented in CATHY_FT to reconstruct mass-conservative velocities from a linear, or $\mathcal{P}_1$, Galerkin solution of Richards' equation. This is done to improve the accuracy and mass balance properties of the companion advective transport model (finite volume-based), which rely on accurate velocity fields as input. Through a comparison between the results from the reconstructed velocities and the $\mathcal{P}_1$ Galerkin velocities, it is shown that a locally mass-conservative velocity field is necessary to obtain accurate transport results. Second, a detailed and novel analysis of the behavior of seepage face boundaries is performed with the flow model of CATHY_FT. The numerical simulations examine the model's performance under complex conditions such as heterogeneity and coupled surface/subsurface flow. It is shown that the overall numerical solution can be greatly affected by the way seepage face boundaries are handled in hydrological models and that careful considerations are required when using simple approximations, in the presence of heterogeneous slopes, and for seepage faces forming on a portion of the land surface. Third, CATHY_FT is implemented and run at the Landscape Evolution Observatory of the Biosphere 2 facility, Arizona. A detailed modeling analysis is performed of the

experimental data collected during an isotope tracer experiment and from an intensively-measured hillslope, including quantity and quality of groundwater discharge and point-scale flow and transport data. This flow and tracer data is used to incrementally explore complex phenomena and associated hypotheses (e.g., heterogeneity, fractionation, and dispersion), progressing from flow to transport and from integrated to point-scale response analysis. This incremental approach highlights the challenges in testing and validating the new generation of integrated hydrological models when considering many types and levels of observation data. Finally, a concluding analysis is performed that relates to all three themes of the thesis, describing some of the features of the CATHY_FT model, discussing key issues associated to its further development, and testing its physical and numerical behavior for both real and synthetic scenarios. This final stage of the thesis addresses the myriad challenges faced in accurately and efficiently resolving the difficult behavior of the advection–dispersion equation for subsurface solute transport, in properly handling the complex boundary conditions for solute interactions across the land surface, and generally in capturing process interactions and feedbacks between flow and transport phenomena in surface and subsurface environments.

Résumé

Le but principal du travail décrit dans cette thèse est d'aporter plusieurs contributions à la modélisation hydrologique dans le cadre spécifique d'un modèle numérique à base physique pour des processus de surface–subsurface et flux-transport intégrés, le modèle CATchment-HYdrology Flow-transport (CATHY_FT). Ces contributions tournent autour des trois thèmes principaux: l'amélioration de la performance numérique des modèles hydrologiques pour les phénomènes de flux et de transport, l'amélioration de notre compréhension des conditions aux limites complexes dans le but de réduire les erreurs associées à la modélisation ainsi que le test et l'analyse comparative des modèles distribués à base physique pour les processus de transport et flux d'eaux souterraines. Pour atteindre ces objectifs, les tarvaux sont divisés en quatre étapes. La première est l'implémentation dans CATHY_FT de l'algorithme de Larson-Niklasson pour la reconstruction des vitesses conservatrices de la masse à partir d'une solution linéaire (ou $\mathcal{P}_1$) de Galerkin de l'équation de Richard. Le but est d'améliorer la précision et les propriétés de bilan de masse du modèle de transport advectif (à base de volumes finis), qui dépend des champs de vitesse utilisés comme input. Une comparaison entre les résultats obtenus avec les vitesses reconstituées et les vitesses de Galerkin $\mathcal{P}_1$ montre la nécessité d'un champ de vitesse conservateur de la masse pour l'obtention des résultats des transports précis. La deuxième est une analyse nouvelle et détaillée du comportement des conditions aux limites dans la zone de suintement réalisée à l'aide du modèle d'écoulement de CATHY_FT. Les simulations numériques examinent la performance du modèle sous des conditions complexes, telles que en présence d'hétérogénéité et d'écoulement de couplage surface/subsurface. Il est montré que la solution numérique générique peut être largement affectée par la façon dont les conditions aux limites dans la zone de suintement sont utilisées dans les modèles hydrologiques et que des considérations soigneuses sont requises dans l'utilisation des approximations simples, dans la présence de pentes hétérogènes ainsi que dans les zones

de suintement qui se forment au niveau de la surface de terre. Dans la troisième étape, CATHY_FT est implémenté et exécuté à partir de données issues du Landscape Evolution Observatory de l'installation Biosphère 2, en Arizona. Une analyse de modélisation détaillée des données expérimentales collectées pendant une expérience de traçage isotopique sur un versant mesuré et surveillé intensivement est réalisée. Ces donnés comprennent la quantité et qualité d'eaux souterraines déchargées et des mesures distribuées d'écoulement et de transport. Les données sont utilisées pour examiner incrémentalement des phénomènes complexes et les hypothèses associées (e.g., hétérogénéité, fractionnement et dispersion), en analysant les réponses du flux au transport et les mesures intégrées ou distribuées. Cette approche incrémentale souligne les défis associés aux tests et validations des modèles hydrologiques de nouvelle génération lorsque plusieurs types et niveaux de données d'observation sont considérés. Finalement, une dernière analyse qui fait un lien avec tous les trois thèmes de la thèse est effectuée. Dans cette analyse quelques particularités du modèle CATHY_FT sont décrites, des questions clés liées à son futur développement sont abordées et son comportement physique et numérique est testé pour des scénarios réels et synthétiques. Cette étape finale de la thèse aborde la myriade des défis rencontrés pour résoudre efficacement et avec précision le comportement complexe de l'équation d'avection-dispersion utilisée pour décrire le transport des solutés de subsurface, pour le traitement de conditions aux limites complexes utilisées pour l'interaction de solutés entre la surface et la subsurface et, en général, pour capturer les interactions de processus entre les phénomènes de flux et transport dans les environnement de surface et subsurface.

Riassunto

Lo scopo di questa tesi è fornire dei contributi all'idrologia e alla modellazione idrologica nell'ambito di un modello numerico specifico, il modello CATchment HYdrology Flow-Transport (CATHY_FT), utilizzato per simulare processi integrati di superficie e sotterranei e di flusso e trasporto. Questi contributi riguardano tre temi principali: il miglioramento del comportamento numerico di modelli idrologici che simulano fenomeni di flusso e trasporto, l'approfondimento di condizioni al contorno complesse con l'obbiettivo di ridurre gli errori relativi alla loro modellazione e il test e l'analisi comparativa di modelli a base fisica utilizzati per simulare processi di flusso e trasporto sotterranei. Il lavoro per raggiungere l'obbiettivo generale viene diviso in quattro step. Nel primo step l'algoritmo di Larson-Niklasson è implementato in CATHY_FT per ricostruire velocità conservatrici della massa a partire da una soluzione lineare (o P1) di Galerkin dell'equazione di Richards, in modo da permettere al modello di trasporto avvettivo (basato sui volumi finiti) di conservare la massa, cosa che dipende strettamente dall'accuratezza del campo di velocità che questo utilizza. Confrontando i risultati ottenuti con le velocità derivanti dalla soluzione P1 di Galerkin e quelle ricostruite, viene mostrato che un campo di velocità localmente conservativo è necessario per ottenere risultati accurati con il trasporto. Nella seconda fase viene effettuata un'analisi dettagliata del comportamento delle condizioni ai limiti nella zona del fronte di infiltrazione con il modello di flusso di CATHY_FT. Le simulazioni numeriche esaminano il comportamento del modello in condizioni complesse come quelle di eterogeneità e di flusso di superficie e sotterraneo accoppiato. Viene dimostrato che la soluzione numerica può essere fortemente influenzata dal modo in cui la zona di infiltrazione viene trattata nei modelli idrologici e che considerazioni accurate sono sempre necessarie quando si usano approssimazioni, in presenza di versanti eterogenei e per le zone di infiltrazione che si formano nella superficie terrestre. Come terzo step, CATHY_FT viene testato al Landscape Evolution Observatory del Biosphere 2 in

Arizona. Viene eseguita un'analisi dettagliata di dati sperimentati raccolti durante un esperimento di tracciante isotopico e da un versante artificiale intensivamente controllato. Le informazioni comprendono la qualità e la quantità della portata sotterranea e dati puntuali di flusso e trasporto. Questi dati di flusso e tracciante sono utilizati per esplorare fenomeni complessi e le ipotesi associate (e.g., eterogeneità, frazionamento e dispersione), procedendo dalla risposta di flusso a quella di trasporto e dalla risposta integrata a quella puntuale. Questo approccio incrementale evidenzia le sfide legate alla validazione della nuova generazione di modelli idrologici integrati quando si guarda a diversi tipi e livelli di dati osservati. Infine, viene eseguita un'analisi conclusiva che si lega a tutti e tre i temi della tesi, descrivendo alcune caratteristiche del modello CATHY_FT, discutendo problemi chiave legati al suo sviluppo futuro e testando il suo compertamento fisico e numerico sia per scenari sintetici che reali. Questo step finale della tesi affronta la miriade di sfide legate alla risoluzione accurata ed efficace del comportamento difficile dell'equazione di avezione-dispersione per processi di trasporto di soluto sotterraneo, alla risoluzione appropriata delle condizioni ai limiti complesse per rappresentare le interazioni di soluto attraverso la superficie terrestre e, in generale, alla rappresentazione delle interazioni tra i fenomeni di flusso e trasporto nell'ambiente superficiale e sotterraneo.

Contents

Synthèse

S.1 Introduction

Les eaux souterraines constituent une composante importante de nombreux systèmes de ressources en eau douce et, pour cette raison, elles ont été largement étudiées par la communauté des hydrogéologues. Les deux principales forces directrices des études sur les eaux souterraines sont la nécessité d'évaluer la dynamique de l'eau des aquifères et le défi de la protection ou la remise en état de la qualité de ces eaux. Une bonne gestion de la quantité et de la qualité de la ressource en eau souterraine nécessite, pour le système géré, des prévisions à court, moyen, et long terme. Les prévisions de la réponse du système peuvent être obtenues en établissant et en résolvant des modèles mathématiques décrivant les phénomènes de flux et de transport au sein d'un domaine. Pour des cas plus pratiques, en raison du niveau d'hétérogénéité présent dans les eaux souterraines et en raison de la forme irrégulière de ses frontières, il est impossible de résoudre les modèles mathématiques analytiquement et ils sont traduits en problèmes numériques résolus à l'aide de programmes informatiques. Ceci, combiné aux avancées continues de la technologie informatique, a fait de la modélisation hydrologique un outil essentiel de la recherche dans la gestion des ressources en eau [e.g., *Bear and Cheng*, 2010].

Un grand nombre de modèles numériques hydrologiques et hydrogéologiques sont disponibles. Les différences entre tous les modèles donnés résident dans la complexité des processus qu'ils simulent, dans leur dimensionnalité, et dans la méthode de résolution numérique qu'ils ont adoptée. Indépendamment de la complexité des modèles, *Paniconi and Putti* [2015] montrent clairement que dans la dernière décennie, la modélisation des eaux souterraines a gagné en intérêt en développant des approches intégrées pour représenter les différents processus hydrologiques et leurs interactions, en particulier entre les eaux de surface et les eaux souterraines et entre l'écoulement et le transport [e.g.,

Fleckenstein et al., 2010]. La prise en compte des interactions entre les cours d'eau et les aquifères est de plus en plus considérée comme pertinente pour la gestion des ressources d'eau douce, car ils jouent un rôle majeur sur l'eau et sur les bilans des solutés aux échelles des bassins versants et sont déterminants pour la construction de l'hydrogramme et des distributions de temps de transit [*Winter et al.*, 1998; *Rodriguez-Iturbe*, 2000].

Des efforts importants ont été consacrés à l'élaboration et le raffinement des modèles numériques à base physique pour les simulations hydrologiques intégrées. Des modèles complexes hydrogéologiques souterraines ont été associés aux modèles d'écoulement de surface existants et une classe entièrement nouvelle de modèles capables de simuler des systèmes couplés comme un continuum a été développée : Parallel Flow (ParFlow) [*Kollet and Maxwell*, 2006], CATchment HYdrology (CATHY) [*Camporese et al.*, 2010], HydroGeoSphere (HGS) [*Therrien et al.*, 2012], OpenGeoSys (OGS) [*Kolditz et al.*, 2012], pour n'en citer que quelques-uns. En comparaison, il y a moins de modèles qui abordent les interactions d'écoulement et de transport entre la surface et la sous-surface [*Weill et al.*, 2011; *Therrien et al.*, 2012]. Malgré toutes les recherches expérimentales et numériques réalisées, il reste de nombreux défis à relever et de tests à mener sur les modèles hydrologiques intégrés actuels. Dans ce contexte, cette étude vise à apporter certaines améliorations à un modèle spécifique, et à tester ce modèle sur un versant expérimental avec un ensemble de données d'observation très détaillées.

S.1.1 Objectifs

Le processus de raffinement des modèles hydrologiques complexes implique une mise à jour constante, apportant des améliorations, l'introduction de nouveaux processus, l'avancement des calculs, la réalisation d'analyses et la capacité à tester de manière exhaustive le modèle. À cet égard l'objectif principal des travaux décrits dans cette thèse est d'aborder certains de ces défis dans le cadre d'un modèle spécifique, le modèle CATchment HYdrology Flow-Transport (CATHY FT) [e.g., *Camporese et al.*, 2010; *Weill et al.*, 2011]. Cet objectif général est développé en quatre objectifs spécifiques:

1. Utiliser une technique de reconstruction du champ de vitesse pour les simulations de transport d'advection: reconstruire les vitesses des eaux souterraines de CATHY_FT, qui sont basés sur les éléments finis et ne respectant le principe de

conservation de la masse, afin d'améliorer la précision du bilan de masse du modèle de transport advectif, qui lui est basé sur les volumes finis et s'appuie sur la précision du champ de vitesse utilisé.

2. Généraliser la condition limite de la zone de suintement pour le modèle d'écoulement: évaluer les erreurs commises lors de l'utilisation des approximations telles que les conditions de Dirichlet (statiques), étudier les interactions entre l'écoulement de surface et l'écoulement de la zone de suintement, et sa dynamique en présence d'hétérogénéité.

3. Simuler des essais de traçage réalisés avec des traceurs isotopiques et effectuées sur les versants artificiels au Landscape Evolution Observatory: explorer les limites du modèle en termes d'écoulement et de transport dans des conditions hétérogènes et variablement saturées et reproduire des réponses ponctuelles et intégrées de différentes variables pour les comparer aux données d'observation très détaillées.

4. Tester le comportement numérique et des algorithmes de couplage du modèle CATHY_FT: contribuer à répondre à des questions importantes de modélisation telles que le contrôle des erreurs de bilan de masse et améliorer la compréhension des interactions des processus et le traitement des conditions aux limites complexes.

S.1.2 Évolution du modèle CATHY_FT et structure de la thèse

Le début du développement du modèle CATHY_FT remonte à de nombreuses années, lorsque les processus souterrains et de surface et les processus d'écoulement et de transport étaient encore traités séparément. De nombreux chercheurs ont travaillé sur le modèle au cours des dernières années en introduisant étape par étape des complexités nouvelles. L'organigramme de la figure 1.1 montre schématiquement une partie des études liées au développement de CATHY_FT, rapportées dans une des sept sections représentant les différents processus simulés par le modèle (écoulement souterrain, écoulement de surface, couplage d'écoulement souterrain et de surface, transport souterrain, transport de surface et le couplage de transport souterrain et de surface), ainsi que les tests du modèle et les applications. L'organigramme montre également les améliorations que cette étude vise à apporter et les place en relation avec les différentes composantes d'évolution et

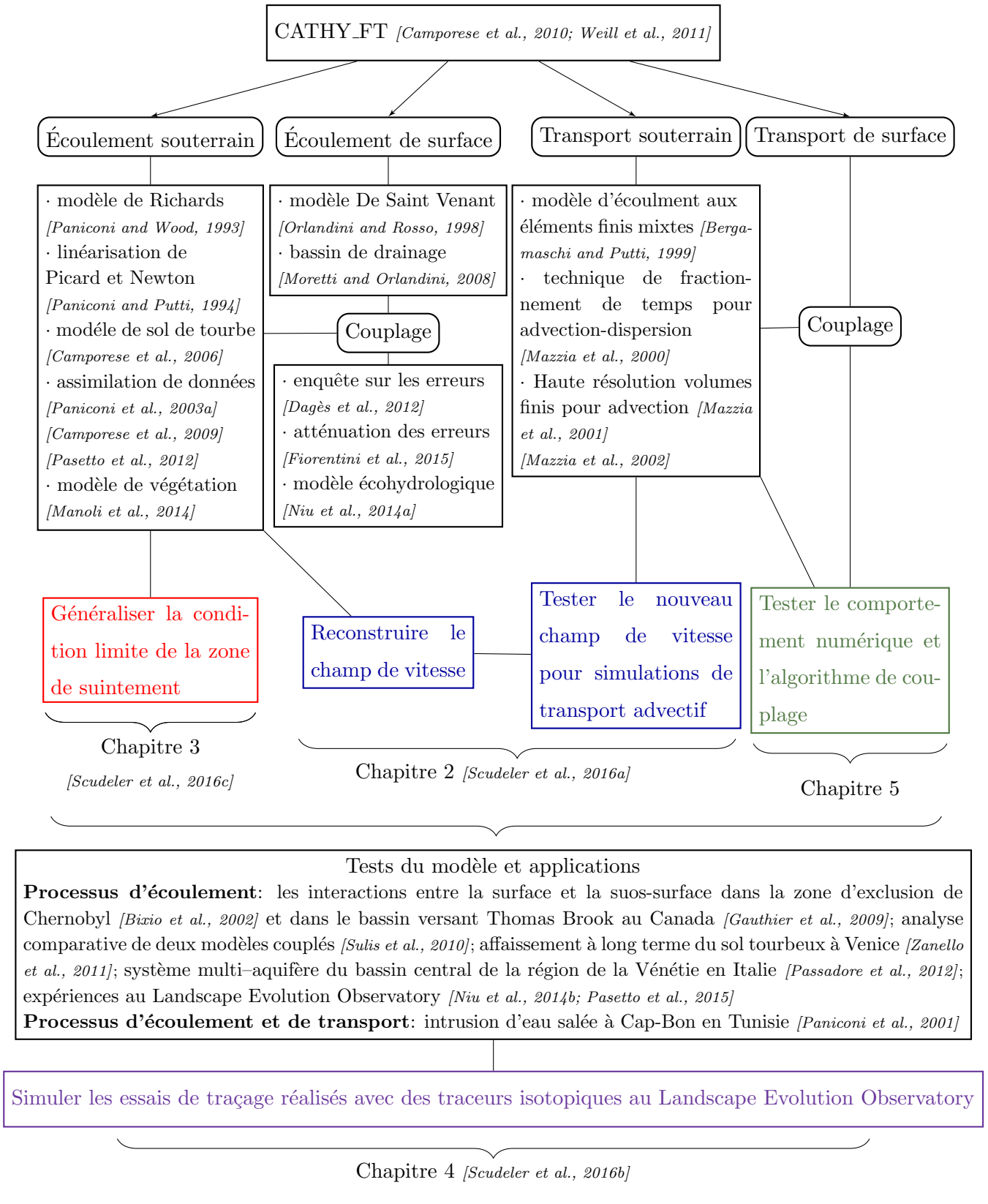

Figure 1: *Processus simulés par le modèle CATHY_FT et résumé des développements réalisés dans le cadre de cette thèse. Les objectifs de cette étude sont mis en évidence en rouge, bleu, vert et violet et sont insérés dans leur contexte.*

de développement du modèle. Chaque objectif sera traité dans un chapitre différent de la thèse, chaque chapitre constituant un document autonome soumis ou en train d'être soumis à une revue:

Chapitre 2 (objectif 1): (C. Scudeler, M. Putti, C. Paniconi, Mass-conservative reconstruction of Galerkin velocity fields for transport simulations, *Advances in Water Resources*, published July 2016). Le contenu est résumé dans la section S.2: Reconstruction des champs de vitesse de Galerkin basé sur le principe de conservation de la masse pour les simulations de transport.

Chapitre 3 (objectif 2) (C. Scudeler, C. Paniconi, D. Pasetto, M. Putti, Examination of the seepage face boundary condition in subsurface and coupled surface/subsurface hydrological models, *Water Resources Research*, submitted in May 2016). Le contenu est résumé dans la section S.3: Étude de la condition aux limites dans la zone de suintement pour des modèles d'écoulement souterrain ou des modèles couplés eau de surface–eau souterraine.

Chapitre 4 (objectif 3) (C. Scudeler, L. Pangle, D. Pasetto, G.-Y. Niu, T. Volkmann, C. Paniconi, M. Putti, P. Troch, Multiresponse modeling of variably saturated flow and isotope tracer transport for a hillslope experiment at the Landscape Evolution Observatory, *Hydrology and Earth System Science*, published September 2016). Le contenu est résumé dans la section S.4: Modélisation multi-réponses d'un essai de traçage en zone non saturée réalisé avec un traceur isotopique au Landscape Evolution Observatory.

Chapitre 5 (objectif 4) (C. Scudeler, C. Paniconi, M. Putti, Process-based model of surface-subsurface and flow-transport interactions: coupling, boundary conditions, and numerical behavior, manuscript in preparation). Le contenu est résumé dans la section S.5: Modélisation à base physique des processus d'écoulement et de transport entre la surface et la sous-surface: couplage, conditions aux limites, et comportement numérique.

Avant de procéder à un résumé de ces quatre chapitres, une brève introduction au modèle CATHY_FT est présentée, qui servira de référence pour les sections suivantes.

S.1.3 Le modèle CATchment HYdrology Flow-Transport

CATHY_FT est un modèle distribué à base physique qui simule les interactions entre la surface et sous-surface pour l'écoulement et de transport. Le modèle combine l'équation de Richards et l'équation d'advection-dispersion, utilisées respectivement pour décrire l'écoulement et le transport dans les milieux poreux variablement saturés, ainsi que l'équation d'onde de diffusion, utilisée pour décrire l'écoulement et le transport de surface. La solution de l'équation de Richards 3D pour la hauteur de charge variable est obtenue en utilisant la méthode des éléments finis linéaires pour la discrétisation spatiale et un système de contrôle des pas de temps appliqué aux différences finies. Le système est linéarisé par un schéma itératif de Picard ou Newton [*Paniconi and Putti*, 1994]. L'équation d'advection-dispersion est résolue au moyen d'une technique de fractionnement du temps qui combine un solver explicite de haute résolution en volumes finis (HRFV) pour l'advection avec un système implicite aux élément finis hybride mixte (MHFE) pour la dispersion. La solution des équations de surface est réalisée numériquement en utilisant la méthode explicite de Muskingum-Cunge. L'intégration des équations de surface et souterraines est réalisée avec une procédure d'itération séquentielle et le couplage est effectué avec un algorithme de changement des conditions aux limites. L'équation de transport est résolue suite à la résolution de celle d'écoulement.

S.2 Reconstruction des champs de vitesse de Galerkin basé sur le principe de conservation de la masse pour les simulations de transport

S.2.1 Introduction

Cette étude porte sur l'application d'un algorithme de recontruction des champs de vitesse qui améliore la précision de la modélisation du transport de solutés dans une matrice poreuse. Les méthodes standards éléments finis (FE) de Galerkin (ou Galerkin $\mathcal{P}_1$) sont souvent choisies pour résoudre les équations des écoulements de sous-surface pour leurs bas coûts de calcul. Cependant, leur utilisation dans ce contexte est connue pour être à l'origine de champs de champs de vitesse non conservatifs et donc pour générer des erreurs dans la résolution des équations de transport [*Klausen and Russell*, 2004; *Dawson*

et al., 2004a]. Deux différentes méthodes ont été testées pour surmonter ce problème : 1) l'utilization d'une méthode localement conservative pour discrétiser les équations (par exemple l'approximation multi-point des flux [*Edwards and Rogers*, 1998] ou la méthode des éléments finis mixtes (MFE) [*Brezzi and Fortin*, 1991; *Farthing et al.*, 2002]) et 2) la reconstruction en post-traitement des champs de vitesse de Galerkin $\mathcal{P}_1$ [*Larson and Niklasson*, 2004]. Dans le second cas, il est possible d'atteindre pratiquement le même niveau de précision qu'avec une méthode localement conservative, mais avec un coût de calcul beaucoup plus bas. C'est pour cette raison que les stratégies de post-traitement sont de plus en plus considérées comme une alternative avantageuse.

S.2.2 Méthodologie

Dans cette étude, l'approche de Lanson-Niklasson (LN) est implémentée au modèle CATchment HYdrology Flow Transport (CATHY_FT) [*Camporese et al.*, 2010; *Weill et al.*, 2011]. Il s'agit du couplage du solver $\mathcal{P}_1$ de Galerkin des équations de Richard avec un solver de haute résolution en volumes finis (HRFV) [*Mazzia and Putti*, 2005] pour l'équation de transport advectif. Les flux conservatifs locaux sont calculés par une méthode locale de post-traitement LN, puis intégrés dans la résolution du transport. Les bilans de masse des solutés sont utilisés pour estimer la qualité des vitesses LN par rapport aux vitesses FE, et ce pour des scénarios numériques avec des écoulements permanents ou transitoires, et du transport de soluté en régime transitoire. Les résultats issus de la méthode standart de Galerkin $\mathcal{P}_1$ sont confrontés aux résultats issus des flux LN. Comme MFE est considérée comme une méthode respectant la conservation de la masse, les flux numériques obtenus avec cette approche sont utilisés comme des solutions de référence [*Putti and Sartoretto*, 2009].

S.2.3 Résultats

Les résultats des deux simulations les plus importantes sont présentés ici. Le premier cas simule un écoulement en régime permanent, dans un milieu entièrement saturé, et avec du transport en régime transitoire. Les écoulements convergent vers une sortie en bas du domaine et celui-ci présente des blocs de conductivité inférieure à celle du reste du sol. La figure 2 montre le domaine ainsi que la paramétrisation correspondante du

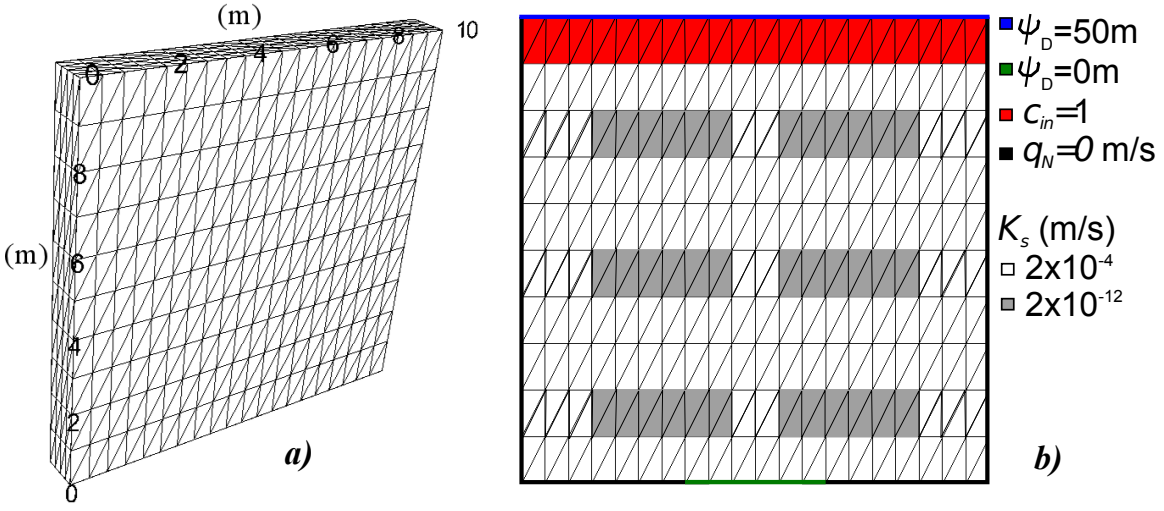

Figure 2: *Maillage du domaine pour le premier scénario (a) et conditions initiales et aux limites correspondantes (b).*

modèle. Le domaine de 10 x 10 m^2 est généré avec une structure en trois dimensions ayant une profondeur unitaire. Le domaine est entièrement saturé, et le régime permanent d'écoulement est assuré par le maintient des conditions aux limites constantes. Une condition limite de type Dirichlet, imposant une pression de $\psi_D = 50$ m en haut du domaine, est imposée. L'exutoire correspond à une portion centrée en bas du domaine sur laquelle il y a la condition $\psi_D = 0$ m. Sur toutes les autres limites, un flux nul est imposé. Six blocs de faible conductivité hydraulique ($K_s = 2 \times 10^{-12}$ m/s, c'est-à-dire huit ordres de grandeur en dessous de la conductivé du sol environnante) sont disposés dans le domaine (montrées en gris sur la figure 2). Le soluté entre dans le domaine par la première couche (montré en rouge sur la figure 2) avec une impulsion dont la concentration sans dimension est fixée à $c_{in} = 1$ et se déplace avec l'eau vers l'exutoire situé dans le bas du domaine.

La figure 3 montre l'évolution temporelle du bilan de masse obtenu avec le champ de vitesse FE. Le graphique represente dans l'ordre : la masse totale de soluté stockée dans le système (M_{st}), la masse cumulée sortie du domaine par la limite de flux imposé (M_{out}), la masse cumulée totale sortie du domain (M_{out_t}), la masse totale stockée dans les 6 blocs de faible K_s (M_{st_f}) et l'erreur sur le bilan de masse cumulée $MBE_1 = M_{in} - M_{st} - M_{out}$, où M_{in} est la masse totale initialement présente dans le système. Les trois variables sont reportées en termes de pourcentage par rapport à M_{in}. Les résultats montrent qu'un

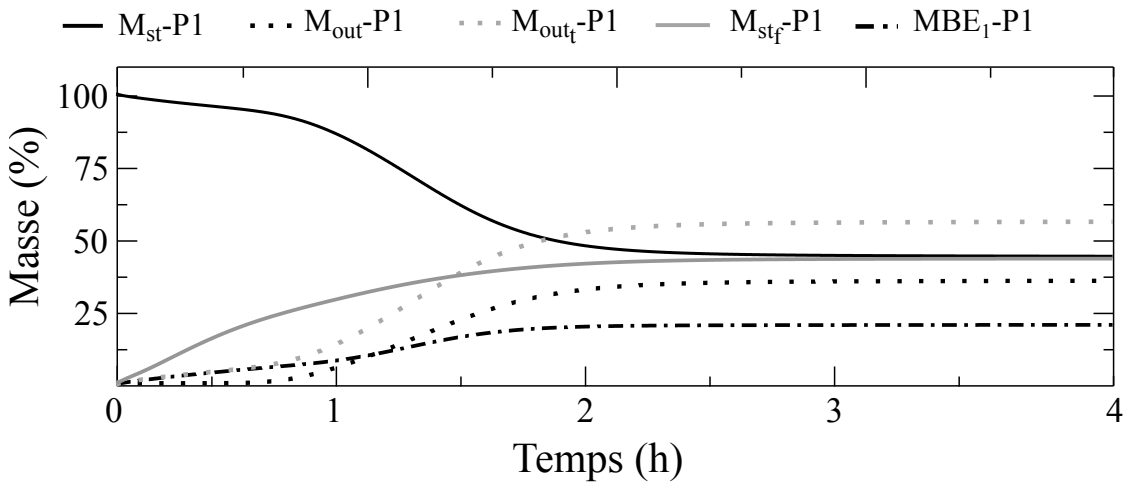

Figure 3: *Bilan de masse obtenu avec les vitesses Galerkin $\mathcal{P}_1$ pour le premier cas testé.*

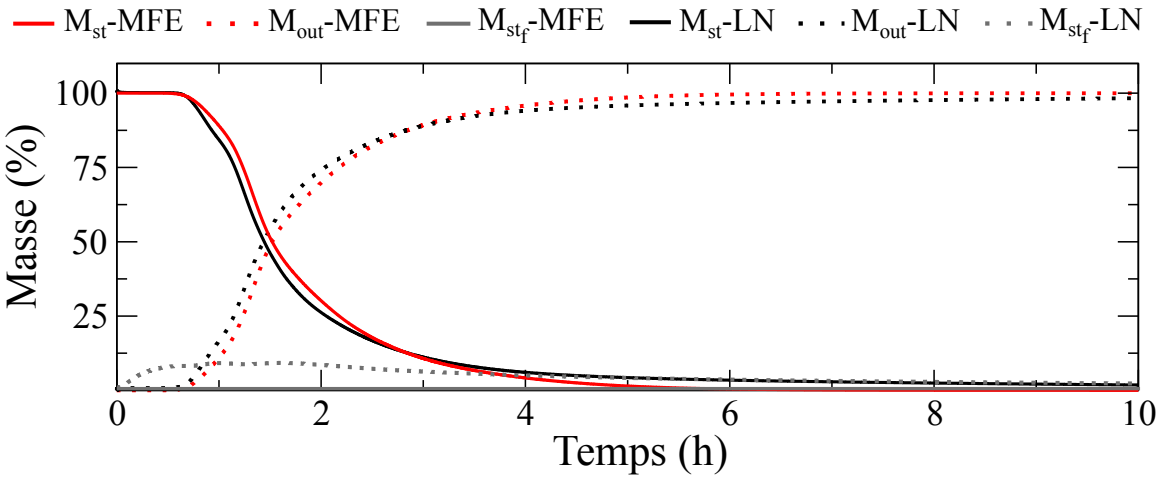

Figure 4: *Bilan de masse obtenu avec les vitesses LN et MFE pour le premier cas testé.*

volume non négligeable de masse de soluté sort par la limite de flux nul imposé. L'erreur relative du bilan de masse à la fin de la simulation est en fait $MBE_1 = 23\%$, tandis que l'erreur sur le bilan global calculé en tenant compte de la masse totale sortie par toutes les limites du domain, $MBE_2 = M_{in} - M_{out_t} - M_{st}$, est seulement de l'ordre de 10^{-3}. De plus, un phénomène de persistance de la masse semble s'illustrer dans la simulation : 4 heures après l'injection, 44% de la masse totale initiale reste piégée de façon permanente dans les 6 blocs de faible K_s. Ces deux phénomènes (le non respect de la condition de flux nul aux limites et l'effet de persistence) représentent une source d'erreur importante dans le bilan de masse. Elle sera mise en évidence en comparant ces résultats avec ceux obtenus avec le champ de vitesse LN et MFE.

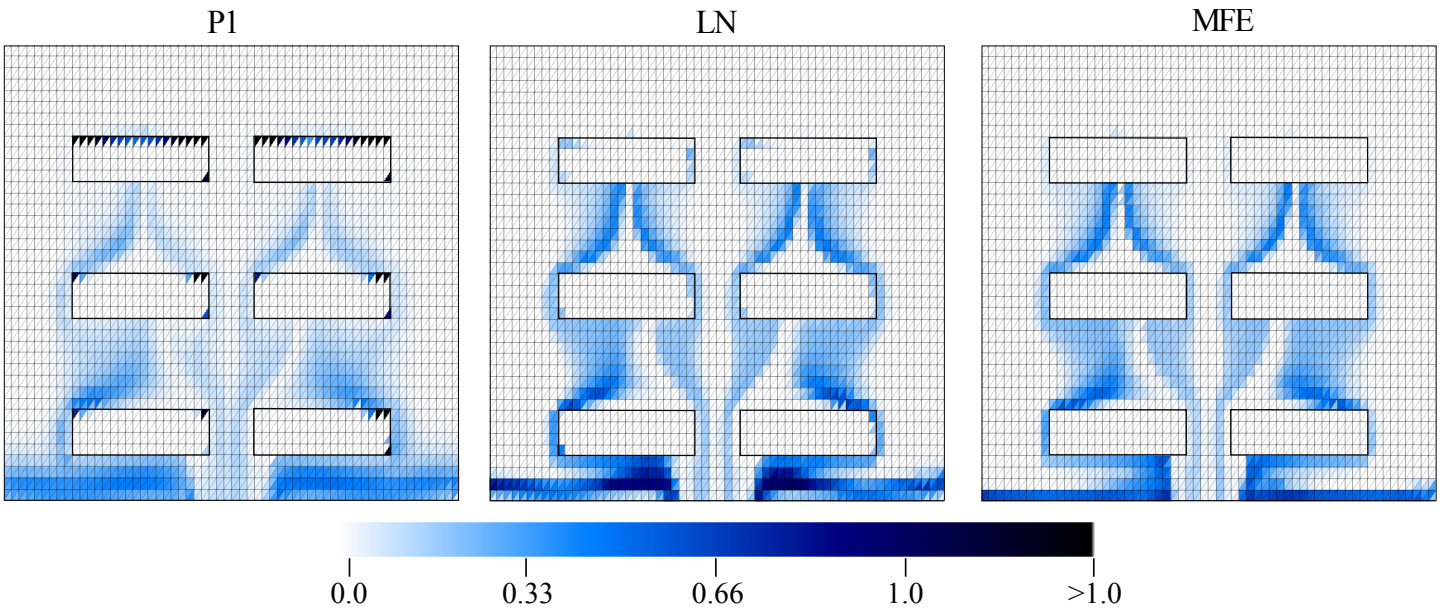

Figure 5: *Comparaison des profils de concentration à t = 1.5 h pour une section verticale du domaine pour le premier scénario obtenus avec les vitesses $\mathcal{P}_1$, LN et MFE.*

La figure 4 présente les résultats de bilan de masse lorsque les champs de vitesse MFE et LN sont utilisés pour la simulation du transport advectif. Dans les deux cas, les erreurs sur le bilan de masse calculées avec $MBE_1 = M_{in} - M_{st} - M_{out}$, sont négligeables (de l'ordre de 10^{-3}%), indiquant que la totalité de la masse quitte le système en passant par la limite d'écoulement de sortie imposée. La différence entre les deux résultats est causée par la forte hétérogénéité. Les flux LN conduisent une petite partie de la fraction de soluté dans les zones de faible K_s mais pas de façon permanente. Ce phénomène de persistance de masse est légèrement plus important que dans le cas MFE mais l'impact qui en résulte est indubitablement plus petit que dans le cas de Galerkin $\mathcal{P}_1$. Le même résultat peut de plus être observé dans la figure 5, où les profils de concentration à t=1.5 h obtenus en utilisant les vitesses $\mathcal{P}_1$ LN et MFE sont comparés. Des profils de concentration similaires sont produits par LN et MFE, avec des valeurs des concentrations toujours inférieurs à 1. Dans le cas Galerkin $\mathcal{P}_1$, au contraire, une accumulation de la masse dans les blocs de faible K_s est évidente, alors que les concentrations dans certains éléments atteignent des valeurs aussi élevées que 15 à l'instant d'observation considéré.

Le respect du principe de conservation de la masse est encore plus important dans le deuxième cas testé qui considère un écoulement et du transport en regime transitoire et variablement saturé. La figure 6 montre le domaine, le maillage utilisé, et la position

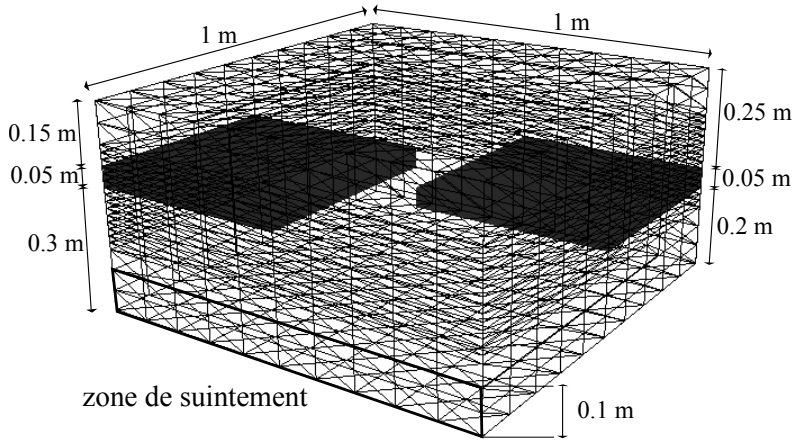

Figure 6: *Domaine tridimensionnel, grille tétraédrique utilisée, position des blocs de faible K_s et condition limite de suintement pour le deuxième cas testé.*

des deux blocs à faible conductivité K_s (huit ordres de grandeur en dessous de la conductivé des autres cellules). Une limite de suintement est située le long de la base au bord du domaine (montrée sur la figure 6). La surface est soumise à deux impulsions de précipitations spatiallement homogène et ayant une vitesse constante. Une première impulsion d'une durée de 12 h a lieu au début de la simulation, alors qu'une seconde impulsion est appliquée à partir de 36 h jusqu'à la fin de la simulation. La durée totale de la simulation est de 100 h. Au début, la nappe phréatique se trouve à la base du domaine et le sol ne contient aucun soluté. L'injection du soluté est réalisée avec la première impulsion de précipitation en imposant une concentration de l'eau de pluie égale à 1.

Outre les résultats obtenus pour le premiere cas testé, pour le cas Galerkin $\mathcal{P}_1$ une masse de soluté est générée artificiellement dans le domaine parce que certains éléments sont soumis à une source artificielle d'une masse d'eau en fonction du temps en raison de l'utilisation d'un champ de vitesse qui ne respecte pas le bilan de masse. Cette source artificielle d'eau est la cause de l'apparition d'une source artificielle de masse de soluté, qui est responsable de la forte augmentation des concentrations numériques de ces éléments, comme on peut le voir sur la figure 7 pour un tétraèdre spécifique, ce qui conduit à l'interruption de la simulation. Ce comportement est complètement rectifié par les vitesses LN, qui permettent de conserver le bilan de masse.

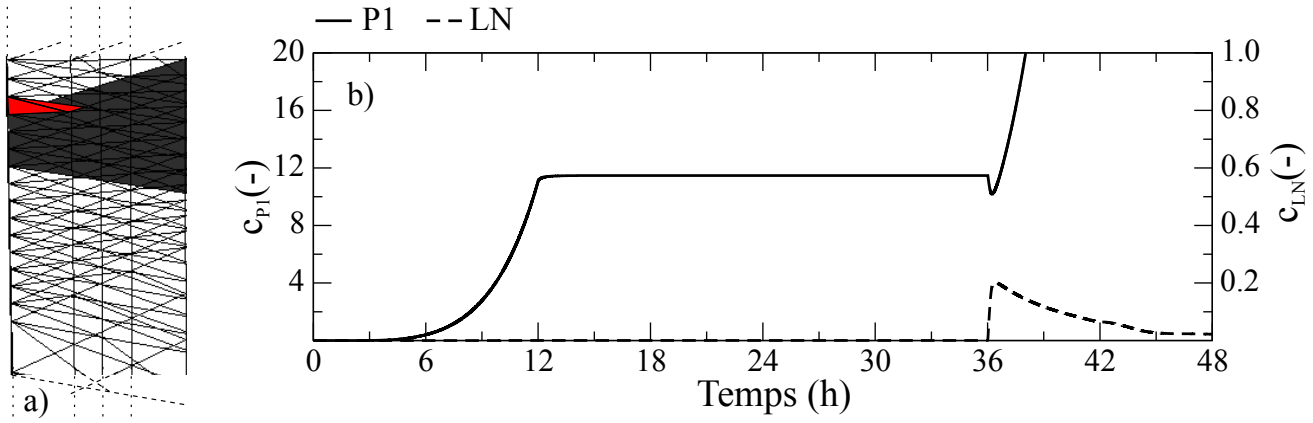

Figure 7: *Comportement de la concentration moyenne entrainée par des vitesses $\mathcal{P}_1$ et par des vitesses LN pour le tétraèdre d'observation montré dans le panneau a.*

S.2.4 Conclusions

Cette étude a porté sur l'application de l'algorithme de reconstruction Larson-Niklasson visant à rétablir les propriétés de conservation des champs de vitesse Galerkin $\mathcal{P}_1$ pour les simulations de transport. Il a été démontré que: 1) lorsqu'elle est entrainée par des vitesses Galerkin $\mathcal{P}_1$, la masse de soluté sort facilement du domaine par des limites de flux nul imposé; 2) le non respect de la condition de flux nul est complètement corrigée par les vitesses LN; 3) une grande partie de la masse de soluté reste piégée de façon permanente dans les zones de faible conductivité lors de l'utilisation des vitesses Galerkin $\mathcal{P}_1$; 4) et seulement une petite partie de la masse de soluté traverse en zones de faible conductivité dans le cas des vitesses LN.

Les résultats pour le cas test en regime variablement saturé, montrent que le champ d'écoulement numérique Galerkin $\mathcal{P}_1$ introduit des sources ou puits artificielles de masse qui entrainent une forte augmentation de la concentration de soluté dans certains éléments de la grille, et éventuellement à l'interruption de la simulation. En revanche, pour le champ d'écoulement généré par LN, aucune de ces inexactitudes n'apparait, ce qui démontre qu'un champ de vitesse localement conservatif est nécessaire pour simuler le transport de soluté avec un bon comportement de bilan de masse.

S.3 Étude de la condition aux limites dans la zone de suintement pour des modèles d'écoulement souterrain ou des modèles couplés eau de surface–eau souterraine

S.3.1 Introduction

Cette étude a pour objectif l'amélioration de la compréhension des conditions aux limites imposées dans les zones de suintement. Il s'agit en premier lieu de limiter les erreurs de modélisation qui pourraient y être associées et plus particulièrement, de déterminer quand ces surfaces de suintement sont nécessaires pour la modélisation ou, au contraire, quand elles peuvent être remplacées par des conditions aux limites plus simples comme celles de Dirichlet. Par la suite, il s'agira de modéliser des systèmes hétérogènes avec des points de sortie multiples. De plus, pour les modèles couplés eau de surface–eau souterraine, on s'interrogera sur l'interaction entre la surface de suintement et la condition à la limite utilisée pour décrire l'écoulement de surface et l'écoulement en rivière.

Une zone de suintement est définie par la surface à travers laquelle l'eau passe du sol saturé dans l'air à pression atmosphérique. Elle est généralement modélisée comme une condition latérale par laquelle l'eau est libre de sortir du domaine de modélisation en cas de saturation. Le point de sortie d'une zone de suintement est défini comme le point de rencontre des zones saturée et non saturée au-dessous duquel l'eau s'écoule. C'est une condition aux limites dynamique puisque dans des conditions transitoires, le point de sortie de la zone de suintement pourra changer de position. Il est important d'étudier le comportement de ces zones puisque la distribution des pressions, le niveau de la nappe phréatique ainsi que le champ des débits sont tous affectés par la manière dont elles sont modélisées. De plus, les cas hétérogènes complexes avec écoulement de surface n'ont pas encore été étudiés en détail dans la littérature.

S.3.2 Méthodologie

Les analyses sont effectuées à l'aide du modèle numérique CATHY [*Camporese et al.*, 2010]. Le modèle d'écoulement souterrain est basé sur une formulation en élément finis de l'équation de Richards tandis que le modèle de surface est basé sur une formulation en différences finies. L'algorithme original qui s'occupe des conditions aux limites pour la

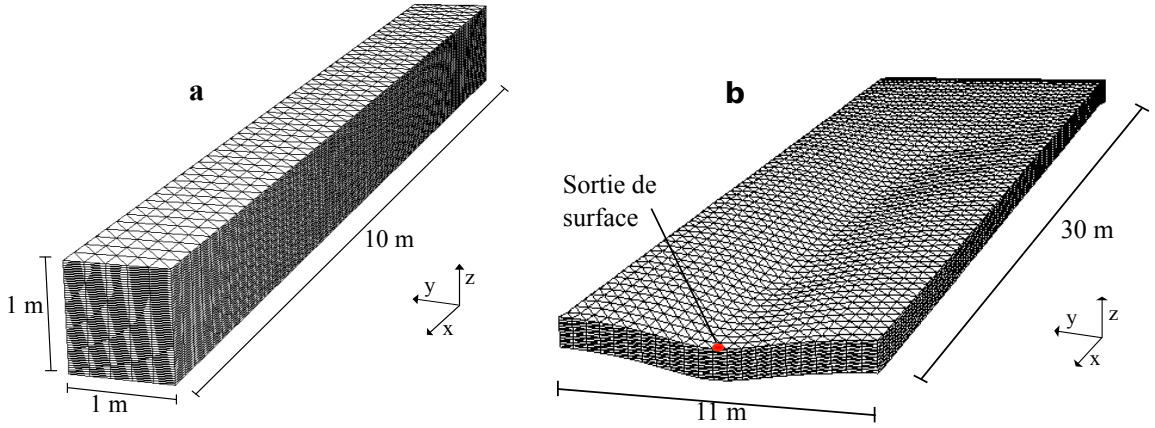

Figure 8: *Grille numérique 3D pour les cas de l'aquifère rectangulaire (a) et du versant de type LEO (b).*

zone de suintement dans CATHY découle de l'approche proposée par *Neuman* [1973] et ne considère qu'un unique point de sortie dont la position est actualisée après chaque itération non linéaire du schéma de Picard utilisé pour résoudre l'équation de Richards [*Paniconi and Putti*, 1994]. Cette thèse propose une généralisation de cette approche classique en simplifiant l'algorithme et en intégrant la possibilité de traiter plusieurs zones de suintement. Le nouvel algorithme prolonge des approches existantes comme celle de *Rulon and Freeze* [1985] qui ne permettait de travailler qu'avec deux points de sortie fixes. Dans cette étude, la zone de suintement est alternativement modélisée comme une limite statique (condition de Dirichlet) puis dynamique (condition mixte de Dirichlet et Neumann) et l'approche dynamique est testée dans des conditions d'hétérogenéité et dans un contexte de couplage des écoulements souterrains et de surface, en examinant ses interactions avec la limite de sortie du bassin versant. Les résultats principaux sont discutés dans la section suivante.

S.3.3 Résultats

La façon la plus simple de traiter une zone de suintement est de fixer la pression hydrostatique relative (par rapport à la pression atmosphérique) à zéro au point le plus profond de la surface de suintement (i.e., condition de Dirichlet) et le flux à zéro sur le reste de la surface (i.e., condition de Neumann sur le flux). Les différentes simulations ont montré que même en régime permanent, les simplifications proposées entrainent des erreurs non

négligeables puisque le point de sortie peut se retrouver ailleurs qu'en bas. Ces erreurs sont analysées en comparant les résultats obtenus avec le traitement statique (condition de Dirichlet) avec ceux obtenus en utilisant l'algorithme généralisé (condition dynamique). La comparaison est réalisée sur le domaine rectangulaire présenté à la figure 8a. Une condition de flux nul est imposée sur à la base de l'aquifère ainsi que sur les plans latéraux exceptés pour la zone de suintement elle-même. Les simulations considèrent une pluie constante et un état initial sec. L'erreur d'approximation est alors donnée par :

$$\epsilon^R = \frac{|Q_d^{ss} - Q_{sf}^{ss}|}{Q_{sf}^{ss}} \times 100 \tag{1}$$

avec Q_{sf}^{ss} et Q_d^{ss} les débits en regime permanent, respectivement pour les algorithme prenant en compte la dynamique de la zone de suintement et uniquement les conditions statiques de Dirichlet. Des conditions différentes de pentes (i=1, 10 et 30%), de conductivité hydraulique à saturation ($K_s = 1 \times 10^{-4}$ and 1×10^{-5} m/s), et d'intensité pluvieuse R sont testées.

La figure 9 rapporte les effets de (a) la conductivité hydraulique K_s (à pente fixe i=10%) et de (b) la pente i (à conductivité hydraulique fixée $K_s = 1.10^{-4}$ m/s) sur les erreurs d'approximation ϵ^R pour différents rapports pluie sur conductivité R/K_s et montre que l'erreur commise suite au traitement statistique de la zone de suintement plutôt que le traitement dynamique peut être relativement importante et augmente avec le rapport R/K_s (atteignant même 45%) comme avec la pente à R/K_s fixe. Pour le cas incluant couches hétérogènes, les figures 11 et 12 montrent l'importance des exutoires multiples dans la zone de suintement. Le test est reconduit pour la situation décrite sur la figure 8a pour une pente fixe i=10%. Une condition limite de suintement est imposée sur le plan vertical à droite. Les conditions atmosphériques (pluie constante à 1×10^{-5} m/s) sont imposées sur la surface, et le flux est fixé à zéro sur les autres limites sauf à l'exutoire. Le cas d'étude est composé de quatre couches d'épaisseur égale et de conductivité hydrauliques différentes (figure 10).

La simulation inclut la présence de trois zones de suintement avec les points de sortie correspondant. La figure 11 montre leur dynamique. Au début, une seule zone de suintement est présente, dont le point de sortie (ligne noire dans la figure 11) est en bas. Une deuxième zone de suintement se développe lorsque l'infiltration atteint la couche 2 (à environ 1.5 h). Son point de sortie (ligne bleue) se situe à l'interface entre les deux

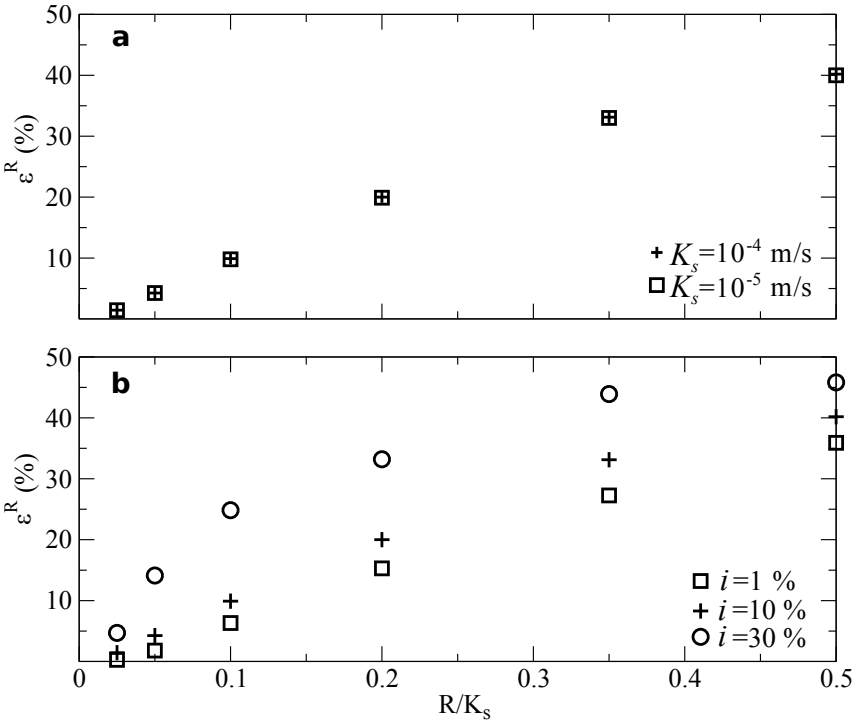

Figure 9: *Erreur d'approximation ϵ^R en fonction du ratio pluie/conductivité, R/K_s, pour les simulations pluvieuses sur un aquifère homogène (a) de pente i=10% à conductivité hydraulique K_s variable et (b) à conductivité hydraulique $K_s = 1 \times 10^{-4}$ m/s et de pente variable.*

premières couches et ne bouge jamais. Une troisième zone de suintement se forme lorsque l'infiltration atteint la couche 4, à environ 7 h, avec son point de sortie (ligne rouge) à la jonction entre les couches 3 et 4. À 8 h, l'eau de pluie atteint le bas et le premier point de sortie s'élève à hauteur du troisième point de sortie, résultant en une fusion de la première et de la troisième zone de suintement. La figure 12 montre le profil de hauteur d'eau en coupe verticale pour les deux derniers mètres du versant à 7 h, quand les trois zones de suintement sont présentes et à l'état stationnaire. À partir des contours de pression nulle, délimités par les lignes noires, les différentes zones de suintement sont facilement visibles.

Les interactions entre une zone de suintement (modèle souterrain) et les limites de sortie de bassin versant (modèle d'écoulement de surface) sont également analysées pour le Landscape Evolution Observatory (LEO) du complexe Biosphere 2 en Arizona [*Hopp et al.*, 2009]. L'analyse est basée sur l'examen de la répartition de l'eau de pluie à l'état stationnaire entre la sortie de la zone de suintement Q_{sf} et l'écoulement de surface Q. Le

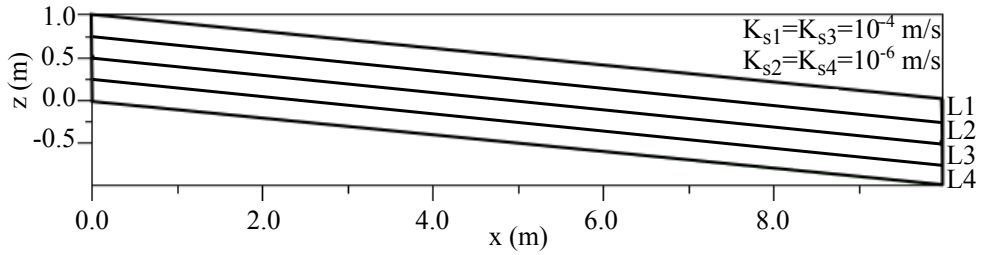

Figure 10: *Coupe verticale de l'aquifère incliné pour les configurations multicouches, montrant les valeurs de conductivité hydraulique ou les rapports utilisés.*

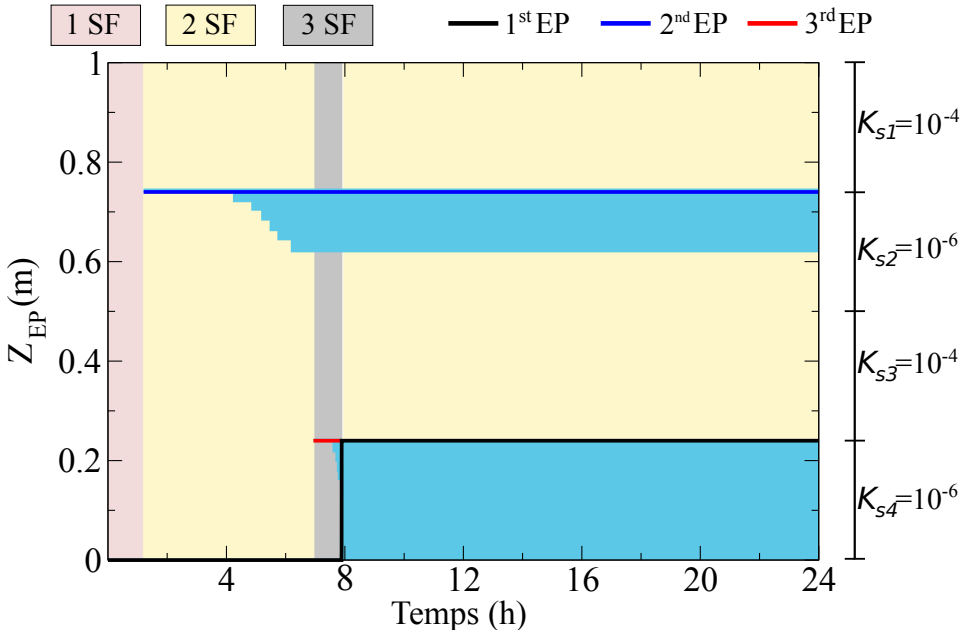

Figure 11: *Dynamique d'écoulement pour le premier (ligne noire), deuxième (ligne bleue) et troisième (ligne rouge) exutoires dans le cas des couches hétérogènes. Les surfaces de suintement (SS) situées sous chaque exutoire sont représentées figurées en bleu ciel. Les zones roses, jaune et grises représentent les durées respectives pendant lesquelles un, deux puis trois SS sont activées.*

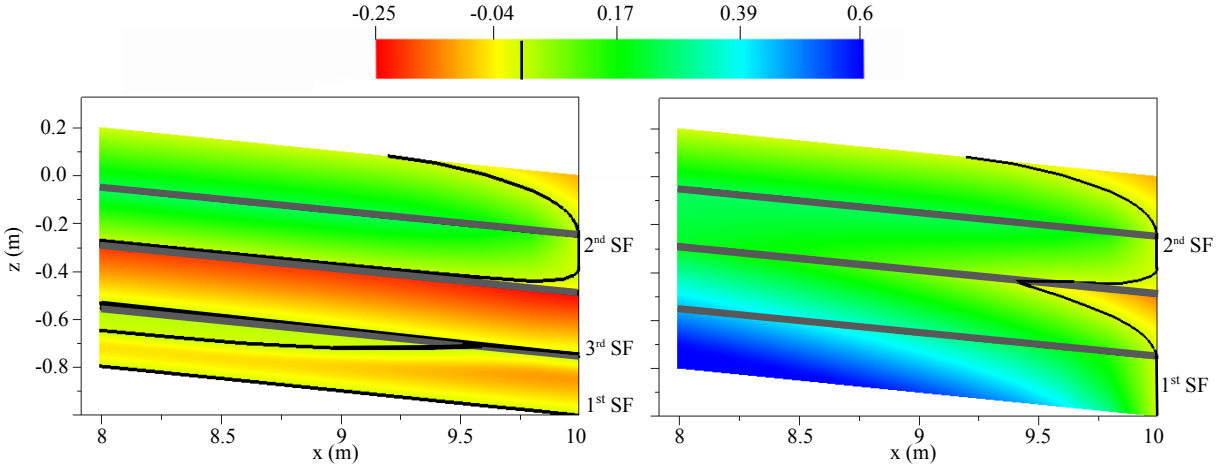

Figure 12: *Aperçus des profils de hauteur d'eau en coupe verticale à 7 h (gauche) et à état stable (droite) d'une portion de 2 m de la pente du versant pour les simulations multicouches. Les interfaces entre couches sont marquées par les lignes grises, et les contours de hauteur piézométrique nulle sont représentés par les lignes noires.*

domaine de LEO est illustré à la figure 8b. Les conditions atmosphériques à la limite de surface, une limite de suintement sur le plan vertical de la pente à droite, et des conditions de flux nul à la limite inférieure et le long des trois autres limites latérales sont imposées. La sortie du bassin versant pour le modèle d'écoulement de surface du CATHY correspond à la cellule de surface montrée en rouge sur la figure 8b. La conductivité hydraulique K_s du système est fixée à 1×10^{-4} m/s et la nappe phréatique est initialement fixée au niveau correspondant à la base. Les simulations sont exécutées pour un ensemble de taux de précipitations R et pour des angles de pentes i de 3, 10 et 20%.

Les résultats, présentés en figure 13, montrent que la contribution Q_{sf}/R de la zone de suintement diminue avec R/K_s et augmente avec i. Des taux de précipitations plus élevés augmentent ainsi l'écoulement de surface alors que des pentes abruptes augmentent l'écoulement à la base du versant. Les résultats montrent aussi que les différences entre les trois courbes deviennent moins significatives à mesure que R/K_s augmente.

S.3.4 Conclusions

Cette étude présente une modélisation des conditions aux limites des zones de suintement. Les aspect spécifiquement examinés sont : 1) les erreurs d'approximations apparaissant avec l'utilisation d'un traitement statique plus simple de la limite représentant une zone

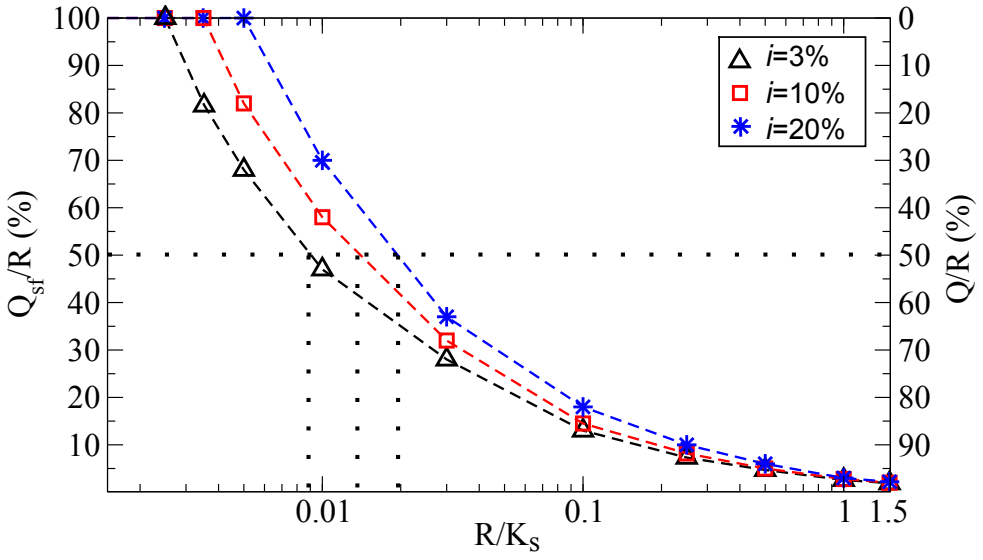

Figure 13: *Répartition de l'eau de pluie R sur le versant LEO entre la sortie Q_{sf} de la zone de suintement (axe de gauche) et le débit Q de l'écoulement de surface (axe de droite) à l'état stable pour un ensemble de rapports précipitations/conductivité (R/K_s) et trois différents angles i de pente. La ligne pointillée horizontale et les trois lignes pointillées verticales donnent les valeurs de R/K_s pour lesquelles les contributions du suintement et de l'écoulement sont identiques (R/K_s = 0.009, 0.012 et 0.02 pour les angles de 3%, 10% et 20% respectivement).*

de suintement au lieu d'une approche dynamique; 2) le comportement des zones de suintement sous conditions d'hétérogénéité ; et 3) les interactions entre une zone de suintement et un exutoire de bassin versant dans les modèles intégrés surface–souterrain. Les résultats montrent que la condition statique (Dirichlet) n'est pas toujours adéquate pour modéliser la zone de suintement dynamique, en particulier en conditions de fortes précipitations, pente abrupte et hétérogénéité; que les versants ayant des couches hétérogènes créent de multiples zones de suintement à l'interface de ces surface contrastées qui peuvent être extrêmement dynamiques; et que les zones de suintement et les limites d'exutoires peuvent coexister dans les modèles hydrologiques intégrés et qu'il jouent chacun un rôle important.

S.4 Modélisation multi-réponses d'un essai de traçage réalisé avec un traceur isotopique au Landscape Evolution Observatory

S.4.1 Introduction

Le but de cette étude est de réaliser des simulations à partir d'un jeu de données d'observations très important incluant des données qualitatives et quantitatives sur l'écoulement des eaux souterraines et des données spatialement distribuées d'écoulement et de transport. Le CATHY_FT est appliqué à des versants d'une maquette du Landscape Evolution Observatory (LEO) [*Hopp et al.*, 2009]. LEO est une infrastructure de recherche de grandes dimensions au service de la communauté gérée par l'université d'Arizona à Oracle aux Etats-Unis (Bâtiment Biosphere 2). Elle est constituée de trois versants convergents, de 30 m de long et 11.5 m de large, contenant 1 m de sol limono sableux. Chaque versant possède un réseau dense de capteurs et d'échantillonneurs capables d'identifier l'hétérogénéité à l'échelle du mètre et l'hétérogénéité latérale de l'humidité du sol, de l'énergie et des flux. Elle possède aussi un système de simulation de pluie innovant qui permet d'appliquer des précipitations entre 3 et 45 mm/h de façon homogène ou hétérogène. Le deutérium (^2H) et l'isotope de l'oxygne (^{18}O) sont utilisés comme traceurs pour marquer l'eau et peuvent être introduits au système à des concentrations connues via le simulateur de pluie. La figure 14 montre une vue depuis le haut d'un des trois versants, le système de collecte d'eau et le simulateur de pluie. Pouvoir réaliser des expériences au LEO représente une opportunité exceptionnelle pour modéliser des processus complexes. De telles modélisations sont possibles grâce aux jeux de données variées provenant d'expériences détaillées et multidisciplinaires (le réseau de bassins versants expérimentaux TERENO [*Zacharias et al.*, 2011] ainsi que le bassin versant artificiel Chicken Creek [*Hofer et al.*, 2012] en sont des exemples récents). La modélisation de ces processus complexes pourra ainsi contribuer activement à l'amélioration de la génération actuelle de modèles hydrologiques intégrés (surface/sous-surface) [*Sebben et al.*, 2013; *Maxwell et al.*, 2014].

A ce jour, deux expériences ont été conduites au LEO, un test impliquant de la pluie et du drainage en février 2013 [*Gevaert et al.*, 2014; *Niu et al.*, 2014b], évaluant les écoulements souterrains et de surface, et un test de traçage isotopique en avril 2013 [*Pangle et al.*, 2015], réalisé avec un sol sec au départ et une pluviométrie moindre dans le but

Figure 14: *Un versant (haut), le collecteur de flux en sortie de la surface de suintement (en bas à gauche) et le simulateur de pluie (en bas à droite) du Landscape Evolution Observatory (LEO).*

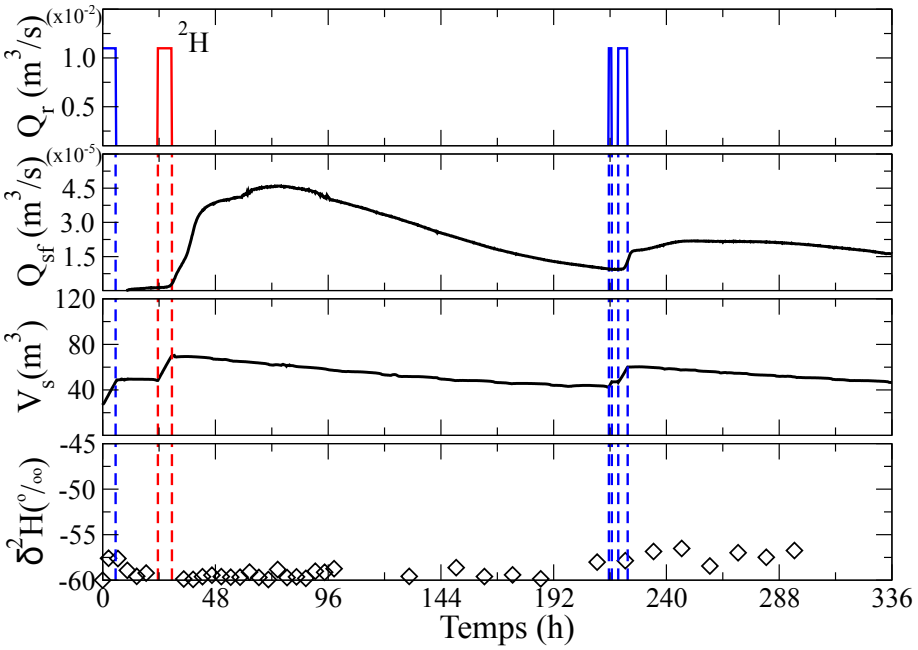

Figure 15: *Réponse hydrologique de l'expérience de traçage sur le site LEO. À partir du haut : périodes d'entrée de pluie mesurées Q_r (l'impulsion rouge est enrichie en deutérium); écoulement à la surface de suintement Q_{sf}; stockage total d'eau V_s; et valeurs de δ_{2H} moyennes à la surface de suintement. Le temps 0 correspond au 13 avril 2013, 9h30.*

de réduire le ruissellement de surface. En utilisant les données intégrées (capteur de charge et surface de suintement) et réparties (mesures ponctuelles dans l'espace d'humidité et de concentration) collectées pendant l'expérience de traçage, l'objectif de cette étude est d'identifier les défis, le comportement des différents processus, que représente la modélisation des écoulements saturés et non saturés ainsi que le transport de solutés à l'aide de modèles 3D complexes à base physique.

S.4.2 Expérience de traçage isotopique

La figure 15 illustre la réponse hydrologique de l'expérience de traçage isotopique. Trois périodes de pluie ont été injectées à un taux de 12 mm/h dans le système: au temps 0, (13 avril 2013, 9h30) pendant 5.5 h, après 23.5 h pendant 6 h, et finalement après 9 jours (215.5 h) pendant 1.25 h + 4 h séparés par 3 h sans pluie. Le deutérium a été introduit dans le système avec la deuxième période de pluie. Auparavant, le déficit de deutérium

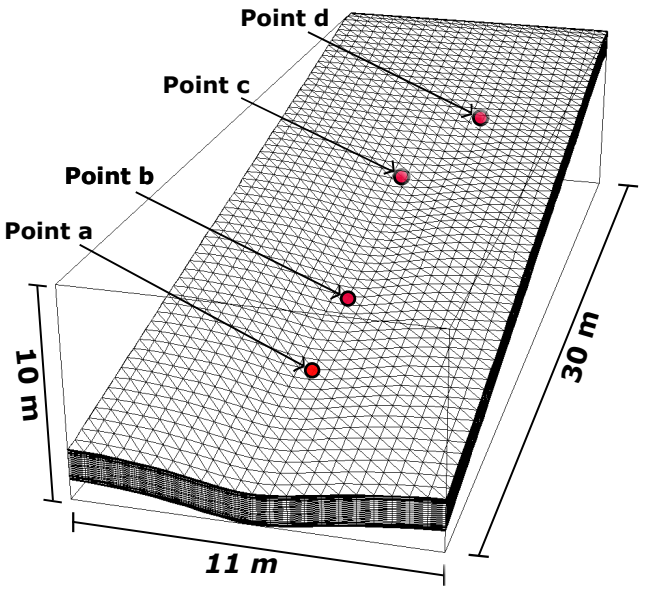

Figure 16: *Grille numérique 3D pour le site LEO. Les points a, b, c et d sont les emplacements où les échantillons ont été récoltés durant l'expérience pour être ensuite analysés en laboratoire.*

(δ_{2H}) mesuré dans le système, dans l'eau de la première et troisième périodes, était de -60‰. Au départ, le système était sec puisqu'il n'avait pas été humidifié durant les 6 semaines précédant l'expérience. Le volume total initial d'eau est estimé à environ 26 m^3 (la capacité de stockage totale du domaine est de 135 m^3). Toute l'eau de pluie injectée s'est infiltrée dans le sol et a généré un écoulement à travers la surface de suintement qui débuta après 5 h. Deux pics d'écoulement ont été observés: le premier après la deuxième période de pluie avec une pointe à 4.5×10^{-5} m^3/s et le deuxième après les deux dernières impulsions avec une pointe à 2.1×10^{-5} m^3/s. Le stockage total d'eau, l'écoulement total à travers la surface de suintement, l'humidité du sol, et la pression ont été mesurés toutes les 15 min durant l'expérience. Sachant que l'évaporation n'a pas été mesurée directement, elle a été estimée à partir de calculs de bilans hydriques. L'eau s'écoulant à travers la surface de suintement et au niveau des senseurs a été échantillonnée et analysée par la suite pour le δ_{2H}. Les données rapportées incluent les échantillons collectés à 5, 20, 50 et 85 cm sous la surface aux quatre emplacements tels qu'illustrés à la figure 16 (points a à d).

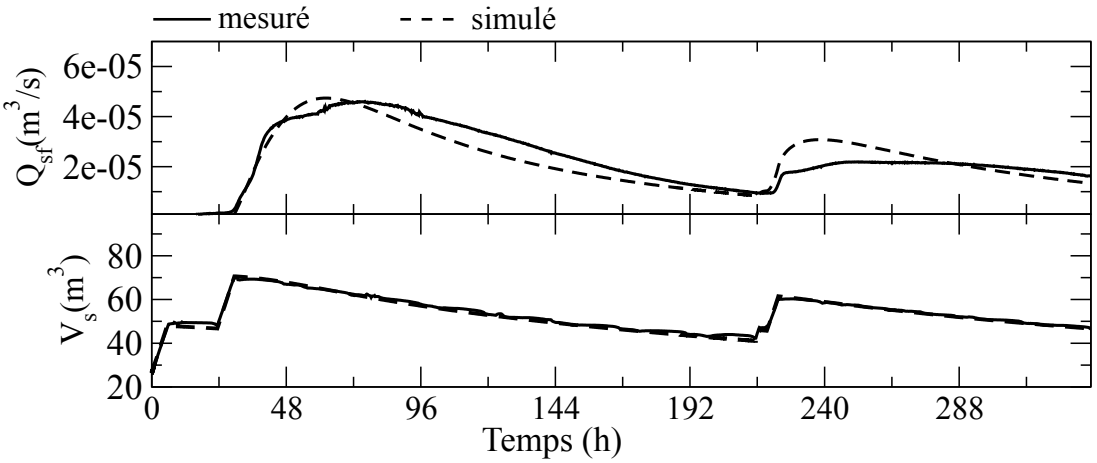

Figure 17: *Analyse des écoulements intégrés sur le domaine. L'écoulement à travers la surface de suintement Q_{sf} (en haut) et le stockage total d'eau V_s (en bas) sont rapportés.*

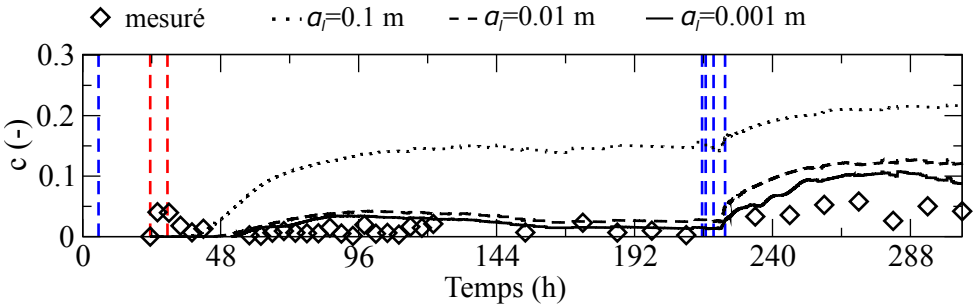

Figure 18: *Réponse du transport intégré sur le domaine pour différentes valeurs de dispersivité. Les lignes pointillées verticales indiquent les temps d'injection.*

S.4.3 Résultats

Les figures 17 and 18 montrent les résultats des simulations du modèle pour la réponse intégrée. La solution pour le flux a été obtenue par une paramétrisation très simple: homogénéité des paramètres hydrauliques du sol, homogénéité de la conductivité hydraulique K_s (sauf pour la surface de suintement, pour laquelle une plus petite valeur a été choisie, en concordance avec les résultats de la première expérience au LEO *Niu et al.* [2014b]) et uniformité spatiale des conditions atmosphériques. Les conditions initiales du modèle ont été établi conformémentles aux mesures d'humidité du sol à chaque emplacement de détecteur. Les résultats de vitesses et de saturation à différentes périodes ont été utilisés dans le modèle de transport pour générer trois scénarios ayant différentes valeurs de dispersitivé pour différentes valeurs de dispersivité longitudinale et transversale (α_l et α_t).

Dans les trois cas, la valeur de α_t a été choisie à un ordre de grandeur inférieur à celui de α_l. Les valeurs de $\delta_2 H$ sont exprimées avec c [-], qui correspond à la concentration par rapport au déficit minimum 0. $c = 0$ signifie que, le déficit dans l'eau est maximal (-60‰), alors que c=1 signifie qu'il n'y a pas de déficit dans l'eau. C'est pourquoi la condition initiale imposée partout est c=0.

Sur la figure 17, on peut voir les flux mesurés et simulés de la surface de suintement et le stockage total. Concernant l'écoulement de la surface de suintement, le modèle simule bien l'arrivée des deux pics dans le temps, mais il surestime légèrement les valeurs du second pic. Dans le cas du stockage total, les différences entre le modèle et la réponse observée sont négligeables. La figure 18 montre les résultats du modèle de transport pour c, sur la surface de suintement et pour des valeurs de dispersivité différentes. Les trois courbes indiquent que la différence entre les valeurs c mesurées et simulées diminue avec α_l. Pour la plus grande valeur de α_l testée (0.1 m), ^2H apparait juste aprés la deuxième impulsion, ce qui diffère de ce qui a été observé ainsi que des résultats du modèle obtenus en réduisant la valeur de α_l de un ou deux ordres de grandeur. Dans les trois cas, le modèle reproduit l'augmentation de c, aprés la dernière impulsion. Cependant, bien que les valeurs simulées soient quatre fois supérieures à quelles observées pour α_l= 0.1 m, pour α_l= 0.01 m et α_l= 0.001 m, elles diminuent significativement.

Pour passer de la réponse intégrée à une réponse spatialement discrétisée du flux, il faut complexifier la paramétrisation du modèle, de façon à obtenir une correspondance appropriée entre les réponses mesurées et simulées. L'analyse se focalise sur les profils volumétriques de teneur en eau, pour les quatre points spécifiques qu'on peut voir sur la figure 16, à 5, 20, 50 et 85 cm de profondeur. Les paramètres hydrauliques de van Genuchten sont changés en foction de la couche. Dans la figure 19, les données du teneur en eau sont comparées avec les résultats du modèle obtenus pour un cas de n_{VG} homogène (utilisé pour l'analyse intégrée) et pour un cas de n_{VG} hétérogéne. La paramétrisation plus précise (avec un n_{VG} variable) donne de meilleurs résultats, bien que pour certaines profondeurs de sol (en particulier, à 50 et 85 cm) et quelques points (point c, notamment) les différences entre les deux séries de temps θ soient assez marquées.

Aucune paramétrisation supplémentaire n'a été tentée pour l'analyse de la réponse du transport distribué, correspondant au profil de concentration à des endroits différents. La figure 20 compare, comme dans la figure 19 pour les profils volumétriques de teneur en eau,

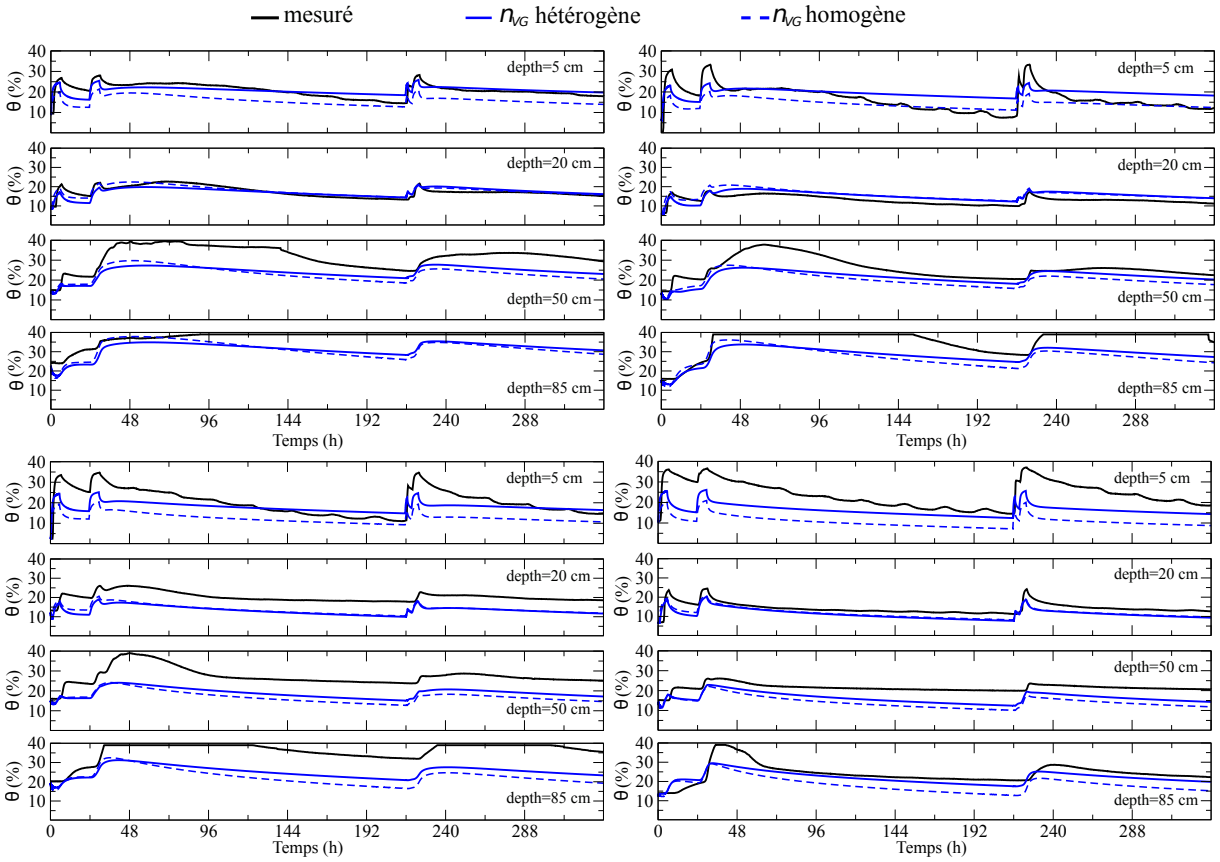

Figure 19: *La réponse hydrologique distribuée (état interne au domaine) pour les profils θ à 5, 20, 50 et 85 cm de profondeur pour quatre emplacements sur le versant LEO: point a (en haut, à gauche), point b (en haut, à droite), point c (en bas, à gauche) et point d (en bas, à droite) de la figure 16.*

les résultats du modèle à des points individuels et pour plusieurs profondeurs obtenues utilisant un paramètre n_{VG} uniforme et variable. Dans les deux cas, les résultats sont obtenus pour une dispersivité α_l=0.001 m. A cause de la durée de l'échantillonnage et des coûts élevés inhérents à l'analyse exhaustive des compositions en isotopes au laboratoire, un nombre plus réduit de données a été pris en compte que dans le cas d'écoulement. Les résultats montrent que le modèle n'obtient pas de bons résultats à plusieurs endroits (en particulier à 20 et 5 cm de profondeur pour le point b). Il est cependant encourageant de constater que les résultats concordent avec ceux obtenus précédemment pour les flux distribués. Bien que les résultats du modèle avec un n_{VG} spatialement variable soient meilleurs que dans le cas d'un n_{VG} uniforme, la performance du modèle à reproduire la réponse mesurée est considérablement pire que pour l'écoulement.

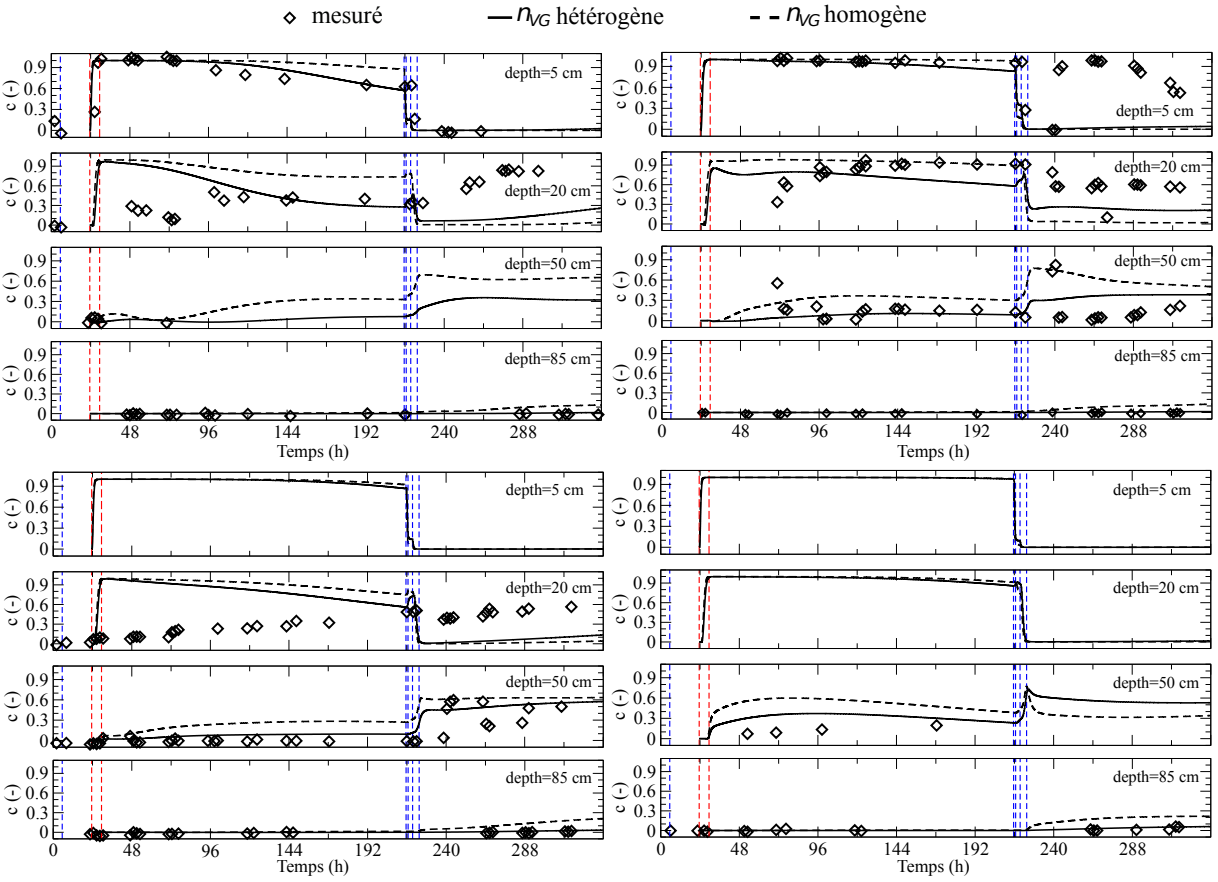

Figure 20: *Réponse hydrologique distribuée (état interne au domaine) de la concentration du traceur à 5, 20, 50 et 85 cm de profondeur pour quatre localisations sur le versant du LEO: point a (en haut à gauche), point b (en haut à droite), point c (en bas à gauche) et point d (en bas à droite) de la figure 16. Aucune mesure de la concentration en traceur n'a été effectuée à 5 cm de profondeur pour le point c et à 5 et 20 cm de profondeur pour le point d. Le modèle de transport est calculé pour α_l=0.001 et α_t=0.0001 m.*

S.4.4 Conclusions

Les résultats issus de la modélisation pour cette première expérience de traçage isotopique au LEO témoignent de la difficulté de tester et valider la nouvelle génération de modèles hydrologiques intégrés. Une bonne adéquation entre les variables intégrées mesurées et simulées a été obtenue en utilisation une paramétrisation simple, tandis qu'en passant au réponse distribuée d'écoulement il a été nécessaire d'introduire une hétérogénéité additionnelle dans les paramètres hydrauliques du sol. L'hétérogénéité additionnelle améliore également l'adéquation entre les points de mesure des concentrations en traceur, même si la performance du modèle à reproduire la réponse mesurée diminue considérablement. Cela suggère la nécessité de complexifier la paramétrisation du modèle ou l'existence de lacunes dans la représentation du processus des phénomènes de transport de soluté dans les sols très secs et hétérogènes. Les limites rencontrées dans ce modèle, d'un point de vue de la procédure expérimentale (concentrations faibles, les conditions initiales sèches et des mesures non constants de la masse de soluté) et de la formulation du modèle, pourront guider les prochaines études au LEO.

S.5 Modélisation à base physique des processus d'écoulement et de transport entre la surface et la sous-surface: couplage, conditions aux limites, et comportement numérique

Les modèles hydrologiques qui intègrent une description et résolution détaillées des interactions du soluté entre la surface et la sous-surface sont à leurs débuts et de nombreuses améliorations spécifiques sont possibles, réalisables uniquement en effectuant des analyses approfondies et rigoureuses de leur comportement physique et numérique. Dans cette étude, ce défi est abordé pour le modèle CATHY_FT, en décrivant certaines de ses caractéristiques et en identifiant quelques-unes des questions clés liées à son développement, comme le contrôle de la dispersion numérique et des erreurs de bilan de masse, le traitement des conditions aux limites complexes, et la description des interactions entre les processus.

CATHY_FT [*Weill et al.*, 2011] est un modèle à base physique en évolution qui couple l'équation 3D de Richards et l'équation d'advection-dispersion, utilisées pour décrire les

processus de flux et de transport souterrains, avec l'équation d'onde diffusive, utilisée pour décrire l'écoulement de surface et la propagation de transport de soluté sur la surface.

La solution des équations de surface est obtenue numériquement en utilisant la méthode Muskingum-Cunge pour le débit d'écoulement Q [L^3/T] et le débit massique de soluté Q_m [M/T]. L'équation de Richards est discrétisée en utilisant la méthode des éléments finis linéaires, ou $\mathcal{P}_1$, de Galerkin pour la discrétisation spatiale et un système de contrôle implicite des pas de temps appliqué aux différences finies, linéarisé par un schéma itératif de Picard. L'équation est résolue dans sa forme conservatrice [*Celia et al.*, 1990a] pour la hauteur piézométrique h [L] et la teneur volumétrique en eau θ [-]. Le champ de vitesse Galerkin $\mathcal{P}_1$ q, post-calculé à partir des valeurs de hauteur piézométrique nodaux, est reconstruit avec l'algorithme de post-traitement Larson-Niklasson (LN) visant à rétablir les propriétés de conservation de la masse [*Scudeler et al.*, 2016a] et est utilisé comme entrée par le modèle de transport souterrain. L'équation de transport souterrain est résolue pour la concentration c au moyen d'une technique de fractionnement de temps qui combine un système explicite de haute résolution en volumes finis (HRFV) pour l'advection avec un système implicite aux élément finis (FE) linéaires de Galerkin pour la dispersion.

L'intégration des équations de surface et de sous-surface est réalisée par une procédure d'itération séquentielle. La solution des équations de flux et de transport est gérée de la même manière car dans la procédure de solution séquentielle, les modules de flux sont résolus avant leurs homologues de transport. Le contrôle sur l'évolution du pas de temps de la procédure globale est fait par le routeur d'écoulement souterrain, sous la seule réserve d'une contrainte de convergence liée au schéma non linéaire. En revanche, la stabilité de la méthode explicite utilisée pour discrétiser les équations de surface est soumise à la constrainte de Courant-Friedrichs-Lewy (CFL) [*Courant et al.*, 1967] sur le pas de temps. Ainsi, pour chaque pas de temps Δt de la sous-surface, de multiples intervalles de temps de surface sont accomplis. Les flux dispersifs de l'équation de transport souterrain ne sont pas limités par conditions de stabilité ou de convergence, donc le pas de temps dispersif est synchronisé avec l'étape de temps de flux souterrain ($\Delta t_d = \Delta t_t$), tandis que plusieurs pas de temps explicites d'advection sont pris par chaque étape dispersive selon la contrainte CFL qui établit la taille du pas de temps d'advection.

La résolution des quatre principales équations couplées est expliquée dans le schéma de la figure 21. Les termes reliant les équations d'écoulement de surface et souterrain sont q_{sf}

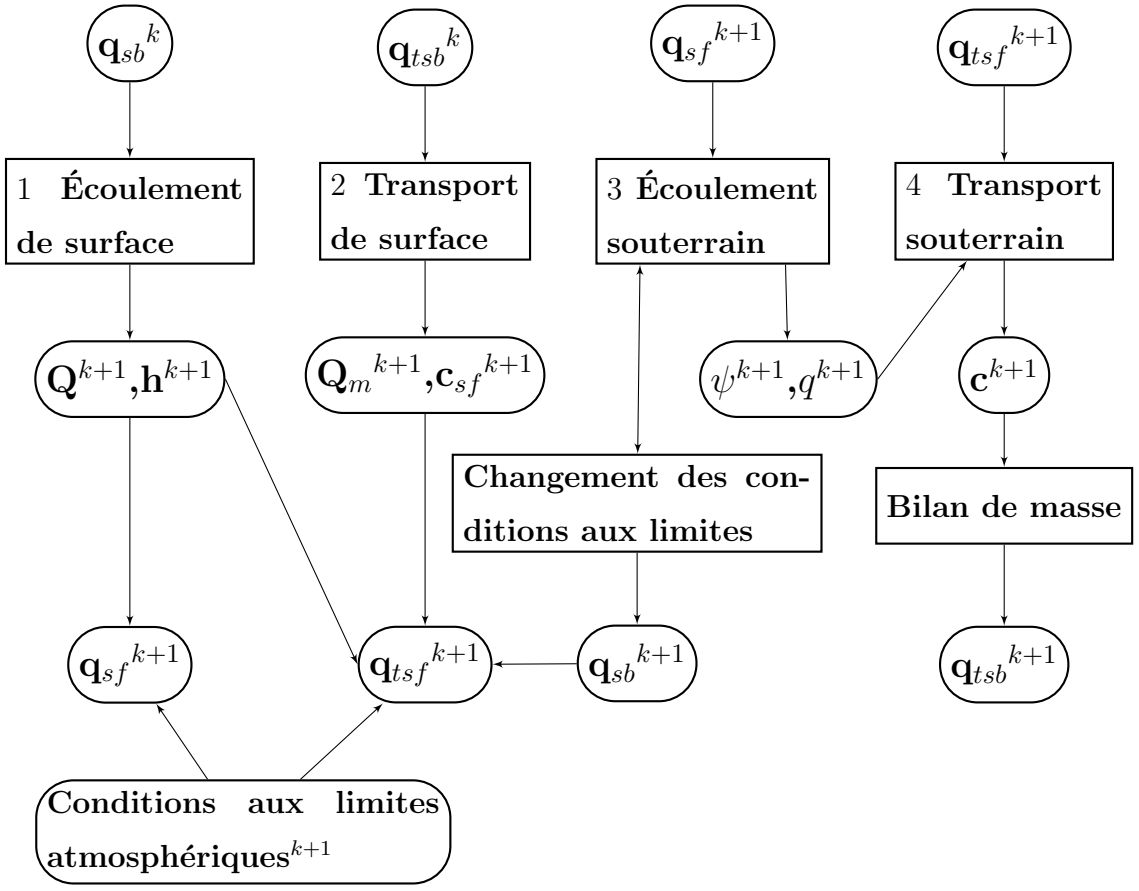

Figure 21: *Solution séquentielle (de 1 à 4 comme indiqué) pour les quatre équations principales dans CATHY_FT. k indique le temps et la solution est évaluée à t^{k+1}. h [L] est la hauteur d'accumulation d'eau au-dessus de la surface relatif à Q et c_{sf} [M/L^3] est la concentration de surface relative á Q_m. Les valeurs q_{sb}^{k+1} et q_{tsb}^{k+1} sont des entrées utilisées à l'étape de temps suivante pour, respectivement, les équations d'écoulement et de transport de surface (en devenant les nouvelles q_{sb}^{k} et q_{tsb}^{k}).*

[$L^3L^{-3}T^{-1}$] et q_{sb} [$L^3L^{-3}T^{-1}$] et représentent, respectivement, les écoulements entrant ou sortant de la surface vers la subsurface et de la sous-surface vers la surface. Ces termes sont déterminés par un algorithme du changement des conditions aux limites. Cet algorithme est conditionné par le module souterrain car c'est cette composante du modèle qui gère les données atmosphériques en entrée qui sont cruciales pour résoudre l'échange. Les termes couplant les équations de transport souterrain sont q_{tsf} [$ML{-}3T^{-1}$] et q_{tsb} [$ML^{-1}T^{-1}$] et représentent respectivement le transport de soluté entrant ou sortant de la surface vers la subsurface et de subsurface vers la surface. Ces termes sont résolus en combinant de façon rigoureuse les conditions aux limites complexes, qui sont nécessaires à la résolution des équations de transport souterrain, et des calculs de bilan de masse qui eux considèrent les différents états issus des solutions des équations d'écoulement (accumulation d'eau en surface, données atmosphériques d'entrée et les écoulements d'eau effectifs à la surface du sol).

Le développement de CATHY_FT a dû faire face au défi d'approximer avec précision et efficacité l'équation complexe d'advection-dispersion. En effet, la résolution de cette équation est toujours difficile car il n'existe pas de méthode numérique optimale sur l'intégralité des problèmes. L'approche par les éléments finis est par exemple idéale pour les processus dispersifs alors que pour les processus où l'advection prédomine, les solutions obtenues montrent un caractère oscillatoire et/ou avec une dispersion numérique excessive proche des forts gradients de concentration [*Guddati and Yue*, 2004]. Cependant, les méthodes qui préservent les forts gradients avec une oscillation et une dispersion numérique minimale, telles que la méthode des volumes finis de type Godunov d'ordre élevé [e.g., *Dawson*, 1993; *Mazzia and Putti*, 2005], ou encore la méthode de Galerkin discontinu [e.g., *Siegel et al.*, 1997; *Cockburn et al.*, 2000], ne sont pas idéales pour discrétiser la composante dispersive et ne sont pas compatibles avec les modèles d'écoulement utilisant les éléments finis [*Dawson et al.*, 2004a; *Klausen and Russell*, 2004]. Des études antérieures liées au modèle CATHY_FT ont montré que l'utilisation d'une technique de fractionnement de temps, qui permet d'adopter une méthode numérique adaptée selon qu'il s'agisse de résoudre l'advection ou la dispersion (e.g., le volumes finis de type Godunov d'ordre élevé et les éléments finis mixtes (MFE) [*Mazzia and Putti*, 2005]), et de méthode localement conservatrice (e.g., MFE [*Putti and Sartoretto*, 2009]) pour la discrétisation des équations d'écoulement, permet d'obtenir des résultats précis mais

avec des temps de calculs très importants, essentiellement dû à l'effort nécessaire pour la résolution des systèmes MFE.

Pour résoudre le compromis entre la précision du modèle et le coût de calcul, et donc éviter l'utilisation d'une discrétisation MFE, dans cette étude il est proposé une interpolation linéaire qui conserve la masse pour combiner la solution du schéma HRFV pour l'advection, obtenue sur les éléments, et la solution du système FE pour la dispersion, obtenue sur les nœuds, avec un opérateur de fractionnement de temps. L'incompatibilité entre le solveur à volumes finis et le modèle FE de Richards est résolue en rétablissant les propriétés de conservation de la masse des vitesses FE avec la technique de post-traitement LN [*Scudeler et al.*, 2016a].

Les résultats des simulations effectuées ont montré comment, pour processus purement advectifs, le nouveau modèle donne une solution avec des propriétés de bilan de masse quasi-parfaites et qui surmonte avec succès les limites associées à la discrétisation FE pour l'advection et la lourdeur des calculs pour la résolution des flux MFE. Cependant, lors de la simulation des processus d'advection-dispersion, la solution numérique présente clairement une diffusion non physique qui provoque la propagation rapide de la masse de soluté dans le domaine, et donc l'efficacité de calcul est obtenue au détriment de précision.

Les conditions aux limites du transport sont une source supplémentaire de complexité numérique et physique dans le développement de CATHY_FT. Un flux dépendant des valeurs (ou condition limite de Cauchy) est utilisé pour représenter le flux de soluté en entrée et en sortie à travers la limite du domaine, avec les échanges advectifs régis par les flux d'eau réels à travers les frontières et les échanges de dispersion régies par le gradient de concentration. Par souci de cohérence numérique, des conditions de Dirichlet de concentrantion sont spécifiées à l'étape advective alors que les conditions de type Neumann sont imposées à l'étape dispersive. Ainsi, une représentation exacte des processus de transport aux frontières repose sur la résolution exacte des flux d'eau et des valeurs de concentration qui doivent éventuellement être imposées. Dans cette étude, il est montré comment ces complexités de modélisation représentent un problème particulièrement difficile lorsque les conditions aux limites sont utilisées pour représenter les interactions de soluté à travers la surface du terrain. Les conditions aux limites et des calculs de bilan de masse sont combinées avec précision pour résoudre les échanges de soluté entre la surface et la subsurface. Des résultats satisfaisants ont été obtenus pour des processus de ruissellement

de surface par saturation (mécanisme de Dunne). Cependant, des tests supplémentaires doivent être menés pour évaluer si la méthode s'étend précisément dans des situations où les processus de surface sont régis par infiltration en excès (mécanisme de Horton) et en présence d'évaporation. D'autres études seront nécessaires pour quantifier et évaluer l'importance des échanges diffusifs entre la surface et la subsurface, actuellement négligés dans CATHY_FT.

De nombreuses améliorations et extensions spécifiques sont possibles pour le modèle. Un défi pour l'avenir sera de résoudre l'efficacité et la précision de la solution numérique pour l'équation d'advection-dispersion en utilisant, par exemple, la reconstruction des moindres carrés [*Coudière et al.*, 1999; *Manzini and Putti*, 2007] pour évaluer les valeurs des variables nodales à partir des moyennes de cellules, au lieu de l'interpolation linéaire actuellement utilisée. Des complexités physiques et numériques supplémentaires seront introduites en incorporant, comme le modèle continue à évoluer, de nouvelles fonctionnalités telles que des réactions chimiques (par exemple, désintégration et adsorption de premier ordre), transport de soluté dépendant de la densité (par exemple, des phénomènes d'intrusion d'eau salée), et un énergétique (y compris l'évapotranspiration et les interactions entre le sol et la végétation).

Chapter 1

Introduction

1.1 Motivation

Groundwater constitutes an important component of many freshwater resource systems and, for this reason, it has been widely studied by the hydrogeologist community. The two main driving forces of groundwater studies are the need to assess the water potential of aquifers and the challenge of protecting or remediating the quality of this water. Quantity and quality problems can be strongly linked as the quality of water is easily deteriorated by intense withdrawal, often beyond permissible limits. For example, excess withdrawal in coastal aquifers can lead to saltwater intrusion problems, causing saline water contamination that makes freshwater unsuitable for human consumption and irrigation [e.g., *Barlow and Reichard*, 2010]. The interest in water quality problems related to aquifers has increased even more because of contamination by hazardous industrial wastes, agricultural activities, leachate from landfills, spills of oils, and so on.

A good management of the quantity and quality of the groundwater resource requires predictions of the short, medium, and long-term response of the managed system. This information enables the comparison of alternative actions and the selection of the best management strategy. Predictions of the system response can be obtained by constructing and solving deterministic mathematical models of the investigated domain and of the flow and transport phenomena that take place in it. These models generally require the solution of partial differential equations that can be achieved either analytically or numerically. Different analytical solutions have been developed to solve the flow and solute-transport equations for simple cases where properties and boundaries of the sys-

tem are idealized [e.g., *Reed*, 1980; *Leij et al.*, 1991]. Nonetheless, for most practical problems, the mathematical advantages of an exact and simple analytical solution are overtaken by the errors arising from the assumptions required. Alternatively, the mathematical models are transformed into a numerical problem solved by means of computer programs. This, together with the continual advances in computational technology, has made hydrological numerical modeling an important field of research in water resource management [e.g., *Bear and Cheng*, 2010].

One of the main themes of this thesis is on improving the numerical performance of state-of-the-art hydrological models of both flow and transport phenomena. The process of groundwater flow is assumed to be governed by Darcy's law, which expresses a relation between the velocity field of the flowing groundwater and the potential or pressure head gradients. This, combined with the statement of mass conservation, gives rise to a partial differential equation written and solved in terms of potential head or pressure head (or mixed volumetric water content-pressure head) depending if the flow is saturated, unsaturated, or variably saturated. Thus, the purpose of a model that simulates groundwater processes is to compute the potential or pressure head at any specified time and place. On the other hand, a solute transport model aims to reproduce the dynamics of the concentration of dissolved contaminants in the same groundwater system. In the case of nonreactive solutes, the changes in concentration occur primarly due to two distinct processes: advective transport, in which the dissolved compounds are moving with the flowing groundwater, and hydrodynamic dispersion, in which molecular diffusion and small-scale variations in the flow velocity through the porous media cause the paths of the dissolved compounds to diverge and spread from the average direction of groundwater flow. Thus, given that the migration of contaminants is obviously affected by the groundwater velocity field, the single most important key to understand and model a solute transport problem relies on an accurate definition of the flow system [*Dawson et al.*, 2004a]. From a numerical standpoint, although the potential (or pressure) head field can be often simulated accurately, the relative velocity field required as input by the companion transport model may be greatly in error. In this context, a first aim of this thesis is to introduce some enhancements to a coupled flow and transport model by focusing on the numerical accuracy of the groundwater velocity field.

Another main theme of this thesis concerns integrated surface water/groundwater

resources management and modeling. Owing to the prevalence of interactions such as between a river or lake and an adjacent aquifer or between rainfall and runoff at the land surface, surface water and groundwater cannot be considered as independent water resources. To give some examples, water from river flows through its beds into the aquifer whenever the water level in the former is higher than in the latter, and vice versa. Base flow in streams and discharge from springs are nothing else than groundwater emerging at the ground surface. These considerations apply also to water quality, as polluted surface water may easily reach and pollute groundwater and vice versa. Thus, it is obvious that the management of water resources should always include both resources, since any control of one resource will eventually affect the other. On the modeling side, integration of surface waters and groundwaters involve complex coupling aspects since their boundary, represented by the land surface, is usually subjected to highly dynamic conditions, which are difficult to handle both physically and numerically. An interesting scenario arises when the water table rises and reaches the ground surface producing seepage face, surface runoff, and surface-subsurface exchange processes. Atmospheric forcing represents another crucial aspect since at the land surface, based both on water levels above and soil conditions below, there occurs the partitioning of potential fluxes (rainfall and evaporation) into actual fluxes (infiltration, exfiltration as evaporation, and exfiltration as return flow) and changes in surface storage. An incorrect representation and resolution of exchange and coupling terms can easily introduce approximation and mass balance errors, particularly difficult to control on solute mass, that affect the overall numerical solution and performance [*Packman and Bencala*, 2000]. In this context, a second aim of this thesis is to improve our understanding of complex boundary conditions and reducing the errors associated with their representation in an integrated groundwater/surface water model.

A final theme of this thesis is related to the testing and benchmarkig of distributed physically-based models for goundwater flow and transport processes. Code verification, model benchmarking, and model testing play an important role since, together, they serve to improve a model's reliability for prediction and as management tools [*Refsgaard*, 1997; *Maxwell et al.*, 2014]. Verification of a code is obtained when it is shown that the model behaves as intended, i.e., that the governing equations are correctly encoded and solved and that the solution has good mass balance properties. The value of a model stands

in its capability to integrate site-specific information with the governing equations describing the relevant processes. In this context, distributed-parameter models are usually preferred over lumped-parameter models as they can be more realistic and flexible for simulating the complex, three-dimensional, and heterogeneous setting characterizing a hydrogeologic field. However, their applicability and reliability are strictly affected by incomplete process understanding and by the large amount of input data (primarily related to the system properties but also to the boundary and initial conditions) that they require. Lack of data introduces uncertainty during the process which seeks to identify the independent set of parameters (e.g., hydraulic conductivity, porosity) by fitting the model results to the available field or experimental datasets. Recent attempts to resolve these issues have looked at automated parameter estimation techniques that rely on numerical optimization methods. However, these procedures do not bound errors arising from an incorrect description of the governing processes or from problems in the numerical solution algorithms. In addition, their application for detailed physically-based numerical models is not feasible when multiple processes and multivariate observations are involved. Thus, testing complex models against many types of observation data of different nature is a challenging problem, compounded by the need to identify the sources of error in the model and to determine their nature (for example if they are related to unresolved processes, model parameterization, or numerical solutions). In this context, a third aim of this thesis is to perform a modeling analysis with a very detailed observation dataset including quantity and quality of groundwater discharge and point-scale flow and transport data.

1.2 State of the art

A large number of hydrological and hydrogeological numerical models are available. The differences between any given models stand in the processes they simulate, in their dimensionality (i.e., one-dimensional, two-dimensional, and three-dimensional), and in the way they are solved numerically (e.g., with a finite difference (FD) or finite element (FE) technique). All the processes are described by a physical equation representing a mass, energy, or momentum balance. Most comprehensive physically-based hydrologic models use Richards' equation and the advective-dispersive equation to represent, respectively, variably saturated groundwater flow and solute transport processes. *Freeze* [1971] is con-

sidered a pioneer of physically-based hydrological modeling since he was amongst the first to develop a nonhomogeneous anisotropic transient three-dimensional model integrating saturated and unsaturated flow processes (earlier models dealt with simpler one- or two-dimensional problems [e.g., *Rubin*, 1968; *Hornberger et al.*, 1969; *Taylor and Luthin*, 1969]) and, thus, he anticipated subsequent model developments for the solution of Richards' equation [e.g., *Huyakorn et al.*, 1986a; *Celia et al.*, 1990a; *Rathfelder and Abriola*, 1994] and the companion advective-dispersive solute transport equation [e.g., *Huyakorn et al.*, 1986b; *Panday et al.*, 1993]. The continual computational and physical (process description) advances not surprisingly enabled the evolution towards more complex models with other features. For example, nowadays there are flow models that integrate subsurface processes with evapotranspiration, with surface processes, with canopy interception, and with snowmelt processes (e.g., tRIBS [*Ivanov et al.*, 2004] and LISFLOOD [*Van Der Knijff et al.*, 2010]), and transport models that deal with multispecies, equilibrium reaction, and physical nonequilibrium reactions (e.g., MODFLOW [*Prommer et al.*, 2003] and HYDRUS [*Šimunek and van Genuchten*, 2008; *Šimunek et al.*, 2008]).

FE and FD are two of the major classes of numerical methods that have come to be well accepted for solving groundwater flow equations [*Wang and Anderson*, 1995]. Standard FE methods are often the schemes of choice for spatial discretization because of their computational efficiency, their ability to handle anisotropy, and, unlike FD techniques, their flexibility to treat irregular boundaries of the aquifer and of parameter zones within the aquifer [*Pinder and Frind*, 1972]. Early examples include the models developed by *Neuman and Witherspoon* [1970], *Cooley* [1983], and *Huyakorn et al.* [1986a]. Other spatial discretization methods have been proposed that can offer advantages under certain conditions. These include locally conservative methods [*Klausen and Russell*, 2004], such as multi-point flux approximations [e.g., *Edwards and Rogers*, 1998], mixed finite elements (MFE) [e.g., *Brezzi and Fortin*, 1991; *Farthing et al.*, 2002], and enhanced cell-centered finite differences [e.g., *Arbogast et al.*, 1998]. On the other hand, traditional FD techniques are often used for time discretization and they can be time-implicit or time-explicit according to the nature of the equation [*Ascher et al.*, 1995] (e.g., time-implicit for parabolic conservation laws such as Richards' equation).

The advective-dispersive solute transport equation is in general more difficult to solve numerically than the groundwater flow equation since it changes mathematical proper-

ties depending upon which terms are dominant in a particular situation: it can be more hyperbolic in nature when advection dominates and more parabolic in nature (similar to groundwater flow equations) when dispersion dominates. The FE method is subjected to Peclet limitations when applied to hyperbolic conservation laws. As a consequence, for advective dominated processes, it requires to be upwinded [e.g., *Huyakorn and Nilkuha*, 1979; *Huyakorn et al.*, 1987] with the undesired effect of introducing numerical diffusion, which smooths the sharp fronts as physical dispersion does. Different numerical methods have been developed to accurately resolve the difficult behavior of the solute transport equation. These include the discontinuous Galerkin approach [e.g., *Cockburn et al.*, 2000], Eulerian-Lagrangian discretization [e.g., *Cheng et al.*, 1984; *Thomson et al.*, 1984; *Celia et al.*, 1990b; *Zhang et al.*, 1993], high order Godunov-type finite volumes [e.g., *Dawson*, 1993; *Mazzia and Putti*, 2005], and time-splitting techniques [e.g., *Valocchi and Malmstead*, 1992]. Another problem arises here since the mass conservation properties of the velocity field (computed by the flow solver, but needed by the transport solver) required by these methods are not satisfied by the FE-based flow model [*Dawson et al.*, 2004a]. In fact, even if the FE is the method of choice in solving subsurface flow equations, the velocity field, post-computed and obtained element-wise from hydraulic head gradients, has its normal component discontinuous at inter-element boundaries, generating problems of mass conservation in any application that relies on accurate flux estimates. Two different ways have been tested to overcome this problem: the use of a locally conservative method for the discretization of the flow equation (e.g., the MFE) or the post-processing reconstruction of the FE velocity field (e.g., *Larson and Niklasson* [2004]). In this last case it is possible to achieve almost the same level of accuracy obtained with a locally conservative method but at a much lower computational cost and for this reason post-processing strategies are increasingly considered as an attractive alternative. Additional numerical complications arise when the solutes affect the density of the solution or they are reactive. In the first case the transport and flow equations are coupled and need to be solved simultaneously or iteratively [e.g., *Huyakorn et al.*, 1987; *Diersch*, 1988; *Putti and Paniconi*, 1995; *Simmons et al.*, 1999; *Simpson and Clement*, 2003]. The second case can include the introduction of strong nonlinearities, nonequilibrium phenomena, and multispecies and multiphase processes [*Rubin*, 1983; *Bahr and Rubin*, 1987].

Paniconi and Putti [2015] provides a survey of catchment deterministic hydrological

modeling and of the related physical and computational advances of the past 50 years. Their paper clearly shows how in the last decades the reasearch performed by the community of groundwater modelers has been driven by the interest in using an integrated approach to represent the different hydrological processes and their interactions, in particular those between surface water and groundwater [e.g., *Furman*, 2008; *Fleckenstein et al.*, 2010]. Process interactions between streams and aquifers are increasingly considered relevant for the management of our freshwater resources since they are one of the major controls on the water and solute budgets at the catchment and river basin scales and are key determinants of hydrograph separation and transit time distributions [*Winter et al.*, 1998; *Rodriguez-Iturbe*, 2000]. Despite all the experimental and numerical investigations performed [e.g., *Harvey and Bencala*, 1993; *Packman and Bencala*, 2000], significant challenges remain in integrating flow and transport processes and in simulating water and solute exchanges across the land surface.

In the current generation of distributed-parameter process-based hydrological models, a variety of models that couple surface and subsurface flow processes has been introduced: Parallel Flow (ParFlow) [*Kollet and Maxwell*, 2006], CATchment HYdrology (CATHY) [*Camporese et al.*, 2010], HydroGeoSphere (HGS) [*Therrien et al.*, 2012], OpenGeoSys (OGS) [*Kolditz et al.*, 2012], Process-based Adaptive Watershed Simulator (PAWS) [*Shen and Phanikumar*, 2010], and Penn State Integrated Hydrologic Model (PIHM) [*Kumar et al.*, 2009]. Besides the numerics and the approximations performed, the differences between models are also in the coupling algorithms used. Mathematically, there are three distinct approaches for integrating surface and subsurface flow: asynchronous linking, sequential iteration, and a globally implicit approach [*Panday and Huyakorn*, 2004]. Physically, the strategies for coupling surface and subsurface flow are: first-order exchange [e.g., *VanderKwaak and Loague*, 2001; *Panday and Huyakorn*, 2004; *Therrien et al.*, 2012], continuity of pressure [e.g., *Kollet and Maxwell*, 2006; *Dawson*, 2008], and boundary condition switching.

Comparatively fewer models address both flow and transport interactions between the subsurface and land surface [*Weill et al.*, 2011; *Therrien et al.*, 2012]. Thus, the differences in numerical and physical approaches for coupling surface and subsurface flow carry over to the few integrated transport models. For example in *Therrien et al.* [2012] a globally implicit approach is used to simultaneously solve the surface and subsurface transport and

flow equations. In contrast, in the CATchment HYdrology Flow–Transport (CATHY_FT) model [*Weill et al.*, 2011], surface and subsurface flow and transport equations are solved within a sequential iterative procedure and coupling is handled with a boundary condition switching algorithm. This requires careful considerations since the stresses involved, such as atmospheric forcing and seepage face conditions, can be highly dynamic and thus difficult to describe physically and numerically. Not surprisingly, many challenges still remain in handling the complexity of boundary conditions coupling surface and subsurface processes.

Progress in hydrological modeling requires any models being used to reveal the truth about a system. This has been usually checked by demonstrating that good results are obtained for problems having known solutions or against site-specific data [*Refsgaard*, 1997]. Benchmark problems have been established to compare different approaches of competing models, such as, for example, the solution of Boussinesq's equation compared to the solution of Richards' equation to simulate hillslope-storage [*Paniconi et al.*, 2003b] or to compare competing models dealing with complex processes as, for example, variable density groundwater flow [e.g., *Konikow et al.*, 1997a], near-surface processes [e.g., *Scanlon et al.*, 2002], land surface processes [e.g., *Henderson-Sellers et al.*, 1993; *Boone et al.*, 2004], radionuclide transport [e.g., *Larsson*, 1992], and reactive transport [e.g., *Pruess et al.*, 2004]. The intercomparison effort for coupled surface-subsurface models has followed the above initiatives. *Sulis et al.* [2010] and *Maxwell et al.* [2014] present a comparison between, respectively, two and seven physics-based numerical models for simulating surface water-groundwater interactions. The same effort should be done to develop additional benchmarks including also coupled surface-subsurface transport processes, in order to guide scientific understanding as integrated models increase in complexity.

While model intercomparison for benchmark test cases has turned out to be an importan means for assessing the physical and numerical limitations of competing models, any modeling case study based on field or experimental data enables advances in model testing and understanding the physics governing complex processes. Valuable data for model testing are available from different tests performed in experimental hillslopes and field sites throughout the world. For example, the Panola Mountain research watershed [*Freer et al.*, 2002; *Tromp-van Meerveld and McDonnell*, 2006] has been designed to study subsurface stormflow. Examples related to both flow and transport processes include the Cap

Cod experiment [*LeBlanc et al.*, 1991; *Hess et al.*, 1992], the Borden test site [*Mackay et al.*, 1986; *Sudicky*, 1986], the Las Cruces trench site [*Hills et al.*, 1991; *Wierenga et al.*, 1991], the Central Nevada Test Area [*Pohlmann et al.*, 2000], and the Amchitka Island site [*Hassan et al.*, 2001]. Recent natural and laboratory experiments assembling extensive datasets from detailed multidisciplinary experiments, e.g., the TERENO network of experimental catchments in Germany [*Zacharias et al.*, 2011], the Landscape Evolution Observatory (LEO) at the Biosphere 2 facility near Tucson in Arizona [*Hopp et al.*, 2009], and the Chicken Creek artificial catchment near Cottbus in Germany [*Hofer et al.*, 2012], represent a unique opportunity to test and improve the current generation of integrated hydrological models for surface-subsurface and flow-transport simulations and, with that, to advance in new scientific understanding.

1.3 Objectives

The development of a physically-based integrated numerical model requires different steps: 1) the selection of the essential features and processes to approximate; 2) the description of these processes mathematically, in the form of partial differential equations; 3) the definition of a computer code that can most effectively meet the purpose of the model; 4) the definition of a generic computational domain (i.e., the type of elements); 5) the development of a suitable numerical model for space and time discretization, possible linearizations, and coupling, which reduces the original partial differential equations into a sparse algebraic system of equations; and 5) the development of a scheme for solving this system. For any application of the generic model it is necessary to define: 1) the grid spacing generating the mesh; 2) the time step to advance in time; 3) the boundary and, for transient problems, initial conditions; and 4) the properties of the system (and their distribution).

Mass balance calculations should always be performed to assess the quality of the model solution. In fact, as the groundwater and solute transport equations of a physically-based model derive from a local mass conservation law, i.e., the continuity equation, any mass balance error indicates that there is something wrong in the numerical solver. The discrepancies between the observed and calculated responses is another typical manifestation of model errors. In this case it is very hard to discover their source as they might be

either conceptual, numerical, or arising from our inability to describe the aquifer properties and stresses [*Konikow and Bredehoeft*, 1992]. For instance, conceptual errors derive from neglecting relevant processes, incorrect representations, or strong and inadequate assumptions (e.g., the use of a steady state condition when the processes are not at steady state, modeling a dynamic boundary with a static assumption, and the application of Darcy's law where the flow is not laminar). Numerical errors derive from the equation-solving algorithms and coupling algorithms (e.g., the use of a non mass-conservative velocity field to simulate transport processes, the introduction of numerical dispersion, and interpolation of parameters and variables which is not of optimal order). The last type of errors derives from the lack of adequate observational techniques of the soil medium parameters and measurement errors. These include the assumption of homogeneity when the soil is heterogeneous, the assumption of time constant boundary conditions when they are time variable, and so on. The modeller has to be aware of the source and nature of these errors in order to find ways to control and reduce them. This implies continual updating, bringing improvements, introducing new processes, advancing computationally, performing analysis, and exhaustively testing the model. In this context, many challenges remain in improving and testing current state-of-the-art models for integrated hydrological simulation, and the overarching aim of the work described in this thesis is to address some of these challenges in the framework of a specific model, the CATchment HYdrology Flow-Transport (CATHY_FT) model [*Camporese et al.*, 2010; *Weill et al.*, 2011].

This general objective is elaborated into four specific objectives that relate to the three main themes of the thesis described earlier:

1. Implementing the velocity field reconstruction technique for advective transport simulations (theme 1, improving the numerical performance of flow and transport simulators);

2. Generalizing the seepage face boundary condition for the flow model (theme 2, complex boundary conditions and integrated surface-subsurface modeling);

3. Simulating the isotope tracer experiments at the Landscape Evolution Observatory (theme 3, model testing and benchmarking using multiprocess and multivariate real data);

4. General testing of the numerical behavior and the coupling algorithms of the

CATHY_FT model (all three themes).

The first objective is to implement the *Larson and Niklasson* [2004] local post-processing algorithm to reconstruct the groundwater velocities of CATHY_FT, which are FE-based and for this reason non mass-conservative. This aims to improve the accuracy and mass balance properties of the advective transport model (finite volume-based), which rely on the velocity field as input. The goals are achieved by estimating the quality of the reconstructed velocities against that of the FE-based model for advective transport simulations. In addition, the results are compared to those obtained using as input a MFE velocity field, which is inherently mass-conservative and for this reason taken as the reference solution, but which imposes a much higher computational cost [*Putti and Sartoretto*, 2009].

As second objective, my reasearch aims to improve our understanding of the seepage face boundary condition and, with that, reduce the errors associated with its modeling. A detailed investigation of the behavior of seepage face boundaries is considered to be important because it is a complex nonlinear dynamic boundary, because the way it is handled can strongly affect the pressure head distribution, the water table configuration, and the flow field, and because complexities under conditions of heterogeneity and surface flow have not been thoroughly analyzed to date. The goals are achieved by performing a detailed and novel analysis that will involve: 1) assessing the errors committed when using approximations such as Dirichlet (static) conditions; 2) investigating the interactions between surface outflow and seepage face outflow; and 3) studying seepage face dynamics in the presence of more than one exit point.

As third objective, it is performed flow and transport modeling with the very detailed observation datasets obtained from controlled experiments performed on artificial hillslopes at the Landscape Evolution Observatory of the Biosphere 2 facility in Arizona [*Pangle et al.*, 2015]. The data includes integrated and point-scale flow and transport measurements of seepage face flow, total internal storage, breakthrough curves at the seepage face and within the domain, and pressure head and soil moisture measured at 496 different sensor locations. This analysis is considered important since very few studies have applied a physically-based hydrological model with this level of flow and tracer data. Thus, this works makes possible not only the thorough testing (and improvement) of our models, but also the exploration of phenomena and associated hypotheses regard-

ing heterogeneity, fractionation, dispersion, etc. The goals are achieved by pushing the boundaries of our ability to model flow and transport under very dry conditions and to capture point-scale and integrated responses of different state variables.

The final objective aims to shed light on important modeling issues related to the CATHY_FT model such as controlling mass balance errors, capturing process interactions and feedbacks, and handling complex boundary conditions. This analysis is considered important since integrated modeling of solute transport in surface water and groundwater is a big challenge involving many interacting processes, complex boundary conditions, and difficult numerics. The goals are achieved by examining and improving the model numerics and testing it for different scenarios. As a first contribution, I use the reconstructed velocities instead of the FE velocity as input for the subsurface transport model. Secondly, for the solution of the advective-dispersive equation I investigate the possibility to combine a time-explicit finite volume technique with a time-implicit FE technique instead of with a time-implicit MFE technique, considering the big savings in computational cost. And lastly, I address issues of model accuracy associated to the algorithm that couples the subsurface and the surface transport processes.

1.4 Evolution of the CATHY_FT model and structure of the thesis

The beginning of the development of the CATHY_FT model dates many years ago, when subsurface and surface processes and flow and transport processes were still treated separately. Many people have worked on the model over the years introducing step by step new complexities. To report some examples, on the flow side, *Paniconi and Wood* [1993] developed the detailed variably saturated subsurface flow model, *Orlandini and Rosso* [1996, 1998] developed the detailed surface flow model, *Moretti and Orlandini* [2008] developed a scheme for automatic delineation of the drainage basin of the surface dem, [*Paniconi and Putti*, 1994] analysed the iterative schemes used to linearize the subsurface flow equation, *Camporese et al.* [2006] developed the hydrological model for peat soils, *Camporese et al.* [2010] introduced the surface-subsurface coupling algorithm, *Sulis et al.* [2010] compared the coupling algorithm with the one of a different physics-based numerical model, *Dagès et al.* [2012] investigated the surface-subsurface coupling errors, recently

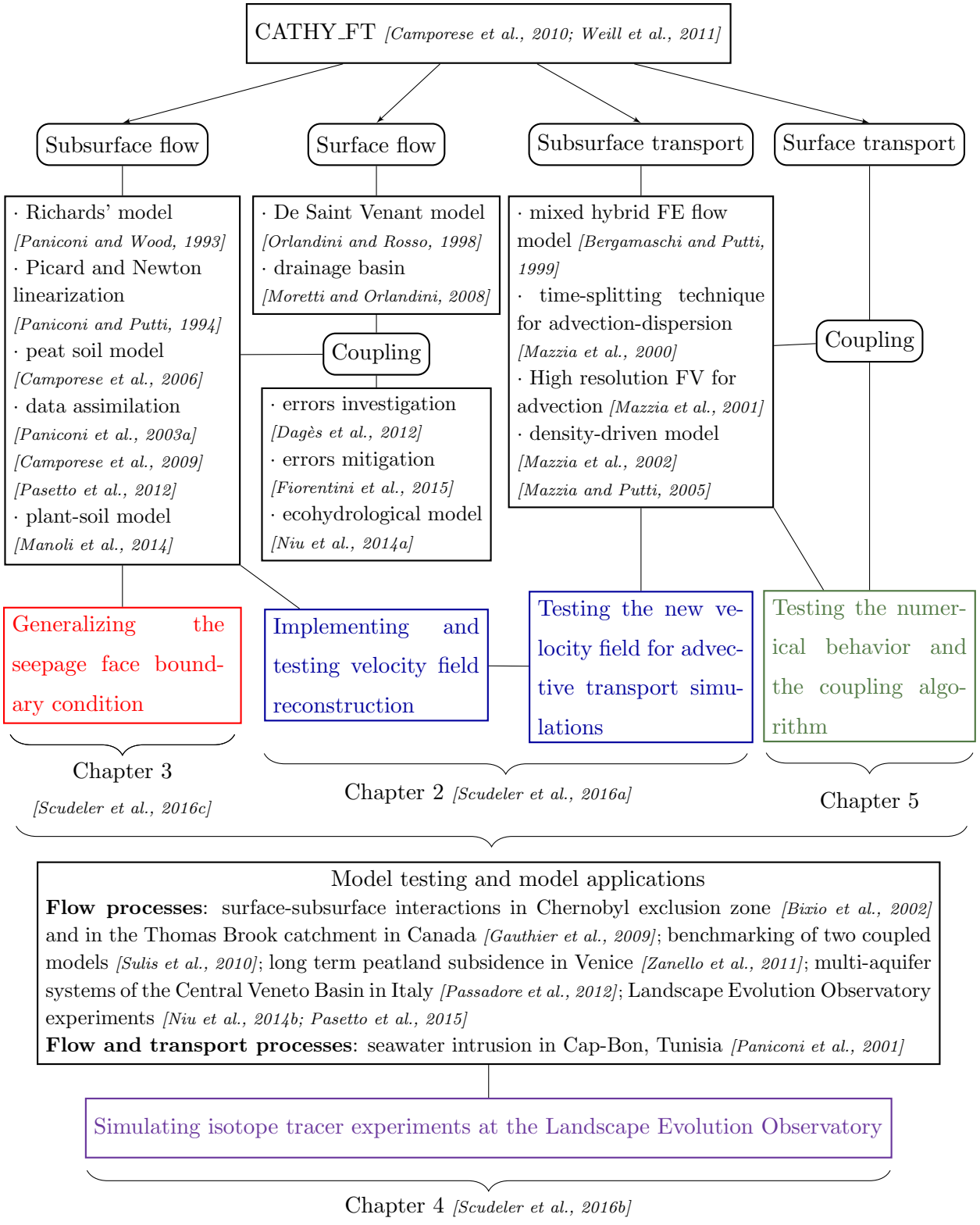

Figure 1.1: *Processes simulated by the CATHY_FT model and summary of the related developments and applications performed. The objectives of my research are shown in red, blue, green, and purple boxes placed in relation to the different model development and evolution components.*

mitigated by the introduction of some numerical strategies [*Fiorentini et al.*, 2015], *Niu et al.* [2014a] developed the catchment-scale ecohydrological model, integrating energy, water, and carbon flux exchanges between land surface and atmosphere, and *Manoli et al.* [2014] developed and tested a soil–plant model. Three different data assimilation techniques, allowing model simulations to be updated with observation data, have also been implemented. These are Newtonian nudging [*Paniconi et al.*, 2003a], the ensemble Kalman filter [*Camporese et al.*, 2009], and the particle filter [*Pasetto et al.*, 2012].

Examples of applications and testing of the flow model include modeling scenarios of the groundwater-surface water interactions in the Chernobyl exclusion zone [*Bixio et al.*, 2002], a modeling study of heterogeneity and surface water-groundwater interactions in the Thomas Brook catchment in Canada [*Gauthier et al.*, 2009], an experimental study and modeling scenarios in the Venice coastland, Italy for long term peatland subsidence [*Zanello et al.*, 2011], the simulation of the processes in the multi-aquifer system of the Central Veneto Basin, Italy [*Passadore et al.*, 2012], and the modeling studies performed for the experiments at the Landscape Evolution Observatory [*Niu et al.*, 2014b; *Pasetto et al.*, 2015].

On the transport side, *Bergamaschi and Putti* [1999] discretized Richards' equation by means of a locally conservative numerical scheme (the mixed finite element scheme in its hybridized form) producing accurate velocity fields for transport simulations, *Mazzia et al.* [2000] and *Mazzia and Putti* [2005] developed a suitable numerical model to solve advection-dominated transport problems avoiding the introduction of numerical dispersion, *Mazzia et al.* [2001] developed the density-dependent flow and transport model to deal with salt contamination and freshwater-saltwater mixing problems, and *Weill et al.* [2011] introduced the surface transport model, the flow-transport coupling, and the surface-subsurface transport coupling. Compared to the flow model, fewer are the applications performed for transport processes. One example is the modeling analysis performed for seawater intrusion in the coastal aquifer of eastern Cap-Bon in Tunisia [*Paniconi et al.*, 2001].

The flowchart in Figure 1.1 shows schematically a summary of these cited studies connected to the development of CATHY_FT, reported under one of seven sections representing the different processes simulated by the model (subsurface flow, surface flow, surface–subsurface flow coupling, subsurface transport, surface transport, and surface-

subsurface transport coupling) and model testing and applications. It is clear from this chart that there is much work to be done in relation to the more recent CATHY_FT developments connected to the transport processes. In the context of testing and improving the model, the flowchart also shows the enhancements that my research aims to bring and places them in relation to the different model development and evolution components. Each objective will be treated in a different chapter of the thesis, each chapter constituting a stand-alone paper submitted or to be submitted to a journal:

Chapter 2 (objective 1): (C. Scudeler, M. Putti, C. Paniconi, Mass-conservative reconstruction of Galerkin velocity fields for transport simulations, *Advances in Water Resources*, published July 2016).

Chapter 3 (objective 2) (C. Scudeler, C. Paniconi, D. Pasetto, M. Putti, Examination of the seepage face boundary condition in subsurface and coupled surface/subsurface hydrological models, *Water Resources Research*, submitted May 2016).

Chapter 4 (objective 3) (C. Scudeler, L. Pangle, D. Pasetto, G.-Y. Niu, T. Volkmann, C. Paniconi, M. Putti, P. Troch, Multiresponse modeling of variably saturated flow and isotope tracer transport for a hillslope experiment at the Landscape Evolution Observatory, *Hydrology and Earth System Science*, published September 2016).

Chapter 5 (objective 4) (C. Scudeler, C. Paniconi, M. Putti, Process-based model of surface-subsurface and flow-transport interactions: coupling, boundary conditions, and numerical behavior, manuscript in preparation).

Before proceeding with these 4 chapters/papers, we give a brief description of the CATHY_FT model, in particular the governing equations for the flow and transport modules and the coupling structure, which will serve as a reference for the subsequent chapters.

1.5 The CATchment HYdrology Flow-Transport model

1.5.1 Surface-subsurface flow model

The CATHY model [*Camporese et al.*, 2010] is a distributed physically-based model that couples the conservative form of Richards' equation [*Celia et al.*, 1990a], used to describe

flow in variably saturated porous media [*Paniconi and Wood*, 1993; *Paniconi and Putti*, 1994], and a FD solver for the diffusion wave equation, describing surface flow propagation over the land surface (overland runoff) and in the stream network (channel flow) [*Orlandini and Rosso*, 1996, 1998]. The mathematical model is described by a system of two partial differential equations:

$$\frac{\theta}{n}S_s\frac{\partial\psi}{\partial t}+\frac{\partial\theta}{\partial t}-\nabla\cdot[K_r(\psi)K_s(\nabla\psi+\eta_z)]=q_{sf}+q_s \tag{1.1a}$$

$$\frac{\partial Q}{\partial t}+c_k\frac{\partial Q}{\partial s}-D_h\frac{\partial^2 Q}{\partial s^2}=c_k q_{sb} \tag{1.1b}$$

where in equation (1.1a) θ [L^3L^{-3}] is the volumetric water content, S_s [L^{-1}] is the aquifer specific storage, ψ [L] is the variable pressure head, t [T] is time, n [L^3L^{-3}] is the porosity, K_s [LT^{-1}] is the saturated hydraulic conductivity tensor, $K_r(\psi)$ [-] is the relative hydraulic conductivity function, $\eta_z=(0,0,1)^T$ with z [L] the vertical coordinate directed upward, q_{sf} [$L^3L^{-3}T^{-1}$] is the inflow or outflow rate from the surface to the subsurface, and q_s [$L^3L^{-3}T^{-1}$] is a source or sink term. In the surface flow equation (1.1b), Q [L^3T^{-1}] is the discharge along the overland and channel network, c_k [LT^{-1}] is the kinematic celerity, s [L] is the coordinate direction for each segment of the overland and channel network, D_h [L^2T^{-1}] is the hydraulic diffusivity, and q_{sb} [$L^3L^{-1}T^{-1}$] is the inflow or outflow rate from subsurface to surface. The inflow or outflow rates q_{sf} and q_{sb} are the coupling terms and represent, respectively, the surface-to-subsurface and subsurface-to-surface exchanges of water. The nonlinear characteristics $\theta(\psi)$ and $K_r(\psi)$ are specified using *van Genuchten* [1980] relationships.

The model includes a number of features. To give some examples, it handles atmospheric, inflow and outflow (Neumann), and fixed pressure head (Dirichlet) boundary conditions that can vary in space and time. It also includes the algorithm proposed by *Neuman et al.* [1975] for seepage face boundary conditions. This algorithm can be generalized and extended to account for a second seepage face as mentioned in *Cooley* [1983] and implemented in *Rulon and Freeze* [1985] for an application to steady state slope stability analysis in the presence of layered heterogeneity.

CATHY works on a three-dimensional domain discretized by means of a regular triangulation formed by tetrahedral elements. The surface boundary represents the catchment digital elevation model (DEM) and it is made up of rectangular cells. The tetrahedral mesh is built by subdividing the grid cell of the DEM into triangles. Thus, each triangle is

made of three nodes of the computational mesh and represents a face of one tetrahedron. The cell-based solution of the surface flow equation (1.1b) is achieved numerically using the Muskingum-Cunge method for the variable Q. The node-based solution of the 3D Richards equation for the variable ψ is achieved using the linear Galerkin FE method for spatial discretization and a backward Euler FD scheme for time integration, and is linearized by a Picard or Newton iterative scheme [*Paniconi and Putti*, 1994].

The numerics of the subsurface model has required updating, for instance to ensure the mass conservation properties of the velocity field. Thus, the MFE method in its hybridized form [*Brezzi and Fortin*, 1991] has been considered and tested for the 2D Richards flow equation [*Bergamaschi and Putti*, 1999] and for the 3D saturated flow equation [*Mazzia*, 1999; *Mazzia et al.*, 2000; *Mazzia and Putti*, 2005]. Although the method gives accurate results in terms of velocity field, the high accuracy is achieved at a much higher computational cost compared to linear FE methods. In addition, it is often affected by ill-conditioning in the presence of strongly anisotropic coefficients [*Mazzia et al.*, 2011]. Given this limitations, it has been suggested that it may still be advantageous to use the linear Galerkin approach and to solve the conservation problems by implementing appropriate post-processing techniques capable of building conservative velocity fields starting from linear Galerkin velocities [e.g., *Larson and Niklasson*, 2004].

1.5.2 Surface-subsurface transport model

The CATHY_FT model [*Weill et al.*, 2011] is an updated version of the CATHY model which simulates not only surface–subsurface flow but also surface–subsurface mass transport and flow-transport interactions. The two additional equations which are solved in the model are:

$$\frac{\partial \theta c}{\partial t} + \nabla \cdot [vc - D\nabla c] = q_{tsf} + q_{ts} \tag{1.2a}$$

$$\frac{\partial Q_m}{\partial t} + c_t \frac{\partial Q_m}{\partial s} - D_c \frac{\partial^2 Q_m}{\partial s^2} = c_t q_{tsb} \tag{1.2b}$$

where (1.2a) is the 3D advection-dispersion equation and (1.2b) is the 1D surface solute transport equation which follows the same dynamic of equation (1.1b). In these equations c [ML^{-3}] is the subsurface solute concentration, v [LT^{-1}] is the Darcy velocity vector, D [$\mathrm{L}^2\mathrm{T}^{-1}$] is the tensor accounting for both mechanical dispersion and molecular diffusion, q_{ts} [$\mathrm{ML}^{-3}\mathrm{T}^{-1}$] is a solute mass source or sink term, q_{tsf} is the solute mass inflow or

outflow rate from the surface to the subsurface [$ML^{-3}T^{-1}$], Q_m [MT^{-1}] is the solute mass discharge, c_t [LT^{-1}] is the kinematic solute celerity, D_c [L^2T^{-1}] is the surface solute diffusivity, and q_{tsb} [$ML^{-1}T^{-1}$] is the solute mass inflow or outflow from the subsurface to the surface. Analogously to the flow equation, q_{tsf} and q_{tsb} are the coupling terms and represent, respectively, the surface-to-subsurface and subsurface-to-surface exchanges of solute.

The CATHY_FT model works on the same computational domain and surface catchment DEM as the flow model. The cell-based solution of the surface transport equation for the variable Q_m is, as for surface flow, achieved numerically using the explicit Muskingum-Cunge method. The advection-dispersion equation (1.2a) is solved by means of a time-splitting technique that allows the combination of explicit time stepping for the advective fluxes with implicit time stepping for the dispersive fluxes. This is done because of the difficulties in approximating the equation when advection dominates and, thus, to maintain the possibility of using an efficient scheme for advection. The solution procedure is achieved with the use of multiple advective sub-time steps per dispersive step since the advective step is constrained by the Courant-Friedichs-Lewy (CFL) [*Courant et al.*, 1967] condition. The advective equation is discretized using the element-based high resolution finite volume (HRFV) scheme and the resulting concentration field is used as input to the time-implicit dispersive step which is discretized by means of the node-based linear Galerkin FE method. In previous works [*Mazzia et al.*, 2000, 2001; *Mazzia and Putti*, 2005] the MFE in its hybridized form has been used for the discretization of the dispersive fluxes. This was done since the HRFV and the MFE use similar functional spaces for the approximation of the dependent variable (in both cases the solution is element-based), making them ideally suited for combination in a time-splitting approach. Considering again the high computational cost required by the MFE method and its ill-conditioning problems, it has been chosen to implement the linear Galerkin method and accurately combine the element-based (for HRFV) and node-based (for linear Galerkin) solutions by interpolating the concentration variable. However, the performance of the new time-splitting operator has not been examined to date.

1.5.3 Coupling algorithms

In the CATHY_FT model we have three levels of coupling: surface–subsurface flow, surface–subsurface transport, and flow–transport interactions. The surface and subsurface equations are solved sequentially and coupling is performed through a boundary condition switching algorithm. This is possible because of the explicit nature of the surface solvers and implicit nature of the subsurface flow and dispersive solvers. Nonetheless, the boundary condition coupling scheme, by invoking a node-to-cell and cell-to-node interpolation algorithm for the main variable, introduces water balance errors that can affect the numerical performance of the model [*Goumiri and Prevost*, 2011]. Additional errors derive from the sequential iterative procedure since the exhanges fluxes between the surface and subsurface compartments are not completely synchronous [*Dagès et al.*, 2012; *Fiorentini et al.*, 2015]. The mass balance errors arising from the boundary condition coupling scheme in CATHY_FT are even more complicated to control. First of all because any water balance error will affect the accuracy of the transport model. Secondly, not only a node-to-cell and cell-to-node but also a node-to-face, face-to-node, cell-to-face, and face-to-cell interpolation algorithm is required. Finally, the solution of transport processes always involves difficult numerics and complex boundary conditions.

The third level of coupling, which links the flow and transport models, is seamlessly handled in the model since in the sequential solution procedure the flow modules are solved before their transport counterparts, such that after the groundwater flow solution the volumetric water content and velocity field are passed as input to the transport solver. This is possible since in this version of the model it is assumed that the solute concentration does not affect the flow field. For density-driven phenomena a physical coupling is also required and the flow and transport equations have to be solved iteratively [*Putti and Paniconi*, 1995; *Gambolati et al.*, 1999; *Mazzia et al.*, 2001; *Mazzia and Putti*, 2005].

Chapter 2

Mass-conservative reconstruction of Galerkin velocity fields for transport simulations

2.1 Abstract

Accurate calculation of mass-conservative velocity fields from numerical solutions of Richards' equation is central to reliable surface–subsurface flow and transport modeling, for example in long-term tracer simulations to determine catchment residence time distributions. In this study we assess the performance of a local Larson-Niklasson (LN) post-processing procedure for reconstructing mass-conservative velocities from a linear ($\mathcal{P}_1$) Galerkin finite element solution of Richards' equation. This approach, originally proposed for a-posteriori error estimation, modifies the standard finite element velocities by imposing local conservation on element patches. The resulting reconstructed flow field is characterized by continuous fluxes on element edges that can be efficiently used to drive a second order finite volume advective transport model. Through a series of tests of increasing complexity that compare results from the LN scheme to those using velocity fields derived directly from the $\mathcal{P}_1$ Galerkin solution, we show that a locally mass-conservative velocity field is necessary to obtain accurate transport results. We also show that the accuracy of the LN reconstruction procedure is comparable to that of the inherently conservative mixed finite element approach, taken as a reference solution, but that the LN scheme has much lower computational costs. The numerical tests examine steady and unsteady, saturated and variably saturated, and homogeneous and heterogeneous cases along with initial and boundary conditions that include dry soil infiltration, alternating solute and water injection, and seepage face outflow. Typical problems that arise with velocities derived from

$\mathcal{P}_1$ Galerkin solutions include outgoing solute flux from no-flow boundaries, solute entrapment in zones of low hydraulic conductivity, and occurrences of anomalous sources and sinks. In addition to inducing significant mass balance errors, such manifestations often lead to oscillations in concentration values that can moreover cause the numerical solution to explode. These problems do not occur when using LN post-processed velocities.

2.2 Introduction

Mathematical models of groundwater flow and solute transport enforce the fundamental principles of fluid and solute mass conservation expressed in the form of a system of partial differential equations, often nonlinear. Any application of such models requires the numerical solution of this system of equations, adapting the discretization to the temporal, geometrical, and structural complexity of available data. This leads to high-dimensional nonlinear algebraic systems whose solution often necessitates advanced high performance computing resources. Quality control of the numerical solution of such systems is typically predicated on demonstrating a convergent and mesh-independent discretization process. At large scales or in three-dimensional (3D) settings, however, mesh refinement procedures become impractical, and alternative metrics based on fixed meshes are used to asses the quality of the discrete solution. One such widely used metric is the mass balance error (MBE) [e.g., *Huyakorn et al.*, 1985; *Konikow*, 2001].

Subsurface solute transport processes are driven by the fluid velocity and saturation fields as calculated from the solution of the companion flow equation. A three-step numerical procedure is generally used: 1) solve the flow equation; 2) calculate the discrete velocity field; 3) solve the solute transport equation. Correspondingly, three MBE sources can be identified within this process, each one feeding into the following step: i) spurious losses or gains of fluid mass arising from the discrete solution of the flow problem; ii) spurious losses or gains of fluid mass present in the numerical velocity field; iii) spurious losses or gains of solute mass occurring in the solution of the transport equation. In this paper we are interested in studying how MBEs arising in step 2 affect the quality of the solution in step 3 by looking at detailed measurements of mass balance errors in the solution of the transport equation, which evidently are cumulative of the errors from all three steps. When continuous Galerkin methods are used to discretize the solute transport equation,

no particular issues related to mass conservation arise if one looks at the appropriate control volume [*Putti and Sartoretto*, 2009]. However, exact mass conservation on the control volume where velocities are defined can only be achieved by finite volume or discontinuous Galerkin methods, which are the ideal setting for first order problems, whose solution can be discontinuous or can display large gradients. Moreover, it is well known that continuous Galerkin methods are subject to Peclet limitations when applied to advection-dominated processes. To avoid unbounded oscillatory behavior one can impose a local grid Peclet restriction, achievable by using a fine spatial discretization but at the expense of high computational effort, or apply an upwinding scheme, obtaining a first order stable solution but with numerical diffusion smearing the front [e.g., *Huyakorn et al.*, 1985]. For this reason, we focus on advection-dominated processes governed by a nearly hyperbolic conservation law solved by a well-established finite volume (FV) method [*Mazzia et al.*, 2000, 2001, 2002; *Mazzia and Putti*, 2005], robust to Peclet number limitations and accurate to second order away from discontinuities. The solution algorithm, which mimics mass balance within a control volume or cell, makes direct use of the normal fluxes defined at inter-element boundaries, thus requiring a locally mass-conservative velocity field [*Dawson et al.*, 2004b].

Modern trends in discretization methods focus on the use of unstructured grids, which, with respect to regular grids, allow better adaptation to geometrical and structural heterogeneities, with consequential savings in computational time. Standard (node-based) Galerkin finite element methods (FEM) are often the schemes of choice for solving subsurface flow equations because of their intrinsic ability to employ unstructured grids and handle anisotropy, in addition to their computational efficiency. However, their use as flow solvers is known to yield nonconservative velocity fields that lead to difficulties in the subsequent solution of the transport equation. In this paper we focus on linear, or $\mathcal{P}_1$, Galerkin methods, that, in contrast to higher order FEMs, have some interesting and desirable features connected with the geometrical properties of the mesh, such as robustness with respect to anisotropic coefficients and monotonicity [*Forsyth*, 1991; *Putti and Cordes*, 1998; *Cordes and Putti*, 2001; *Mazzia et al.*, 2011]. The methods presented in this paper are however also adaptable to other higher order FEMs. Moreover, we focus on Richards' equation-based models, as they represent a class of highly nonlinear systems that pose severe problems in their numerical solution.

The general reason for the nonconservative behavior of $\mathcal{P}_1$ Galerkin methods is that they are not within the class of locally conservative (LOC) discretization schemes. Following *Edwards et al.* [2002] and *Klausen and Russell* [2004], in a LOC method i) the sum of the fluxes over each element face is equal to the total change in storage plus or minus any source or sink term and ii) the flux is continuous across each inter-element boundary. These two properties cannot be satisfied by a velocity field obtained from $\mathcal{P}_1$ discretizations, as can be easily derived from simple considerations on the continuity of the $\mathcal{P}_1$ solution at element faces. In other words, the element-wise velocity field, post-computed from the pressure head solution of Richards' equation, does not conserve mass, i.e., its divergence over an element does not balance the discrete mass accumulation [*Farthing et al.*, 2002]. This local violation of the mass balance principle gives rise to approximation errors in the advective transport solution or, more generally, in any application that relies on accurate flux estimates.

The nonconservative nature of the numerical velocity field corresponds to a violation of the local maximum/minimum principle in the flow equation [*Forsyth*, 1991; *Cordes and Putti*, 2001; *Putti and Sartoretto*, 2009]. Typical symptoms, discernible already in the behavior of the pressure head solution, are the presence of spurious oscillations leading to an unphysical behavior of the discrete velocity field [*Forsyth*, 1991], which manifests itself with numerically generated mass sources or sinks. As a consequence, when these velocity fields are used to drive a transport equation, numerical discretization schemes cannot be conservative unless these sources or sinks are taken somehow into account in the transport equation. The development of discretization methods that satisfy a local maximum principle is an active field of research [e.g., *Ciarlet*, 1970; *Kershaw*, 1981; *Brezzi et al.*, 1989; *Knabner and Angermann*, 2003; *Bertolazzi and Manzini*, 2005; *Le Potier*, 2005; *Cordes and Putti*, 2001; *Forsyth*, 1991; *Mazzia*, 2008; *Putti and Cordes*, 1998], and simple discretizations that satisfy this principle are still elusive, with nonlinearities often introduced to achieve monotonicity [*Bertolazzi and Manzini*, 2005; *Le Potier*, 2005]. Although no second order linear finite difference scheme satisfies a local maximum principle [*Kershaw*, 1981], conservative linear schemes that lead to locally conservative velocity fields do exist. Examples include multi-point flux approximations [*Edwards and Rogers*, 1998], enhanced cell-centered finite differences or finite volumes [*Arbogast et al.*, 1998], and mixed finite elements (MFE) [*Brezzi and Fortin*, 1991; *Farthing et al.*, 2002], all widely investigated

for coupled flow–transport problems [*Mazzia et al.*, 2001; *Mazzia and Putti*, 2005]. These methods have in common that the discrete mass balance is enforced over a control volume (i.e., the element) that coincides with the volume over which the velocity solution is defined. By contrast, the $\mathcal{P}_1$ Galerkin pressure head solution is node-based while velocities are evaluated element-wise, thus local mass conservation is satisfied only on a dual nodal control volume (e.g., a Voronoi cell in two-dimensional Delaunay triangulations). Control-volume FEMs try to exploit this property by proper definition of these control volumes and associated basis functions [*Forsyth*, 1991; *Durlofsky*, 1994]. However, the use of dual meshes may lead to ill-conditioning and grid-alignment problems for severely deformed unstructured meshes. All these schemes use flux information defined on inter-element boundaries (edges in 2D and faces in 3D) and often employ degrees of freedom located on the cell gravity centers or on the cell boundaries. This approach typically leads to relatively large stencils and large dimensions of the system matrices. Thus, there are decisive computational advantages in using a node-based $\mathcal{P}_1$ Galerkin approach for the solution of Richards' equation. In fact, in unstructured triangulations, the number of cells is on average 3 times the number of nodes, and the number of edges is more than 10 times the number of nodes. In addition, face-based discretizations such as MFE and mixed-hybrid finite elements (MHFE) are often affected by ill-conditioning in the presence of strongly anisotropic coefficients [*Mazzia et al.*, 2011]. A more computationally attractive alternative is the use of appropriate post-processing techniques to build conservative velocity fields starting from Galerkin velocities.

Different post-processing algorithms for the reconstruction of Galerkin velocities have been developed. Early schemes such as those proposed by *Yeh* [1981] and successively modified by different authors [e.g., *Srivastava and Brusseau*, 1995; *Zhou et al.*, 2001] lack robustness, exhibiting significant accuracy losses and sub-optimal convergence for heterogeneous problems [*Cainelli et al.*, 2012]. More recently, *Larson and Niklasson* [2004] proposed a post-processing technique for the accurate evaluation of Galerkin gradients to be employed in a-posteriori error estimation. This technique was later used and expanded as a means to achieve conservation in the velocity field for applications to reactive transport driven by saturated groundwater flow [*Sun and Wheeler*, 2006]. Application of the Larson-Niklasson (LN) correction algorithm in the context of variably saturated groundwater flow has been proposed by *Kees et al.* [2008] and *Cheng et al.* [2010], where

convergence rates analogous to those attainable by MFE were reported. Additional experiments were performed by *Povich et al.* [2013] using the LN approach for a problem of variable density groundwater flow and transport and by *Kees et al.* [2011] who reconstruct with the LN algorithm the velocities arising from a residual-based variational multiscale model of the Navier-Stokes equations, used to describe two-fluid incompressible flow processes. A thorough investigation on idealized test cases for two-dimensional steady state diffusion problems was conducted by *Schiavazzi* [2011], where streamlines calculated with the nonconservative $\mathcal{P}_1$ scheme were compared to conservative reconstructed velocities.

The LN approach is inspired by research developed during the 1980s and 90s. Early contributions are found in *Kelly* [1984], where a self-equilibrated configuration of the residual forms the basis for a complementary a-posteriori energy estimation of the finite element discretization error. Further generalizations were provided by *Ainsworth and Oden* [1992, 1993] and *Agarwal and Oden* [1993], where local problems on clusters of elements sharing the same node were addressed. The LN scheme applies these ideas to restore element-wise conservative fluxes starting from the velocities obtained from $\mathcal{P}_1$ Galerkin solutions. The process involves the calculation of face-based corrections of the original velocities by means of the solution of node-based systems of dimension equal to the number of elements in the nodal patch. This yields a computationally efficient and intrinsically parallelizable procedure.

Accurate evaluation of the practical performance of the LN approach can be achieved only by means of realistic test cases. To achieve this aim, we have implemented the LN approach within the CATchment HYdrology Flow-Transport (CATHY_FT) model [*Camporese et al.*, 2010; *Weill et al.*, 2011], which couples a $\mathcal{P}_1$ Galerkin FEM solver for Richards' equation and a high resolution FV (HRFV) solver [*Mazzia and Putti*, 2005] for the advective transport equation. Inter-element based and locally conservative fluxes are computed by an LN local post-processing method and then fed to the FV-based hyperbolic solver.

In this study we assess model performance by measuring the accuracy of the numerical solution as the ability of the transport model to conserve mass. In this context, we propose a comparison, performed for a range of test cases, between the results obtained using as input the velocity field directly arising from the $\mathcal{P}_1$ Galerkin solution and the velocity field reconstructed with the LN local post-processing technique. The test cases

range from simple scenarios under saturated steady flow and unsteady transport and in the presence of convergent streamlines towards an outlet, to more complex scenarios involving enhanced streamline curvatures generated by the presence of localized heterogeneity and variably saturated and unsteady flow. For the fully saturated test cases, we also compare the results obtained with LN to those obtained using MFE velocity fields that are inherently mass-conservative [*Putti and Sartoretto*, 2009]. The test cases are used to elucidate the different errors in the FV-based solute transport solution that can arise when a nonconservative velocity field is used as input. These errors (e.g., mass flowing out from zero flux boundaries, mass permanently entrapped in zones of low hydraulic conductivity, spawning of artificial sink/source terms) are not always taken into account in mass balance computations, which are typically calculated by simply comparing the mass entering and exiting across the entire boundary with the mass change within the domain. We thus demonstrate that while large mass balance errors are always evidence of a poor solution, a perfect mass balance is not necessarily proof that an accurate solution has been achieved or that a model is valid.

2.3 Methodology

2.3.1 Mathematical model

The conservative form of Richards' equation [*Celia et al.*, 1990a] coupled with a purely advective transport equation can be written as:

$$\frac{\theta}{n} S_s \frac{\partial \psi}{\partial t} + \frac{\partial \theta}{\partial t} + \nabla \cdot v = q_s \tag{2.1a}$$

$$v = -K_r(\psi) K_s (\nabla \psi + \eta_z) \tag{2.1b}$$

$$\frac{\partial \theta c}{\partial t} + \nabla \cdot [vc] = q_{ts} \tag{2.1c}$$

where $\theta(\psi)$ is the volumetric moisture content [$-$], n is the porosity of the medium [$-$], S_s is the aquifer specific storage [L^{-1}], ψ is the pressure head [L], t is time [T], ∇ is the spatial gradient operator [1/L], v is the Darcy velocity vector [LT^{-1}], K_s is the saturated hydraulic conductivity tensor [LT^{-1}], $K_r(\psi)$ is the relative hydraulic conductivity function [-], z is the vertical coordinate directed upward [L], $\eta_z = (0, 0, 1)^T$, and q_s is a source or sink term [$\mathrm{L}^3\mathrm{L}^{-3}\mathrm{T}^{-1}$]. In the advective solute transport equation (2.1c), c is the subsurface

solute concentration [ML^{-3}] and q_{ts} is a term incorporating an external solute sink or source [$ML^{-3}T^{-1}$]. The water content–pressure head and relative conductivity–pressure head dependencies will be described here by means of *van Genuchten* [1980] relationships. Appropriate boundary and initial conditions complete the mathematical model.

2.3.2 Numerical discretization

We work on a three-dimensional domain Ω discretized by means of a regular triangulation $\mathcal{T}_h(\Omega)$ formed by N nodes and E tetrahedral elements. The triangulation will be characterized by the following sets. The set of nodes of $\mathcal{T}_h(\Omega)$ is defined as $\mathcal{N}$. Given a tetrahedron $T \in \mathcal{T}_h(\Omega)$, the set of nodes that define T is denoted by $\mathcal{N}_T$ and the set of faces F is given by $\mathcal{F}_T$. The set of nodes that define F is denoted by $\mathcal{N}_F$. All the tetrahedra sharing node i are grouped in the set $\mathcal{E}_i$, called the element patch of node i. In what follows we will not distinguish between elements of these sets and the global indices used to number them, as is usual in a FEM or FV approach. Thus, T will indicate both the tetrahedron index (thus we sum on them) and the subregion of Ω containing points of T, and $\mathcal{E}_i$ will identify both the set of elements as a subregion of Ω as well as the set of indices of the tetrahedra forming that region within a global (mesh-wise) enumeration.

The spatial discretization of Richards' equation is obtained by means of linear ($\mathcal{P}_1$) Galerkin finite elements [*Paniconi and Putti*, 1994], while the transport equation is solved by means of second order Godunov type finite volumes [*Mazzia and Putti*, 2005]. It is well known that the latter scheme requires conservative velocity fields to maintain monotonicity of the numerical solution [*Klausen and Russell*, 2004]. For this reason the velocity field arising from the FEM flow solution is reconstructed at each time step using the Larson-Niklasson post-processing technique. The LN velocities are then used by the FV module to solve the transport equation, with linear interpolation in time constrained by a Courant-Friedrichs-Lewy (CFL) condition.

In the next sections the important features of the modeling approach are described, with an emphasis on details related to conservation principles, such as the interpolation of relevant quantities between elements, nodes, and faces.

2.3.2.1 Finite element approximation for Richards' equation

In the $\mathcal{P}_1$ Galerkin FEM implementation for the flow module, equation (2.1b) is first substituted into (2.1a) to obtain the classical mixed form of Richards' equation. Then, the solution pair (ψ, θ) and the velocity vector v are approximated by (ψ_h, θ_h) within the space of the linear test functions and by v_h within the space of element-wise constant functions:

$$\psi(t,x) \simeq \psi_h(t,x) = \sum_{j=1}^{N} \psi_j(t)\phi_j(x) \tag{2.2a}$$

$$\theta(t,x) \simeq \theta_h(\psi_h(t,x)) = \sum_{j=1}^{N} \theta_j(\psi_j(t))\phi_j(x) \tag{2.2b}$$

$$v(t,x) \simeq v_h(t,x) = \sum_{T=1}^{E} v_T(t)\chi_T(x) \tag{2.2c}$$

where $x \in \Omega$ is the vector of three-dimensional coordinates, ϕ_i, $i = 1, \ldots, N$, are the $\mathcal{P}_1$ Galerkin basis functions, and χ_T is the characteristic function of element T. Note that the nodal water content θ_j is a function of the pressure head $\psi_j(t)$ at the same node j and thus, indirectly, of time but not of space. In what follows, we refer to $\mathcal{P}_1$ Galerkin velocities as those directly derived from the $\mathcal{P}_1$ Galerkin solution (v, equation (2.2c)). Note that this does not mean $\mathcal{P}_1$ representation of the velocity field. For the FEM discretization of Richards' equation, the set of nodes $\mathcal{N}$ of the computational mesh is the union $\mathcal{N}_D \cup \mathcal{N}_N \cup \mathcal{N}_I$, where $\mathcal{N}_D$ is the set of Dirichlet nodes, $\mathcal{N}_N$ is the set of Neumann nodes, and $\mathcal{N}_I$ is the set of internal nodes. The Dirichlet and Neumann boundaries of $\partial\Omega$ are defined as Γ_D and Γ_N, respectively. The discrete variational formulation of equation (2.1a) can then be written as:

$$\int_\Omega \frac{\theta_h(\psi_h)}{n} S_s \frac{\partial \psi_h}{\partial t}\phi_i \, dx + \int_\Omega \frac{\partial \theta_h(\psi_h)}{\partial t}\phi_i \, dx + \int_\Omega K_r(\psi_h) K_s(\nabla\psi_h + \eta_z)\cdot\nabla\phi_i \, dx - \int_\Omega q_s\phi_i \, dx + \int_{\Gamma_N} q_N\phi_i \, ds = 0 \qquad i = 1, ..., N \tag{2.3}$$

where q_N is the prescribed Neumann flux $[L/T]$. Note that if q_N is positive, water leaves the domain across the boundary Γ_N. After spatial discretization, the resulting system of nonlinear ordinary differential equations is solved in time by the backward Euler finite

difference scheme. The final discrete nonlinear system is:

$$F(\Psi_h^{k+1}) = H(\Psi_h^{k+1})\Psi_h^{k+1} + \frac{1}{\Delta t^k}C_1(\Psi_h^{k+1})\Psi_h^{k+1} + \frac{1}{\Delta t^k}C_2\Theta_h(\Psi_h^{k+1}) + b_1(\Psi_h^{k+1}) - \frac{1}{\Delta t^k}C_2\Theta_h(\Psi_h^k) - \frac{1}{\Delta t^k}C_1(\Psi_h^{k+1})\Psi_h^k + b_2 = 0 \quad (2.4)$$

where k is the time step counter, $\Psi_h^k = \left\{\psi_i^k\right\}$ is the vector containing nodal pressure heads, $H(\Psi_h^k) = \left\{h_{ij}(\Psi_h^k)\right\}$ $(i,j = 1,...,N)$ is the stiffness matrix having coefficients that are nonlinear functions of Ψ_h^k, Δt^k is the time step size, $\Theta_h(\Psi_h^k) = \left\{\theta_i(\psi_i^k)\right\}$ is the vector containing the nodal water contents, $C_1(\Psi_h^k) = \left\{c_{1,ij}(\Psi_h^k)\right\}$ and $C_2 = \left\{c_{2,ij}\right\}$ are mass matrices, $b_1 = \left\{b_{1,i}(\Psi_h^k)\right\}$ is the vector accounting for the gravitational term with coefficients that are nonlinear functions of Ψ_h^k, and $b_2 = \left\{b_{2,i}\right\}$ is the vector containing the boundary and source/sink terms. The expressions of the stiffness and mass matrices are:

$$h_{ij}(\Psi_h) = \int_\Omega K_r(\Psi_h)K_s\nabla\phi_j \cdot \nabla\phi_i \, dx \quad (2.5a)$$

$$c_{1,ij}(\Psi_h) = \int_\Omega \frac{\theta_h(\Psi_h)}{n}S_s\phi_i\phi_j \, dx \quad (2.5b)$$

$$c_{2,ij} = \int_\Omega \phi_i\phi_j \, dx \quad (2.5c)$$

The i^{th} elements of vectors b_1 and b_2 are given by:

$$b_{1,i}(\Psi_h) = \int_\Omega K_r(\Psi_h)K_s\eta_z \cdot \nabla\phi_i \, dx \quad (2.6a)$$

$$b_{2,i} = \int_{\Gamma_N} q_N\phi_i \, ds - \int_\Omega q_s\phi_i \, dx \quad (2.6b)$$

The integrals in (2.5a), (2.5b), and (2.6a) are evaluated using the midpoint rule, by performing the Gauss integration for each element with one point (defined at the barycenter of the element) and unit weight, while the other integrals are evaluated analytically. Higher order integration may be warranted for the nonlinear terms, but its effect is not explored in this paper.

The nonlinear system (2.4) is solved by means of a mixed Newton/Picard iteration with time step adaptation [*Celia et al.*, 1990a; *Paniconi and Putti*, 1994]. This approach applies Newton linearization to the third term of (2.4) (the term involving $\Theta_h(\Psi_h^{k+1})$) and Picard linearization to all the remaining nonlinear terms. Following this procedure, at each nonlinear iteration r, the following symmetric and positive definite system of linear

equations is solved:

$$\begin{aligned}\left[H(\Psi_h^{k+1,r}) + \frac{1}{\Delta t^k}C_1(\Psi_h^{k+1,r}) + \frac{1}{\Delta t^k}C_2 J_\theta(\Psi_h^{k+1,r})\right]\delta\psi &= -F(\Psi_h^{k+1,r}) \\ = -\left(H(\Psi_h^{k+1,r}) + \frac{1}{\Delta t^k}C_1(\Psi_h^{k+1,r})\right)\Psi_h^{k+1,r} &- \frac{1}{\Delta t^k}C_2\Theta_h(\Psi_h^{k+1,r}) - b_1\left(\Psi_h^{k+1,r}\right) \\ &+ \frac{1}{\Delta t^k}C_1(\Psi_h^{k+1,r})\Psi_h^k + \frac{1}{\Delta t^k}C_2\Theta_h(\Psi_h^k) - b_2 \quad (2.7)\end{aligned}$$

where $\delta\psi = (\Psi_h^{k+1,r+1} - \Psi_h^{k+1,r})$ and $J_\theta(\psi_h) = \mathrm{diag}\{\partial\theta_i(\psi_i)/\partial\psi_i\}$ is the diagonal Jacobian matrix of Θ_h. We use mass lumping on matrices C_1 and C_2 to improve conditioning of the linear system matrices by enhancing diagonal dominance, and to maintain symmetry on the product $C_2 J_\theta$.

At the end of the time step, Darcy's velocity on element T is calculated by testing (2.1b) on piecewise constant basis functions (the characteristic functions of equation (2.2c)) and again using the midpoint quadrature formula, yielding:

$$\begin{aligned}v_T^{k+1} &= -\frac{1}{|T|}\int_T K_r(\Psi_h^{k+1})K_s(\nabla\Psi_h^{k+1} + \eta_z)\,dx \\ &\simeq -K_r(\psi_T^{k+1})K_s^{(T)}(\nabla\Psi_h^{k+1} + \eta_z) = -K_r(\psi_T^{k+1})K_s^{(T)}(\sum_{j\in\mathcal{N}_T}\psi_j^{k+1}\nabla\phi_j + \eta_z)\end{aligned} \quad (2.8)$$

where $|T|$ indicates the measure (volume) $[L^3]$ of element T, $K_s^{(T)}$ is the constant element-averaged saturated hydraulic conductivity in T, and ψ_T^{k+1} is the value of Ψ_h at time t^{k+1} calculated at the center of gravity of T:

$$\psi_T = \frac{1}{4}\sum_{i\in\mathcal{N}_T}\psi_i \quad (2.9)$$

2.3.2.2 Larson-Niklasson post-processing velocity reconstruction

A direct calculation shows that the element-wise constant velocity field calculated in (2.8) yields discontinuous normal fluxes across element faces, thus violating the local mass conservation property [*Klausen and Russell*, 2004]. To obviate this problem, we use the LN procedure as described in *Larson and Niklasson* [2004] and *Kees et al.* [2008] to construct a new velocity field that is locally mass-conservative and that can be used in the FV discretization of the transport equation.

The LN approach can be derived within the framework of a global mass conservation principle, as expressed in our case by the semi-discrete nodal Galerkin equation (2.3).

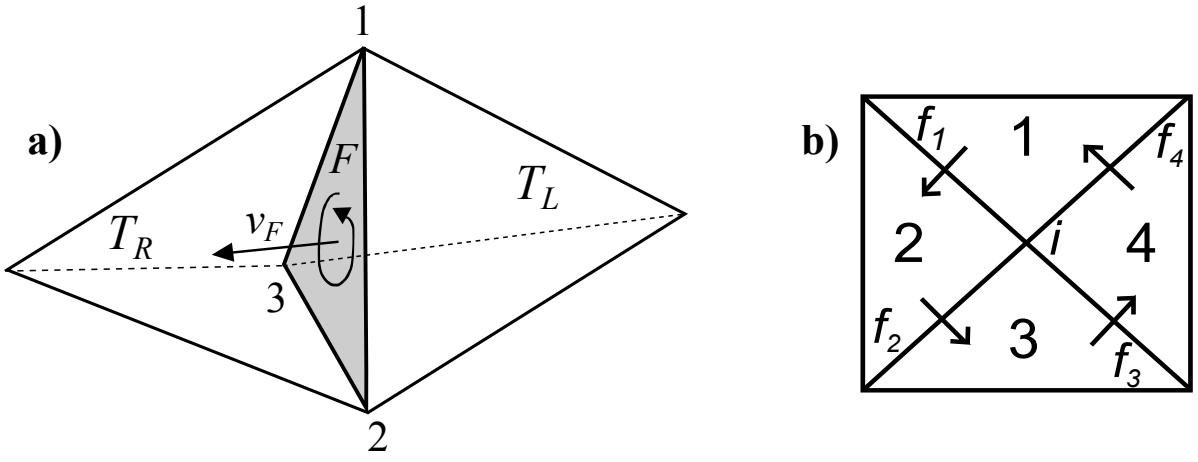

Figure 2.1: *(a) Orientation of the unit normal ν_F to face F and the tetrahedron to its right (T_R) and to its left (T_L); (b) typical element star for a 2D problem, centered at node i. The normal direction is indicated by the arrows.*

Since LN is a post-processing scheme, it is performed at the end of each time step, so that Ψ_h^{k+1} is the converged solution of the nonlinear solver. Using the fact that the integral over the domain is equal to the sum of the integrals over each element and that the union of all tetrahedra sharing node i coincides with the support of ϕ_i, we obtain:

$$\sum_{T\in\mathcal{E}_i} R_T^{(i)} = \sum_{T\in\mathcal{E}_i} \left\{ \int_T \frac{\theta_h(\psi_h)}{n} S_s \frac{\partial \psi_h}{\partial t} \phi_i \, dx + \int_T \frac{\partial \theta_h(\psi_h)}{\partial t} \phi_i \, dx \right.$$
$$\left. + \int_T K_r(\psi_h) K_s \left(\nabla \psi_h + \eta_z\right) \cdot \nabla \phi_i \, dx - \int_T q_s \phi_i \, dx + \int_{\partial T \cap \Gamma_N} q_N \phi_i \, ds \right\} \quad (2.10)$$

which, in words, asserts that the mass balance equation for node i is given by the sum of elemental residuals $R_T^{(i)}$ of all elements T sharing node i. This can be rewritten in fully discrete form as:

$$\sum_{T\in\mathcal{E}_i} R_T^{(i)} = \sum_{T\in\mathcal{E}_i} \left\{ \sum_{j\in\mathcal{N}_T} \left[\frac{1}{\Delta t^k} c_{1,ij}^{(T)}(\Psi_h^{k+1}) \left(\psi_j^{k+1} - \psi_j^k\right) + \frac{1}{\Delta t^k} c_{2,ij}^{(T)} \left(\theta_j(\psi_j^{k+1}) - \theta_j(\psi_j^k)\right) \right.\right.$$
$$\left.\left. + \; h_{ij}^{(T)}(\Psi_h^{k+1}) \psi_j^{k+1} \right] + b_{1,i}^{(T)}(\Psi_h^{k+1}) + \; b_{2,i}^{(T)} \right\} \quad (2.11)$$

where $c_{1,ij}^{(T)}$, $c_{2,ij}^{(T)}$, $h_{ij}^{(T)}$, $b_{1,i}^{(T)}$, and $b_{2,i}^{(T)}$ are the components of the corresponding local (element T) mass and stiffness matrices and load vectors. This equation is a simple rearrangement of equation (2.4) before the elemental assembly phase. Note that if $i \in \mathcal{N}_D \cup \mathcal{N}_I$, the

sum of elemental residuals $R_T^{(i)}$ of all elements T sharing node i is zero (i.e., the sums of the residuals in (2.10) and (2.11) are equal to zero), while if $i \in \mathcal{N}_D$, substitution of the solution Ψ_h^{k+1} into equation (2.11) yields a nonzero value that is the exact flow entering or exiting node i, i.e., $\sum_{T\in\mathcal{E}_i} R_T^{(i)}$.

The discrete mass balance equation (2.10) can be obtained by application of Green's lemma on each element instead of over the entire domain and then summing over all elements. If we do this we obtain an extra flux term on the boundaries of each tetrahedron:

$$\sum_{T\in\mathcal{E}_i}\left\{\int_T \frac{\theta_h(\psi_h)}{n} S_s \frac{\partial\psi_h}{\partial t}\phi_i\,dx + \int_T \frac{\partial\theta_h(\psi_h)}{\partial t}\phi_i\,dx + \int_T K_r(\psi_h)K_s(\nabla\psi_h+\eta_z)\cdot\nabla\phi_i\,dx - \int_T q_s\phi_i\,dx + \int_{\partial T} q_F^T\phi_i\,ds\right\} = 0 \quad (2.12)$$

where q_F^T $[L/T]$ is the exact flux associated to face $F \in \partial T$ and $q_F^T = q_N$ if $i \in \mathcal{N}_N$ and $F \in \partial\Omega$. The superscript T in q_F^T indicates that the flux, if positive, is outflowing from ∂T. In what follows, we indicate with ν_F the unit normal to face F and with ν_F^T the unit normal to face F directed outward from element T. The orientation of ν_F is fixed in the counterclockwise direction defined in accordance to the nodal numbering of face F, as illustrated in Figure 2.1a. Thus, $q_F^T = q_F(\nu_F\cdot\nu_F^T)$, where q_F is the exact flux oriented according to ν_F. Denoting with Γ_T the set of faces of element T that are not on a Neumann boundary, the previous equation becomes:

$$\sum_{T\in\mathcal{E}_i}\left\{\int_T \frac{\theta_h(\psi_h)}{n} S_s \frac{\partial\psi_h}{\partial t}\phi_i\,dx + \int_T \frac{\partial\theta_h(\psi_h)}{\partial t}\phi_i\,dx + \int_T K_r(\psi_h)K_s(\nabla\psi_h+\eta_z)\cdot\nabla\phi_i\,dx - \int_T q_s\phi_i\,dx + \sum_{F\in\partial T\cap\Gamma_N}\int_F q_N\phi_i\,ds + \sum_{F\in\Gamma_T}\int_F q_F^T\phi_i\,ds\right\} = 0 \quad (2.13)$$

Comparing (2.13) with (2.10), we obtain immediately a form of the local conservation principle:

$$\sum_{T\in\mathcal{E}_i}\left[\sum_{F\in\Gamma_T}\int_F q_F^T\phi_i\,ds\right] = \begin{cases} 0 & i\in\mathcal{N}_N\cup\mathcal{N}_I \\ -\sum_{T\in\mathcal{E}_i} R_T^{(i)} & i\in\mathcal{N}_D \end{cases} \quad (2.14)$$

The above equation states that the face fluxes q_F^T satisfying (2.14) must be continuous across all internal faces of the elements in $\mathcal{E}_i$, for $i = 1, ..., N$, and must be equal to the exact flux entering or exiting a Dirichlet node $i \in \mathcal{N}_D$. A natural approximation of optimal

order for q_F is the arithmetic mean $\bar{v}_F$ of the $\mathcal{P}_1$ Galerkin velocity v_T (calculated with equation (2.2c)) with respect to the elements at the left and right sides of F projected along the normal to the face F, i.e., $q_F \simeq \bar{v}_F \cdot \nu_F = \bar{q}_F$. This flux approximation is of optimal order but it is not element-wise conservative, i.e., it does not satisfy equation (2.13). A correction q'_F needs to be introduced to render $\bar{q}_F$ mass-conservative:

$$q_F = \bar{q}_F + q'_F \tag{2.15}$$

The correction is subdivided into two components, one for each neighboring tetrahedron, so that:

$$q_F = \bar{q}_F + q'_F = \bar{v}_F \cdot \nu_F + (U_{T_L} - U_{T_R}) \quad , \quad \bar{v}_F = \frac{1}{2}\left(v_{T_L} + v_{T_R}\right) \tag{2.16}$$

Here we denote with $F = T_R \cap T_L$ the face common to elements T_R and T_L, with the subscripts R and L denoting the "right" and "left" tetrahedra, respectively, so designated according to the local counterclockwise reference system mentioned above and illustrated in Figure 2.1a. Thus, $\nu_F^T \cdot \nu_F$ is positive (+1) when $T = T_L$. It follows that if $F \in \Gamma_D$, the average velocity $\bar{v}_F$ is v_{T_L} if $\nu_F^T \cdot \nu_F = 1$ and v_{T_R} if $\nu_F^T \cdot \nu_F = -1$. Likewise, if $F \in \Gamma_D$, q'_F is U_{T_L} if $\nu_F^T \cdot \nu_F = 1$ and $-U_{T_R}$ otherwise. Substituting equations (2.16) into (2.13) and setting each term of the sum to zero, we obtain a symmetric positive semidefinite system of linear equations for the correction terms that can be written as:

$$\begin{aligned} &\int_T \frac{\theta_h(\psi_h)}{n}\frac{\partial \psi_h}{\partial t} S_s \phi_i \, dx + \int_T \frac{\partial \theta_h(\psi_h)}{\partial t}\phi_i \, dx + \int_T K_r(\psi_h) K_s(\nabla \psi_h + \eta_z) \cdot \nabla \phi_i \, dx - \int_T q_s \phi_i \, dx \\ &+ \sum_{F \in \Gamma_N} \int_F q_N \phi_i \, ds + \sum_{F \in \Gamma_T} \int_F \bar{v}_F \cdot \nu_F^T \phi_i \, ds + \sum_{F \in \Gamma_T} \int_F (U_{T_L} - U_{T_R}) \nu_F^T \cdot \nu_F \phi_i \, ds = 0 \qquad T \in \mathcal{E}_i \end{aligned} \tag{2.17}$$

Using the midpoint rule to evaluate the integrals, the full discretized system reads:

$$Bu^{(i)} = r$$

where:

$$\begin{aligned} B &= \left\{b_{TK}\right\} \qquad b_{TK} = \sum_{F \in \mathcal{F}_T \cap \mathcal{F}_K} \int_F (2\delta_{T,K} - 1)(\delta_{T,T_R} - \delta_{T,T_L}) \nu_F^T \cdot \nu_F \phi_i \, ds \\ r &= \left\{r_T\right\} \qquad r_T = R_T^{(i)} + \sum_{F \in \Gamma_T} \bar{q}_F \int_F \phi_i \, ds \\ u^{(i)} &= \left\{u_K^{(i)}\right\} \qquad\qquad\qquad\qquad\qquad\qquad\qquad\qquad T, K = 1, \ldots, N_{\mathcal{E}_i} \end{aligned}$$

where $u_K^{(i)}$ is the correction U_K which is assumed to be constant on element K for node i and $N_{\mathcal{E}_i}$ is the cardinality of $\mathcal{E}_i$. The element residual $R_T^{(i)}$ is given by:

$$R_T^{(i)} = \left\{ \sum_{j \in \mathcal{N}_T} \left[c_{1,ij}^{(T)}(\Psi_h^{k+1}) \frac{\left(\psi_j^{k+1} - \psi_j^k\right)}{\Delta t^k} + c_{2,ij}^{(T)} \frac{\left(\theta_j(\psi_j^{k+1}) - \theta_j(\psi_j^k)\right)}{\Delta t^k} \right.\right. \\ \left.\left. + \; h_{ij}^{(T)}(\Psi_h^{k+1})\psi_j^{k+1} \right] + b_{1,i}^{(T)}\left(\Psi_h^{k+1}\right) + \; b_{2,i}^{(T)} \right\} \quad (2.18)$$

As shown in *Larson and Niklasson* [2004], this system has rank $N_{\mathcal{E}_i} - 1$. This is in agreement with the fact that equation (2.14) is still valid if multiplied by a constant. We choose to solve this problem by setting to zero one of the unknowns. After solving the system of equations, the conservative normal constituent face flux (i.e., associated to node i) for the face F is computed as:

$$q_{Fi} = \bar{q}_F + (U_{T_L}^{(i)} - U_{T_R}^{(i)}) \quad (2.19)$$

The procedure is then repeated for each node of the mesh so that the final conservative normal flux on each face F can be computed as:

$$q_F = \frac{1}{3} \sum_{i \in \mathcal{N}_F} q_{Fi} \quad (2.20)$$

If needed, this can then be used to recover the mass-conservative elemental velocity by using lowest-order Raviart-Thomas (RT0) interpolation. It has been shown that RT0 interpolated velocities have accuracy that is comparable to the mixed finite element approach [*Kees et al.*, 2008; *Schiavazzi*, 2011]. They are locally mass-conservative, in the sense that they have, by construction, continuous normal fluxes across mesh faces, thus satisfying equation (2.13). With respect to lowest order MFE velocities, however, RT0-interpolated velocities exhibit some inaccuracies in cases where there are large jumps in conductivity coefficients, with more mass entering low conductivity zones compared to the mixed approach [*Schiavazzi*, 2011]. However, since the matrices of the local systems that are solved for each node depend only on mesh geometry, these velocities are not affected by ill-conditioning when strong anisotropy occurs, in contrast to MFE velocities [*Mazzia et al.*, 2011].

To demonstrate the LN procedure, we consider the simple 2D problem of Figure 2.1b. For this element patch, equation (2.11) becomes:

$$R_1^{(i)} + R_2^{(i)} + R_3^{(i)} + R_4^{(i)} = 0 \quad (2.21)$$

where, for example, $R_1^{(i)}$ is:

$$R_1^{(i)} = \sum_{j\in\mathcal{N}_1} \frac{d\psi_j}{dt} \int_{T_1} \frac{\theta_h(\psi_h)}{n} S_s \phi_j \phi_i dx + \sum_{j\in\mathcal{N}_1} \frac{d\theta_j(\psi_j)}{dt} \int_{T_1} \phi_j \phi_i dx + \\ + \sum_{j\in\mathcal{N}_1} \psi_j \int_{T_1} K_r(\psi_h) K_s \nabla\phi_j \cdot \nabla\phi_i dx + \int_{T_1} K_r(\psi_h) K_s \eta_z \cdot \nabla\phi_i dx - \int_{T_1} q_s \phi_i dx \quad (2.22)$$

with $\mathcal{N}_1$ the set of nodes of element T_1. For each element $T \in \mathcal{E}_i$ equation (2.17) becomes:

$$2R_1^{(i)} + \bar{v}_{f_1} \cdot \nu_{f_1}^1 l_{f_1} + \bar{v}_{f_4} \cdot \nu_{f_4}^1 l_{f_4} = -(U_1^{(i)} - U_2^{(i)}) l_{f_1} + (U_4^{(i)} - U_1^{(i)}) l_{f_4} \quad (2.23a)$$

$$2R_2^{(i)} + \bar{v}_{f_2} \cdot \nu_{f_2}^2 l_{f_2} + \bar{v}_{f_1} \cdot \nu_{f_1}^2 l_{f_1} = -(U_2^{(i)} - U_3^{(i)}) l_{f_2} + (U_1^{(i)} - U_2^{(i)}) l_{f_1} \quad (2.23b)$$

$$2R_3^{(i)} + \bar{v}_{f_3} \cdot \nu_{f_3}^3 l_{f_3} + \bar{v}_{f_2} \cdot \nu_{f_2}^3 l_{f_2} = -(U_3^{(i)} - U_4^{(i)}) l_{f_3} + (U_2^{(i)} - U_3^{(i)}) l_{f_2} \quad (2.23c)$$

$$2R_4^{(i)} + \bar{v}_{f_4} \cdot \nu_{f_4}^4 l_{f_4} + \bar{v}_{f_3} \cdot \nu_{f_3}^4 l_{f_3} = -(U_4^{(i)} - U_1^{(i)}) l_{f_4} + (U_3^{(i)} - U_4^{(i)}) l_{f_3} \quad (2.23d)$$

and so:

$$B = \begin{pmatrix} -l_{f_1} - l_{f_4} & l_{f_1} & 0 & l_{f_4} \\ l_{f_1} & -l_{f_2} - l_{f_1} & l_{f_2} & 0 \\ 0 & l_{f_2} & -l_{f_3} - l_{f_2} & l_{f_3} \\ l_{f_4} & 0 & l_{f_3} & -l_{f_3} - l_{f_4} \end{pmatrix} \quad (2.24)$$

$$u^{(i)} = \begin{pmatrix} U_1^{(i)} \\ U_2^{(i)} \\ U_3^{(i)} \\ U_4^{(i)} \end{pmatrix} \quad (2.25)$$

$$r = \begin{pmatrix} \bar{v}_{f_4} \cdot \nu_{f_4}^1 l_{f_4} + \bar{v}_{f_1} \cdot \nu_{f_1}^1 l_{f_1} + 2R_1^{(i)} \\ \bar{v}_{f_1} \cdot \nu_{f_1}^2 l_{f_1} + \bar{v}_{f_2} \cdot \nu_{f_2}^2 l_{f_2} + 2R_2^{(i)} \\ \bar{v}_{f_2} \cdot \nu_{f_2}^3 l_{f_2} + \bar{v}_{f_3} \cdot \nu_{f_3}^3 l_{f_3} + 2R_3^{(i)} \\ \bar{v}_{f_3} \cdot \nu_{f_3}^4 l_{f_3} + \bar{v}_{f_4} \cdot \nu_{f_4}^4 l_{f_4} + 2R_4^{(i)} \end{pmatrix} \quad (2.26)$$

where l_f is the length of edge f and ν_f^T is the corresponding unit normal directed outward from element T. Note that B has zero row-sum and thus any constant vector c satisfies $Bc = 0$. Hence the solution of the system can be obtained by setting $U_1^{(i)}$=0 and then solving for $U_2^{(i)}$, $U_3^{(i)}$, and $U_4^{(i)}$. The mass-conservative constituent face fluxes are computed

from equation (2.19) as:

$$q_{f_1 i} = \bar{v}_{f_1} \cdot \nu_{f_1} - U_2^{(i)} \tag{2.27a}$$

$$q_{f_2 i} = \bar{v}_{f_2} \cdot \nu_{f_2} + (U_2^{(i)} - U_3^{(i)}) \tag{2.27b}$$

$$q_{f_3 i} = \bar{v}_{f_3} \cdot \nu_{f_3} + (U_3^{(i)} - U_4^{(i)}) \tag{2.27c}$$

$$q_{f_4 i} = \bar{v}_{f_4} \cdot \nu_{f_4} + U_4^{(i)} \tag{2.27d}$$

where ν_{f_j} is the unit vector normal to edge j oriented in the counterclockwise direction as defined in Figure 2.1b.

2.3.2.3 High resolution finite volume approximation for the advective transport equation

The HRFV scheme used to solve the advective transport equation is based on a Godunov type slope limited second order accurate finite volume discretization [*Mazzia and Putti*, 2005]. Denoting by G the advective flux, equation (2.1c) can be written as:

$$\frac{\partial \theta c}{\partial t} + \nabla \cdot G = q_{ts} \tag{2.28}$$

$$G = vc \tag{2.29}$$

The solution c is approximated by c_T within the space of element-wise constant basis functions χ_T taking the value one on element T and zero elsewhere:

$$c \simeq \sum_{T=1}^{E} c_T \chi_T \tag{2.30}$$

Multiplying equation (2.28) by χ_T and integrating in space and time, with advective time step size Δt_a over the time interval $\left[t^{k_a}; t^{k_a+1}\right]$, the following semi-discrete equation for element T is obtained:

$$(\theta_T c_T)^{k_a+1} = (\theta_T c_T)^{k_a} - \frac{\Delta t_a}{|T|} \int_T (\nabla \cdot G^{k_a} + q_{ts}^{k_a}) dx \tag{2.31}$$

where k_a is the advective time step index, $\theta_T = \theta_T(\psi_T)$ with the elemental pressure defined in equation (2.9), c_T is the element-averaged concentration, and $q_{ts} = q_s c_{ts}$ with q_s the water source or sink term and with c_{ts} either set to $c_T^{k_a}$ (when q_s is a sink) or the imposed source concentration (when q_s is a source). Application of the divergence theorem in the

above equation and use of the midpoint rule to evaluate the element integral yields:

$$(\theta_T c_T)^{k_a+1} = (\theta_T c_T)^{k_a} - \frac{\Delta t_a}{|T|} \sum_{F \in \mathcal{F}_T} \int_F G^{k_a} \cdot \nu_F^T ds + q_{ts,T}^{k_a} \Delta t_a \tag{2.32}$$

where $q_{ts,T}^{k_a}$ is the value of q_{ts} at the center of gravity of T. The approximation of the line integrals in the above equation is obtained by a two-step procedure, the reconstruction and the evolution steps. The reconstruction step approximates the values of concentration over each element starting from $c_T^{k_a}$. Second order accurate reconstruction is achieved by the use of a linear interpolant in combination with a limiting procedure that explicitly prevents the formation of overshoots and undershoots. The linear interpolant is obtained by least squares using the set of five concentration values in cell T and all its neighbors. The gradient is then limited using the Barth-Jespersen approach [*Barth and Jespersen*, 1989]. This method guarantees that the scheme is monotone when subjected to the CFL constraint [*Mazzia and Putti*, 2005].

In the evolution step, the reconstructed values are used to define the concentration values at the right ($c_{F,R}$) and left ($c_{F,L}$) of each face F (i.e., the boundary conditions of the local Riemann problem). The distinction between right and left is made again with respect to a local counterclockwise reference system defined in accordance to the nodal numbering of face F. The reconstructed values $c_{F,L}$ and $c_{F,R}$ and the normal flux q_F, obtained from the solution of the flow equation (the LN post-processed fluxes), are used to compute the FV advective flux approximation on each face F. With this information the local Riemann problem is solved at each face and the concentration $c_T^{k_a+1}$ is obtained by computing the following mass balance:

$$c_T^{k_a+1} = \left(\theta_T^{k_a} c_T^{k_a} - \frac{\Delta t_a}{|T|} \sum_{F \in \mathcal{F}_T} (q_F^T)^{k_a} c_{F,X} A_F + q_{ts,T}^{k_a} \Delta t_a \right) \frac{1}{\theta_T^{k_a+1}} \tag{2.33}$$

where A_F is the area of F, $q_F^T = q_F(\nu_F^T \cdot \nu_F)$, and $c_{F,X}$ is $c_{F,L}$ if $\nu_F \cdot \nu_F^T = 1$ and $c_{F,R}$ if $\nu_F \cdot \nu_F^T = -1$. More details of the FV procedure are given in *Mazzia and Putti* [2005].

2.3.2.4 Time step consideration

The advective transport time step is subject to a CFL stability constraint while the flow time step is subject to a convergence constraint related to the nonlinear scheme. Time step evolution for the flow model is generally less restrained than for the transport model,

thus the time step Δt of the overall scheme is determined by the solution of the flow equation, and for each Δt a number $n_a = \Delta t/\Delta t_a$ of advective time steps is performed in accordance with the CFL condition that establishes Δt_a. The flow variables used as input by the transport model, i.e., the reconstructed normal face fluxes and the cell averaged water content calculated at times t^k and t^{k+1}, are updated at each advective time step by simple component-wise linear interpolation.

2.4 Numerical results

While mass balance in numerical models is typically invoked as a global principle, we have seen that the Larson-Niklasson method is predicated on the imposition of local mass conservation linked to locally conservative velocities. A flux field that is continuous across each inter-element face guarantees that the same mass flowing out from one cell enters the neighboring cell. The local mass balance inherently enforced by the finite volume solver (equation (2.33)) necessitates that the sum of q_F^T over each $F \in \mathcal{F}_T$ be equal to the mass temporal change in the cell T plus any external source or sink term incident on T. Hence, local mass imbalances are equivalent to the occurrence of a cell-wise spurious source or sink of solute mass. This corresponds to the presence in the numerical concentration field of oscillations that cannot be controlled by the finite volume limiter, which is applied before the mass balance check. In some instances these overshoots and undershoots accumulate, eventually leading to divergence of the numerical concentration. In the following test cases we therefore examine both global and local mass balance errors.

Global mass balance is computed on solute mass by considering the entire domain and the fluxes across its boundary. We calculate it in two ways: as the balance between the mass entering and exiting across the prescribed inflow and outflow boundaries of the domain and the mass change within the domain (MBE_1) and as the balance between the mass entering and exiting across the entire boundary of the domain and the mass change within the domain (MBE_2).

Local mass balance is computed on water mass by directly applying the definition found in *Klausen and Russell* [2004]. We measure the inaccuracy of the velocity field by performing at each time step a water mass balance $\mathcal{Q}_T(t)$ [L^3] over a selected, or observation, tetrahedron. Local mass balance requires that the sum of the fluxes over

each element face equals the total change in storage plus (or minus) any external source (or sink) term. Thus, neglecting the elastic response and in absence of external sinks and sources, in an observation tetrahedron T we calculate:

$$\mathcal{Q}_T(t^{k+1}) = \theta_T^{k+1}|T| - \theta_T^{k}|T| + \Delta t \sum_{F\in\mathcal{F}_T} q_F^{k+1} A_F = \mathcal{Q}_T^{+}(t^{k+1}) - \mathcal{Q}_T^{-}(t^{k+1}) \tag{2.34}$$

where q_F^{k+1} is $q_F^{T,k+1}$ for the LN-reconstructed fluxes and $\bar{q}_F^{T,k+1}$ for the $\mathcal{P}_1$ Galerkin fluxes. The mass balance terms $\mathcal{Q}_T^{+,-}$ represent the positive and negative (in absolute value) components. Note that, since outgoing fluxes are positive, a nonzero $\mathcal{Q}_T(t)$ represents an artificial sink if positive and an artificial source if negative.

All test cases involve the solution of a transient or steady state flow equation. The ensuing velocity field is used as a driver for a linear, purely advective transport equation that simulates the movement of a conservative solute with no molecular diffusion or mechanical dispersion. This allows us to better assess the effectiveness of velocity field reconstruction, since hydrodynamic dispersion could otherwise smooth out mass balance error impacts on the numerical solution. In all cases we compare results from standard $\mathcal{P}_1$ Galerkin flux fields ($\bar{q}_F$ of equation (2.16)) against those from LN-reconstructed fluxes (q_F of equation (2.20)). In addition, since lowest order Raviart-Thomas mixed finite elements (in its hybridized solution form) are considered inherently mass-conservative, for the saturated flow test cases the numerical fluxes obtained with this approach are used as a reference solution [*Putti and Sartoretto*, 2009]. We show our results in terms of cumulated MBE relative to the total or initial inflow. The MBE magnitude starts from machine precision at the beginning of a simulation and increases as time progresses.

The first set of test cases revises the tests proposed in *Schiavazzi* [2011]. They involve steady state, fully saturated groundwater flow coupled with unsteady transport in the presence of a convergent outflow boundary. The inclusion of block spatial heterogeneities increases the difficulty of the problem. The final test case is a realistic example of water infiltration in a three-dimensional domain drained by a lateral ditch, adapted from *Cordes and Putti* [2001]. Again, the presence of heterogeneous blocks exacerbates $\mathcal{P}_1$ Galerkin velocity errors.

The linear systems arising from the $\mathcal{P}_1$ and MFE discretizations are solved with the conjugate gradient method, setting the convergence tolerance to 10^{-10}. The tolerance for the Picard/Newton linearization scheme ($\mathcal{P}_1$ Galerkin case only) is set to 10^{-6}. The

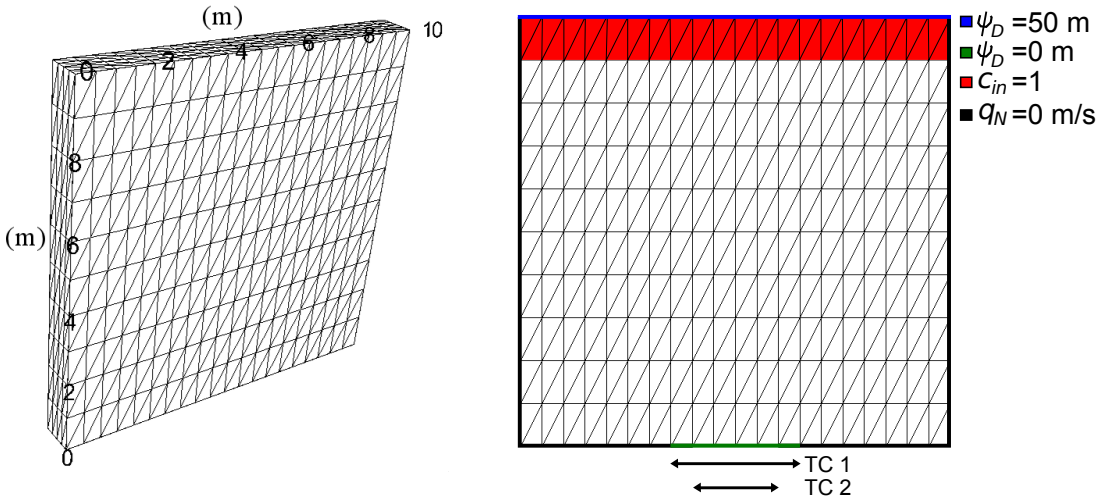

Figure 2.2: *Domain triangulation for Test Cases 1 and 2 (left) and corresponding boundary and initial conditions (right).*

local systems arising from the LN reconstruction are solved with the direct Gaussian elimination method.

2.4.1 Saturated steady flow and unsteady transport tests

2.4.1.1 Homogeneous soil

We consider an essentially two-dimensional 10×10 m^2 domain simulated on a three-dimensional prism of unit width (Figure 2.2). Flow is fully saturated and steady state with inflow at the top boundary, simulated via a Dirichlet condition imposing a pressure head of ψ_D=50 m, outflow constrained to a central portion of the bottom boundary, where ψ_D=0 is imposed, and zero flux Neumann boundary conditions elsewhere. For the transport equation, we set $c_D = 0$ on the inflow boundary, while the outflow boundary and the zero flux boundary are governed by the velocity field. We simulate an initial pulse of solute in the first layer, of dimensionless concentration $c_{in} = 1$, moving with the water velocity towards the outlet. The total initial solute mass in the system is 3.9 (dimensions of the first layer 10 m x 1 m x 1 m, domain porosity 0.39). We design two test cases (TC1 and TC2) by varying the width of the outflow boundary (Figure 2.2) so as to increase the streamline curvatures for TC2 compared to TC1. The tetrahedral mesh is obtained by duplicating a uniform triangulation of a surface rectangle (10×1 m^2) in the vertical direction to form 10 equally spaced layers. The surface triangulation is characterized by

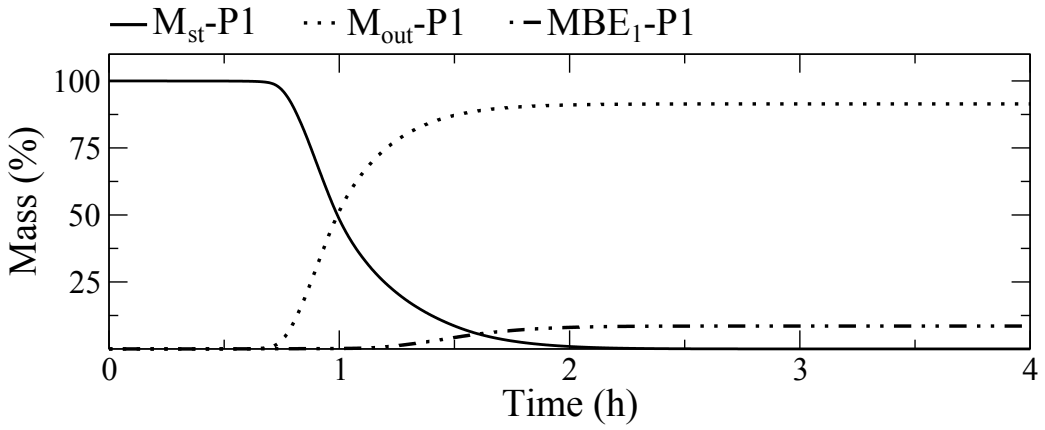

Figure 2.3: *Mass balance results with the $\mathcal{P}_1$ Galerkin velocities for Test Cases 1 (top) and 2 (bottom). M_{st} denotes the total mass stored in the system and M_{out} the cumulated mass that has exited the domain from the prescribed outflow boundary. $MBE_1 = M_{in} - M_{out} - M_{st}$ is the cumulated mass balance error, with M_{in} the total mass initially present in the system. The right panels show the distribution of the relative cumulated mass, reported as a percentage of M_{in}, that has flowed out from different segments of the boundary by the end of the simulation (the green segment is the prescribed outflow boundary as depicted in Figure 2.2).*

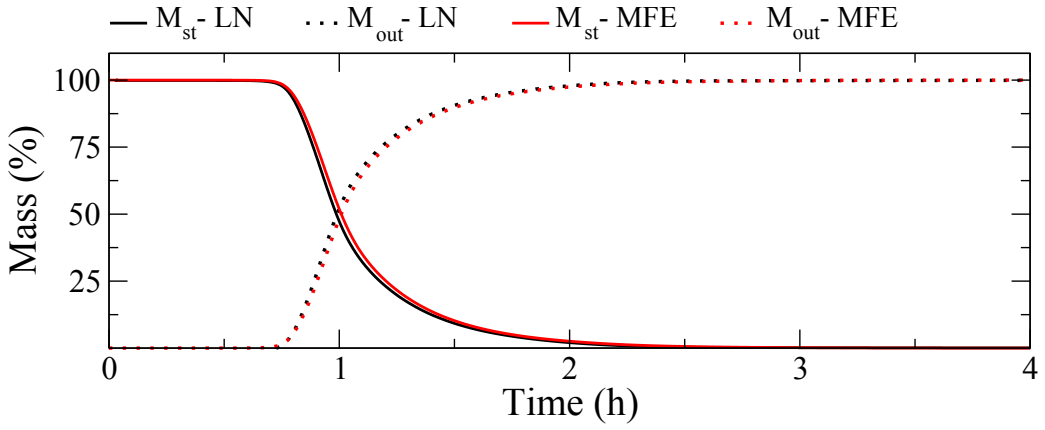

Figure 2.4: *Mass balance results obtained with the MFE and LN-reconstructed velocities for Test Cases 1 (top) and 2 (Bottom). The notation is the same as in Figure 2.3.*

21×5 nodes, yielding a three-dimensional tetrahedral mesh with 1155 nodes and 4800 cells (Figure 2.2). Both test cases consider a homogeneous soil with K_s=2×10^{-4} m/s, n=0.39, and S_s=5×10^{-4} 1/m. The transport simulations, driven by the steady flux field calculated by the flow equation, are run until all the mass initially present in the system is flushed out of the outflow boundary.

The numerical results in Figure 2.3 show that, in the case of the $\mathcal{P}_1$ Galerkin velocity field, a non-negligible volume of solute mass exits from no-flux boundaries, especially in TC2, which corresponds to the smaller outflow aperture and, consequently, stronger streamline curvatures. This error is completely corrected by the LN-reconstructed velocity field (Figure 2.4). Figure 2.3 shows the time behavior of the mass balance calculated with $\mathcal{P}_1$ Galerkin fluxes. For the two test cases, we report the total solute mass stored in the system (M_{st}), the cumulated solute mass that has exited the domain from the prescribed outflow boundary (M_{out}), and the cumulated mass balance error $\text{MBE}_1 = M_{in} - M_{st} - M_{out}$, where M_{in} is the total mass initially present in the system. The three variables are reported as a percentage of M_{in}. At the end of the simulation we obtain a relative mass balance error MBE_1=8.6% for TC1 and MBE_1=11.1% for TC2. The right panels of Figure 2.3 show the percentage of M_{in} that flows out from the different portions of the domain. The zero flux boundary violation is larger closer to the outflow boundary, and the errors increase as the boundary aperture is diminished (from TC1 to TC2), because of the increased velocity variations caused by the smaller outflow boundary.

The results obtained with the MFE and the LN-postprocessed fluxes are shown in Figure 2.4. For both approaches and for both test cases, the MBE_1 values are negligible and of order 10^{-5}% for MFE and 10^{-4}% for LN, showing the conservation properties of both velocity fields. Relatively small differences in the timing of the mass breakthrough are discernible between the MFE and LN-reconstructed fields, but they do not impact substantially the movement of the concentration front.

For the $\mathcal{P}_1$ Galerkin simulations of TC1 and TC2, when we consider the balance between mass entering and exiting across the entire domain boundary and mass change within the domain (i.e., MBE_2), the mass balance error is on the order of 10^{-4}% (the mass outflow over the different segments of the domain boundary, shown in the right panels in Figure 2.3, sums to 100%). This global mass balance error is on a par with the MBE_1 results obtained with the conservative MFE and LN schemes, and this misleading

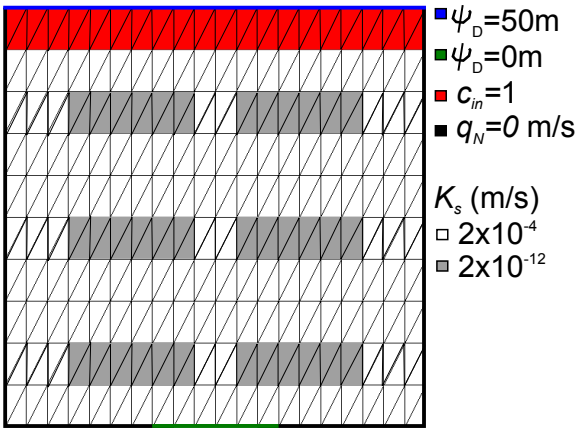

Figure 2.5: *Boundary conditions, transport initial conditions, and computational mesh for a vertical cross section of the domain for Test Case 3.*

result demonstrates that, even for this simple test case, global mass balance metrics are not always reliable indices of model performance. The heterogeneous test case considered next sheds further light on the complexities of mass balance error estimates.

2.4.1.2 Heterogeneous soil

The purpose of Test Case 3 is to analyze the mass balance errors committed in the presence of heterogeneity, which generates strong streamline curvatures. The domain discretization, the boundary conditions, and the transport initial conditions are the same as in Test Case 1. Six internal blocks of low hydraulic conductivity (K_s=2×10^{-12} m/s, eight orders of magnitude smaller than the surrounding soil) are inserted as shown in Figure 2.5. Test Case 4 solves the same probem as TC3 but with a finer mesh of 12710 nodes, obtained by uniformly refining the initial grid by factors of 3 and 4 along the main horizontal and vertical directions, respectively.

The numerical results (Figure 2.6) confirm the behavior of the $\mathcal{P}_1$ Galerkin fluxes that cause solute mass to exit the domain from no-flux boundaries. An additional phenomenon becomes apparent in these simulations. A considerable portion of the mass initially present in the system enters and remains trapped in the internal low-permeability blocks. This is a well known behavior of the Galerkin approach that is related to the fact that $\mathcal{P}_1$ asserts the mass balance on dual cells [*Putti and Cordes*, 1998; *Putti and Sartoretto*, 2009; *Cainelli et al.*, 2012]. More precisely, assuming for simplicity a two-dimensional setting

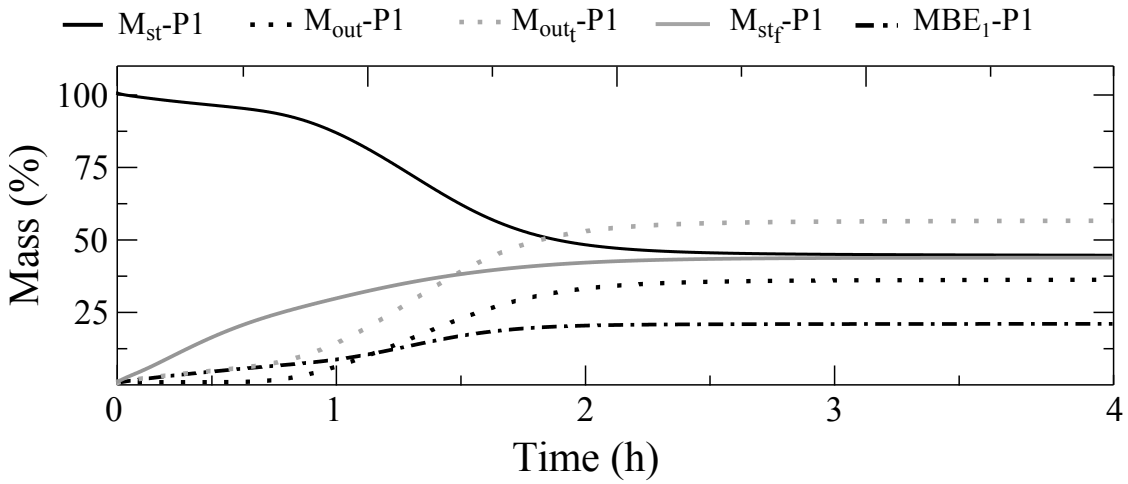

Figure 2.6: *Mass balance results obtained with the $\mathcal{P}_1$ Galerkin velocities for Test Case 3. MBE_1, M_{out}, and M_{st} are as defined for Figure 2.3. M_{out_t} is the cumulated outflow mass from all boundaries, and M_{st_f} is the total mass stored in the 6 low-permeablity blocks.*

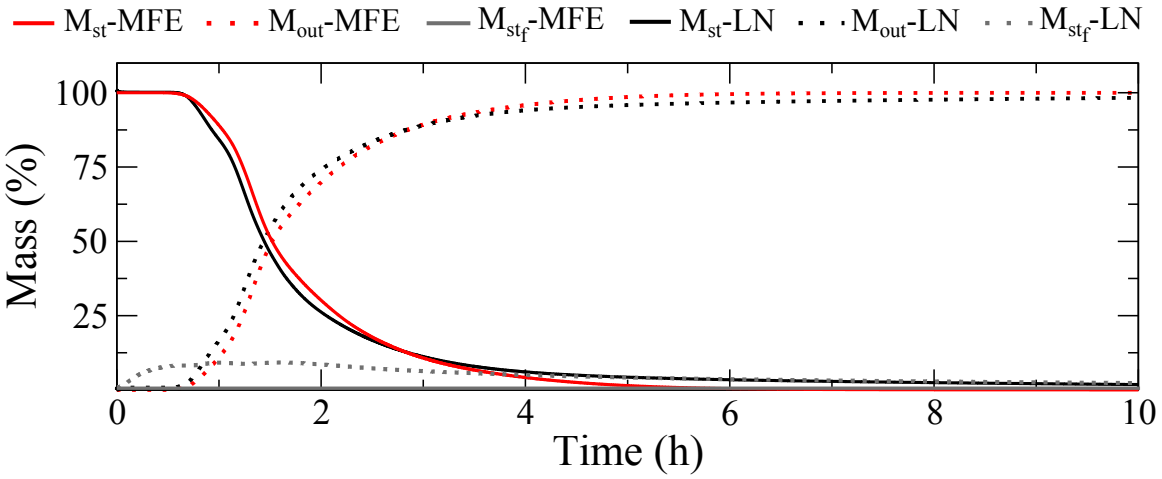

Figure 2.7: *Mass balance results obtained with the MFE and LN velocities for Test Case 3. M_{st} and M_{out} are as defined for Figure 2.3, while M_{st_f} is as defined for Figure 2.6.*

and a scalar hydraulic conductivity coefficient, the $\mathcal{P}_1$ Galerkin approach performs the mass balance by evaluating the total fluxes entering or exiting from the boundary of the nodal Voronoi cell, the dual cell of a Delaunay triangle patch [*Cordes and Putti*, 2001]. This is equivalent to the use of a constant gradient and applying to it an arithmetic average of the two conductivities defined on the two neighboring elements. This arithmetic average, although numerically consistent, for a fixed mesh causes an overestimation of the effective conductivity. As a consequence, the ensuing velocity field drives a non-negligible portion of the initial solute mass into the low-conductivity zones. Once entered, the mass is advected by a velocity field with magnitude proportional to the block hydraulic conductivity and, because of its extremely low value, never exits the domain within a reasonable simulation time. In contrast (Figure 2.7), MFE and LN-reconstructed velocities impose flux continuity on inter-element boundaries, which can be equivalently interpreted as the use of harmonic averages. It is well known that, in the case of large conductivity contrasts, the harmonic average remains closer to the smaller values than does the arithmetic mean. This fact, together with the imposed edge continuity on the flux, forces the flow field to border the blocks and thus effectively prevents the solute from entering the low-conductivity zones.

The very different behaviors of node-based and edge-based methods are clearly seen in comparing Figures 2.6 and 2.7. In Figure 2.6 the mass balance results for Test Case 3 are shown for the natural $\mathcal{P}_1$ Galerkin velocity field. It is apparent that in this test case 44% of the total initial mass remains in the system 4 h after injection, with negligible further mass outflow expected beyond the 4 h simulation period. The mass balance error MBE_1 shown in Figure 2.6 is 20.7%, which is more than double the MBE obtained for the $\mathcal{P}_1$ Galerkin simulation of the TC1 case, illustrating the degree of numerical difficulty introduced by the heterogeneity. As was done for TC1 and TC2, when the global mass balance error is calculated considering mass outflow over the entire domain boundary (i.e., $\mathrm{MBE}_2 = M_{in} - M_{out_t} - M_{st}$, where M_{out_t} plotted in Figure 2.6 is the cumulated outflow mass from all boundaries), the mass balance error falls to 10^{-3}%, but this is a misleading result as described earlier. In addition to higher MBE compared to TC1, the heterogeneity also causes the mass persistence exhibited by the $\mathcal{P}_1$ Galerkin result, with the entrapped mass clearly attributable to the 6 low-permeablity blocks ($M_{st_f} \approx M_{st}$ at $t = 4$ h in Figure 2.6, where M_{st_f} is the total mass stored in the 6 low-K_s blocks). This

is another significant source of mass balance error, as will be apparent from comparison with the results from the LN and MFE schemes.

Figure 2.7 reports the mass balance results for Test Case 3 when MFE and LN-reconstructed velocity fields are used in the advective transport. In both cases the mass balance errors calculated as $\text{MBE}_1 = M_{in} - M_{st} - M_{out}$ are negligible (on the order of $10^{-3}\%$), indicating that all of the mass that exits the system does so across the prescribed outflow boundary. As in TC1 and TC2 (Figure 2.4), a small difference between the MFE and LN cases can be seen in the timing of the mass breakthrough. Another difference between the two schemes is caused by the strong heterogeneity. The LN-reconstructed fluxes drive a small fraction of the solute into the low-conductivity zones and slowly drives it out. This mass persistence is quite small (about 2% by the end of the simulation), and much less significant than was the case for the $\mathcal{P}_1$ Galerkin simulation, but it is nonetheless larger than the entrapped mass for the MFE case (which is barely visible in Figure 2.7). This phenomenon was already reported in *Schiavazzi* [2011], who showed the mass entrapment to be restricted (or localized) within corner elements of the low-permeability block. *Schiavazzi* [2011] also proposed a method to partially fix this problem, consisting in performing a second correction step for the element patches near permeability contrasts after LN post-processing. Modified algebraic systems are formulated for each of these patches by adding a constraint, written in terms of Lagrange multipliers, imposing the condition that, for each element of the patch, the norm of the total flux be equal to the norm of the $\mathcal{P}_1$ derived total flux.

In Figure 2.8 we examine the impact of mesh refinement (Test Case 4 compared to the coarser mesh of Test Case 3) on the balance error caused by the entrapped mass produced by the $\mathcal{P}_1$ Galerkin and LN-reconstructed velocity fields. The results show that the trapping effect is greatly reduced as the mesh is refined, but that the error caused by this phenomenon remains high for the $\mathcal{P}_1$ Galerkin scheme whereas it tends to disappear for the LN case. This can also be seen in Figure 2.9, where we compare the concentration profiles at $t = 1.5$ h for Test Case 4 obtained with the $\mathcal{P}_1$, LN, and MFE velocities. The LN and MFE profiles look very similar, with concentration values that never exceed one. The differences between the LN and MFE results are concentrated at a small number of corner elements of the low-permeability blocks, where we perceive nonzero concentration values for the LN case, and along the zero flux portion of the bottom boundary of the

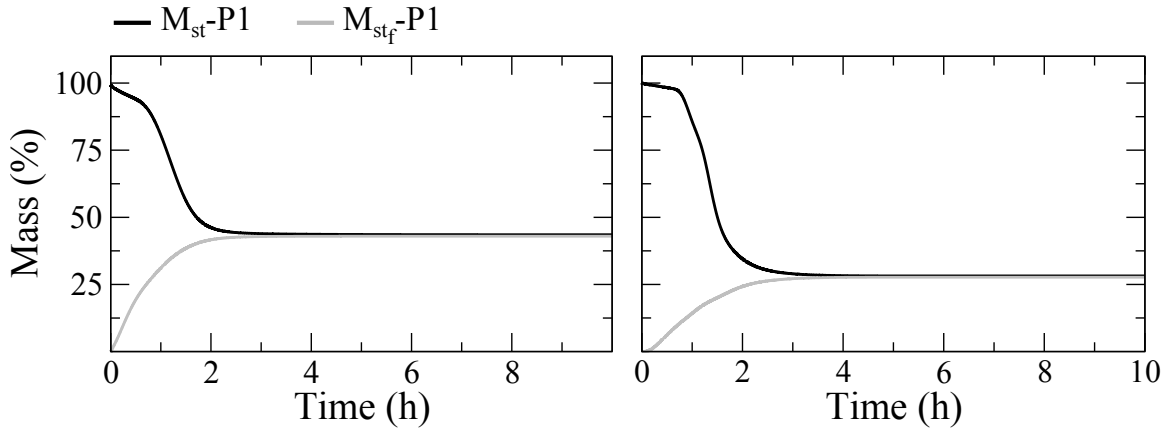

Figure 2.8: *Comparison between the total mass in the system (M_{st}) and the total mass in the low-permeability blocks (M_{st_f}) for the coarse (left panels; Test Case 3) and refined (right panels; Test Case 4) meshes in the case of $\mathcal{P}_1$ velocities (top panels) and LN-reconstructed velocities (bottom panels).*

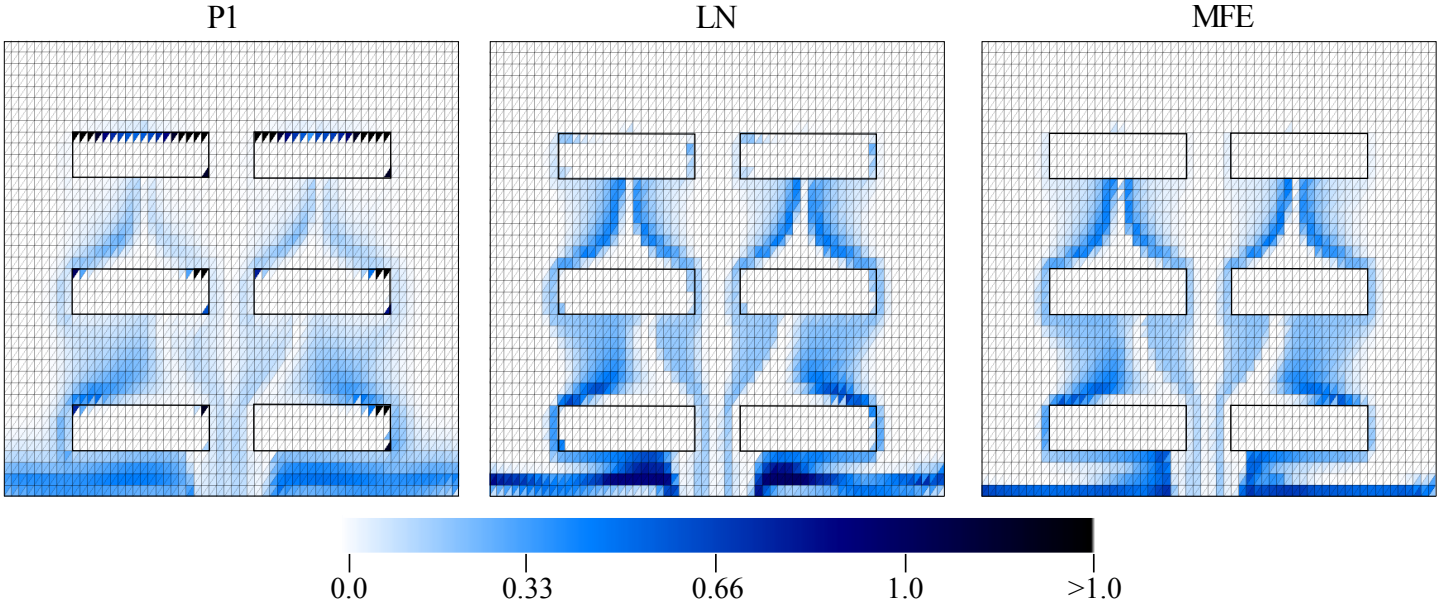

Figure 2.9: *Comparison of concentration profiles at $t = 1.5$ h for a vertical cross section of the domain for Test Case 4 obtained with the $\mathcal{P}_1$, LN, and MFE velocities.*

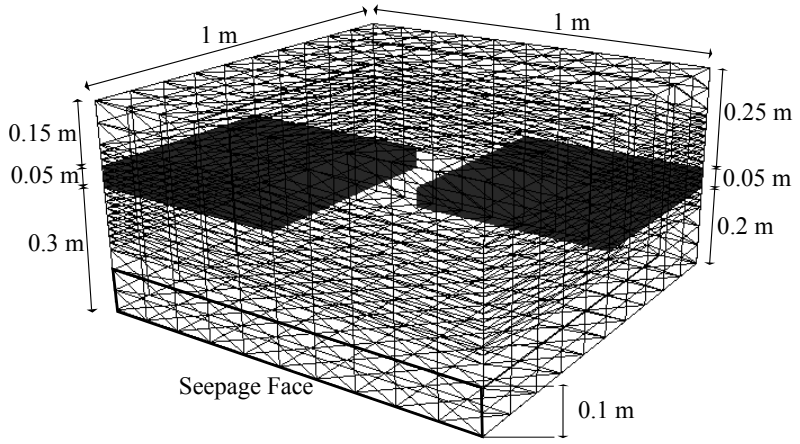

Figure 2.10: *Three-dimensional domain, tetrahedral mesh, and location of the low-permeability blocks and seepage face outflow boundary for Test Case 5.*

domain. The $\mathcal{P}_1$ case, on the other hand, clearly indicates that mass is accumulating in the low-permeability blocks, with many more affected elements than the LN case and with the concentrations within some of these elements reaching values as high as 15 for this snapshot. Consequently, although the plume shape outside the 6 blocks is very similar to the LN and MFE cases, the concentration values within the plume are notably abated. As noted earlier, the FV advection scheme is strictly monotone and thus guarantees that no oscillations in the reconstructed concentrations are generated. Hence, eventual overshoots can only emerge in the mass balance calculation of the evolution step (equation (2.32)) and must be attributable to non mass-conservative velocity fields.

We can conclude from the first four test cases that the LN-reconstructed velocity fields yield accurate and reliable results for saturated groundwater flow and transport, also in the case of spatially variable velocity fields. We need to assess now if the same conclusion holds in the case of variably saturated and unsteady flow conditions.

2.4.2 Variably saturated unsteady flow and transport tests

The last test case (Test Case 5) involves transient, variably saturated flow and transport in a fully three-dimensional setting. An initially unsaturated heterogeneous soil block of dimension 1 m x 1 m and thickness 0.5 m is subjected to unsteady rainfall. The test case is a revised version of a problem originally described in *Cordes and Putti* [2001]. Figure 2.10

shows the domain, mesh, and geometrical positioning of two thin, fine-textured, low-conductivity layers. The non-intersecting low-permeablity blocks are each of dimension 0.5 m x 0.5 m and thickness 0.05 m. A seepage face outflow boundary representing a drainage ditch is situated along the base at one edge of the domain. The domain is discretized with a surface grid of 10×10 square cells, yielding a surface mesh of 200 triangles. This surface mesh is duplicated vertically to form 20 layers of varying thickness, with refinement around the low-conductivity lenses. Each prism is subdivided into 3 tetrahedra to obtain the final mesh composed of 2541 nodes and 12000 tetrahedra.

The soil is represented with a saturated hydraulic conductivity of $K_s = 2 \times 10^{-4}$ m/s, a specific storage of $S_s = 5 \times 10^{-4}$ 1/m, and a porosity of n=0.39, while the low-permeability lenses have $K_s = 2 \times 10^{-12}$ m/s and the same S_s and n as the soil. The van Genuchten retention curves are used with parameters $n_{VG} = 1.6$ (van Genuchten fitting parameter), residual moisture content S_{wr}=0.05, and ψ_{sat}=-0.5 m (parameter related to the air entry suction).

Aside from the surface and seepage face boundaries, no-flow conditions are imposed along all other boundaries of the domain. Initially the pressure head is distributed hydrostatically, with the water table set at the bottom. The surface is subjected to two pulses of spatially homogeneous rainfall at a constant rate of 10^{-5} m/s, the first pulse at the beginning of the simulation and of duration 12 h and the second pulse beginning at 36 h and of duration 66 h, to the end of the simulation at $t = 100$ h. Between pulses a no flow condition is in effect. For the advective transport equation, the soil is initially solute-free, and the surface is the inflow boundary where a Dirichlet condition of $c = 1$ is imposed during the first pulse of rain and $c = 0$ during the second pulse. This simulates the injection and subsequent flushing of a solute and allows us to track the migration of the first pulse through the domain and out of the seepage face. Between pulses the surface boundary condition for the transport model is governed by the velocity field, as are the seepage face boundary and the zero flux boundaries.

Figure 2.11 compares the results in terms of solute mass obtained using the LN-reconstructed and $\mathcal{P}_1$ Galerkin velocity fields. The plots report the time behavior of the different components of the mass balance normalized with respect to the cumulated mass injected into the system at a given time t. Note the different scales used for the ordinate axes. For the LN scheme, we see that the mass balance errors remain negligible

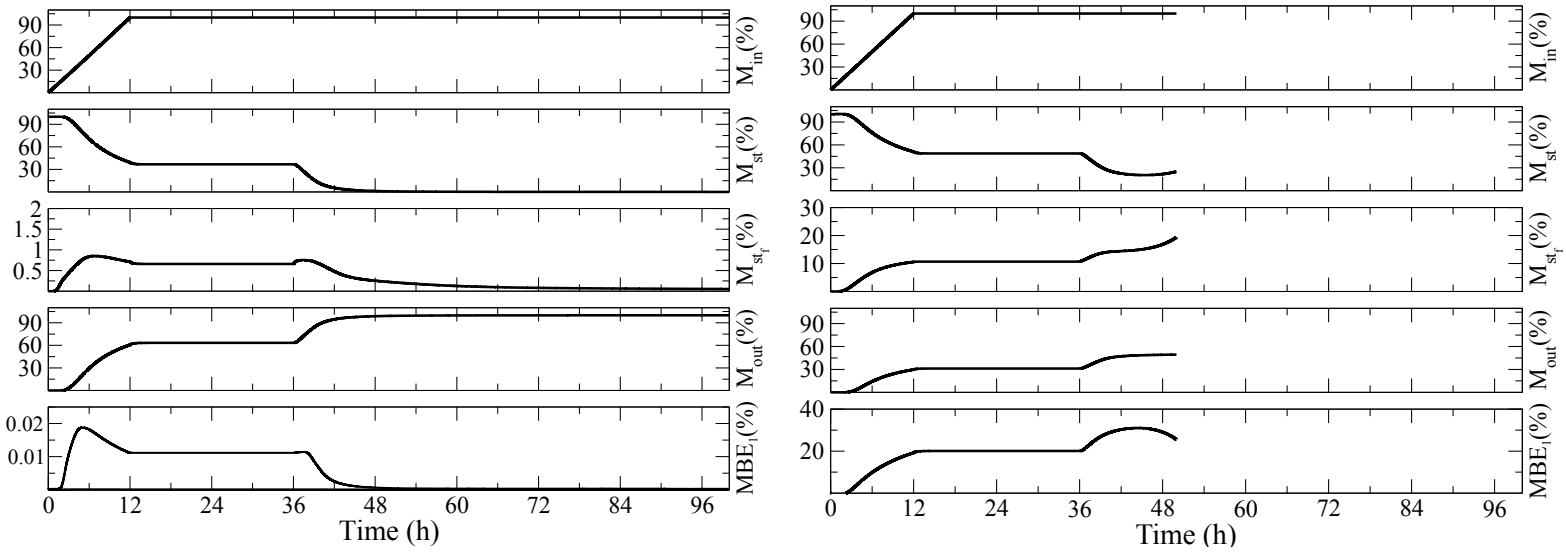

Figure 2.11: *Mass balance results obtained with the LN (left) and $\mathcal{P}_1$ (right) velocities for Test Case 5. From top: cumulative mass injected (M_{in}), total mass stored (M_{st}), mass stored in the two low-permeability lenses (M_{st_f}), mass outflow from the seepage face (M_{out}), and mass balance error $MBE_1 = M_{in} - M_{st} - M_{out}$.*

for the entire run, always below 0.02%. The mass stored in the system remains at 100% until outflow from the seepage face commences. Solute dilution begins in earnest at the beginning of the second rainfall event (at $t = 36$ h), and we also observe at this time a sharp jump in outflow flux. The mass trapped in the low-conductivity lenses is never larger than 1%, and at the beginning of the second rain period, after a small overshoot, this mass starts decreasing towards zero.

The results for the $\mathcal{P}_1$-based runs are very different. First we note that MBE_1 is large, greater than 20% for most of the simulation, and shows an increasing trend at the beginning of the second rainfall pulse. The amount of water stored in the low-conductivity lenses is more than 10% and also increases rapidly after the beginning of the second rain event. The most striking result, however, is that the solution becomes unreliable from approximately $t = 50$ h onward, due to $\mathcal{P}_1$ concentrations in some elements exploding because of local mass imbalance.

We can examine in more detail the sources of this mass balance error. Figure 2.12a plots the cumulative mass balance error for $\mathcal{P}_1$-driven concentrations calculated considering outflow only from the seepage boundary (MBE_1) and taking into account outflowing fluxes from the entire domain boundary (MBE_2). The negative trend in MBE_2 signifies

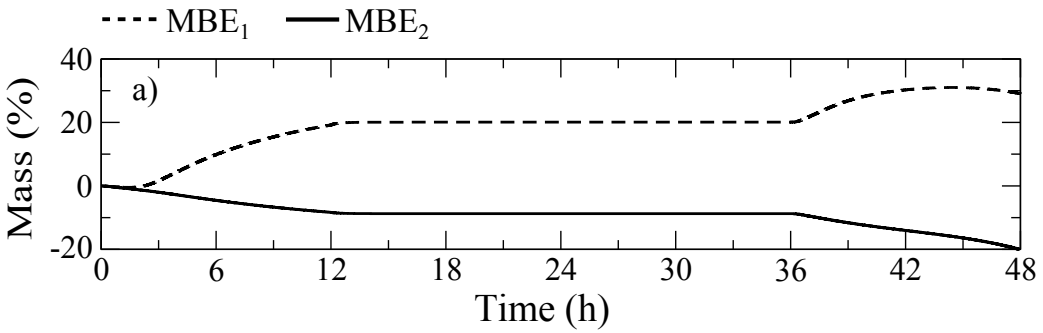

Figure 2.12: *(a) Mass balance errors obtained with the $\mathcal{P}_1$ Galerkin scheme for Test Case 5 calculated considering mass outflow across the seepage boundary (MBE_1) and considering mass outflow over the entire domain boundary (MBE_2); (b) behavior of the average concentration in the observation tetrahedron shown in Figure 2.13 driven by $\mathcal{P}_1$ velocities and by LN-reconstructed velocities.*

that the outgoing mass flux plus internal storage exceeds the mass injected via rainfall. Thus the numerical flow field introduces artificial sources or sinks of mass that are generated or lost within the domain and that are eventually advected out from the boundaries. The artificial generation of mass is responsible for the escalation in numerical concentrations mentioned above, and can be seen in Figure 2.12b for one particular tetrahedron, discussed further below.

We next analyze the concentration history on one of the elements of the computational mesh where concentration divergence occurs. The tetrahedron under observation is located in the corner of the domain and is just above one of the low-conductivity lenses (Figure 2.13a). We focus on water mass balance results with the aim of verifying the artificial occurrence of solute mass generation due to flux imbalance. In Figure 2.13b we report the behavior of the cumulative artificial source and sink fluxes $\mathcal{Q}_T^+(t)$ and $\mathcal{Q}_T^-(t)$, respectively (see equation (2.34)) vs time calculated for the observation tetrahedron using $\mathcal{P}_1$ Galerkin and LN-reconstructed velocities. For the LN case the two components are both very small (on the order of 10^{-8}) and of similar magnitude, so their difference is even smaller, leading to a negligible $\mathcal{Q}_T$ for each time t. Sudden mass imbalance jumps occur at the end of the first and at the beginning of the second rain period. These jumps are very small and are most probably due to discontinuities in the time derivative of water saturation as a consequence of the discontinuity in the atmospheric boundary condition. By contrast, the $\mathcal{P}_1$ Galerkin case displays a negligible sink term (10^{-13}) but a relatively large

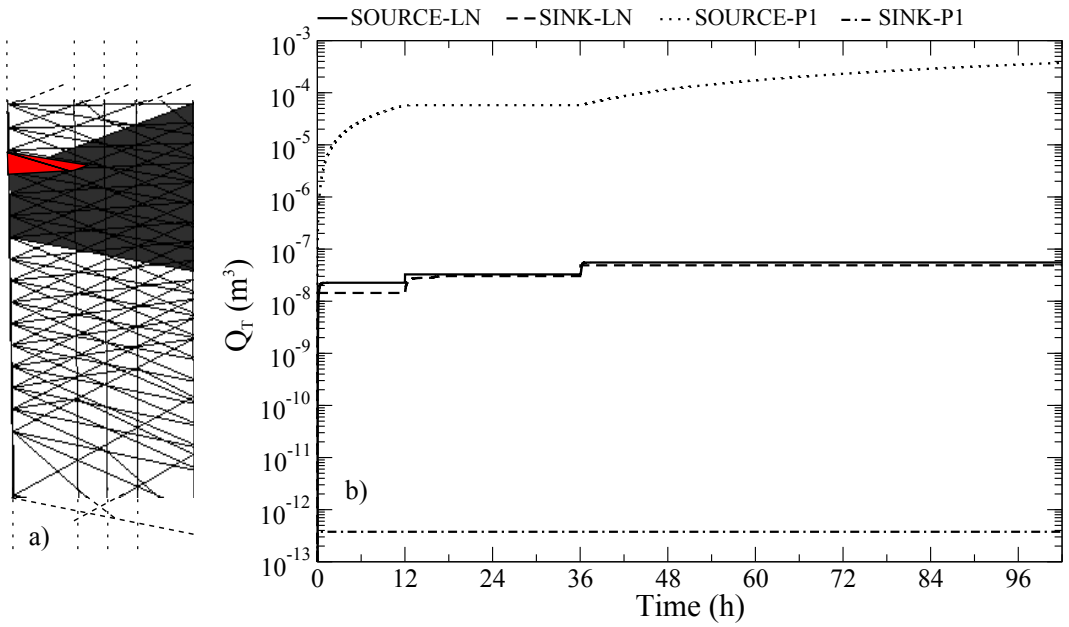

Figure 2.13: *(a) Location of the observation tetrahedron (in red), one of the domain elements where concentration divergence is observed with the $\mathcal{P}_1$ velocities for Test Case 5; (b) artificial source ($\mathcal{Q}_T^+$) and sink ($\mathcal{Q}_T^-$) fluxes cumulated in time as calculated for the observation tetrahedron using $\mathcal{P}_1$ and LN-reconstructed velocities.*

cumulated mass generation that continuously increases during rainfall. At the end of the simulation period (100 h) the generated mass is greater than 10^{-4} m^3, an unacceptably large value if compared to the cell volume $|T| = 2.75 \times 10^{-5}$ m^3. Thus, this tetrahedron is subject to a time-dependent artificial source of mass that leads to the divergence of the elemental concentration during the finite volume procedure (Figure 2.12b). This behavior is completely rectified by the LN-reconstructed velocity fields, which are locally conservative, or, equivalently, which lead to normal fluxes that are continuous across inter-element boundaries.

To conclude the analysis, we discuss for this test case the efficiency of the method implemented by comparing the computational cost to obtain a $\mathcal{P}_1$ Galerkin solution and the LN post-processed velocity field with the cost to obtain an MFE solution in its hybrid form. The computational cost is measured in terms of AXPY operations ($\alpha x+y$), assumed to be of similar cost to a scalar product, and normalized to the number N of mesh nodes. The LN reconstruction is obtained by means of N linear system solutions of dimension at most m, where m is the total connection (number of first adjacent nodes). In our examples

$m \leq 18$. Each LN system is solved by Gaussian elimination and requires $\mathcal{O}(m^3)$ operations, leading to a global computational cost for the LN reconstruction of $\mathcal{O}(m^3)$ AXPY operations. The FEM (Galerkin or mixed hybrid) nonlinear system is solved by a modified Picard iteration, with time step adapted so that convergence is ensured within a maximum of 10 iterations. An inexact Cholesky preconditioned conjugate gradient (PCG) scheme is used to solve the linear systems. Now we need to distinguish between $\mathcal{P}_1$ Galerkin and MHFE methods. For the former method the maximum number of nonzero elements in a row is exactly m. Thus, one PCG iteration costs $2m + 7$ AXPY operations. The MHFE matrix has exactly 7 nonzero elements per row, but a dimension of approximately $11N$ (the ratio of number of faces to number of nodes is approximately 11). Thus one PCG iteration for MHFE costs $2 \times 11 \times 7 + 7 = 175$ AXPY operations. Concluding, assuming 10 nonlinear iterations and 100 linear iterations per nonlinear iteration for both $\mathcal{P}_1$ Galerkin and MHFE, and taking $m = 20$, the operation count is $1000 \times 47 + 8000 = 55000$ AXPY in the case of $\mathcal{P}_1$ Galerkin plus LN and $1000 \times 175 = 175000$ AXPY for MHFE. There is thus a strong computational advantage in using a node-based $\mathcal{P}_1$ Galerkin approach for the solution of Richards' equation combined with a post-processing algorithm to restore the mass conservation properties compared to using a locally conservative MFE method.

2.5 Conclusions

This study has focused on the application of the local Larson-Niklasson algorithm to improve the accuracy of solute transport modeling in porous media. The technique, based on a post-processing of $\mathcal{P}_1$ Galerkin velocities from a Richards equation flow solver, restores the element-wise conservation properties of the velocity field. The performance of the LN technique was investigated for finite volume-based simulations of purely advective transport. FV models, by mimicking a mass balance within each cell of the computational domain, make direct use of the normal fluxes defined at inter-element boundaries, and thus require a locally mass-conservative velocity field. In the test problems analyzed, solute mass balances were used to provide an estimate of the quality of the LN post-processed velocities against classical $\mathcal{P}_1$ Galerkin velocities. For the saturated flow test cases, the results were also compared to those obtained using a mixed finite element-derived velocity field, which is inherently mass-conservative.

The test cases performed involve the solution of a steady state and fully saturated (TC1, TC2, TC3, and TC4) or transient and variably saturated (TC5) flow equation combined with a transient transport equation. The results of the first set of simulations (TC1-TC4) show that 1) when driven by $\mathcal{P}_1$ Galerkin velocities, solute mass easily exits from no-flux boundaries, especially in the presence of a small outflow aperture; 2) the violation of no-flux boundaries is completely corrected by the LN-reconstructed velocities; 3) a large portion of solute mass remains permanently entrapped in zones of low hydraulic conductivity when using $\mathcal{P}_1$ Galerkin velocities; 4) only a small portion of solute mass crosses into zones of low hydraulic conductivity in the case of LN velocities; and 5) the phenomenon of mass entrapment is greatly diminished for the LN case as the mesh is refined, whereas the error remains high for the $\mathcal{P}_1$ Galerkin case. The impact of local mass conservation is even more dramatic in the last test case (TC5) that features a time-variable, 3D, variably-saturated velocity field. The results show that in this case the $\mathcal{P}_1$ Galerkin numerical flow field introduces artificial sources or sinks of mass generated or lost within the domain and eventually advected out from the boundaries. Because of these local imbalances, not only is the global mass balance not maintained (i.e., the outgoing mass from the entire boundary plus internal storage exceeds the mass injected into the domain), but the solute concentration within some grid elements explodes, causing the simulation to eventually abort. In contrast, for the LN-generated flow field, none of these inaccuracies appears, demonstrating that a locally conservative velocity field is necessary for simulating solute transport with good mass balance behavior.

In addition to these findings, our analysis shows that a perfect global mass balance does not always guarantee that a solution is accurate. Specifically, we show how two widely used global mass balance measures for assessing the quality of a discrete solution, MBE_1 and MBE_2, can produce deceiving results for the $\mathcal{P}_1$ Galerkin-based simulations. Indeed, for the saturated test cases (TC1-TC4) driven by $\mathcal{P}_1$ velocities, MBE_1 values are quite high while MBE_2 values are negligible, correctly indicating that there are inaccuracies due to mass exiting from no-flux boundaries. But it would be false to conclude from the low MBE_2 result that boundary outflow is the only source of error, since neither of these metrics gives any indication of the significant errors being committed by mass entrapment within the computational domain.

Chapter 3

Examination of the seepage face boundary condition in subsurface and coupled surface/subsurface hydrological models

3.1 Abstract

A seepage face is a nonlinear dynamic boundary that strongly affects pressure head distributions, water table fluctuations, and flow patterns. Its handling in hydrological models, especially under complex conditions such as heterogeneity and coupled surface/subsurface flow, has not been extensively studied. In this paper we compare the treatment of the seepage face as a static versus dynamic boundary condition, we assess its resolution under conditions of layered heterogeneity, we examine its interaction with a catchment outlet boundary, and we investigate the effects of surface/subsurface exchanges on seepage faces forming at the land surface. The analyses are carried out with an integrated catchment hydrological model. Numerical simulations are performed for a synthetic rectangular sloping aquifer and for an experimental hillslope from the Landscape Evolution Observatory. The results show that the Dirichlet boundary condition is not always an adequate stand-in for a seepage face boundary condition, especially under conditions of high rainfall, steep slope, or heterogeneity; that hillslopes with layered heterogeneity give rise to multiple seepage faces that can be highly dynamic; that seepage face and outlet boundaries can coexist in an integrated hydrological model and both play an important role; and that seepage faces at the land surface are not always controlled by subsurface flow. The paper also presents a generalized algorithm for resolving seepage face outflow that

handles heterogeneity in a simple way, is applicable to unstructured grids, and is shown experimentally to be equivalent to the treatment of atmospheric boundary conditions in subsurface flow models.

3.2 Introduction

A seepage face is the boundary between a saturated flow field and the atmosphere or between a saturated flow field and a stream channel along which groundwater discharges by downhill movement in response to the force of gravity. The study of seepage faces is a central component of many geotechnical, hydrogeological, and geomorphological studies. In geotechnical engineering, seepage analysis is of interest for the design of hydraulic structures such as earth dams or river embankments [*Hirschfeld and Poulos*, 1973; *Milligan*, 2003] and in slope stability analysis [*Rulon and Freeze*, 1985; *Crosta and Prisco*, 1999; *Lee et al.*, 2008]. In hydrogeology, seepage faces play a central role in the interactions between surface water and groundwater [*Sophocleous*, 2002], enhancing, for example, the flow to a stream channel within the time frame of a storm hydrograph [*Beven*, 1989], and in contamination migration and attenuation, controlling flow paths in the riparian zone [*Hill*, 1990] and the spreading of solutes in tailing impoundments [*Heikkinen et al.*, 2009; *Ferguson et al.*, 2009].

Early analyses of groundwater flow in the presence of a seepage face involved flow net techniques [*Casagrande*, 1937]. This approach is valid if the soil is homogeneous and saturated, the boundaries well defined, and the system at steady state, conditions that are rarely encountered in reality. Numerical models provide a more flexible and accurate approach to solving groundwater flow and seepage problems. Early subsurface hydrological models were limited to solving the saturated flow equation or various simplifications of this equation based on, for example, hydraulic groundwater theory [*Troch et al.*, 2013]. In saturated flow models the seepage boundary that regulates groundwater drainage is often treated as a Dirichlet condition, with atmospheric pressure assigned to the designated outflow nodes. This is a static, and therefore approximate, treatment of this dynamic boundary. Alternatively, in saturated flow models based on the free surface approach, the position of the phreatic surface, and thus of the exit point along the seepage boundary, can evolve over time [e.g., *Isaacs*, 1980; *Shamsai and Narasimhan*, 1991].

Advances in numerical techniques together with the increased performance of high-speed digital simulation computers have led to numerical models based on Richards' equation for flow in variably saturated porous media becoming a widely used current approach for representing and solving seepage face problems. *Freeze* [1971] presented one of the first three-dimensional (3D) finite difference models for transient saturated-unsaturated groundwater flow and used it for the study of heterogeneous anisotropic aquifers in the presence of a seepage face boundary. In the early finite element variably saturated flow models of *Rubin* [1968], *Neuman et al.* [1975], and *Cooley* [1983], an algorithm for locating the exit point of the seepage face at each iteration of the nonlinear system solver was incorporated into the overall numerical procedure. The localization scheme positions the exit point such that all nodes below it are at atmospheric pressure (a Dirichlet condition), allowing outflow to occur, while all nodes above it are assigned a no-flow (Neumann) condition, so that the nodes take on negative pressures (atmospheric pressure is the zero datum). The presence of a surface water body (hydrostatic Dirichlet nodes below the exit point) can also be incorporated [*Tracy and Mariño*, 1987]. The seepage face is thus treated as a combination of Dirichlet and Neumann boundary conditions that evolves in time and space, with the exit point rising during rainfall events, for example, and falling during recession periods.

Numerical models are essential for resolving flow dynamics in the presence of soil heterogeneity. Spatial variability of hydraulic properties may lead to complex interactions between the saturated and unsaturated zones, formation of perched water tables, and multiple seepage faces and exit points, which are impossible to model with graphical or analytical approaches. *Eigenbrod and Morgenstern* [1972] investigated a layered slope located in a river valley near Edmonton, Alberta, and their analysis revealed the presence of two perched water tables. A study performed by *Sterrett and Edil* [1982] shows how a complex flow system with double seepage faces formed at the land-lake interface along the shoreline of Lake Michigan (Wisconsin) due to inhomogeneities of the glacial materials. *Cooley* [1983] was the first to model drainage involving double seepage faces, for a case involving two soil layers separated by an impeding layer. A similar soil configuration was considered by *Rulon et al.* [1985] for their laboratory sand-tank experiments. In a steady-state flow analysis using the finite element model of *Neuman* [1973] modified to account for a double seepage face, *Rulon et al.* [1985] showed that the response of the exit points

is strongly dependent on the position of the impeding layer. Subsequently, *Lam et al.* [1987] simulated the same experiment considering transient conditions and infiltration.

Detailed physically-based models that couple surface and subsurface flow are relatively recent and still require careful assessment of various implementation details, including the consistency and interactions between the outflow boundary conditions of each component model. Intriguing scenarios can arise when a catchment outlet condition (surface routing model) and a seepage face (subsurface model) coexist, the former inducing convergent flow patterns towards the land surface while the latter drives flow towards the base of the hillslope. This was seen recently during the first experiment performed on one of the artificial hillslopes at the Landscape Evolution Observatory (LEO) of the Biosphere 2 facility in Arizona [*Gevaert et al.*, 2014]. The experiment experienced both saturation excess overland flow and outflow from the vertical downslope plane and thus required both a surface outlet and a dynamic seepage face boundary to be reproduced [*Niu et al.*, 2014b].

Even in absence of vertical downslope planes (e.g., sharp riverbanks), seepage face conditions can arise, for instance, in riparian zones at the transition between hillslope and channel terrain, and here as well a consistent treatment of outlet, atmospheric, and seepage face boundary conditions is needed. The complexities in this case originate from the diversity of runoff generation mechanisms (infiltration excess runoff, saturation excess runoff, return flow) and overland flow dynamics, including re-infiltration, ponding, and direct seepage to the stream channel [*Freeze*, 1974; *Beven and Wood*, 1983]. Simple models of saturation excess runoff are of the conceptual, lumped-parameter type [e.g., *Boughton*, 1990; *Willgoose and Perera*, 2001]. The saturation mechanism has also been widely investigated with the use of subsurface flow numerical models [e.g., *Beven*, 1977; *Ogden and Watts*, 2000; *Cloke et al.*, 2003]. More recently, *Beaugendre et al.* [2006] simulated water exfiltration at the ground surface with a coupled surface/subsurface model and compared the results with those obtained by using a simpler subsurface seepage face model. They show how, for simple scenarios involving constant slope and rainfall, the two approaches yield similar results. However, in their analysis re-infiltration processes are neglected.

In this study we address the following four groups of questions relating the behavior of seepage face boundary conditions:

1. When is it acceptable to use a simpler, static (Dirichlet boundary condition) treatment of a seepage boundary in lieu of the dynamic condition of a classical seepage face approach? What are the approximation errors when using the simpler approach?

2. How do we resolve seepage face outflow under conditions of heterogeneity? What are the resulting dynamics?

3. In the context of integrated surface/subsurface modeling, how does a seepage face boundary interact with the catchment outlet boundary condition used in overland and channel flow models? Can the two types of boundary condition coexist?

4. What are the effects of re-infiltration processes when simulating water exfiltration at the land surface and overland flow? What is the relationship between the treatment of seepage face and atmospheric boundary conditions?

To answer these questions, we use the numerical model CATHY [*Camporese et al.*, 2010], which couples a finite element solver for 3D subsurface flow with a finite difference solver for overland and channel routing. The original algorithm that handles the seepage face boundary condition in CATHY derives from the approach proposed by *Neuman* [1973] and is based on a single exit point whose position is updated during each nonlinear iteration of the Picard scheme that is used to solve the nonlinear Richards equation [*Paniconi and Putti*, 1994]. Here we propose a generalization of this approach that simplifies the classic algorithm and that deals also with multiple seepage faces in the presence of layered and random heterogeneity. The new algorithm extends other approaches, such as the one proposed by *Rulon and Freeze* [1985], in performing the update at each nonlinear iteration and in allowing the presence of more than two seepage faces. The simulations to address points 1 and 2 above are performed for a simple rectangular hillslope. Different scenarios are tested by changing the soil parameterization, the slope, and the atmospheric and initial conditions. The tests are designed to first analyze the approximation errors committed when modeling the outflow from the base of the hillslpe as a simple fixed Dirichlet condition instead of as a dynamic seepage face condition. Secondly, the tests are used to examine the water table configurations and the dynamics of the different seepage faces and exit points arising from the presence of layered heterogeneity. To analyze the seepage face and surface outlet interactions (point 3), we consider a numerical model

of the artificial hillslope constructed for the LEO project at Biosphere 2. In this real scenario we look at the steady state rainfall partitioning between seepage face flow and surface outflow for different combinations of rainfall rate and average slope. The last set of simulations, addressing point 4, are run for a rectangular hillslope and are used to investigate the behavior of seepage face conditions for complex runoff generation and routing scenarios.

3.3 Methodology

3.3.1 Hydrological model

CATHY (CATchment HYdrology) is a distributed physically-based model that couples Richards' equation, describing flow in variably saturated porous media, and a finite difference solver for the diffusion wave equation, describing flow propagation over the land surface (overland runoff) and in the stream network (channel flow) [*Camporese et al.*, 2010]. The mathematical model consists of the following system of two partial differential equations:

$$S_w(\psi)S_s\frac{\partial\psi}{\partial t} + \phi\frac{\partial S_w}{\partial t} = \nabla\cdot[K_r(\psi)K_s(\nabla\psi+\eta_z)] + q_{ss} \tag{3.1a}$$

$$\frac{\partial Q}{\partial t} + c_k\frac{\partial Q}{\partial s} = D_h\frac{\partial^2 Q}{\partial s^2} + c_k q_s \tag{3.1b}$$

where in equation (3.1a) $S_w(\psi)$ $[L^3L^{-3}]$ is the water saturation, S_s $[L^{-1}]$ is the aquifer specific storage, ψ $[L]$ is the pressure head, t $[T]$ is time, ϕ $[L^3L^{-3}]$ is the porosity, K_s $[LT^{-1}]$ is the saturated hydraulic conductivity tensor, $K_r(\psi)$ is the relative hydraulic conductivity function, $\eta_z = (0,0,1)'$ with z $[L]$ the vertical coordinate directed upward, and q_{ss} $[L^3L^{-3}T^{-1}]$ is a source or sink term that includes the exchange fluxes from the surface to the subsurface. From S_w and ϕ the volumetric water content is defined as $\theta = S_w\phi$ $[L^3L^{-3}]$. In the surface flow equation (3.1b) Q $[L^3T^{-1}]$ is the discharge along the overland and channel network, c_k $[LT^{-1}]$ is the kinematic celerity, s $[L]$ is the coordinate direction for each segment of the overland and channel network, D_h $[L^2T^{-1}]$ is the hydraulic diffusivity, and q_s $[L^3L^{-1}T^{-1}]$ is the inflow or outflow rate from the subsurface to the surface.

The 3D Richards equation is discretized by a P1 Galerkin finite element scheme in space using tetrahedral elements and by a backward Euler scheme in time with adaptive

time step. The resulting system of nonlinear equations is linearized by the Picard iterative scheme [*Paniconi and Putti*, 1994]. The nonlinear characteristics $S_w(\psi)$ and $K_r(\psi)$ are specified using *van Genuchten* [1980] relationships.

At every time step CATHY couples equations (3.1a) and (3.1b) as follows: atmospheric inputs (rainfall or potential evaporation) are first partitioned into effective rainfall or evaporation and surface runoff via a boundary condition switching procedure [*Camporese et al.*, 2010]. CATHY then solves the surface equation and updates the new surface to subsurface fluxes q_{ss}. Finally, the subsurface equation is solved and the model updates the subsurface to surface exchange fluxes for the start of the next time step. Besides atmospheric forcing, other boundary conditions in CATHY include prescribed pressure head (Dirichlet) and flux (Neumann) conditions imposed on the lateral and bottom boundaries and that can vary in space and time. With the Dirichlet condition we generate inflow or outflow which can vary according to the assigned pressure head and the internal system state. With the Neumann condition we impose directly inflow or outflow from the boundary and the model calculates the pressure head. The model also uses Dirichlet and Neumann conditions to handle the seepage boundary (next section), typically imposed at the downslope lateral boundary. Additional details on the model features and numerics can be found in *Camporese et al.* [2010] and *Paniconi and Putti* [1994].

3.3.2 Seepage face boundary condition

A seepage face is the boundary between a saturated flow field and the atmosphere, typically modeled as a lateral boundary (e.g., a riverbank) where water is free to exit from the domain in case of saturation. A seepage face can also form on portions of the land surface, such as along a gently sloping riparian zone. In the case of homogeneous porous media the exit point of a seepage face separates the saturated and unsaturated flow fields: below the exit point groundwater discharges at atmospheric pressure, while there is no outflow on the portion of the boundary above the exit point. This definition needs to be generalized for heterogeneous cases, where several exit points may occur. The seepage face is a dynamic boundary since for unsteady flow the exit point position changes in time, typically rising when the aquifer is recharging and dropping as the aquifer drains. The exit point position cannot be imposed *a priori* but rather is determined by the internal system state, i.e., by the level of the water table as it intersects the land surface.

For homogeneous porous media, the standard approach to handling seepage face boundary conditions in numerical models of variably saturated subsurface flow is described in numerous classic studies [e.g., *Neuman*, 1973; *Cooley*, 1983; *Huyakorn et al.*, 1986a]. Here we propose a simplification and a generalization of this classic algorithm.

3.3.2.1 Standard algorithm

In the classic approach the nodes of the computational mesh forming the seepage face boundary are subdivided into distinct vertical or sloping lines. The nodes on each of these lines are reordered in a consecutive way, from the bottom to the top, in such a way as to easily identify the exit point position along the vertical. The algorithm computes the exit point position at each iteration of the nonlinear scheme. For each seepage face line, the initial position of the exit point is calculated considering the initial ψ distribution: by checking the pressure from bottom to top, the exit point is set below the first node with negative ψ (atmospheric pressure is taken to be zero). As boundary condition for the next iteration the algorithm sets zero pressure head (Dirichlet condition) at the exit point and all nodes below it, and zero flux (Neumann condition) at the nodes above the exit point. At each nonlinear iteration the position of the exit point is adjusted based on the evolving ψ solution and the computed fluxes at the Dirichlet nodes. If an unphysical positive flux (inflow) is encountered at a node below the exit point, the exit point position is lowered for the next iteration. On the other hand, if a positive value of ψ is encountered at a node above the exit point, its position is raised. In CATHY the user is given two options for identifying the new position of the exit point. In the first option the seepage face convergence can be added as an additional constraint on convergence of the subsurface solver. If this option is selected, the subsurface solver converges, and thus can progress to the next time step, if both the Picard scheme converges and the exit points on all seepage lines are unchanged between the previous and current iterations. The second option proposes an alternative search for the new exit point by raising or lowering by only one node the exit point computed at the previous nonlinear iteration. For the numerical tests performed in this study the standard seepage face algorithm with either of the two options produced largely similar results.

The standard algorithm for modeling seepage face boundaries is particularly suited to vertically-structured computational grids where the 2D surface mesh is replicated down-

ward. In this configuration, identification of the new exit point requires only the position of the exit point at the previous time, reducing the number of nodes to consider in the search. In addition to allowing handling of multiple exit points, the generalization of the seepage face algorithm proposed next can also be applied to unstructured 3D grids.

3.3.2.2 Generalized approach

In the generalized approach the seepage face handling is greatly simplified by doing away with the notion of individual seepage face lines and the consequent ordering of nodes by elevation. In fact, the new algorithm only requires identification of the nodes belonging to the seepage outflow plane, without any additional ordering based on elevation or lateral position. At the start of the simulation and after every nonlinear iteration, the Dirichlet or Neumann assignation is performed according to the same procedure used in the classic algorithm, but without following a bottom to top (or any other) order. Instead of focusing on the identification of the exit points, the new algorithm simply finds the "active" nodes of the seepage face boundary by checking node by node for the presence of positive pressures with an associated outflow (i.e., the Dirichlet nodes). Once this operation is performed, it is possible (but not necessary for the computation of the numerical solution at the next iteration) to identify the active portions of the seepage face boundary by grouping the contiguous Dirichlet boundaries (contiguous nodes along the seepage face having a Dirichlet condition). With this idea the exit points can be associated to the nodes at the highest elevations of an active portion.

In addition to its simplicity of implementation, the new algorithm automatically handles multiple seepage faces in the presence of layered and random heterogeneity, and it reveals similarities between the way seepage face and atmospheric boundary conditions are handled that are not as apparent in the classic formulation. From a computational point of view, the proposed algorithm may be slightly slower than the classic algorithm, since at each iteration the check for the seepage face Dirichlet nodes is done on all the nodes along the seepage face, while previously only the nodes under the exit point where considered. However, the cost of this operation is negligible with respect the cost of the solution of the nonlinear iteration. Moreover, the new algorithm can be applied to any unstructured 3D mesh, as mentioned earlier.

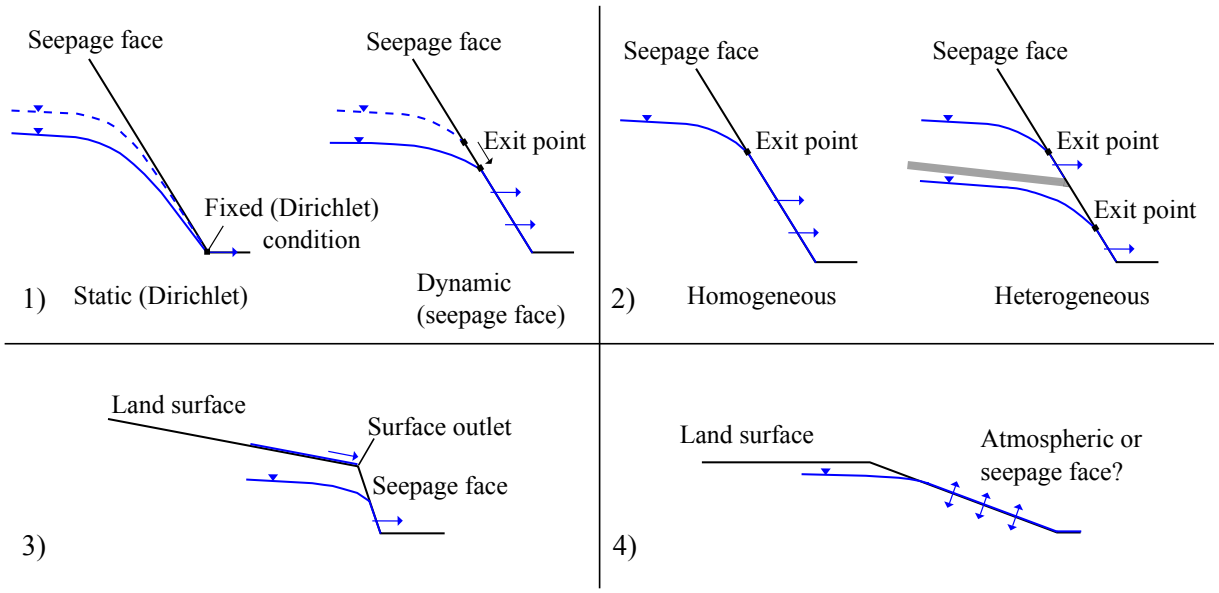

Figure 3.1: *Conceptual representation of the boundary conditions implemented in the four analyses performed.*

3.3.3 Setup of numerical experiments

We perform four analyses: in the first set we look at the difference between treating a seepage face as a static (Dirichlet) or dynamic (according to the algorithms presented in section 3.3.2) boundary (Figure 3.1.1); in the second we study the seepage face response in the presence of layered heterogeneity (Figure 3.1.2); in the third we analyze the interactions between the seepage face and surface outlet (Figure 3.1.3); and finally we investigate possible similarities between seepage face and atmospheric boundary condition switching algorithms for cases where seepage faces form on portions of the land surface (Figure 3.1.4). Table 3.1 summarizes the parameter combinations and setup for each simulation performed in the four sets of experiments. In the first set, which features a homogeneous domain, we also verified that the classic and generalized seepage face algorithms give the same results.

3.3.3.1 Static versus dynamic treatment of the seepage boundary

One common and easy way to treat a seepage face is to set to 0 (atmospheric pressure) the pressure head at the bottom of the outflow plane (i.e., a fixed Dirichlet boundary condition) and to 0 the flux on all the other nodes of the plane (i.e., a no-flow Neumann

Table 3.1: *Parameter values for the four sets of numerical experiments. The initial position of the water table for the simulations with rainfall is at the bottom of the domain, while for the simulations with zero rainfall it is at the surface.*

Numerical experiment		**Saturated hydraulic conductivity** K_s (m/s)				**Aquifer slope** i (%)	**Rainfall** R (m/s)
Static versus dynamic	**Drainage simulations**	1×10^{-3}				10	0
		1×10^{-4}				10	0
		1×10^{-5}				10	0
		1×10^{-4}				1	0
		1×10^{-4}				30	0
	Rainfall simulations	1×10^{-4}				10	$0.025\text{-}0.5\times10^{-4}$
		1×10^{-5}				10	$0.025\text{-}0.5\times10^{-5}$
		1×10^{-4}				1	$0.025\text{-}0.5\times10^{-4}$
		1×10^{-4}				30	$0.025\text{-}0.5\times10^{-4}$
Layered heterogeneity	**Two-layer**	**Top layer** K_{s1}		**Bottom layer** K_{s2}			
		1×10^{-4}		1×10^{-5}		10	0
		1×10^{-4}		1×10^{-6}		10	0
		1×10^{-5}		1×10^{-4}		10	0
		1×10^{-6}		1×10^{-4}		10	0
		1×10^{-4}		1×10^{-5}		10	1×10^{-5}
		1×10^{-4}		1×10^{-6}		10	1×10^{-5}
		1×10^{-5}		1×10^{-4}		10	1×10^{-6}
		1×10^{-6}		1×10^{-4}		10	1×10^{-7}
	Single-layer with impeding lens	**Soil** K_s		**Lens** K_{sL}			
		1×10^{-4}		1×10^{-6}		10	1×10^{-5}
		1×10^{-4}		1×10^{-8}		10	1×10^{-5}
	Multiple-layer	K_{s1}	K_{s2}	K_{s3}	K_{s4}		
		1×10^{-4}	1×10^{-6}	1×10^{-4}	1×10^{-6}	10	1×10^{-5}
Seepage face and surface outlet interactions		**Soil hydraulic conductivity** K_s (m/s)					
		1×10^{-4}				3	$0.0015\text{-}1.5\times10^{-4}$
		1×10^{-4}				10	$0.0015\text{-}1.5\times10^{-4}$
		1×10^{-4}				20	$0.0015\text{-}1.5\times10^{-4}$
Seepage face versus atmospheric						i_b (%)	
		1×10^{-4}				20	1.5×10^{-6}
		1×10^{-4}				50	1.5×10^{-6}
		1×10^{-4}				100	1.5×10^{-6}

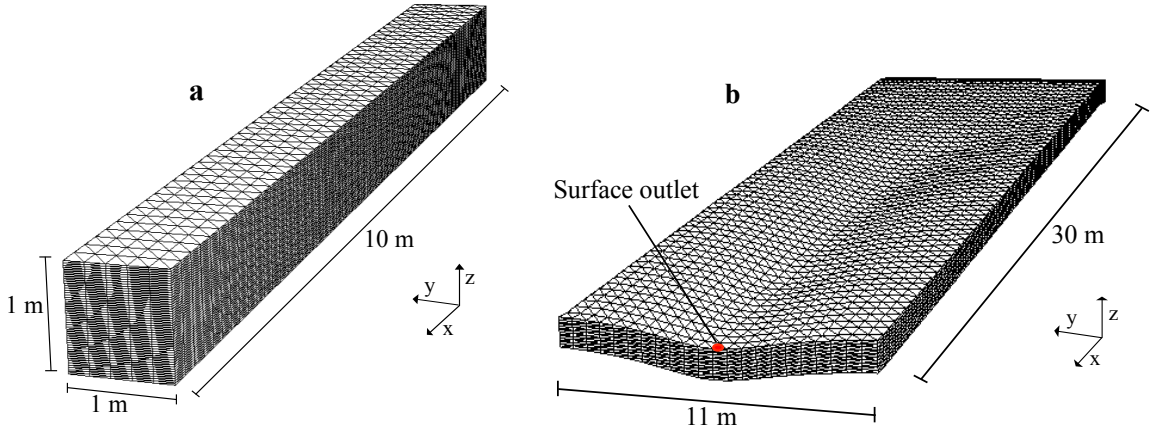

Figure 3.2: *3D numerical grid for the rectangular sloping aquifer (a) and for the LEO hillslope (b).*

boundary condition). This can lead to large approximation errors since the actual exit point can be elsewhere than at the bottom, and its position can vary greatly during the course of a simulation. To investigate these errors we compare the results obtained with the static Dirichlet treatment with those from the seepage face algorithm. The comparison is performed on the synthetic rectangular sloping aquifer depicted in Figure 3.2a. The domain is 10 m long, 1 m deep, and 1 m wide and is discretized into 100 x 5 grid cells in the lateral direction and 50 layers of equal thickness in the vertical direction. The bottom of the aquifer as well as all lateral boundaries except for the downslope outflow plane are assigned no-flow conditions. We perform simulations during which the hillslope drains water out through the outflow plane from fully saturated initial conditions (drainage test cases) and from initially dry conditions subjected to constant rainfall.

For the drainage runs we set no-flow conditions at the land surface to preempt overland flow. The initial pressure head is hydrostatically distributed with the water table at the surface. The approximation error at time t is quantified as:

$$\epsilon^D(t) = \frac{|V_D(t) - V_{sf}(t)|}{V_{sf}(t)} \times 100 \tag{3.2}$$

where $V_{sf}(t)$ and $V_D(t)$ are the cumulative outflow volumes from, respectively, the seepage face and Dirichlet cases. Different combinations of saturated hydraulic conductivity (K_s = 1×10^{-3}, 1×10^{-4}, and 1×10^{-5} m/s) and slope angle (i =1, 10, and 30%) were run (see Table 3.1).

For the rainfall tests we set atmospheric conditions at the land surface with a constant

rainfall rate. The initial pressure head is hydrostatically distributed with the water table at the bottom of the domain. The approximation error is quantified as:

$$\epsilon^R = \frac{|Q_d^{ss} - Q_{sf}^{ss}|}{Q_{sf}^{ss}} \times 100 \tag{3.3}$$

where Q_{sf}^{ss} and Q_D^{ss} are the steady state volumetric flow raised from, respectively, the seepage face and Dirichlet cases. Note that for these runs, and for all test cases that involve rainfall, the rainfall rate are quite high (in realistic terms over long time periods), but the R/K_s ratios are perfectly realistic. Different parameter combinations included slope angles equal to i=1, 10, and 30%, saturated hydraulic conductivities equal to $K_s = 1 \times 10^{-4}$ and 1×10^{-5} m/s, and rainfall rates R set in such a way that a ratio R/K_s between 0.025 and 0.5 was sampled for each slope angle and K_s combination (see Table 3.1).

3.3.3.2 Layered heterogeneity

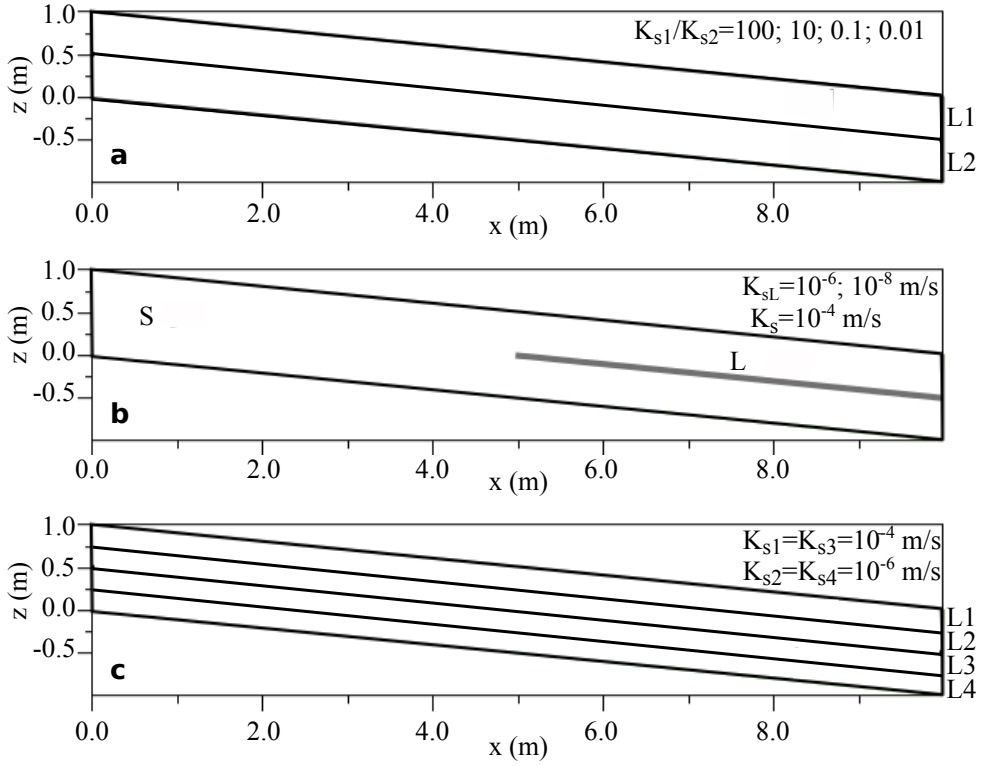

Figure 3.3: *Vertical cross section of the sloping aquifer for the two-layer (a), single-layer with impeding lens (b), and multiple-layer (c) configurations, showing the hydraulic conductivity values or ratios used in each case.*

For the layered heterogeneity analysis we again use the domain depicted in Figure 3.2a, with fixed slope i=10%. A seepage face boundary is set on the downslope outflow plane, atmospheric conditions are set on the surface boundary during rainfall, otherwise no-flow conditions are set, and no-flow conditions are set on all the other boundaries. We ran three sets of simulations: two-layer, single-layer with impeding lens, and multiple-layer heterogeneity (Figure 3.3), in the first set under both drainage and rainfall conditions and in the other two sets under rainfall conditions only. The initial water table position for all drainage runs was at the land surface (with no-flow conditions at the surface to preempt overland flow), whereas for all rainfall runs it was at the bottom of the domain. All simulations were run to steady state.

For the two-layer test case the ratio of upper layer K_{s1} to lower layer K_{s2} hydraulic conductivity was set to 100, 10, 0.1, and 0.01. In the rainfall runs, the rain rate was set to one order of magnitude less than K_{s1}. For the impeding lens test case the lens conductivity K_{sL} was set to 2 and 4 orders of magnitude lower than the soil K_s conductivity. The rainfall rate was again one order of magnitude less than K_s. The multiple-layer test case featured four layers of equal thickness and of conductivity (top to bottom) 1×10^{-4}, 1×10^{-6}, 1×10^{-4}, and 1×10^{-6} m/s and a rainfall rate of 1×10^{-5} m/s. The parameter values for these various configurations are summarized in Table 3.1.

3.3.3.3 Seepage face and surface outlet interactions

In this analysis we look at the scenarios arising in the presence of both a seepage face and a surface outlet. To perform the simulations we consider the LEO model (Figure 3.2b). This is a 30 m long, 1 m deep, and 11 m wide convergent landscape and is discretized into 22 x 60 grid cells in the lateral direction and 10 layers of equal thickness in the vertical direction. We set atmospheric conditions at the surface boundary, a seepage boundary on the downslope vertical plane (the nodes that intersect this plane and the land surface are designated as atmospheric nodes), and no-flow conditions at the bottom boundary and along the three other lateral boundaries. The catchment outlet for the CATHY surface routing model is the land surface cell shown in red in Figure 3.2b. We set the hydraulic conductivity K_s of the system to 1×10^{-4} m/s and initially the water table at bottom with (negative) pressure head hydrostatically distributed. We ran simulations for a range of rainfall rates such that R/K_s ranged from 0.005 to 1.5, and for slope angles i of 3, 10, and

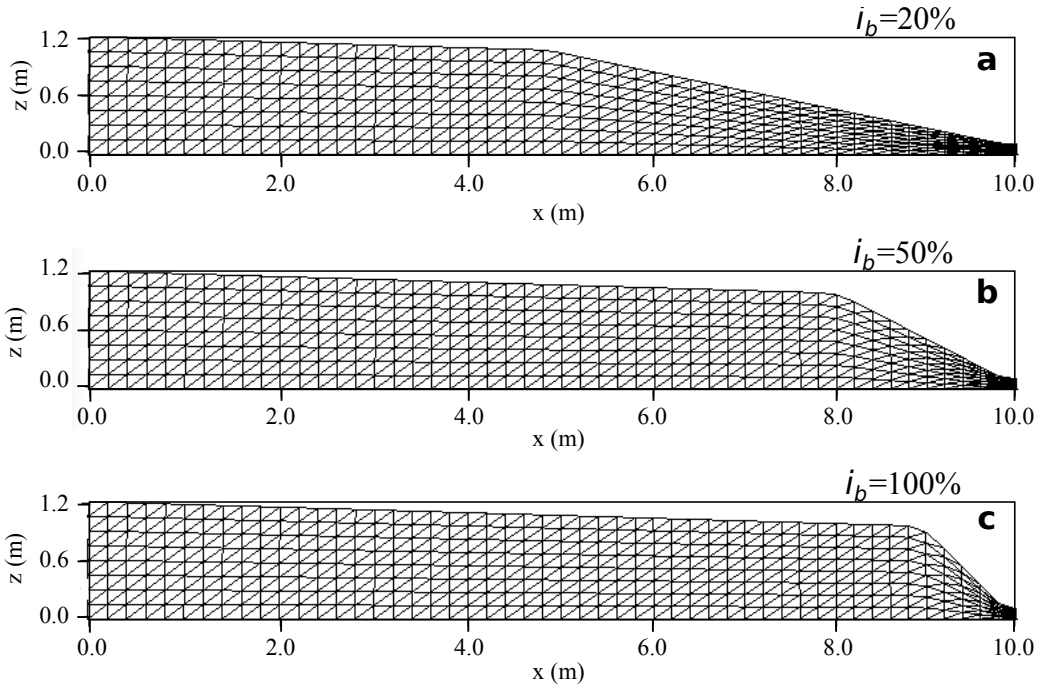

Figure 3.4: *Vertical cross section and computational mesh of the domain used in the three numerical experiments for the seepage face versus atmospheric conditions analysis.*

20%. Table 3.1 summarizes these configurations. The analysis is based on examination of the rainfall partitioning at steady state between seepage face flow Q_{sf} and surface flow Q, considering that when the process is at steady state the change in total water storage is zero and the total inflow (R) is equal to the total outflow (Q_{sf}+Q).

3.3.3.4 Seepage face versus atmospheric conditions

Seepage faces forming on portions of the land surface can be modeled either with a seepage face condition or via atmospheric boundary condition switching. In this analysis we assess the differences between these two approaches. The comparison is performed on the three domains shown in Figure 3.4 that are 10 m long, 1.2 m deep (at the upslope boundary), and 1 m wide and are discretized into 50 x 5 grid cells in the lateral direction and 8 layers of varying thickness. The i_b values of 20, 50, and 100% indicated in Figure 3.4 are the slope angles of the downslope 5, 2, and 1 m portions, respectively, of hillslopes a, b, and c. On this portion of the land surface we set either atmospheric conditions or seepage face conditions. The atmospheric case is simulated in three ways: with CATHY in subsurface-only mode (any exfiltration leaves the domain instantaneously; ponding and re-infiltration

cannot occur); in coupled mode (exfiltrating water can produce ponding and overland flow, and can re-infiltrate); and in coupled mode but with very high kinematic celerity (this very fast surface routing case should in principle approach the subsurface-only case). In the two coupled cases the outlet cell for the surface routing model is situated at the intersection of the downslope vertical plane and the land surface, at the center of the hillslope in the transverse direction. On the remaining portion of the land surface (upslope 5, 8, and 9 m respectively of hillslopes a, b, and c) we set a constant rainfall rate of 1.5×10^{-6} m/s (this was found to be a maximal rate applicable to all three hillslopes that avoids generating runoff on this portion of the land surface). All lateral boundaries and the bottom boundary are assigned a no-flow condition. The hydraulic conductivity is set to 1×10^{-4} m/s and the water table initially at bottom with pressure head hydrostatically distributed (Table 3.1). The simulations were are until steady state. We examine the differences over time between the seepage face volumetric flow and the exfiltration volumetric flow (for the subsurface-only atmospheric case) and outlet atmospheric flow (for the coupled case), as well as the differences in water table distance from the outlet, X_{WT}, calculated by averaging along the transverse direction.

3.4 Results

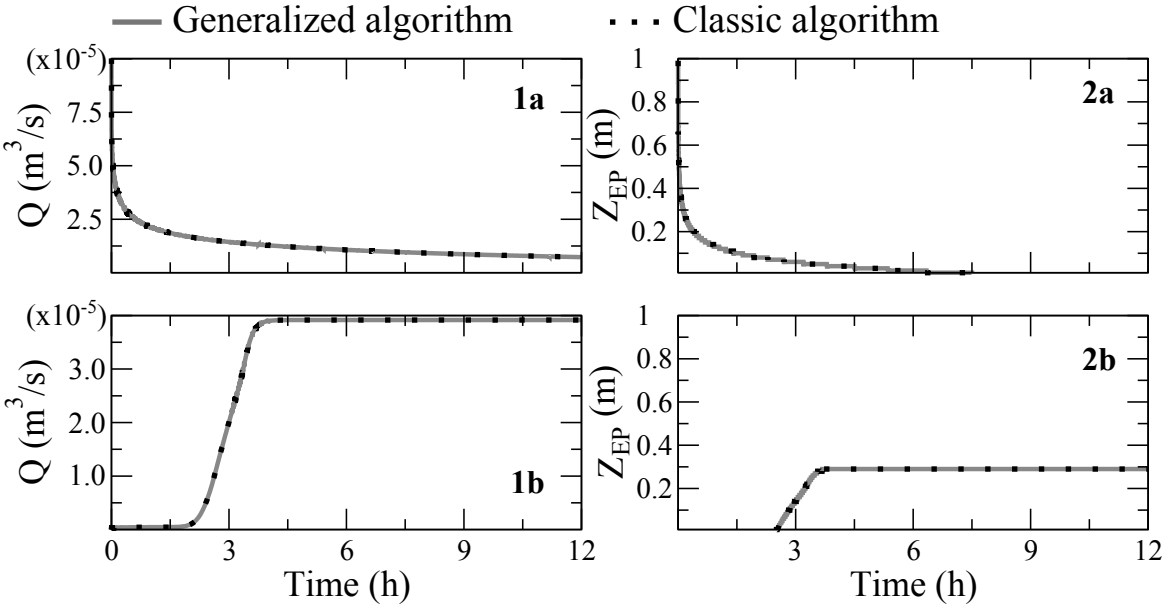

Figure 3.5: *Results obtained with the classic and generalized seepage face boundary condition algorithms for a drainage simulation (panels a) and a rainfall simulation (panels b) showing the seepage face volumetric outflow Q (panels 1) and the exit point height Z_{EP} from the bottom (panels 2). The simulations are for a homogeneous sloping aquifer with hydraulic conductivity $K_s = 1 \times 10^{-4}$ m/s, inclination i=10%, and, for the rainfall case, $R = 1 \times 10^{-5}$ m/s.*

For all the simulations involving homogeneous conditions, we first verified that the generalized and classic seepage face boundary condition algorithms gave the same results. Figure 3.5 reports the comparison for a drainage and a rainfall test case summarized in Table 3.1 ($K_s = 1 \times 10^{-4}$ m/s, i=10%, $R = 1 \times 10^{-5}$ m/s for the rainfall case), and it can be seen that the dynamics of the seepage face outflow Q and exit point height Z_{EP} (measured from the bottom of the domain) are identical. This was confirmed for all the other homogeneous test cases.

3.4.1 Static versus dynamic treatment of the seepage boundary

3.4.1.1 Drainage simulations

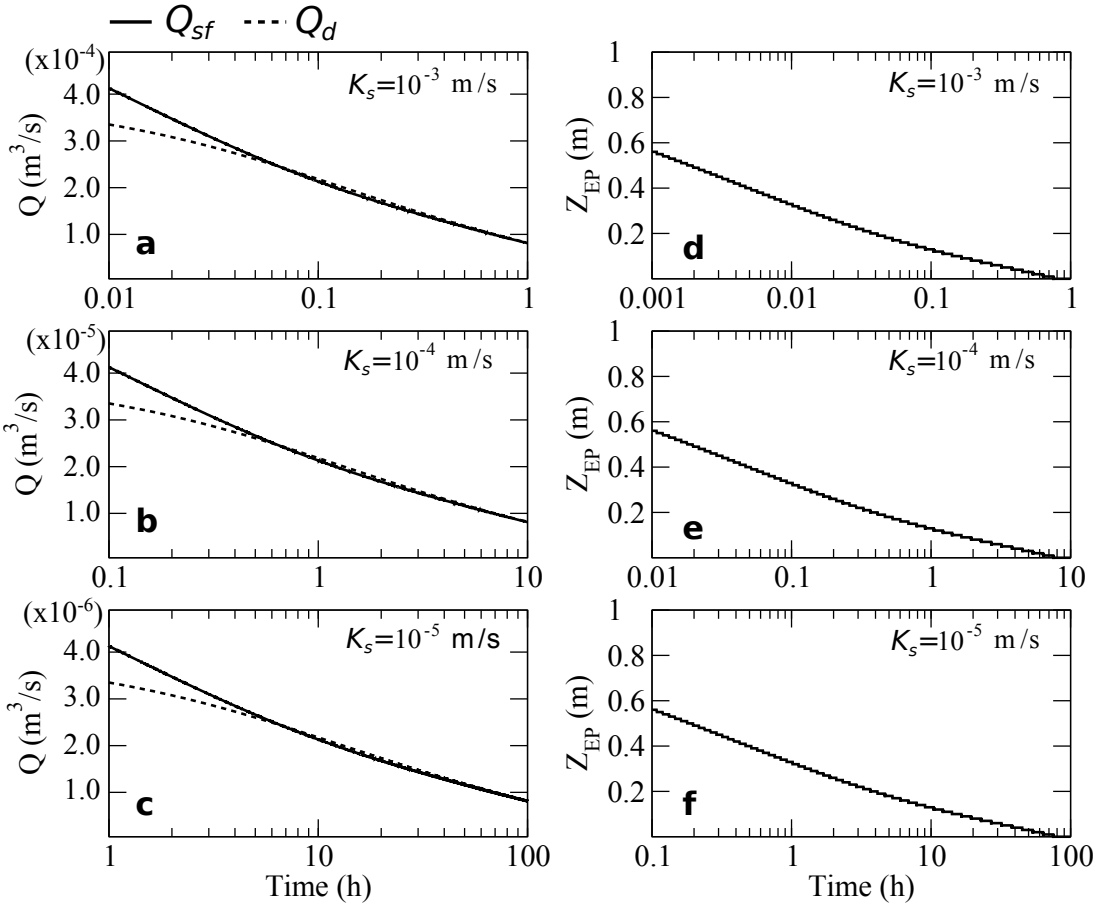

Figure 3.6: *Results for the drainage simulations with a homogeneous sloping aquifer of inclination 10% and varying hydraulic conductivity K_s. Panels (a), (b), and (c): volumetric outflow for static (Q_d) and dynamic (Q_{sf}) treatment of the seepage face boundary; panels (d), (e), and (f): exit point height Z_{EP} for the dynamic treatment case.*

For the drainage tests the effect of hydraulic conductivity on the approximation errors committed when using a static (Dirichlet) boundary condition to model a seepage face boundary is reported in Figures 3.6 and 3.7a. In the left graphs of Figure 3.6 we compare the volumetric outflow over time obtained for the static treatment (Q_d) and for the dynamic treatment (Q_{sf}) for the three different K_s. In the right graphs we report the corresponding exit point height (Z_{EP}) over time for the dynamic case. The results show that Q_{sf} is higher than Q_d early in the simulation, that the differences diminish over

time, and that the solutions converge by the time the position of the exit point for the dynamic treatment case converges to the position of the Dirichlet node, at the bottom of the domain. From the scaling of the time axis in Figure 3.6 it is also apparent that, all other parameters being equal, the seepage outflow response for both boundary condition treatments and the exit point response for the dynamic case scale exactly with K_s. In Figure 3.7 we plot over time the approximation error ϵ^D (equation 3.2) for the various K_s simulations at fixed slope angle (Figure 3.7a) and for the various slope cases at fixed K_s (Figure 3.7b). Here we see that the error committed using a static treatment for the seepage boundary rather than a dynamic treatment can be quite high (about 35% for all runs) early in the simulation, and falls to zero by the end of the simulation. The time to convergence (zero error) scales with K_s for the varying hydraulic conductivity runs (Figure 3.7a), as was pointed out also in Figure 3.6. For the varying slope runs, the time to convergence corresponds, as was the case also for the varying K_s runs, to the time required for the position of the exit point in the dynamic case to reach the bottom of the hillslope. This is shown in Figure 3.8. The time to convergence increases as the slope angle increases.

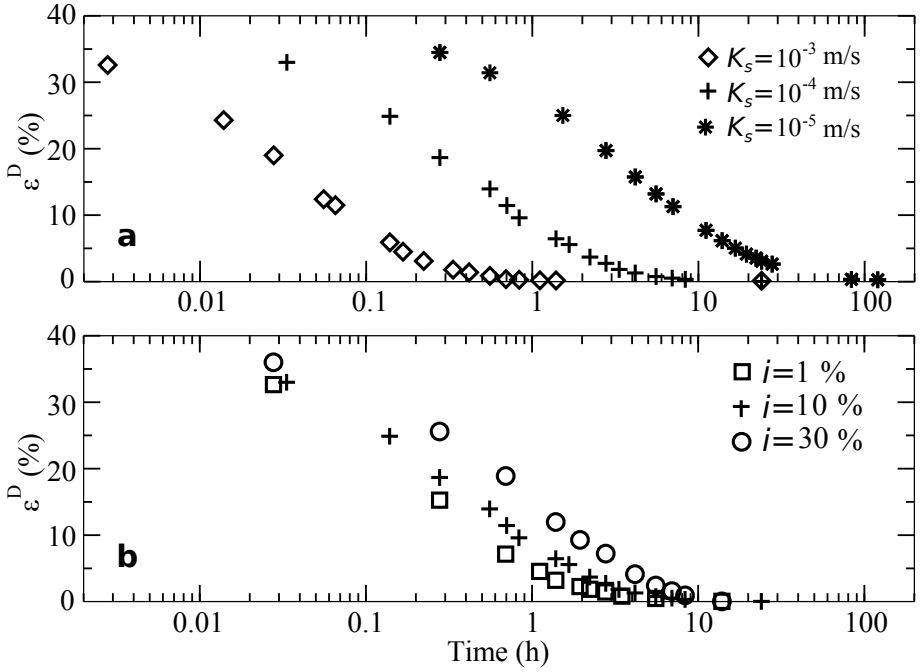

Figure 3.7: *Approximation error ϵ^D over time for the drainage simulations with a homogeneous sloping aquifer of inclination 10% and varying hydraulic conductivity K_s (a) and of hydraulic conductivity $K_s = 1 \times 10^{-4}$ m/s and varying inclination i (b).*

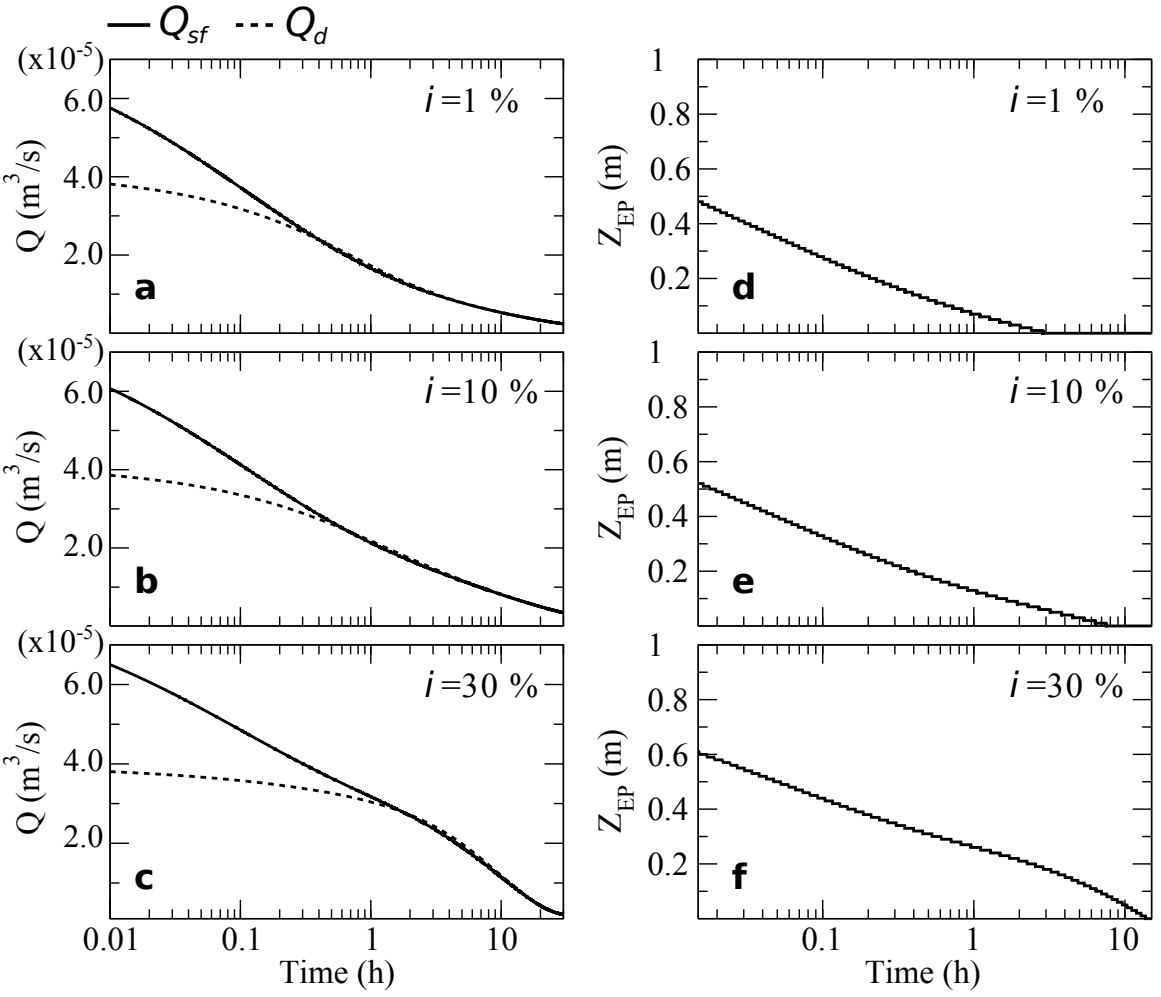

Figure 3.8: *Results for the drainage simulations with a homogeneous sloping aquifer of hydraulic conductivity $K_s = 1 \times 10^{-4}$ m/s and varying inclination i. Panels (a), (b), and (c): volumetric outflow for static (Q_d) and dynamic (Q_{sf}) treatment of the seepage face boundary; panels (d), (e), and (f): exit point height Z_{EP} for the dynamic treatment case.*

3.4.1.2 Rainfall simulations

For the rainfall tests the approximation errors committed when using a static boundary condition to model a seepage face are shown in Figures 3.9 and 3.10. In the left graphs of Figure 3.9 for different rainfall rate R we report the time behavior of the volumetric flow obtained using dynamic conditions (Q_{sf}) and static conditions (Q_d) to model the seepage face, while in the right graphs we report the corresponding height of the exit point Z_{EP} for the dynamic case. The results show that for fixed K_s and fixed i the differences between the two approaches increase with rainfall rate R, as does the final

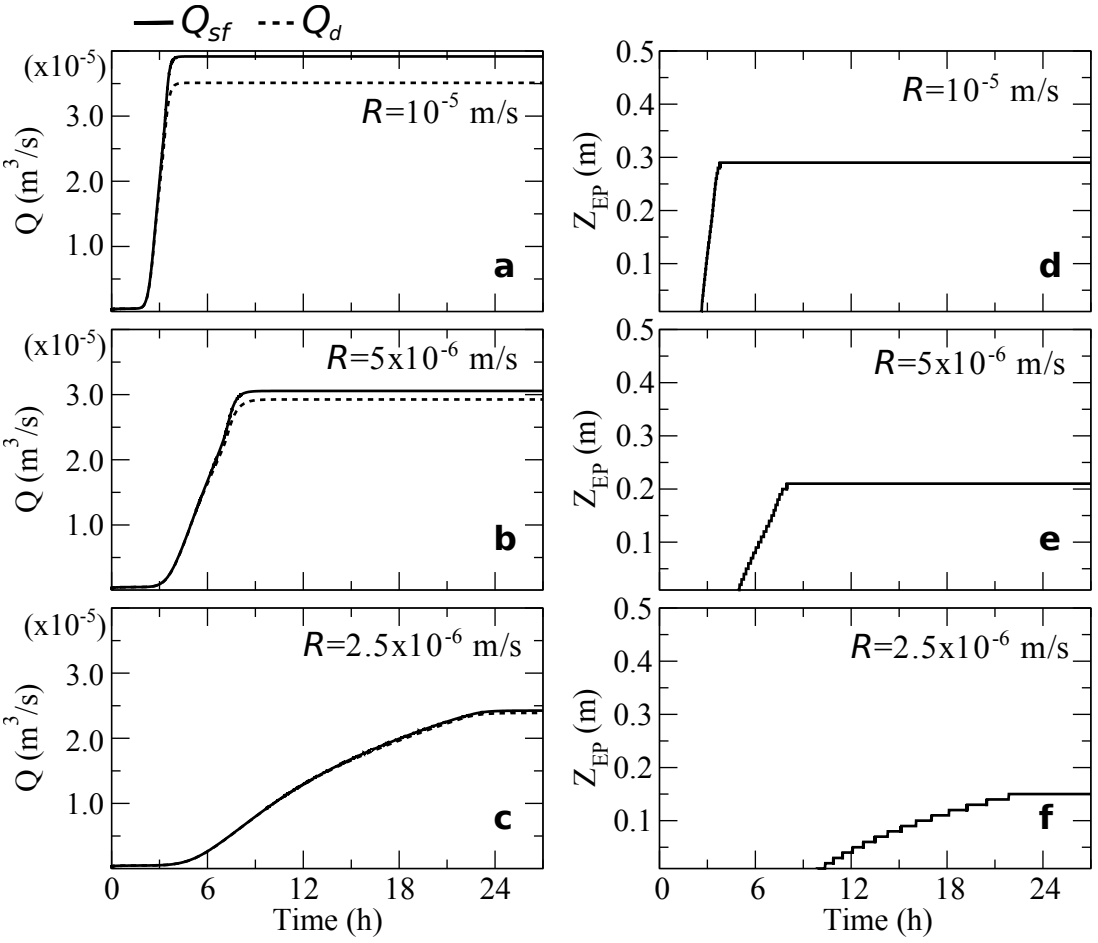

Figure 3.9: *Results of the rainfall simulations with a homogeneous sloping aquifer of inclination 10%, hydraulic conductivity* 1×10^{-4} *m/s, and varying rainfall rate R. Panels (a), (b), and (c): volumetric outflow for static* (Q_d) *and dynamic* (Q_{sf}) *treatment of the seepage boundary; panels (d), (e), and (f): exit point height* Z_{EP} *for the dynamic treatment case.*

(steady state) position of the seepage face exit point. In Figure 3.10 we report the effects of (a) hydraulic conductivity K_s (fixed i=10%) and (b) slope i (fixed K_s=1×10^{-4} m/s) on the approximation errors ϵ^R calculated at steady state (equation 3.3) for different ratios R/K_s. The error committed using a static treatment for the seepage boundary rather than a dynamic treatment increases significantly with R/K_s (reaching 45%), and also with i for fixed R/K_s. The error does not vary with K_s for a fixed R/K_s ratio.

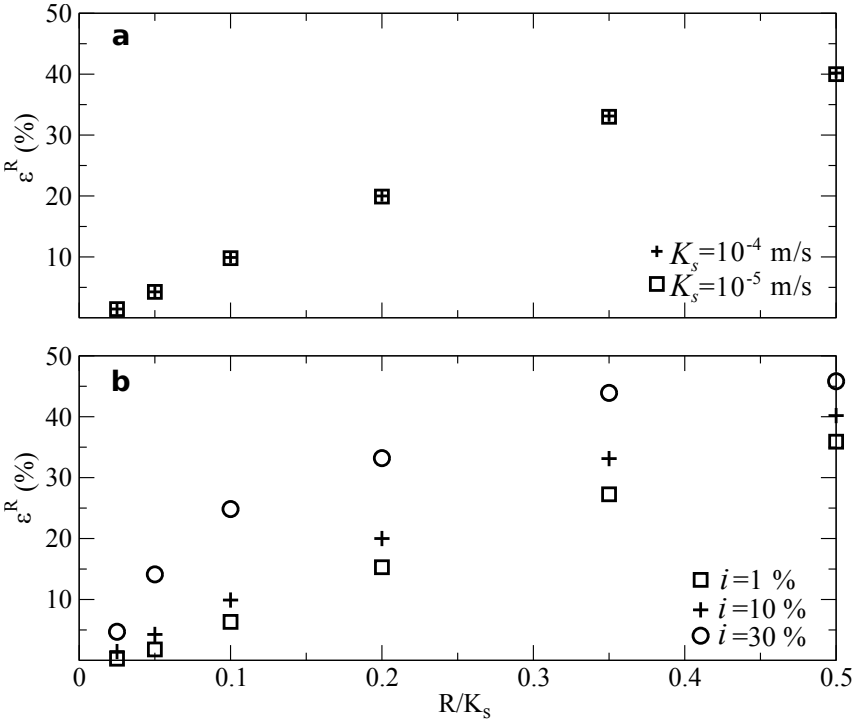

Figure 3.10: *Approximation error ϵ^R as a function of rainfall/conductivity ratio R/K_s for the rainfall simulations with a homogeneous sloping aquifer of (a) inclination i=10% and varying conductivity K_s and (b) conductivity $K_s = 1 \times 10^{-4}$ m/s and varying inclination i.*

3.4.2 Layered heterogeneity

3.4.2.1 Double layers

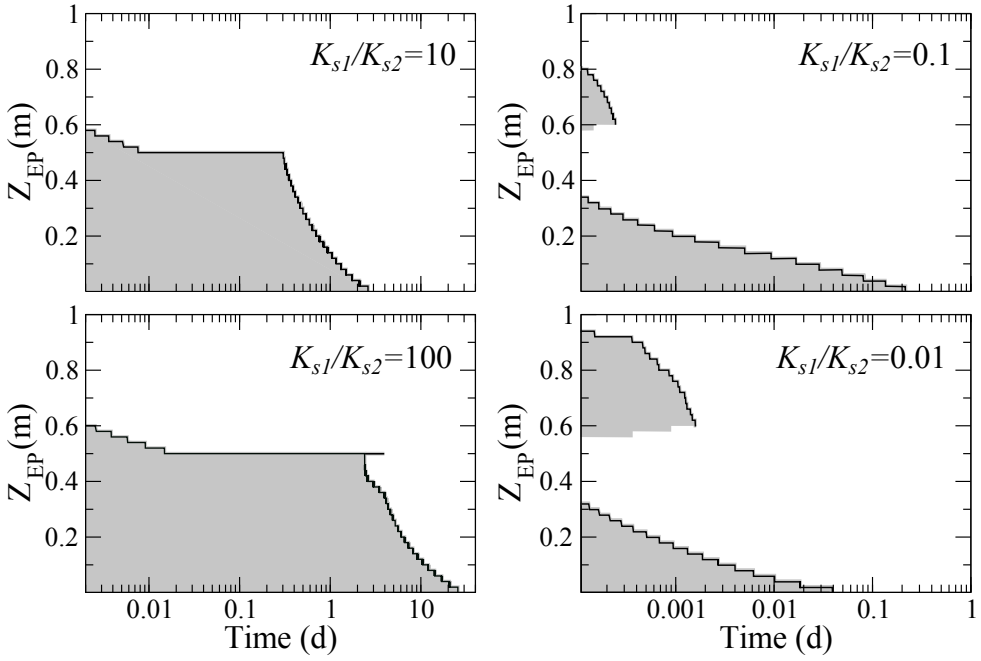

Figure 3.11: *Evolution of the seepage face exit point height Z_{EP} for the two-layer drainage simulations with four different conductivity contrasts between the top (K_{s1}) and bottom (K_{s2}) layers. The shaded areas represent the seepage face outflow planes below each exit point.*

Figures 3.11 and 3.12 show the dynamics of seepage face exit points for, respectively, the drainage and rainfall simulations for the two-layer hillslope and four combinations of K_{s1}/K_{s2} (K_{s1} is the top layer; the parameter values are given in Table 3.1). We refer to the first and the second exit point as the one corresponding, respectively, to the first and second seepage face forming on the seepage outflow plane. The results of Figure 3.11 show that under drainage from initial full saturation (water table close to the surface), the only case that does not feature a second exit point is K_{s1}/K_{s2}=10. For K_{s1}/K_{s2}=100 the position of the first exit point quickly drops from the surface to the interface between the two layers and after about 2 d it starts dropping towards the bottom (reached after about 25 d from the beginning of the simulation). At this time a second exit point appears at the interface of the two layers and persists for about 2 d. Setting the hydraulic conductivity

of the top layer one or two orders of magnitude smaller than that of the bottom layer also results in the formation of two seepage faces, but in this case the dual exit points occur very early in the simulation and the top seepage face has a very short duration (about 250 s and 500 s, respectively, for the K_{s1}/K_{s2}=0.1 and K_{s1}/K_{s2}=0.01 cases).

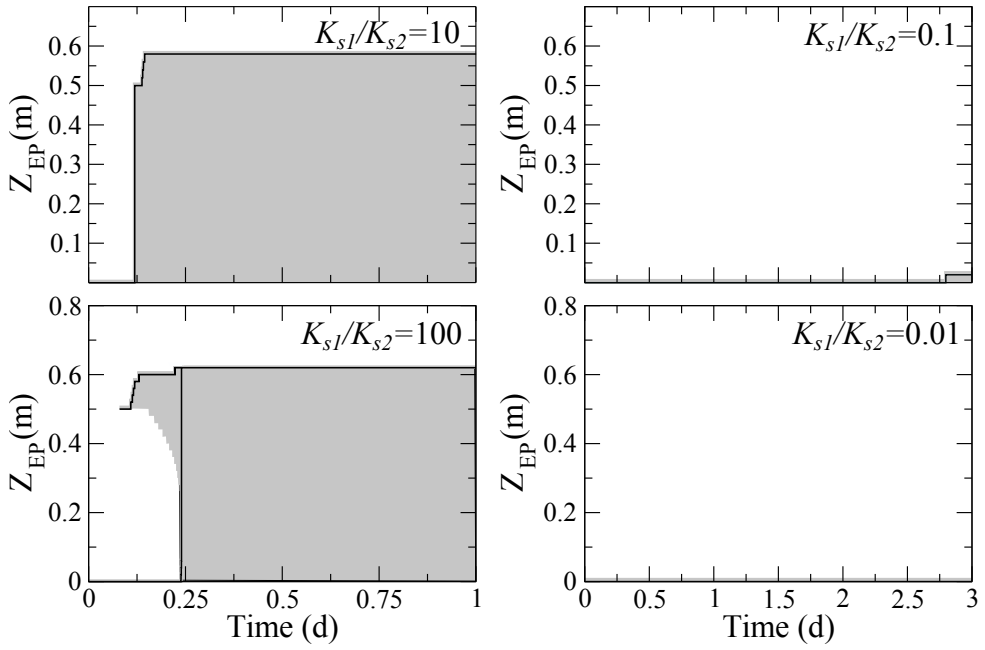

Figure 3.12: *Evolution of the seepage face exit point height Z_{EP} for the two-layer rainfall simulations with four different conductivity contrasts between the top (K_{s1}) and bottom (K_{s2}) layers. The shaded areas represent the seepage face outflow planes below each exit point.*

The results of Figure 3.12 are relative to the simulations with constant rainfall (of intensity one order of magnitude smaller than the hydraulic conductivity of the top layer) and infiltration from initially dry conditions (water table at bottom). In these runs the only case that features a second exit point is K_{s1}/K_{s2}=100. For this case only one exit point, whose position Z_{EP} is at the bottom, is present from the beginning of the simulation until 2.5 h (0.1 d), at which time the infiltration front reaches the interface between the two layers and a second exit point develops. It initially sits at the interface and then rises to Z_{EP}=0.6 m. After 6 h from the beginning of the simulation the rainfall water reaches the bottom and, in turn, starts feeding the first seepage face. As a consequence, the first exit point rapidly rises to reach the second exit point and the two seepage faces merge.

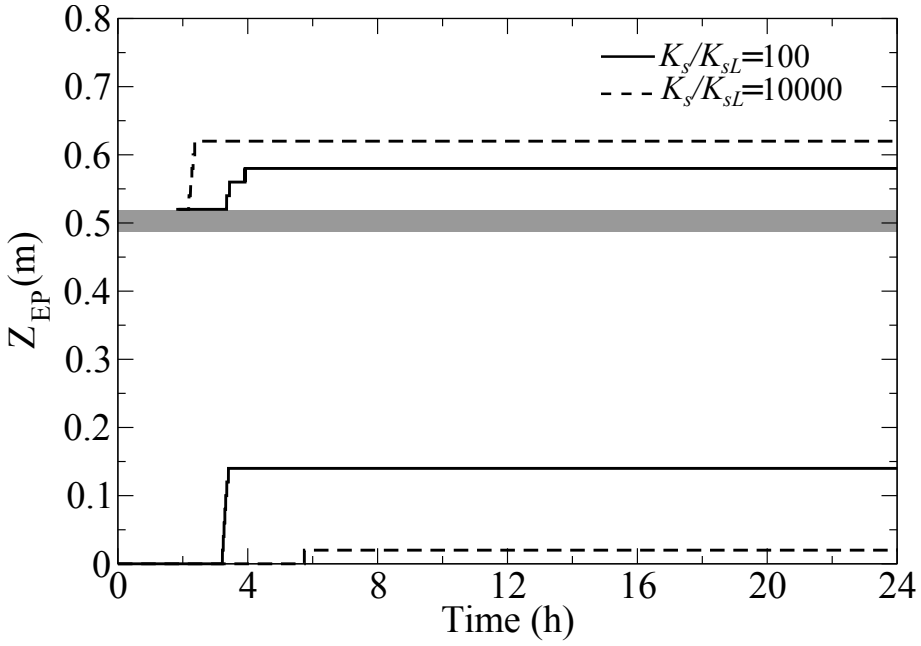

Figure 3.13: *Evolution of the seepage face exit point height Z_{EP} above and below an impeding lens (shown as the gray strip) for two different conductivity contrasts between the aquifer (K_s) and the lens (K_{sL}).*

3.4.2.2 Single layer with a thin impeding lens

Figure 3.13 reports the dynamics of the first and second exit points for the single-layer with impeding lens test case (see Table 3.1 for the parameter values). We refer to the first and second seepage face and relative exit point as those forming, respectively, below and above the impeding lens. In both cases (K_s/K_{sL}=10000 and K_s/K_{sL}=100), a second exit point appears when the infiltration front reaches the impeding lens (at about 1.5 h from the beginning of the simulation). For the K_s/K_{sL}=10000 case this second exit point rises rapidly, while for the K_s/K_{sL}=100 case more water is able to percolate across the impeding lens, making the second exit point rise more slowly. The dynamics of the first seepage face is also different between these two permeability contrast cases. When K_s/K_{sL}=100 the first exit point starts rising at 3.5 h whereas when K_s/K_{sL}=10000 the first seepage face can only be fed by rainfall water that drains from upslope (much less percolation through the lens), and as a consequence the first exit point starts rising only at 6 h. Not surprisingly, at steady state the heights of the first and second exit points are, respectively, higher and lower for K_s/K_{sL}=100 than for K_s/K_{sL}=10000. In Figure 3.14

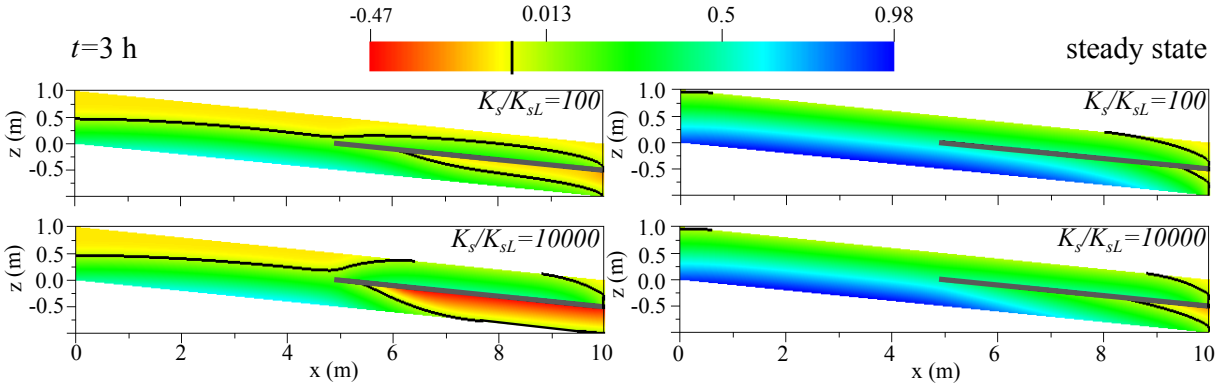

Figure 3.14: *Pressure head profiles (m) and zero pressure head contours (shown in black) in vertical cross section and at times 3 h (left) and steady state (right) for the simulations with an impeding lens (shown in gray) with conductivity contrast between the aquifer (K_s) and the lens (K_{sL}) of K_s/K_{sL}=100 (top) and K_s/K_{sL}=10000 (bottom).*

we compare the pressure head profile in vertical cross section at 3 h (about one hour after the appearance of the second exit point) and at steady state. The profile at 3 h clearly shows that the soil below the lens is much wetter for the K_s/K_{sL}=100 case, while the water table above the lens is more developed for the K_s/K_{sL}=10000 case. In both cases at steady state the soil below the lens is wet and two water tables are present, at bottom and above the lens.

3.4.2.3 Multiple layers

The simulation performed for the multiple seepage face case features the presence of three seepage faces and corresponding exit points. Figure 3.15 shows their dynamics and in what follows we refer to the first, second, and third seepage face/exit point as they appeared chronologically. At the beginning only one seepage face with its exit point (black line in Figure 3.15) at bottom is present. A second seepage face develops when the infiltration front reaches layer 2 (at approximatly 1.5 h). Its exit point (blue line) sits at the interface between the first two layers and neither rises nor falls for the duration of the simulation. A third seepage face forms when the infiltration front reaches layer 4, at around 7 h, with its exit point (red line) at the inteface between layers 3 and 4. At 8 h the rainfall water reaches the bottom and the first exit point rises to the height of the third exit point such that the first and third seepage faces merge for the remainder of the simulation, to

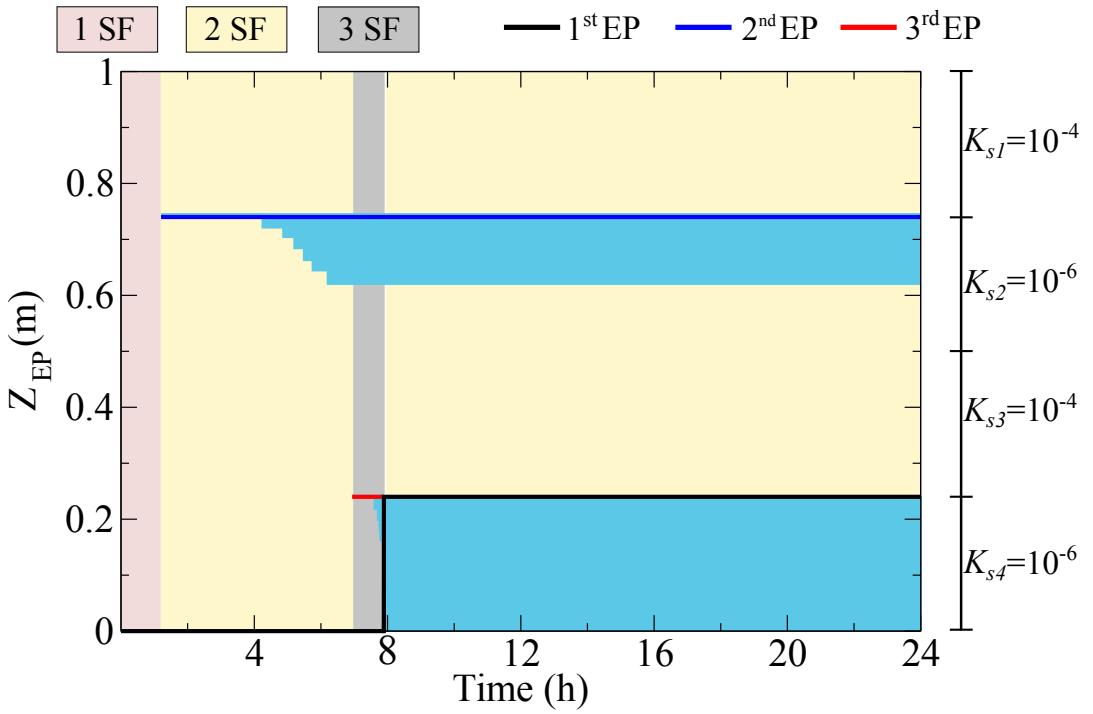

Figure 3.15: *Dynamics of the first (black line), second (blue line), and third (red line) exit point (EP) for the multiple-layer test case. The seepage face (SF) outflow planes below each exit point are shown as the light-blue areas. The pink, yellow, and gray areas show the time spans during which, respectively, one SF, two SFs, and three SFs are present.*

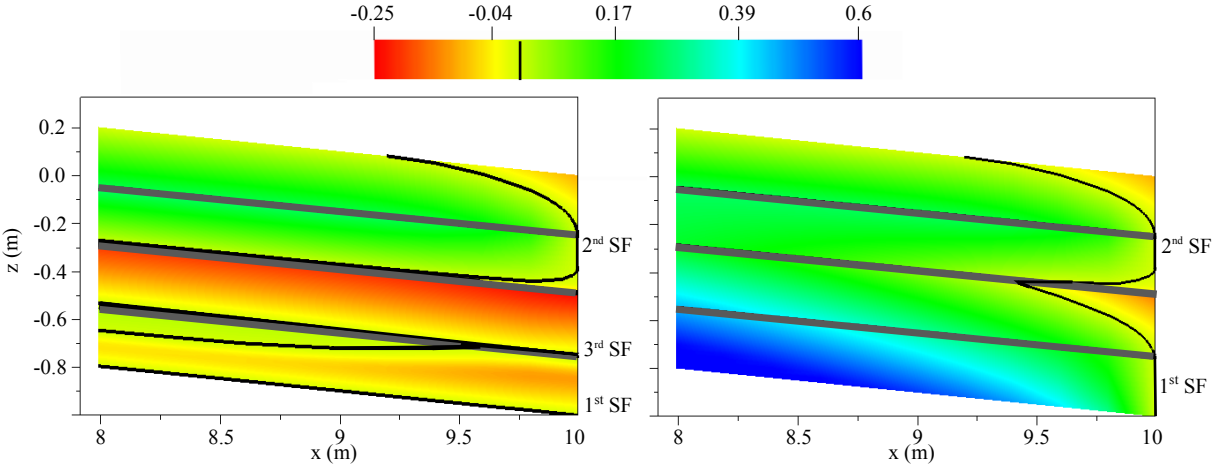

Figure 3.16: *Snapshots at 7 h (left) and at steady state (right) of the profiles of pressure head (m) in vertical cross section at the downslope 2 m portion of the hillslope for the multiple-layer simulation. The interfaces between layers are shown by the gray lines while the contours of zero pressure head are traced by the black lines.*

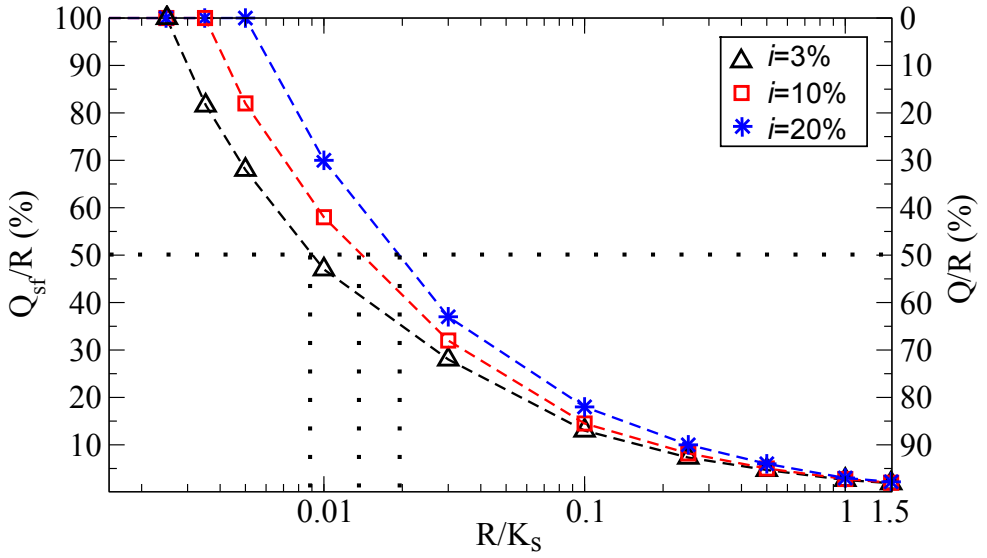

Figure 3.17: *Partitioning of rainfall R on the LEO hillslope between seepage face outflow Q_{sf} (left axis) and surface outlet discharge Q (right axis) at steady state for a range of rainfall/conductivity (R/K_s) ratios and three different slope angles i. The horizontal and three vertical dotted lines give the R/K_s value at which seepage and outlet contributions are equal (R/K_s = 0.009, 0.012, and 0.02 for slope angles 3%, 10%, and 20%, respectively).*

steady state. In Figure 3.16 we show the pressure head profile in vertical cross section for the downslope 2 m portion of the hillslope at 7 h, when three seepage faces are present, and at steady state. From the zero pressure head contours, shown as black lines, the different seepage faces are easily discerned. The profile at 7 h shows: the first seepage face at bottom, the second seepage face in layer 2 and at the interface between the first two layers, and the third seepage face at the interface between layers 3 and 4. The steady state profile shows: the first seepage face in layer 4 and at the interface between layers 3 and 4 and the second seepage face in a portion of layer 2 and at the interface between the first two layers.

3.4.3 Seepage face and surface outlet interactions

The results of a series of simulations on the LEO hillslope to examine seepage face and surface outlet interactions are presented in Figure 3.17 and show the steady state rainfall (R) partitioning between seepage face flow Q_{sf} and surface outflow Q for different ratios of R/K_s (the hydraulic conductivity was fixed at $K_s = 1 \times 10^{-4}$ m/s) and three slope

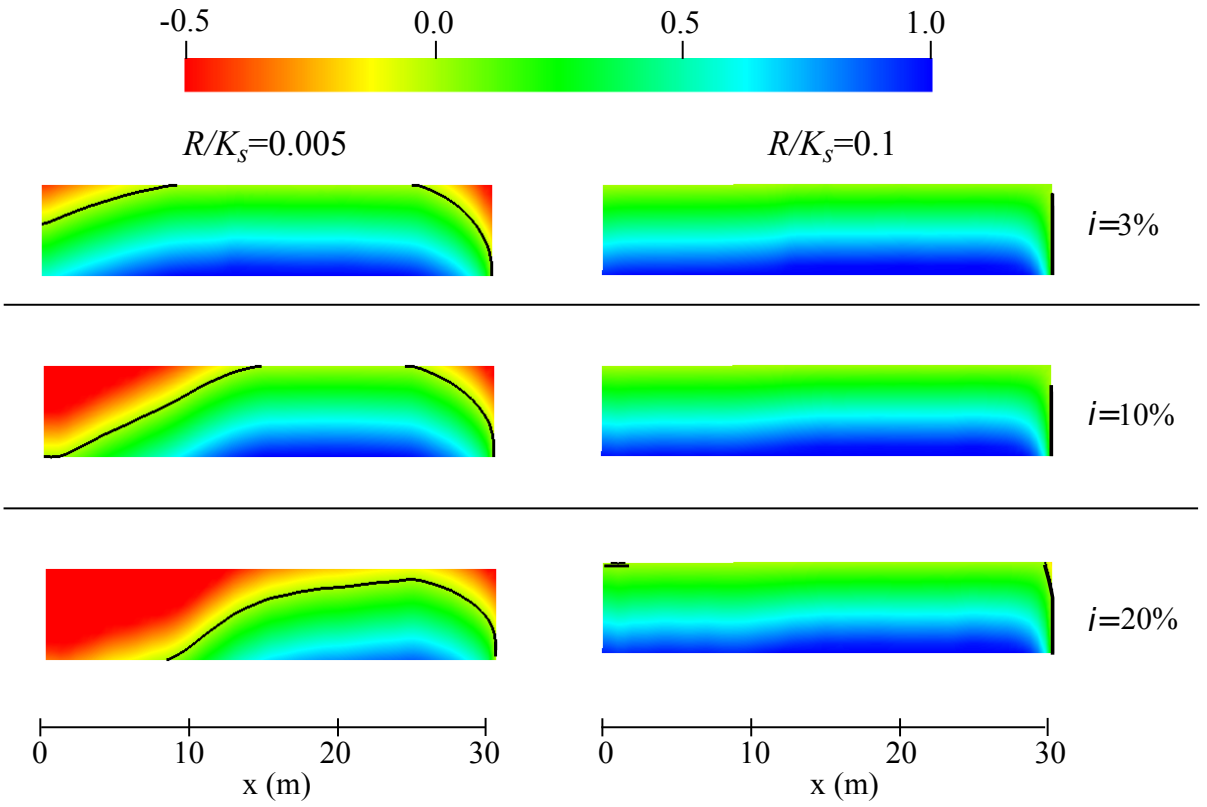

Figure 3.18: *Steady state profiles of pressure head (m) (color map) and water table (black lines) for the LEO hillslope aken in vertical cross section along the x direction (midpoint in the y direction). The seepage boundary is at x=30 m. The results are shown for two rainfall/conductivity (R/K_s) ratios and three slope angles i.*

angles i. The results show that the seepage face contribution Q_{sf}/R decreases with R/K_s and increases with i. Thus, higher rainfall rates enhance overland flow while steep slopes enhance flow from the base of the hillslope. They also show that the differences between the three slope angles become less significant as R/K_s increases. In addition, it is seen that the R/K_s value at which seepage face and outlet contributions are equal increases with i. Thus, the R/K_s range for which seepage face flow is greater than surface flow increases with i. These results can be better understood by looking at the profiles shown in Figures 3.18 and 3.19. Here the steady state pressure head and velocity profiles for the different slopes are plotted for a case in which the seepage face contribution exceeds the surface flow contribution (R/K_s=0.005) and for a case in which the surface flow contribution exceeds the seepage face contribution (R/K_s=0.1). In accordance with what has been noted from Figure 3.17, the differences between profiles for the three different

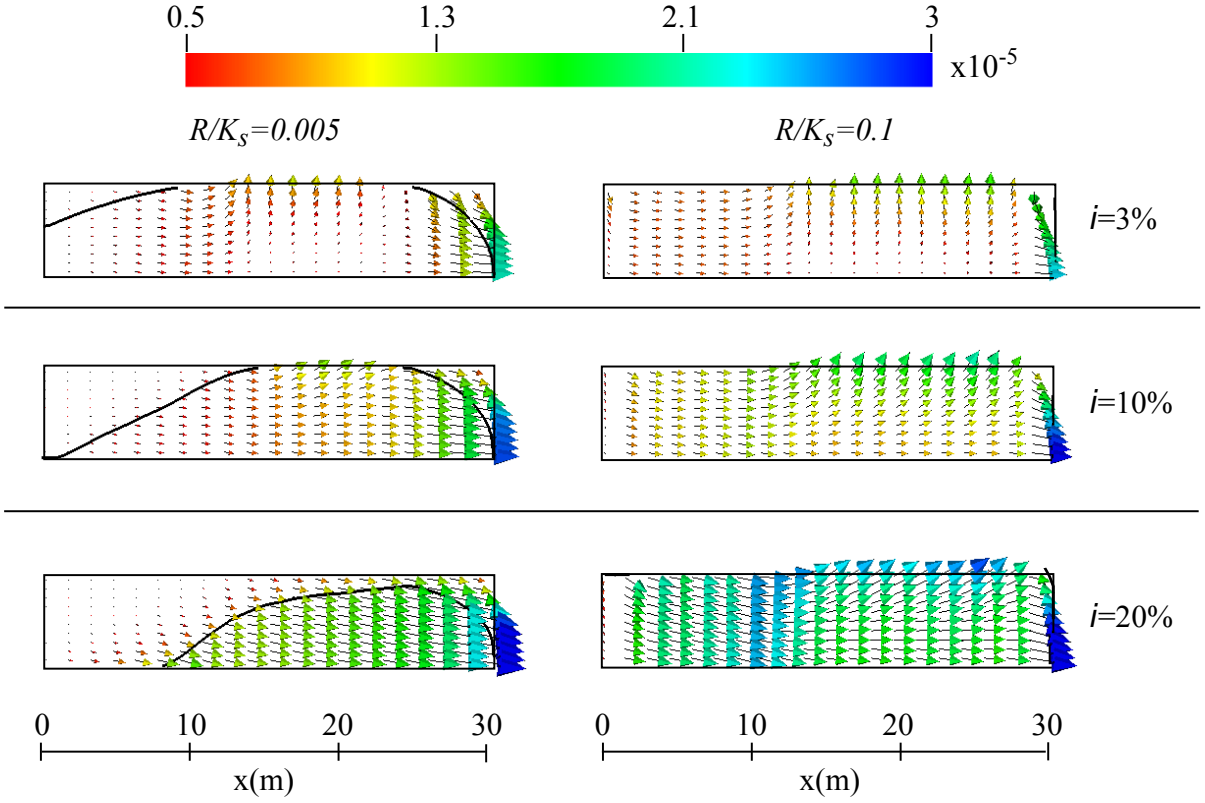

Figure 3.19: *Steady state profiles of Darcy velocity for the LEO hillslope taken in vertical cross section along the x direction (midpoint in the y direction). The seepage boundary is at x=30 m. The results are shown for two rainfall/conductivity (R/K_s) ratios and three slope angles i.*

slope angles are greater for the R/K_s=0.005 case than for the R/K_s = 0.1 case. The differences include a smaller portion of the land surface intersected by the water table, the water table mound further downslope, less water exfiltration at the land surface, and higher velocities at the seepage face for increasing i. In addition, while for the R/K_s=0.005 case, where unsaturated areas persist for all three slopes and most of the outflow is from the seepage face, the fully saturated conditions encountered for the R/K_s=0.1 case give rise to enhanced convergent velocity trajectories towards the surface outlet.

3.4.4 Seepage face versus atmospheric conditions

In this final set of tests we examine seepage face formation on the land surface and compare the behavior of the seepage face boundary condition algorithm to the classic atmospheric boundary condition switching procedure used in catchment hydrological models. For

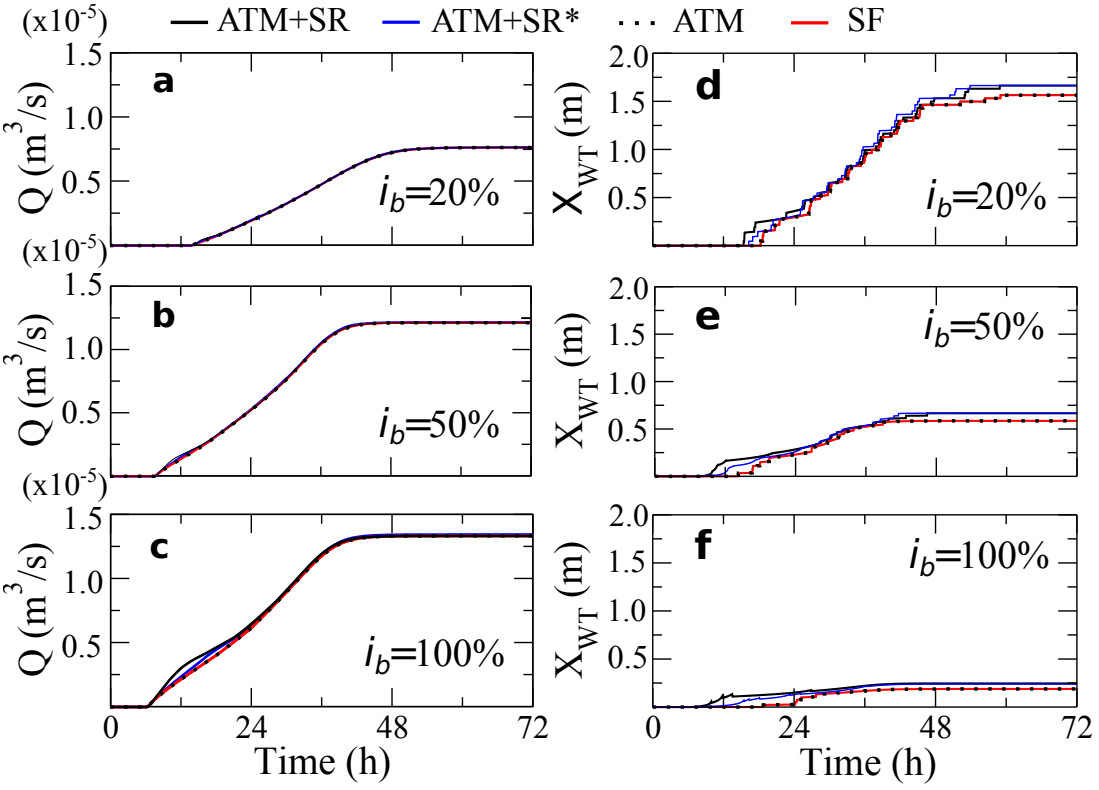

Figure 3.20: *Results of the seepage face versus atmospheric conditions simulations with a homogeneous aquifer of hydraulic conductivity* 1×10^{-4} *m/s and different downslope land surface inclinations* i_b*. Panels (a), (b), and (c): volumetric outflow* Q *over time from the land surface. Panels (d), (e), and (f): average distance of the water table,* X_{WT}*, from the outlet. The results are shown for four different boundary condition treatments of the downslope portion (see Figure 3.4) of the test hillslopes: as a seepage face boundary condition (SF, red lines); as atmospheric boundary conditions in subsurface-only mode (ATM, dotted black lines); as atmospheric conditions in coupled mode, i.e., with surface routing (ATM+SR, solid black lines); and as atmospheric conditions in coupled mode with high kinematic celerity, i.e., with very fast routing (ATM+SR*, blue lines).*

the hillslopes shown in Figure 3.4 and parameter values given in Table 3.1, Figure 3.20 presents the volumetric flow Q out of the downslope portion of the land surface and the average distance of the water table X_{WT} from the outlet. The four curves in each graph represent the different boundary condition treatments of the downslope portion (see Figure 3.4) of the test hillslopes: as seepage face boundary conditions (SF); as atmospheric boundary conditions with the CATHY model in subsurface-only mode (ATM); as atmospheric conditions with CATHY in coupled mode, i.e., with surface routing (ATM+SR); and as atmospheric conditions in coupled mode with high kinematic celerity, i.e., with very fast routing (ATM+SR*). In the ATM case there is no surface routing and thus any exfiltrating water is immediately removed as outflow. The ATM curves in Figure 3.20 coincide exactly with the SF curves for all three hillslopes and in both outflow and water table dynamics. The algorithms that handle boundary condition switching between Dirichlet and Neumann status that are used for land surface atmospheric forcing and for seepage faces are thus entirely consistent. When CATHY is run in coupled mode, the atmospheric boundary condition switching algorithm is extended to accommodate ponding [*Camporese et al.*, 2010], and the feedback between overland routing and boundary condition updating allows for re-infiltration and other complex surface/subsurface interactions. The ATM+SR results in Figure 3.20 are therefore different from the SF and ATM curves, although the responses are nevertheless quite similar. When the kinematic celerity parameter in CATHY is set to a very high value, the fast routing triggered by this condition approaches the instantaneous removal of exfiltrating water that occurs in the ATM case. The ATM+SR* results in Figure 3.20 are thus closer to the SF and ATM results than the ATM+SR case was. This final series of tests has shown the algorithmic consistency between the handling of seepage face and atmospheric boundary conditions in a hydrological model. Atmospheric conditions are generally more complex however than seepage face conditions, in particular for integrated groundwater/surface water models where rainfall-infiltration-runoff partitioning is not controlled solely by subsurface flow. Even in subsurface-only mode, atmospheric boundary condition switching in a model such as CATHY also handles evaporation processes, which are usually not relevant in classic seepage flow analyses.

3.5 Conclusions

We have presented a modeling study of the seepage face boundary condition. The analysis has been performed with the numerical model CATHY, which couples a finite element solver for the 3D Richards equation for subsurface flow with a finite difference solver for the diffusion wave approximation of the Saint-Venant equation for overland and channel routing. A generalization of the classic algorithm for handling seepage faces was proposed that extends easily to multiple seepage faces such as arise under conditions of heterogeneity. Four specific aspects of the seepage face boundary condition were examined: 1) the approximation errors that arise when using a simpler, static treatment of a seepage face instead of the classic dynamic approach; 2) the behavior of seepage faces under heterogeneity; 3) the interactions between a seepage face and a catchment outlet in integrated surface/subsurface modeling; and 4) the similarities and differences between seepage face and atmospheric boundary conditions in subsurface and coupled hydrological models.

In the results we first confirmed that the generalized algorithm behaves just as the classic algorithm for homogeneous aquifers and that it handles any degree of heterogeneity unambiguously. The static (Dirichlet) condition was shown to not always be an adequate stand-in to model the dynamic seepage face boundary, and that the error committed in using static conditions increases with rainfall rate and slope angle. In the context of groundwater/surface water modeling we then showed how seepage face and outlet boundary conditions can coexist, and we examined how they interact. In particular, rainfall partitioning between surface and subsurface flow is strongly affected by the rainfall rate and the slope angle, the first enhancing water exfiltration at the land surface and convergent streamlines towards the outlet boundary and the second intensifying outflow from the base of the aquifer. In the final set of tests, it was seen that seepage faces forming on the land surface are not controlled solely by subsurface flow since ponding, overland routing, and re-infiltration also impact saturation patterns and dynamics at the land surface. An algorithm based on automatic switching of atmospheric boundary conditions between Dirichlet and Neumann is used in CATHY to properly resolve these surface/subsurface interactions in integrated modeling, but it was shown that in the case where the model is run in subsurface-only mode, the seepage face and atmospheric boundary condition algorithms are equivalent.

In a more general sense, the sequence of test cases examined in this work illustrates the complexity of flow phenomena at the atmosphere/land surface/subsurface interface. The attempt to develop generalized algorithms for the handling of boundary conditions at this interface and to show a degree of consistency between historically very different treatments applied to these conditions is important in the context of integrated hydrological modeling. Even with valid boundary condition algorithms, however, many challenges remain in accurately resolving surface/subsurface interactions. An example that involves the coexistence of catchment outlet and seepage face boundary conditions is reported in *Sulis et al.* [2011], where neglecting to represent the latter due to computational constraints (the fine grid needed to discretize stream channel geometries, including riverbanks) inevitably leads to a wet bias from overly shallow water tables that develop in response to the outlet at the land surface.

Chapter 4

Multiresponse modeling of variably saturated flow and isotope tracer transport for a hillslope experiment at the Landscape Evolution Observatory

4.1 Abstract

This paper explores the challenges of model parameterization and process representation when simulating multiple hydrologic responses from a highly controlled unsaturated flow and transport experiment with a physically-based model. The experiment, conducted at the Landscape Evolution Observatory (LEO), involved alternate injections of water and deuterium-enriched water into an initially very dry hillslope. The multivariate observations included point measures of water content and tracer concentration in the soil, total storage within the hillslope, and integrated fluxes of water and tracer through the seepage face. The simulations were performed with a three-dimensional finite element model that solves the Richards and advection-dispersion equations. Integrated flow, integrated transport, distributed flow, and distributed transport responses were successively analyzed, with parameterization choices at each step supported by standard model performance metrics. In the first steps of our analysis, where seepage face flow, water storage, and average concentration at the seepage face were the target responses, an adequate match between measured and simulated variables was obtained using a simple parameterization consistent with that from a prior flow-only experiment at LEO. When passing to the distributed responses, it was necessary to introduce complexity to additional soil hydraulic parameters to obtain an adequate match for the point-scale flow response. This

also improved the match against point measures of tracer concentration, although model performance here was considerably poorer. This suggests that still greater complexity is needed in the model parameterization, or that there may be gaps in process representation for simulating solute transport phenomena in very dry soils.

4.2 Introduction

Simulation models of water and solute interaction and migration through complex geologic media are essential tools for addressing fundamental and practical problems, ranging from basic scientific understanding of critical zone processes [*Brooks et al.*, 2015] to improving the management of our freshwater resources [*Gorelick and Zheng*, 2015]. Physically based distributed numerical models require a careful definition of spatially variable parameters and time variable boundary conditions, and can produce information for numerous response variables at different levels of spatio-temporal aggregation. It is increasingly acknowledged that proper implementation and verification of these models, in terms of both process representation and parameter identification, requires detailed, multiresponse field or laboratory data, in contrast to traditional model evaluation based on a single, integrated response variable such as total discharge [*Paniconi and Putti*, 2015]. However, multiobjective parameter estimation for nonlinear or coupled models with a high number of degrees of freedom is very challenging [*Anderman and Hill*, 1999; *Keating et al.*, 2010], since classical techniques developed for simpler hydrological models [e.g., *Gupta et al.*, 1998; *Fenicia et al.*, 2007] are not readily extendable, in terms of robustness and efficiency, to more complex models. Traditional challenges, on both experimental and modeling sides, are associated with soil heterogeneity, variability in parameters, and variably saturated conditions [e.g., *Binley et al.*, 1989; *Woolhiser et al.*, 1996; *Neuweiler and Cirpka*, 2005]. An added source of complexity arises when passing from flow modeling to flow and transport modeling [e.g., *Ghanbarian-Alavijeh et al.*, 2012; *Russo et al.*, 2014].

While many hydrologic model assessment studies have reported good agreement between simulated and observed data when performance is measured against a single response variable, there are comparatively few studies that have made use of observation data from multiple response variables. *Brunner et al.* [2012], for instance, examined the performance of a one-dimensional (1D) unsaturated zone flow model when water

table measurements were supplemented by evapotranspiration and soil moisture observations. *Sprenger et al.* [2015] assessed the performance of three inverse modeling strategies based on the use of soil moisture and pore water isotope concentration data for a 1D unsaturated flow and transport model. *Kampf and Burges* [2007] obtained encouraging results for a 2D Richards equation flow model using integrated (subsurface outflow) and internal (piezometric water level and volumetric water content) measurements from a hillslope-scale experiment. *Kumar et al.* [2013] used multiple discharge measurements to calibrate and apply a distributed hydrologic model to 45 subcatchments of a river basin in Germany. Investigations based on hypothetical experiments are more common. *Mishra and Parker* [1989], for example, obtained smaller errors for simultaneous estimation of flow and transport parameters than for sequential estimation based on synthetically-generated observations of water content, pressure head, and concentration.

In this study we perform a modeling analysis of the experimental data collected from an intensively-measured hillslope at the Landscape Evolution Observatory (LEO) of the Biosphere 2 facility [*Hopp et al.*, 2009]. The simulations were conducted with the CATHY (CATchment HYdrology) model [*Camporese et al.*, 2010; *Weill et al.*, 2011], a physics-based numerical code that solves the 3D Richards and advection-dispersion equations and includes coupling with surface routing equations. The availability of extensive observational datasets from detailed multidisciplinary experiments (recent examples in addition to LEO include the TERENO network of experimental catchments [*Zacharias et al.*, 2011] and the Chicken Creek artificial catchment [*Hofer et al.*, 2012]) can contribute vitally to testing and improving the current generation of integrated (surface-subsurface) hydrological models [*Sebben et al.*, 2013; *Maxwell et al.*, 2014].

Two experiments have been conducted to date at LEO, a rainfall and drainage test in February 2013 [*Gevaert et al.*, 2014; *Niu et al.*, 2014b], which featured both subsurface and overland flow, and an isotope tracer test in April 2013 [*Pangle et al.*, 2015], run under drier soil conditions and with reduced rainfall rates to avoid occurrence of surface runoff. Both of these experiments were performed on the first of the three hillslopes at LEO to be commissioned, hereafter referred to as LEO-1.

Using both integrated (load cell and seepage face) and distributed (point-scale soil moisture and concentration) data collected during the tracer experiment, the objective of this study is to explore the challenges of multiresponse performance assessment for a

3D variably saturated flow and solute transport model. In a first step we consider only integrated flow responses, and the CATHY model is initially parameterized according to analyses of the February 2013 experiment. As integrated transport and point-scale flow and transport observations are progressively introduced in the analysis, the impact of different configurations (spatially uniform versus spatially variable parameters, treatment of initial and boundary conditions, etc) on the model's ability to capture the expanding and increasingly detailed response variables is examined. The boundary condition configurations, for instance, include a sink-based treatment of isotope fractionation to allow only a portion of the tracer to evaporate with the water.

4.3 Study site: Biosphere 2 Landscape Evolution Observatory

LEO is a large-scale community-oriented research infrastructure managed by the University of Arizona at the Biosphere 2, Oracle, U.S.A. [*Hopp et al.*, 2009; *Huxman et al.*, 2009; *Pangle et al.*, 2015]. It consists of three identical convergent artificial landscapes (or hillslopes) constructed with the aim of advancing our predictive understanding of the coupled physical, chemical, biological, and geological processes at Earth's surface in changing climates. For the first years of LEO operation, vegetation is not present and the research is focused on the characterization of the hydrological response of the hillslopes in terms of water transit times, generation of seepage and overland flow, internal dynamics of soil moisture, and evaporation. The three hillslopes are 30 m long and 11 m wide and of 10° average slope. The local slope varies from upslope positions to the convergence zone, with a maximum slope of 17° near the convergence zone. The landscapes are filled with 1 m of basaltic tephra ground to homogeneous loamy sand, chosen mainly for its primary elemental composition that includes critical nutrients for plant growth. The three landscapes are housed in a 2000 m^2 environmentally controlled facility. Each landscape contains a sensor and sampler network capable of resolving meter-scale lateral heterogeneity and submeter-scale vertical heterogeneity in water, energy, and carbon states and fluxes. The density of sensors and the frequency at which they can be polled allows for a monitoring intensity that is impossible to achieve in natural field settings. Additionally, each landscape has 10 load cells embedded into the structure that allow measurement of changes in total system mass and an engineered rain system that allows application of

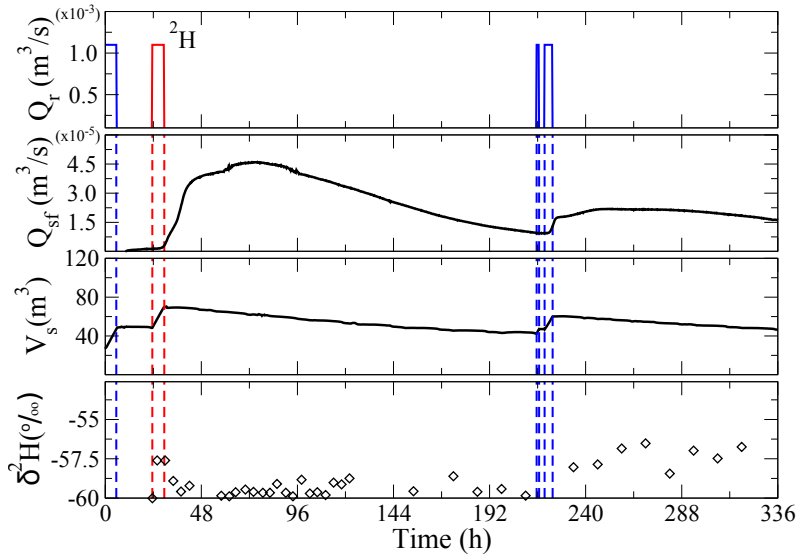

Figure 4.1: *Hydrological response to the tracer experiment at the LEO-1 hillslope. From top: measured rain input pulses Q_r (the red pulse is deuterium-enriched); seepage face flow Q_{sf}; total water storage V_s; and mean δ^2H values at the seepage face. Time 0 corresponds to 9:30 am, 13 April 2013. The vertical dashed lines indicate the timing of the three pulses of rain (red when the water is deuterium-enriched and blue when it is not).*

precipitation at rates between 2 and 40 mm/h. Each landscape at LEO has 5 independent plumbing circuits, each including a different array of sprinkler heads, and therefore generating a different rain flux. Tracers can be introduced into the system via the rainfall simulator at a constant or time-varying rate. The embedded soil water solution and soil gas samplers facilitate the use of these tracers to study water and solute movement within the hillslopes at a very dense spatial scale.

4.4 Methodology

4.4.1 Isotope tracer experiment

The first tracer experiment performed at the LEO-1 hillslope began at 9:30 am on April 13, 2013. The experiment consisted of three rainfall events that were applied over 10 days (Fig. 4.1). During each event the rainfall was applied at a rate of 12 mm/h for durations respectively of 5.5 h, 6 h, and 5.25 h. Rainfall was interrupted for 2.75 h during the third event (1.25 h from the start) due to necessary equipment maintenance, then

restarted. During the second event deuterium-enriched water was introduced into the rain system. The enriched water had a hydrogen isotopic composition (expressed using the delta-notation as $\delta^2 H$) of approximately 0‰, which corresponds to an enrichment of approximately 60‰ compared to typical (non-enriched) rainfall source water.

At the time of this experiment we consistently used one plumbing circuit because the spatial distribution of rainfall produced by this circuit had been well characterized by in situ testing. This allowed us to examine the possible influence of spatially heterogeneous rain patterns on flow and transport. The purpose of the first rain application was to increase the average moisture content of the landscape, which had received no rain for more than 40 days prior. The second rainfall application was used to introduce the deuterium tracer. No additional rain was applied for multiple days so that the tracer transport within, and out of the landscape, would be affected by soil moisture redistribution and evaporation. The third and final rainfall application was applied with the intention of forcing additional tracer mass beyond the seepage face boundary, to reveal additional detail in the measured breakthrough curve. In retrospect, and following laboratory analysis that spanned several weeks, we only observed the initiation of the tracer breakthrough curve at the seepage face.

The initial conditions of the system were very dry. The estimated total initial volume of water was about 26 m^3 (the total water storage capacity of the hillslope is approximately 130 m^3). All the rain water applied infiltrated into the soil. Seepage face outflow at the downslope vertical plane started 5 h after the beginning of the experiment. Two outflow peaks were observed: the first one after the second pulse of rain, with a peak of 4.5×10^{-5} m^3/s, and the second one after the final pulse, with a peak of 2.1×10^{-5} m^3/s. Temporal changes in total soil water storage were monitored via the load cell measurements, flow from the seepage face boundary was measured with electronic flow meters and tipping bucket gauges, and matric potential and water content were measured at 496 locations with, respectively, MPS-2 and 5TM Decagon sensors installed at depths 5 cm, 20 cm, 50 cm, and 85 cm from the landscape surface. Cumulative fluxes and instantaneous state variables were recorded at 15-min intervals. The estimated evaporation rate, derived from the seepage face measurements and load cell data and calculated as the difference between the change in water volume and the cumulative volume flowing out from the seepage face over the selected time interval, was, on average, 1.9×10^{-5} m^3/s (5.0 mm/d)

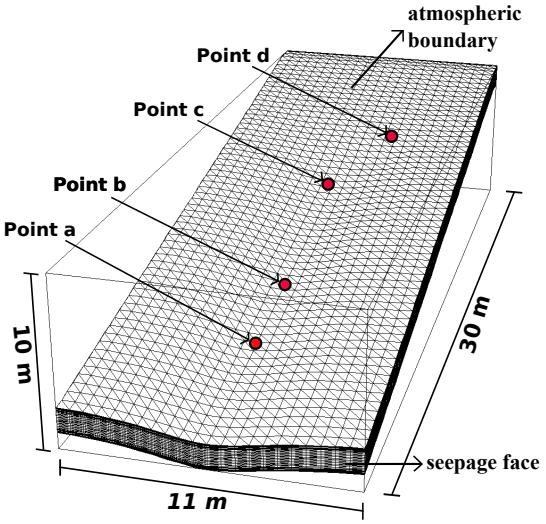

Figure 4.2: *3D numerical grid for the LEO landscape. Points a, b, c, and d are the locations where samples were extracted during the experiment for subsequent laboratory analysis.*

between rain pulses and 1.5×10^{-5} m^3/s (3.9 mm/d) after the third rain pulse.

The movement of the deuterium-enriched water within and out of the landscape was monitored through manual sampling and subsequent laboratory analysis. Prenart quartz water sampling devices were used to extract soil water samples periodically throughout the experiment. Data reported in this manuscript include samples collected at 5, 20, 50, and 85 cm depth from surface at the four locations shown in Fig. 4.2. Flow from the seepage face boundary was collected with a custom autosampler (sampling cylinders of 5 cm length and 3 cm circumference). The deuterium concentration within all water samples was measured via laser spectroscopy (LGR LWIA Model DLT-100) at the University of Arizona. Analytical precision was better than 0.5‰ for δ^2H. All isotopic data are expressed relative to the international reference VSMOW or VSMOW-SLAP scale. The seepage face isotopic data indicate that the residual soil water in the landscape prior to the experiment had become enriched in deuterium (compared to the rainfall water) during evaporation. In fact, during evaporation, hydrogen preferentially goes into the vapor phase compared to deuterium, so that the liquid phase remaining in the soil easily becomes deuterium-enriched. Thus, the δ^2H values in the early seepage face flow may reflect some mixing of the new rain water with the evaporatively-enriched water. This slight enrichment disappears in the seepage flow at later times because of the dilution by

the newly infiltrating water.

4.4.2 Hydrological model

The CATHY (CATchment HYdrology) model [*Camporese et al.*, 2010] used to simulate the isotope tracer experiment has been previously implemented for LEO to study coupled surface and subsurface flow [*Niu et al.*, 2014b] and sensor performance [*Pasetto et al.*, 2015]. The description here will thus be limited to aspects pertaining particularly to the implementation for LEO of the solute transport component of the model. The numerical solver for the advection-dispersion transport equation is described in detail in *Putti and Paniconi* [1995], and, like the flow solver, is based on a three-dimensional finite element discretization in space and a weighted finite difference discretization in time. The velocity field and nodal saturation values computed by the flow solver are passed as input at given time steps to the transport solver. The governing equations for the flow and transport solvers are:

$$S_w S_s \frac{\partial \psi}{\partial t} + n \frac{\partial S_w}{\partial t} = \nabla \cdot [K_r(\psi) K_s (\nabla \psi + \eta_z)] + q \tag{4.1}$$

$$\frac{\partial (n S_w c)}{\partial t} = \nabla \cdot (D \nabla c) - \nabla \cdot (vc) + f_c \tag{4.2}$$

where S_w=θ/θ_s is the water saturation $[-]$, θ is the volumetric moisture content $[-]$, θ_s is the saturated moisture content $[-]$ (generally equal to the porosity n $[-]$), S_s is the aquifer specific storage coefficient $[1/L]$, ψ is the pressure head $[L]$, t is the time $[T]$, ∇ is the gradient operator $[1/L]$, $K_r(\psi)$ is the relative hydraulic conductivity function $[-]$, K_s is the hydraulic conductivity tensor $[L/T]$ (considered to be diagonal, with k_s the saturated hydraulic conductivity parameter for the isotropic case and k_v and k_h, respectively, the vertical and horizontal hydraulic conductivity parameters for the anisotropic case), η_z=$(0,0,1)^T$, z is the vertical coordinate directed upward $[L]$, q is a source (when positive) or sink (when negative) term $[1/T]$, c is the solute concentration $[M/L^3]$, D is the dispersion tensor $[L^2/T]$, $v = (v_1, v_2, v_3)^T$ is the Darcy velocity vector $[L/T]$, and f_c is a correction term $[M/TL^3]$ used in the treatment of the surface boundary condition for the transport equation during evaporation. The velocity vector is obtained from the flow equation as $v = -K_r K_s (\nabla \psi + \eta_z)$ while the dispersion tensor can be expressed as:

$$D_{ij} = n S_w \tilde{D}_{ij} = \alpha_t |v| \delta_{ij} + (\alpha_l - \alpha_t) \frac{v_i v_j}{|v|} + n S_w D_o \tau \delta_{ij} \quad i,j = 1,2,3 \tag{4.3}$$

where $|v| = \sqrt{v_1^2 + v_2^2 + v_3^2}$, α_l is the longitudinal dispersivity $[L]$, α_t is the transverse dispersivity $[L]$, δ_{ij} is the Kronecker delta $[-]$, D_o is the molecular diffusion coefficient $[L^2/T]$, and τ is the tortuosity (we assume τ=1) $[-]$. The evaluation of integrals arising in finite element discretization of the dispersion fluxes is performed using a rotated reference system spanned by the unit vectors (x_1, x_2, x_3) that are aligned with the principal directions of anisotropy of D, whereby $x_1 = v/|v|$. Within this reference system, D becomes diagonal, with the three components defined as:

$$D_{11} = \alpha_l |v| + nS_w D_o \tau \tag{4.4}$$

$$D_{22} = D_{33} = \alpha_t |v| + nS_w D_o \tau \tag{4.5}$$

The soil moisture–pressure head and relative conductivity–pressure head dependencies are described by the *van Genuchten* [1980] relationship:

$$S_e = \left[1 + \left(\frac{|\psi|}{|\psi_{sat}|}\right)^{n_{VG}}\right]^{-m} \tag{4.6}$$

$$K_r(\psi) = S_e^{0.5}\left[1 - (1 - S_e^{\frac{1}{m}})^m\right]^2 \tag{4.7}$$

where $S_e = (S_w - S_{wr})/(1 - S_{wr})$ is the effective saturation $[-]$, S_{wr} is the residual water saturation $[-]$, $m = (1 - 1/n_{VG})$, n_{VG} is a fitting parameter ranging between 1.25 and 6 $[-]$, and ψ_{sat} is related to the air entry suction $[L]$.

The transport equation (4.2) is solved in its conservative form, i.e., without applying the chain rule to the advective and storage terms. Using Euler time stepping, the resulting discretized system is:

$$([A + B]^{k+1} + \frac{1}{\Delta t_k} M^{k+1})\hat{c}^{k+1} = \frac{1}{\Delta t_k} M^k \hat{c}^k - b^{t,k+1} \tag{4.8}$$

where k is the time counter, $\hat{c}$ is the vector of the numerical approximation of c at each node of the grid, and the coefficients of the, respectively, dispersion, advection, and mass matrices are:

$$a_{ij} = \int_\Omega D \nabla \phi_i \nabla \phi_j d\Omega \tag{4.9}$$

$$b_{ij} = \int_\Omega \nabla (v\phi_j)\phi_i d\Omega \tag{4.10}$$

$$m_{ij} = \int_\Omega nS_w \phi_i \phi_j d\Omega \tag{4.11}$$

where $i, j = 1, .., N$ with N the number of nodes, Ω is the discretized domain, and ϕ are the basis functions of the Galerkin finite element scheme. The boundary condition vector for the discretized transport equation is:

$$b_i^t = \int_{\Gamma^t} (-D\nabla c) \cdot \nu \phi_i d\Gamma^t = \int_{\Gamma^t} q_n^t \phi_i d\Gamma^t \tag{4.12}$$

where Γ^t is the boundary of the domain Ω, q_n^t $[M/(L^2T)]$ is the Neumann (dispersive) flux, and ν is the outward normal vector to the boundary. Cauchy, or mixed, boundary conditions can be easily implemented as variations of Eq. (4.12), involving an additional term in the system matrix implementing the advective component of the Cauchy condition.

4.4.3 Model setup for the LEO tracer experiment

We discretized the 30 m x 11 m x 1 m LEO hillslope into 60 x 22 grid cells in the lateral direction and 30 layers in the vertical direction (Fig. 4.2). The resulting surface mesh consists of 1403 nodes and 2640 triangular elements. This horizontal discretization was chosen in order to have the nodes of the computational mesh aligned with the sensor and sampler locations, thereby allowing us to directly compare simulated and measured distributed responses. This same principle was used to guide the vertical discretization (the interface between two layers is set at the sensor and sampler heights). The surface mesh was projected vertically to form a 3D tetrahedral mesh with parallel layers of varying thickness, with the thinnest layers assigned to the surface and bottom layers. This allows the numerical model to accurately capture infiltration/evaporation processes at the surface and the formation of base flow at the bottom of the domain. From top to bottom the thickness of the 30 layers is: 0.01 m for the first five layers, 0.025 m from layer 6 to layer 9, 0.05 m for layer 10, 0.06 m from layer 11 to layer 20, 0.05 m for layer 21, 0.025 m from layer 22 to layer 25, and 0.01 m from layer 26 to layer 30.

Measurements showed that the average $\delta^2 H$ of the rain source water at LEO was -60‰. For the transport model, we used a normalized concentration defined as:

$$c = \frac{\delta^2 H_{ref} - \delta^2 H}{\delta^2 H_{ref}} \tag{4.13}$$

where $\delta^2 H_{ref}$=-60‰ and $\delta^2 H$ is the actual value. Thus the initial conditions, as well as the concentrations of the first and third pulses, were c=0, while the second pulse had an

Table 4.1: *Treatment of boundary conditions at the land surface during the rainfall and evaporation periods for the flow and transport models*

Simulation (see Table 4.3)	Rain with ^2H-enriched water (second pulse)		Rain with no ^2H-enriched water (first and third pulses)		Evaporation (between rain pulses and after the third pulse)	
	Flow (mm/h)	Transport (c^*=1)	Flow (mm/h)	Transport	Flow	Transport
a-f, g-i	q_n^f=-12	$q_c^t = v \cdot \nu c^*$	q_n^f=-12	q_c^t=0	q_n^f=5 or 3.9 mm/h	q_c^t=0
j	q_n^f=-12	$q_c^t = v \cdot \nu c^*$	q_n^f=-12	q_c^t=0	Sink q (Fig. 4.3)	Source f_c (Fig. 4.3)
k	q_n^f=-12	$q_c^t = v \cdot \nu c^*$	q_n^f=-12	q_c^t=0	Sink q (Fig. 4.3)	Source f_c, $f_c = -qc$

imposed concentration of c=1. Note that, with this transformation, the dimension of the term f_c of Eq. (4.2) becomes $1/T$.

A careful treatment of boundary conditions was essential to modeling the isotope tracer experiment, in particular at the land surface where three different cases needed to be considered. These cases are schematically summarized in Table 4.1, in relation to the simulations performed, and further noted here: 1) Rain with ^2H-enriched water, handled as a Neumann prescribed flux condition for flow ($q_n^f = -K_s K_r(\psi)(\nabla\psi + \eta_z) \cdot \nu = v \cdot \nu$) and a Cauchy prescribed advective flux condition for transport ($q_c^t = (vc - D\nabla c) \cdot \nu = v \cdot \nu c^*$); 2) Rain with no ^2H-enriched water, handled with the same Neumann condition as case 1 for flow and a zero Cauchy prescribed total flux condition for transport ($q_c^t = (vc - D\nabla c) \cdot \nu = 0$ with the concentration values at the surface nodes computed by the model); 3) Evaporation, handled with the same Neumann condition as case 1 for flow and a zero Neumann prescribed dispersive flux condition for transport ($q_n^t = -D\nabla c \cdot \nu = 0$ with the concentration values at the surface nodes computed by the model). With the zero dispersive flux condition of case 3, all the isotopic mass in solution with the evaporating water leaves the domain by advection.

In addition to this "base case" treatment of rainfall and evaporation, we also introduced some variations on the surface boundary conditions. For rainfall (cases 1 and 2 above), we tested both uniform and variable spatial distributions. For the latter, a rainfall pattern with slightly higher rates towards the center of the landscape was used, as indicated by measurements taken during testing of the engineered rain system. This pattern was generated in such a way that the mean rainfall rate and the total volume of water injected were preserved. For evaporation, since there were no measurements of soil evaporation isotopic composition at the LEO landscape, we tested two other hypotheses —

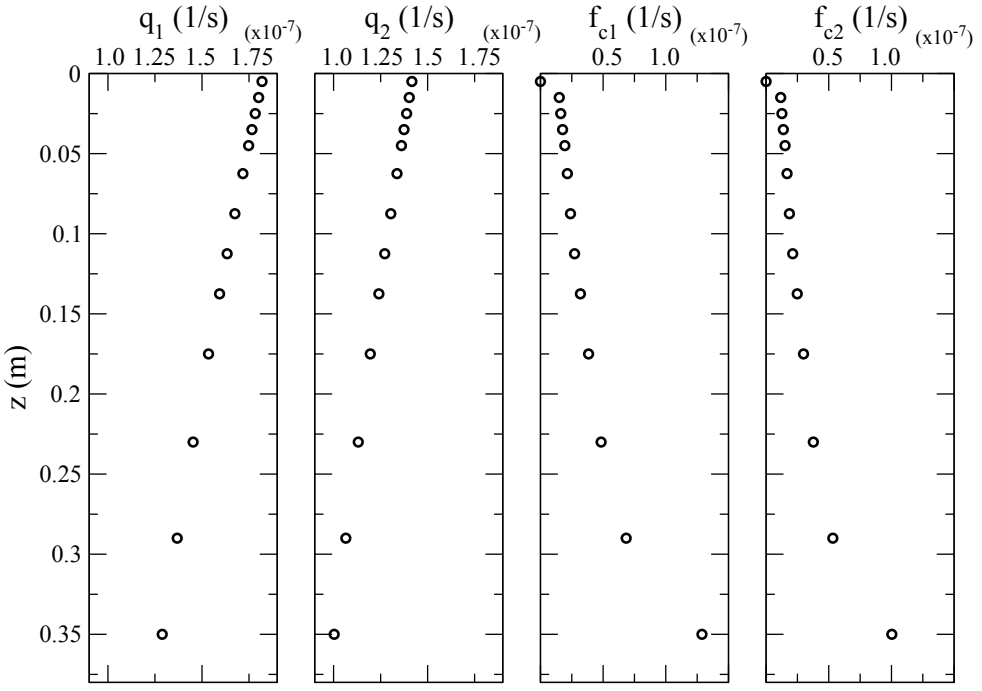

Figure 4.3: *Sink term q and correction source term f_c over depth z added to the flow and transport equations, respectively. q_1 and f_{c1} are applied between rain pulses 1, 2, and 3, while q_2 and f_{c2} are applied after rain pulse 3.*

that none or only a portion (fractionation) of the isotope tracer evaporated — in addition to the zero dispersive flux condition of case 3.

To prevent isotope tracer from leaving the system through the landscape surface, we treated the evaporation as a sink term in the flow model, distributed exponentially from the surface to a depth of 38 cm, rather than as a Neumann boundary condition. In generating the sink term, we ensured that the total volume of water evaporated was the same as in the Neumann boundary condition treatment. The sink term function q in Eq. (4.1) applied to each layer i (i=1,...,13 for a total depth of 38 cm) is:

$$q_i = \frac{F_{ev}}{\sum_{i=1}^{13}(e^{-\lambda z_i}\Delta z_i)} e^{-\lambda z_i} \tag{4.14}$$

where q_i is applied to each tetrahedron of layer i, λ $[1/L]$ is a parameter set to 1 m^{-1} in this case, z_i is the depth from surface to the center of layer i, Δz_i is the thickness of layer i, and F_{ev} $[L/T]$ is the homogeneous evaporative flux used in the Neumann boundary condition case (with rates -5.8×10^{-8} m/s between rain pulses and -4.5×10^{-8} m/s after

the third pulse). The applied sink fluxes are shown schematically in Fig. 4.3. Note that if the element reaches the residual water saturation, parameterized by its corresponding pressure head level, the evaporation process becomes soil-limited. When this occurs, the actual sink term function is automatically smaller than the imposed value. To ensure that all the tracer mass stays in the system, for the transport model we set the correction term f_c in Eq. (4.2) equal to -qc. In this way we inject back into the system the same amount of tracer mass that has exited with the sink term q.

Most land surface hydrological models still neglect fractionation, even though it can significantly influence the mass exchange at the land surface and the concentration profiles in the soil. *Barnes and Allison* [1988] examined isotope transport phenomena under both saturated and unsaturated conditions. In the latter case they experimentally observed that at steady state the maximum concentration of the heavier isotope species (e.g., ^2H) occurs a short distance below the surface and decreases rapidly beyond that depth. The resulting profile can be explained as the result of vapor diffusion and isotopic exchange dominating the zone above the drying front and the balance between capillary and diffusive liquid water transport below the drying front [*Craig and Gordon*, 1965; *Clark and Fritz*, 1997; *Horita et al.*, 2008]. Alternative conceptualizations of the fractionation process have also been recently developed [e.g., *Braud et al.*, 2009; *Haverd and Cuntz*, 2010]. In this work the fractionation process was incorporated into the CATHY model using the sink term approach described above, setting 38 cm as the soil depth at which the maximum ^2H tracer concentration occurs (thereby assuming that the soil above is dominated by water vapor diffusion due to evaporation). The correction source term f_c introduced into the transport equation is now modified such that there is no tracer mass re-injection in the first layer, and the amount re-injected progressively increases from $qc/12$ to qc between layers 2 and 13 (Fig. 4.3). The reasoning here is that the rate at which tracer evaporates increases with evaporation and water vapor diffusion close to the surface.

Besides the surface boundary, we set up a seepage face condition at the 23 x 30 nodes that constitute the downslope lateral boundary. For the transport equation the seepage face nodes have a zero Neumann (dispersive) assigned flux so that ^2H is allowed to exit the domain through advection with the outflowing water. All other LEO boundaries (the three other lateral boundaries and the base of the hillslope) were set to a zero Neumann condition for both the flow and transport equations (with a zero water flux this implies

Table 4.2: *Configurations for the 6 simulations of the integrated flow analysis.*

Simulation	Saturated hydraulic conductivity (m/s)			Initial conditions	Rainfall
	Horizontal, k_h	Vertical, k_v	Seepage face, k_{sf}		
a	1.4×10^{-4}	1.4×10^{-4}	1.4×10^{-4}	Uniform	Spatially uniform
b	6×10^{-4}	1.4×10^{-4}	1.4×10^{-4}	Uniform	Spatially uniform
c	6×10^{-4}	1.4×10^{-4}	2.2×10^{-5}	Uniform	Spatially uniform
d	6×10^{-4}	1.4×10^{-4}	2.2×10^{-5}	Steady state	Spatially uniform
e	6×10^{-4}	1.4×10^{-4}	2.2×10^{-5}	Interpolated soil moisture measurements	Spatially uniform
f	6×10^{-4}	1.4×10^{-4}	2.2×10^{-5}	Interpolated soil moisture measurements	Spatially variable

that the advective flux for the transport equation is also zero).

The time stepping for the flow model is adaptive (based on convergence of the iterative scheme used to linearize Richards' equation (4.1)) and we set the time step range between 10^{-4} s and 90 s. The results in terms of velocity and saturation values were saved every 90 s or 900 s, respectively, during and between the rain events. These were linearly interpolated in time and read as input by the transport model, which was run with a fixed time step of 90 s for the entire simulation.

4.4.4 Simulations performed

The model simulations were used to interpret the integrated and point-scale flow and transport responses of the LEO hillslope. The guiding idea was to assess the need to increase the complexity of the model in progressing from first trying to reproduce the integrated flow response, then the integrated transport response, and finally the point-scale flow and transport responses. With the requirement that each new parameterization still had to satisfy the observation dataset from the previous level, the space of admissible solutions was progressively reduced. Initially the soil was assumed to be homogeneous and isotropic. The values of the van Genuchten parameters (n_{VG}=2.26, ψ_{sat}=-0.6 m, and θ_r=0.002), the porosity (n=0.39), the saturated hydraulic conductivity (k_s=1.4×10^{-4} m/s), and the specific storage (S_s=5×10^{-4} m^{-1}) were obtained from laboratory analyses and simulations of prior LEO experiments [*Niu et al.*, 2014b; *Pasetto et al.*, 2015]. From this base set of parameter values for the first simulations, anisotropy and other variations were progressively introduced in the model.

In the first step of this procedure (integrated flow response), we examined the influence

of spatial variability and anisotropy in saturated hydraulic conductivity (different k_s at the seepage face and over the rest of the hillslope, on the basis of a clogging hypothesis from accumulation of fine particles [*Niu et al.*, 2014b]; higher k_h than k_v, on the basis of a hypothesis of slight vertical compaction leading to enhanced flow in the horizontal direction), rainfall (spatially uniform; spatially variable), and initial conditions (uniform; generated from a steady state simulation under drainage and evaporation; matching the soil moisture distribution at each sensor location). Six simulations were run in the first step. The configurations for each run are summarized in Table 4.2. For the initial conditions, in all three configurations (uniform for runs a through c, steady state for run d, and matching sensors for runs e and f), the same total initial water storage (26 m^3 as reported earlier) was used. For the atmospheric forcing, the spatially uniform rainfall rate (runs a through e) was the mean measured rate reported earlier (12 mm/h), while the spatially variable case (run f) was handled as described earlier. The evaporation rate, on the other hand, was kept spatially uniform for all 6 simulations and equal to the mean rate of 5.0 mm/d between the three pulses and 3.9 mm/d after the third pulse.

In the second step (integrated transport response), the effects of the dispersivity coefficients α_l and α_t and of isotope evaporation mechanisms on the amount of tracer at the seepage face outlet were explored. In the third step (flow point-scale data), the analysis focused on the soil moisture profiles obtained by averaging the observations and model results at specific depths (5, 20, 50, and 85 cm), and spatially variable (by layer) soil hydraulic properties (n_{VG}) were introduced. Finally, for the point-scale transport we compared the results obtained from some of the different parameterizations used in the previous steps.

The simulations performed are summarized in Table 4.3. Model performance was assessed against available observations using the coefficient of efficiency (CE) on seepage face flow Q_{sf} for the integrated flow response and the root mean squared error ($RMSE$) on concentration c at the seepage face for the integrated transport response and on averaged θ profiles for the flow point-scale response. The CE and $RMSE$ metrics, also reported in Table 4.3, are calculated as in *Dawson et al.* [2007]:

$$CE = 1 - \frac{\sum_{i=1}^{n_o}(Q_i - \hat{Q}_i)^2}{\sum_{i=1}^{n_o}(Q_i - \bar{Q})^2} \tag{4.15}$$

$$RMSE = \sqrt{\frac{\sum_{i=1}^{n_o}(Q_i - \hat{Q}_i)^2}{n}} \tag{4.16}$$

where n_o is the total number of observed data available at the different times, Q_i and $\hat{Q}_i$ are the observed and modeled values, respectively, and $\bar{Q}$ is the observed average value.

Table 4.3: *Simulation descriptions, parameter configurations, and performance metrics (coefficient of efficiency CE and root mean squared error $RMSE$) for the integrated flow, integrated transport, and point-scale analysis steps.*

Integrated flow analysis			**Simulations**					CE for Q_{sf}
Effect on seepage face flow Q_{sf}	Effect on total water storage V_s	a	base case [*Niu et al.*, 2014b]					-0.62
		b	anisotropy					0.64
		c	heterogeneity					0.79
		d	initial conditions					0.28
		e	initial conditions					0.82
		f	rainfall distribution					0.85
Integrated transport analysis			α_l			evaporation		$RMSE$
Effect on concentration c at the seepage face (flow configuration from simulation f)		g	0.1			all solute		0.12
		h	0.01			all solute		0.037
		i	0.001			all solute		0.026
		j	0.001			fractionation		0.03
		k	0.001			no solute		0.045
Point-scale analysis								$RMSE$ for averaged θ (at 5, 20, 50, 85 cm depth)
Effect on averaged θ profiles	Effect on point-scale θ profiles	Effect on c point-scale profiles (transport configuration from simulation i)	f	depth (cm)	5	20	50	85	10.36, 1.17, 1.73, 3.78
				n_{VG} (homogeneous)	2.26				
			l	depth (cm)	5	20	50	85	5.61, 1.43, 0.95, 1.72
				n_{VG} (heterogeneous)	1.8	2.26	2.0	1.9	

4.5 Results

4.5.1 Integrated flow response

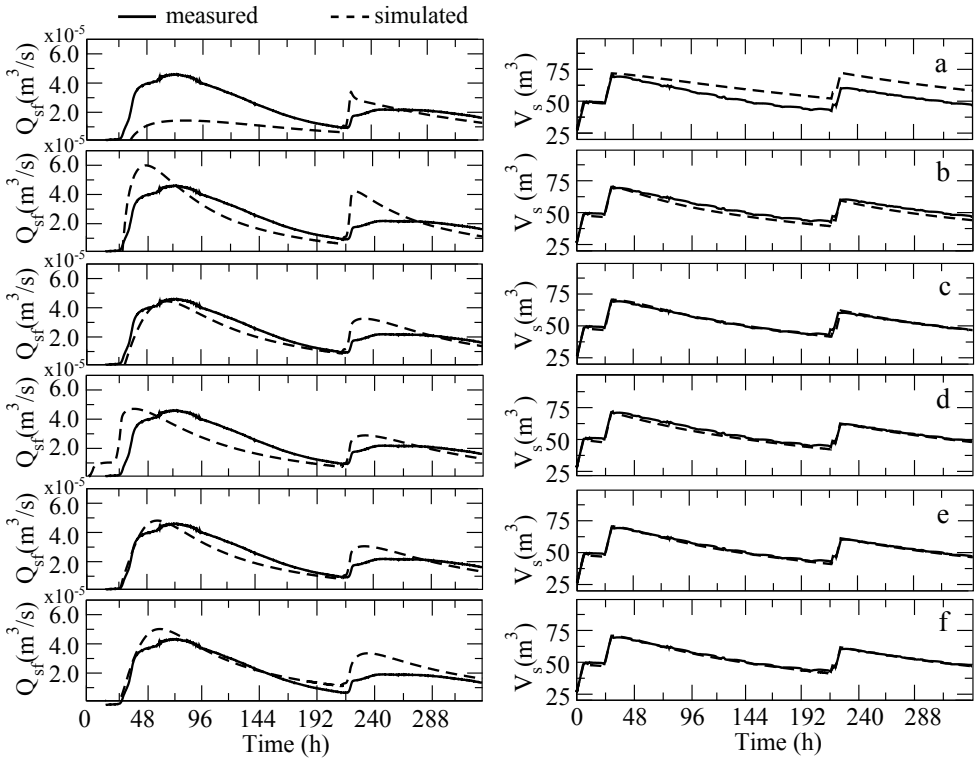

Figure 4.4: *Results for the 6 simulations of the integrated flow response analysis (see Table 4.2). For each case the seepage face flow Q_{sf} (left) and total water storage V_s (right) are reported.*

In the first set of simulations we attempt to reproduce two integrated flow responses of the LEO hillslope, the measured seepage face flow and the measured total water storage. The results of the 6 simulations are presented in Fig. 4.4. The water balance partitioning between seepage face flow and internal storage was found to be strongly affected by the introduction of anisotropy and variability in the hydraulic conductivity. We also found that the distribution of initial condition determines the timing of the first simulated seepage face peak and its shape. The spatial distribution of rain, on the other hand, was not found to have a significant impact on the model response. These general findings are described in more detail below.

In the first simulation (Fig. 4.4a), under the assumption of homogeneity, isotropy, uniform initial conditions, and spatially uniform rainfall and evaporation, the discrepancy between the simulated and observed response was large (a negative CE is reported in Table 4.3), with the first and second peaks of the discharge hydrograph, respectively, underestimated and overestimated by the model. In the second simulation, with the introduction of anisotropy (increasing the horizontal hydraulic conductivity k_h to 6×10^{-4} m/s), the overall model results for the seepage face flow improved notably compared to simulation a (CE passed from -0.62 to 0.64) and the match for the total water storage was improved significantly (Fig. 4.4b). Next, the introduction of low k_s at the seepage face lowered the hydrograph peaks and smoothed out its overall shape (Fig. 4.4c), moving the simulated hydrograph closer to the measured one (and increasing CE to 0.79). The effect of using distributed instead of uniform initial conditions is seen in comparing Figs. 4.4c, 4.4d, and 4.4e. Under uniform starting conditions the response was delayed in time, compared to the steady state case (generated under a drainage and evaporation run from initially wet conditions), where the response to the first rain pulse was faster. This faster response resulted in increased drainage due to longer recession periods, adversely affecting the match for the second pulse but improving the result for the third pulse. The simulation for Fig. 4.4e, with initial conditions closest to the initial state of the hillslope, resulted in a further increase in CE to 0.82. For this run, the good match for the first hydrograph peak from simulation c of Table 4.2 was recovered, whilst retaining the good match for the second peak from simulation d. The simulated total water storage dynamics was already very well captured by simulation c and was not greatly affected by the initial conditions. The initial conditions from simulation e were used for all subsequent simulations discussed in this study. In the final simulation for the integrated flow response analysis, incorporating the spatial distribution of rainfall had a nominal impact on the results (Fig. 4.4f), with a slight increase in CE to 0.85. Thus the actual distribution of atmospheric forcing, so long as it is not highly variable (which was part of the experimental design for the LEO tracer experiment), is less important than capturing the correct mean rate and total volume of these hydrologic drivers.

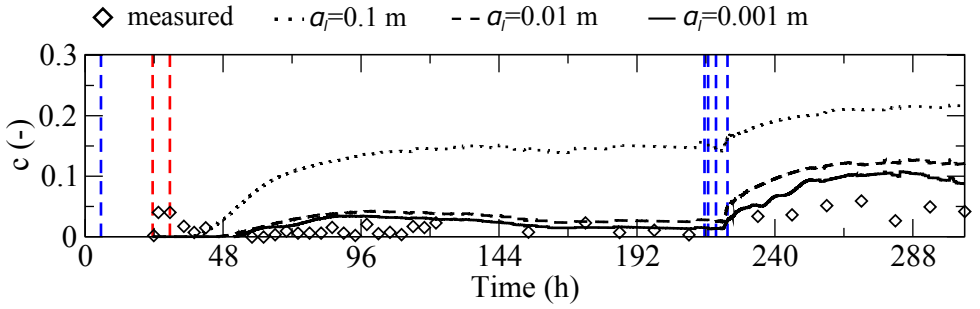

Figure 4.5: *Results for the integrated transport response analysis for different values of dispersivity (simulations g, h, and i of Table 4.3). The vertical dashed lines indicate the timing of the three pulses of rain (red when the water is ^2H-enriched and blue when it is not).*

4.5.2 Integrated transport response

The velocity field and saturation obtained from the sixth flow simulation (simulation f) of the preceding section were used as input to the transport model. Fig. 4.5 and Table 4.3 show, respectively, the results for the average tracer concentration at the seepage face and the $RMSE$ for different longitudinal dispersivity α_l values, namely 0.1 m, 0.01 m, and 0.001 m. The transverse dispersivity α_t was set one order of magnitude smaller than α_l. The three graphs and the $RMSE$ values show that the discrepancy between the measured and simulated outflow concentration decreases with α_l. The results show that the effect of the high dispersivity makes the tracer percolate down quickly to then flow out of the domain from the seepage face boundary. In fact, at the highest value, significant levels of ^2H-labeled water appeared in the outflow discharge after the second pulse, whereas in the measured data and in the model results for the smaller dispersivity values the levels were much lower. In all three cases the model reproduced the increase in tracer concentration after the last pulse, but whereas for α_l=0.1 m the values were four times higher than the observed ones, for α_l=0.01 m and α_l=0.001 m they decreased significantly. The simulation using the lowest value of dispersivity was able to reproduce reasonably well the integrated measure of tracer response for the LEO hillslope.

To assess model accuracy, we report in Fig. 4.6 the mass balance results for the α_l=0.001 m case, in terms of a balance between the cumulative mass of deuterium that entered the hillslope (with the second rainfall pulse), that exited the system (through

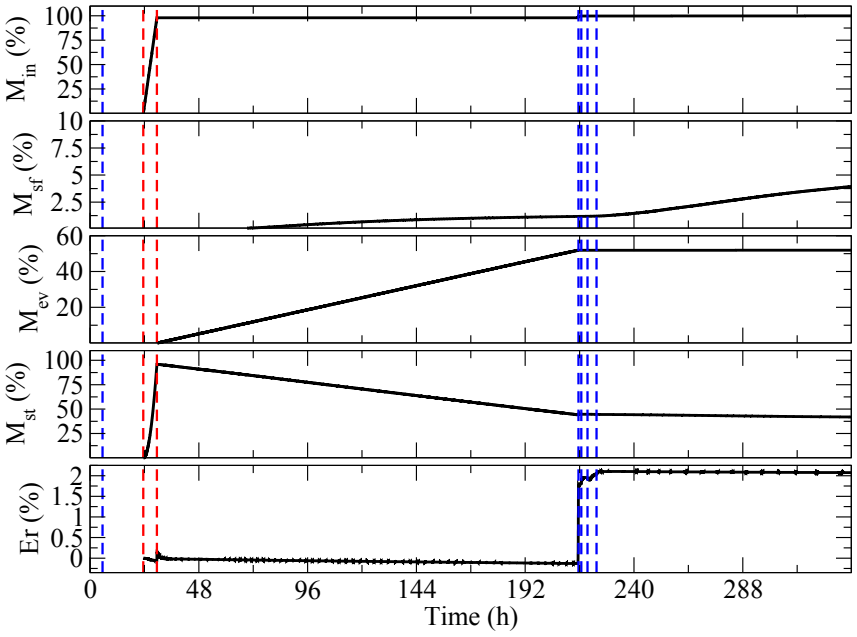

Figure 4.6: *Simulated mass balance results for α_l=0.001 m (simulation i of Table 4.3). From top to bottom: ^2H mass that enters the system, M_{in} (normalized with respect to the total mass added to the system during the simulation); that exits through the seepage face, M_{sf}; that exits through evaporation, M_{ev}; and that remains in storage, M_{st}. The bottom graph shows the cumulative mass balance error E_r=$(M_{in} - M_{sf} - M_{ev} - M_{st})$. The vertical dashed lines indicate the timing of the three pulses of rain (red when the water is ^2H-enriched and blue when it is not).*

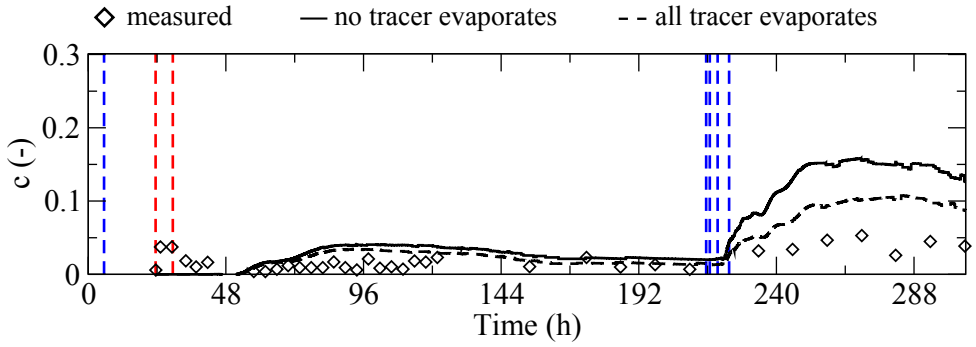

Figure 4.7: *Measured and modeled average tracer concentration at the seepage face for the cases in which no tracer and all tracer leaves the system with evaporation (simulations i and k of Table 4.3). Both simulations are run for α_l=0.001 m and α_t=0.0001 m. The vertical dashed lines indicate the timing of the three pulses of rain (red when the water is ^2H-enriched and blue when it is not).*

seepage face outflow and evaporation), and that remained in storage. The results show that for α_l=0.001 m and α_t=0.0001 m, at the end of the simulation (after 14 d), 52% of the mass of ^2H injected has been lost through evaporation, about 4% has seeped out, and the rest remained in storage, minus a cumulative mass balance error of about 2% with respect to the total mass injected. The sudden mass balance error jump which occurs at the beginning of the third pulse of rain is most probably due to discontinuities in the time derivative of concentration and water saturation close to the surface (since the soil is very dry at this level and after the long evaporation period) as a consequence of the discontinuity in the atmospheric boundary condition. The high evaporative component computed by the model is a direct outcome of the zero dispersive flux surface boundary condition for the transport equation, through which any tracer in solution with evaporating water is advected away with the water. We examine next the impact of the sink term treatment of tracer exchange across the land surface boundary, preventing any isotope tracer from evaporating.

The results of the sink term simulation in terms of average seepage face tracer concentration and mass balance are reported, respectively, in Fig. 4.7 and 4.8. As expected, the seepage face concentration has now increased, but only slightly, compared to the previous simulation. In mass terms, the seepage component has increased from 4% to 8% by the end of the simulation. With no tracer mass now exiting via the landscape sur-

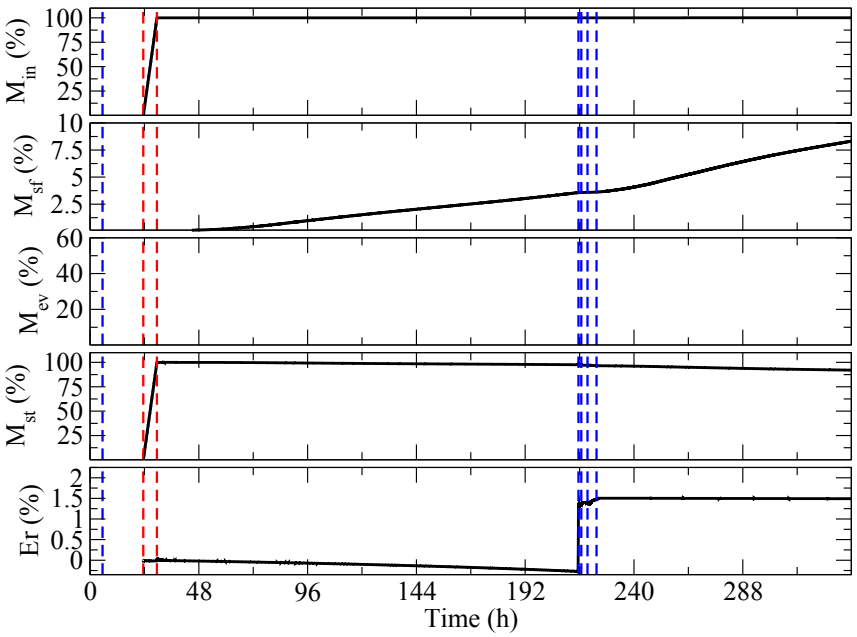

Figure 4.8: *Simulated mass balance results for α_l=0.001 m when the sink term is used to perform evaporation and the correction term f_c added to the transport equation is used to force all the isotopic mass to stay in the system (simulation k of Table 4.3). From top to bottom: ^2H mass that enters the system, M_{in} (normalized with respect to the total mass added to the system during the simulation); that exits through the seepage face, M_{sf}; that exits through evaporation, M_{ev}; and that remains in storage, M_{st}. The bottom graph shows the cumulative mass balance error E_r=($M_{in} - M_{sf} - M_{ev} - M_{st}$). The vertical dashed lines indicate the timing of the three pulses of rain (red when the water is ^2H-enriched and blue when it is not).*

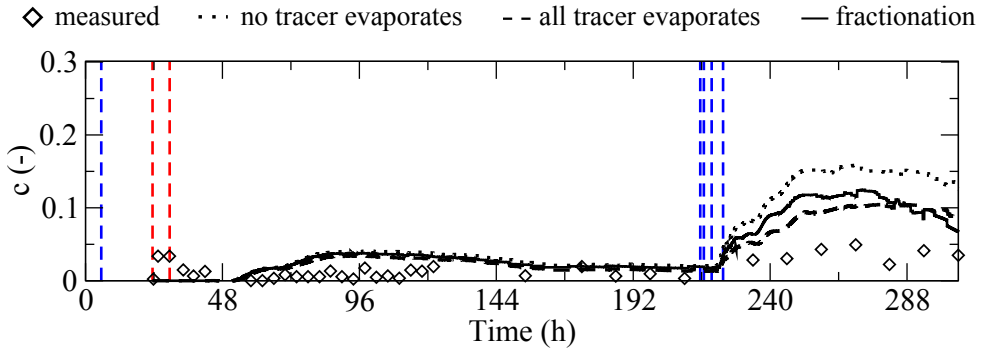

Figure 4.9: *Measured and modeled average tracer concentration at the seepage face for the cases in which no tracer, all tracer, and some tracer (fractionation) leaves the sytem with evaporation (simulations i, j, and k of Table 4.3). The three simulations are run for α_l=0.001 m and α_t=0.0001 m. The vertical dashed lines indicate the timing of the three pulses of rain (red when the water is ^2H-enriched and blue when it is not).*

face, it is found instead that much more of the mass has remained in storage (about 90% compared to about 40% when the tracer was allowed to evaporate with the water). This result strongly suggests that the tracer does not percolate far (deep) into the hillslope, perhaps as a result of the very dry conditions initially and during the whole experiment. A negative consequence of not allowing any tracer mass to evaporate, combined with low percolation, is an intense accumulation of the mass near the landscape surface, with tracer concentrations as high as 15. A compromise between allowing zero or all isotope tracer to leave the system via evaporation is to introduce isotopic fractionation processes into the model.

The results of the isotope fractionation simulation are reported in Figs. 4.9 and 4.10, respectively, for the average tracer concentration at the seepage face and the model mass balance results. The curve for the average concentration in Fig. 4.9 justly lies between the curves obtained by making all and no isotope evaporate with water. The mass balance shows that at the end of the simulation 6.5% of the total mass injected has gone out through the seepage face, this result also falling between the previous simulations where zero or all isotope tracer in solution with the evaporating water was lost via evaporation. As expected, the evaporative mass loss is now significant (38%), but not as high as obtained when evaporation was treated as a land surface Neumann boundary condition (52%). The final mass balance error (0.75%) is lower than for the two previous simulations,

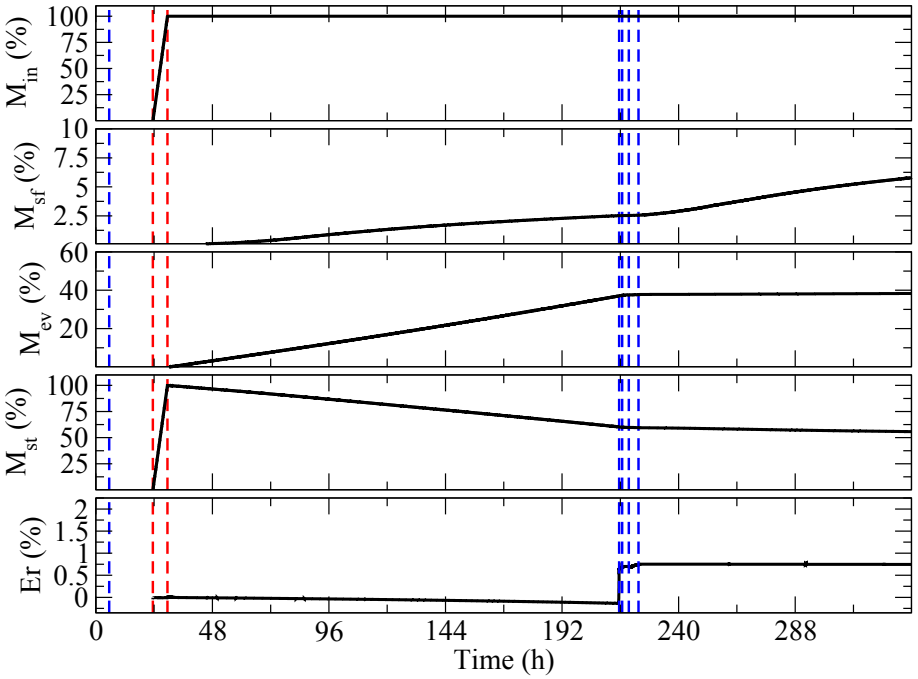

Figure 4.10: *Simulated mass balance results for α_l=0.001 m when the correction source term f_c is added to the transport equation to perform isotopic fractionation (simulation k of Table 4.3). From top to bottom: ^2H mass that enters the system, M_{in} (normalized with respect to the total mass added to the system during the simulation); that exits through the seepage face, M_{sf}; that exits through evaporation, M_{ev}; and that remains in storage, M_{st}. The bottom graph shows the cumulative mass balance error E_r=($M_{in} - M_{sf} - M_{ev} - M_{st}$). The vertical dashed lines indicate the timing of the three pulses of rain (red when the water is ^2H-enriched and blue when it is not).*

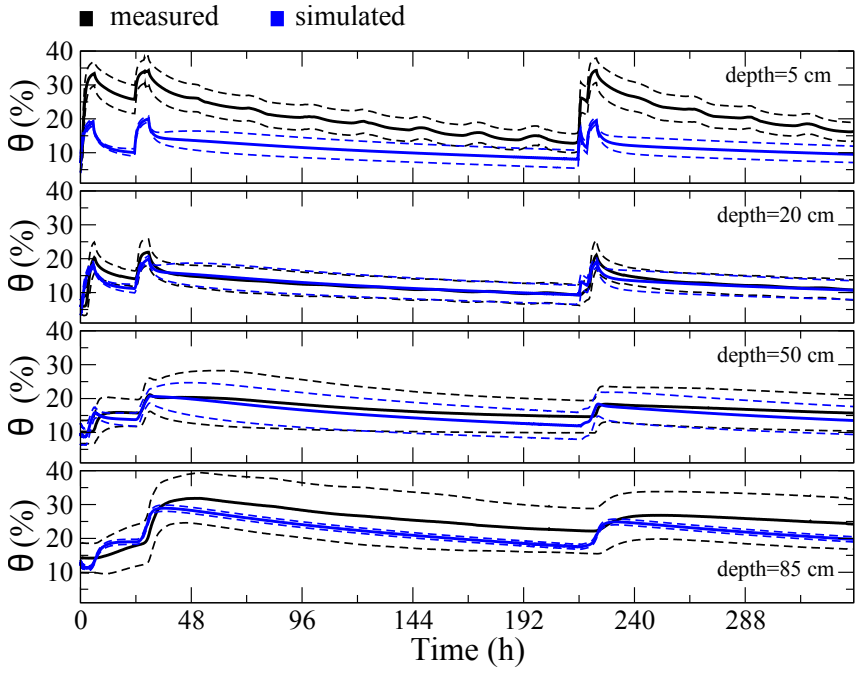

Figure 4.11: *Averaged θ profiles at 5, 20, 50, and 85 cm depth from the surface. In each graph the deviation from the mean (one standard deviation above and below) is shown as dashed lines. The results are obtained for simulation f reported in Table 4.3.*

and the accumulation of isotope mass just below the land surface that occurred in the preceding case was not observed in this simulation.

4.5.3 Distributed flow response

For the distributed flow response analysis we first examined the behavior in time of the averaged soil water content value at the 4 depths of the sensor network (5, 20, 50, and 85 cm). That is, we compared the average of all sensor measurements at a given depth to the average of all simulated nodal θ values at that depth. The graphs for the results of simulation f from Table 4.2 (the configuration that best retrieved the integrated flow response) are shown in Fig. 4.11, while the $RMSE$ values are reported in Table 4.3. The results show that at 50 cm there is a small underestimation by the model and that the model does not perform well at 5 cm and 85 cm compared to the profile at 20 cm. At 85 cm depth the observed and calculated deviation from the mean are also completely different (for the model it is almost 0).

To address this problem we increased the retention capacity of the soil by reducing,

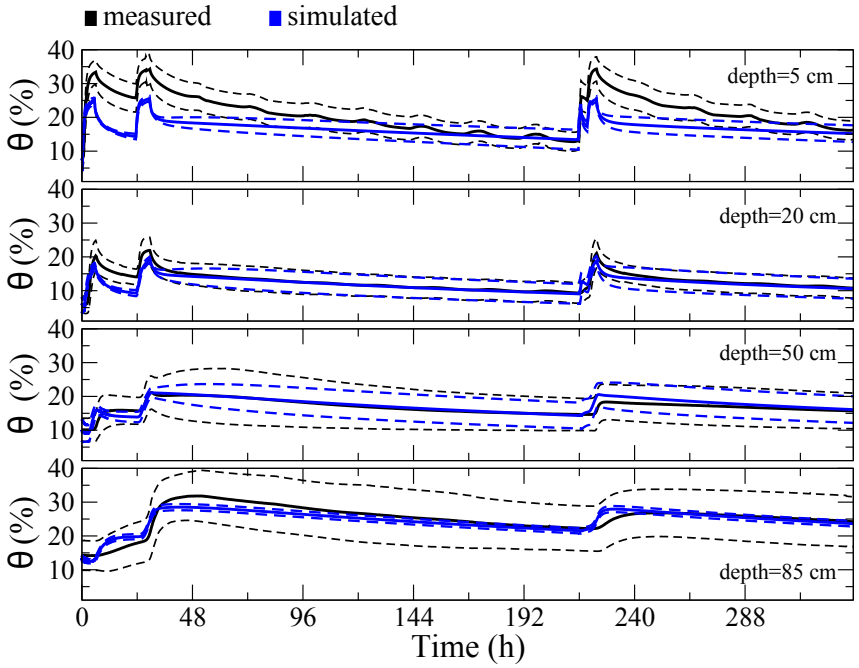

Figure 4.12: *Averaged θ profiles at 5, 20, 50, and 85 cm depth from the surface. In each graph the deviation from the mean (one standard deviation above and below) is shown as dashed lines. The results are obtained for simulation l reported in Table 4.3.*

selectively, the n_{VG} parameter of the van Genuchten hydraulic functions as reported in Table 4.3. We subdivided the soil profile into 4 strata encompassing the 4 sensor depths, and we decreased n_{VG} for the strata closest to the surface (from 0 to 10 cm, n_{VG}=1.8), from 32 to 68 cm (n_{VG}=2.0), and from 68 cm to bottom (n_{VG}=1.9). For the second stratum (from 10 cm to 32 cm) the retention parameter was left unaltered from all previous simulations (n_{VG}=2.26) since the model already captured the observed response for the sensor at 20 cm depth quite well. The highest retention capacity (lowest n_{VG} value) was set in the first stratum since the observation data show that the water content close to the landscape surface remains quite high, both during infiltration and drainage. The n_{VG} values for the 4 strata reported here are the combination, from many trials, that best retrieved the observed averaged θ profiles. The results of this simulation are shown in Fig. 4.12 and reported in Table 4.3. Compared to the results of the homogeneous n_{VG} case, the model response improves significantly for the average profile at 5, 50, and 85 cm, even if the deviations at 85 cm are still very different.

To take the distributed flow response analysis further, in Fig. 4.13 we show the water

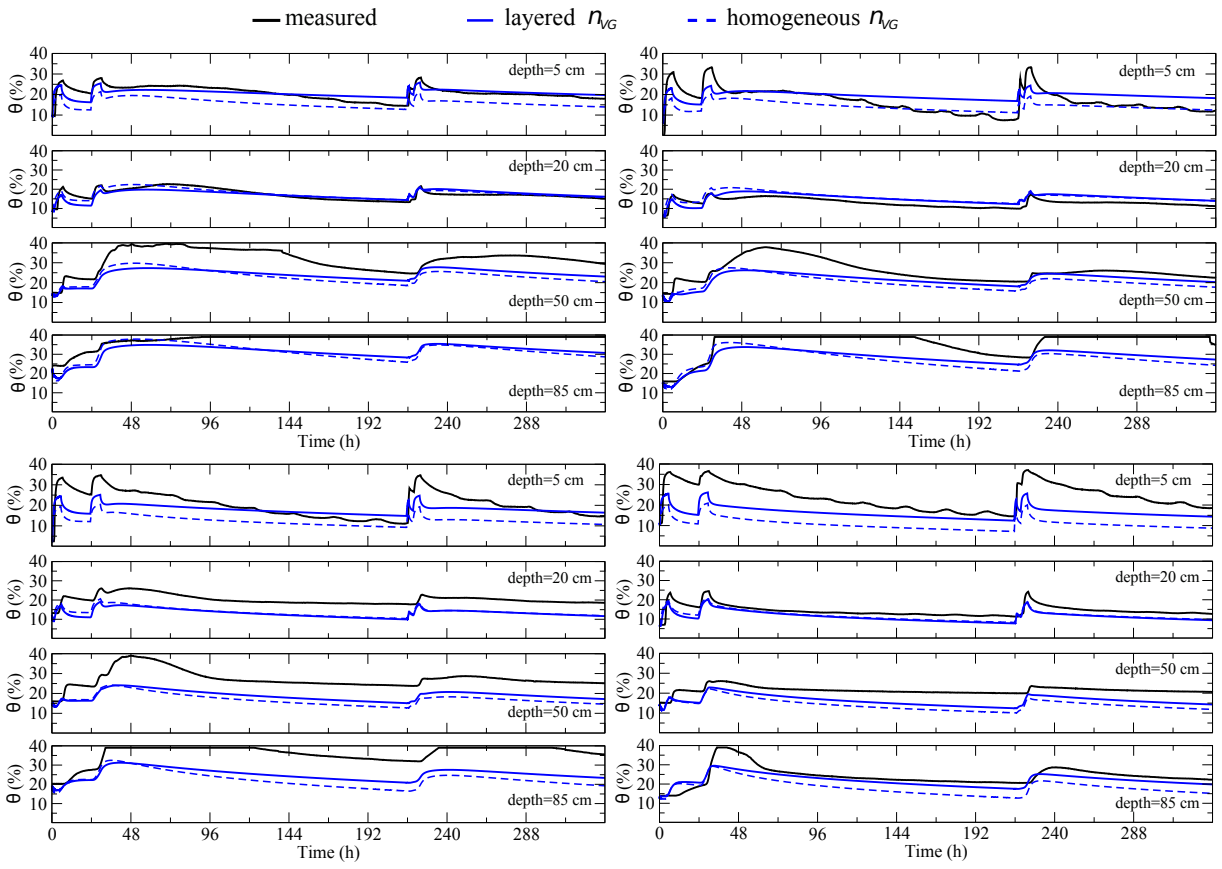

Figure 4.13: *Distributed (internal state) hydrological response for the θ profiles at 5, 20, 50, and 85 cm depth from the surface for four locations on the LEO-1 hillslope: point a (top left), point b (top right), point c (bottom left), and point d (bottom right) of Fig. 4.2. The results are obtained for simulations f and l reported in Table 4.3.*

content time series at the four specific points shown in Fig. 4.2, at 5, 20, 50, and 85 cm depth from the surface. Sensor data at each of the 4 points and for each of the 4 soil depths is compared against both the homogeneous n_{VG} case (simulation f from Table 4.2) and the layered n_{VG} case (different value for each of the four strata). Once again the more detailed parameterization (simulation l from Table 4.3, variable n_{VG}) gives better results, although for some of the soil depths (in particular at 50 cm and 85 cm) and for some of the points (in particular point c) the discrepancies between simulated and measured θ time series are quite marked. It should be remarked that we did not run, as we did for the simulation summarized in Fig. 4.12, repeated trials to find a best fit, so it may perhaps be possible to optimize the fits against both the averaged θ data and the point data (Fig. 4.13) by manipulating the soil retention capacity for the 4 strata. However, it seems more likely that in going from a distributed but nonetheless averaged response variable to a distributed, point-scale response variable, additional model parameter complexity is needed to obtain an adequate response for all individual response variables.

4.5.4 Distributed transport response

For the distributed transport response analysis we compared, as we did in Fig. 4.13 for the internal state flow response, the model results at individual points (a, b, c, d from Fig. 4.2) and individual soil depths (5, 20, 50, and 85 cm) for simulations using uniform (corresponding to configuration f from Table 4.2) and spatially variable (simulation l from Table 4.3) soil retention capacity. The results are shown in Fig. 4.14, and it can be seen that the model does not perform well at several locations within the hillslope (consistently at 20 cm depth, and at 5 cm depth for point b). Encouragingly, however, there is consistency with the previous distributed flow results, in that the variable n_{VG} run performs noticeably better than the spatially uniform case. For instance, with variable n_{VG} the results are improved at the bottom of the hillslope, at 50 cm (for points b and c the modeled response gets closer to the measurements particularly after the third flush), and slightly at 5 cm (for point a).

For the distributed transport analysis we did not examine averaged concentration profiles at each of the 4 sensor depths (as we did for soil water content in Fig. 4.12) due to insufficient data. The sampling time and laboratory analysis costs for exhaustive measurement of isotopic compositions were prohibitive, thus there are much less data

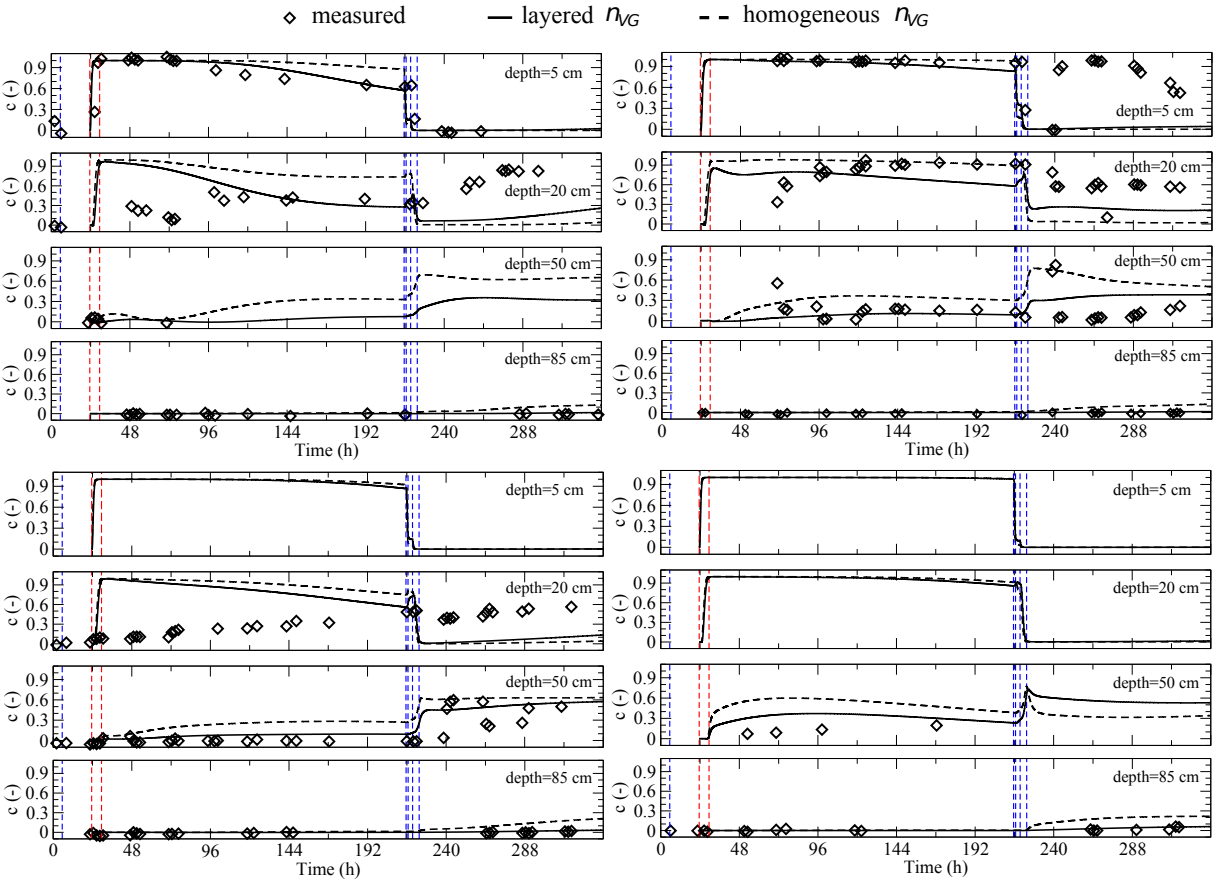

Figure 4.14: *Distributed (internal state) hydrological response for the tracer concentration breakthrough curves at 5, 20, 50, and 85 cm depth from the surface for four locations on the LEO-1 hillslope: point a (top left), point b (top right), point c (bottom left), and point d (bottom right) of Fig. 4.2. There were no tracer concentration measurements at 5 cm depth for point c and at 5 and 20 cm depth for point d. The transport model is run for α_l=0.001 m and α_t=0.0001 m. The vertical dashed lines indicate the timing of the three pulses of rain (red when the water is ^2H-enriched and blue when it is not).*

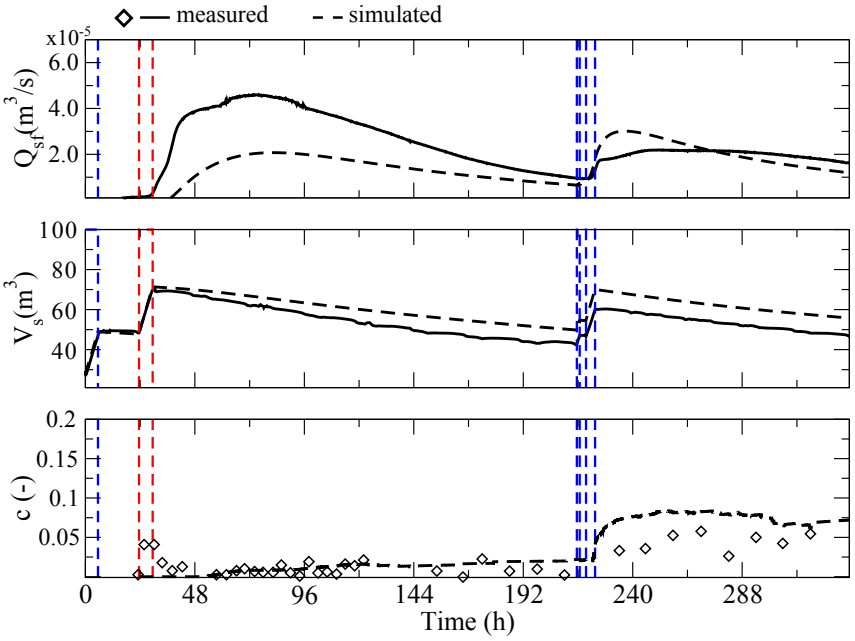

Figure 4.15: *Performance of the model against integrated flow and transport responses (seepage face flow Q_{sf}, total water storage V_s, and average tracer concentration c at the seepage face) using the additional parameterization from the distributed analyses (spatially variable soil retention capacity, simulation l of Table 4.3). The vertical dashed lines indicate the timing of the three pulses of rain (red when the water is ^2H-enriched and blue when it is not).*

available for the distributed transport analysis compared to the flow case. The data gaps are also evident in Fig. 4.14: there are no measurements for 3 of the graphs, and scarce data at 50 cm depth for points a and d. It is also important to note that no additional parameterization was attempted for the distributed transport analysis. The main explicit parameters in the transport equation are the dispersivity coefficients, and these were experimented with in the integrated transport analysis. The transport equation is of course strongly dependent on flow velocities, and thus implicitly on the conductivity and other soil hydraulic parameters that were assessed in the flow model analyses. These and other parameterization issues will be further discussed in the next section.

To complete the sequence of analyses from integrated flow and then transport to distributed flow and transport, we used the simulation results from the additional parameterization introduced for the distributed analyses (spatially variable soil retention capacity) to assess model performance against the integrated flow and transport responses. The

results (Fig. 4.15) show that while the match against tracer concentration at the seepage face has somewhat improved (compare with Fig. 4.9), the match against both of the integrated flow responses (seepage outflow and total water storage) has significantly deteriorated (compare with simulation f of Fig. 4.4). This is not a surprising result, given that no attempt was made to parameterize the model in tandem against both integrated and point-scale observations (nor against joint flow and transport data); the implications will be discussed below.

4.6 Discussion

Mass transport in unsaturated soils is extremely important in the context of biosphere, critical zone, and Earth systems research because of exchanges of water and solutes that occur across the land surface interface. The study of hillslope transit time distributions [e.g., *Fiori and Russo*, 2008; *Botter et al.*, 2010; *Heidbüchel et al.*, 2013; *Tetzlaff et al.*, 2014] is a good example of the need for a better understanding of such water and solute exchanges and the consequent subsurface flowpaths. The simulation of unsaturated zone mass transport phenomena is however known to be a particularly complex problem, compounded by any presence of heterogeneity. *Wilson and Gelhar* [1981], for instance, showed that spatial variations in moisture content affect solute plume spreading even without dispersive mixing, and that the rates of solute displacement are typically much smaller than the rates of moisture displacement. *Birkholzer and Tsang* [1997] demonstrated significant channeling effects (preferential solute pathways, with accompanying higher dispersion) at the extremes of very low saturation and full saturation. Studies that have combined comprehensive experimental observation with detailed subsurface simulation have also documented some of the challenges faced in modeling solute transport under unsaturated and heterogeneous conditions [e.g., *Haggerty et al.*, 2004; *Zheng et al.*, 2011]. In this context, for the tritium and bromide tracer experiments at the Las Cruces trench site, standard models gave good prediction of wetting front movement during infiltration but poor prediction of point soil water content and tracer transport [*Hills et al.*, 1991; *Wierenga et al.*, 1991]. For the macrodispersion (MADE) experiment, *Russo and Fiori* [2009] found that heterogeneity further enhances solute spreading and breakthrough curve arrival times when the unsaturated zone is relatively dry or deep. In the present

study, the additional complexity introduced for the point-scale responses (namely spatially variable soil retention capacity) did not match as favorably the integrated (flow) observation dataset (Fig. 4.15). While this could perhaps be remedied using more rigorous or quantitative parameter estimation, the particular difficulties in capturing the point-scale concentration profiles, especially near the landscape surface, can be taken as further evidence for flaws or gaps in theoretical understanding and model formulation (process representation) for simulating solute transport phenomena in very dry, heterogeneous soils.

Various hypotheses have been invoked to explain possible factors that affect the migration and distribution of solutes under unsaturated, heterogeneous conditions, including: turbulent mixing due to high rainfall [*Havis et al.*, 1992]; solute transfer between mobile and immobile water [*De Smedt and Wierenga*, 1984]; mobile-immobile exchange and hysteresis [*Butters et al.*, 1989; *Russo et al.*, 1989a,b, 2014]; lateral mixing due to velocity fluctuations [*Russo et al.*, 1998]; isotope effects [*Barnes and Allison*, 1988; *LaBolle et al.*, 2008; *Zhang et al.*, 2009]; variable, state-dependent anisotropy [*McCord et al.*, 1991]; non-Gaussian early-time mean tracer plume behavior [*Naff*, 1990]; non-Fickian solute migration at low water contents [*Padilla et al.*, 1999] and for macroscopically homogeneous sand [*Bromly and Hinz*, 2004]; and saturation-dependent dispersivity [*Raoof and Hassanizadeh*, 2013]. In addition, *Konikow et al.* [1997b] and *Parker and van Genuchten* [1984] discuss the importance of boundary condition treatment (e.g., water-solute injection, solute exchange between soil and atmosphere). Given the many open questions, for this first analysis of the LEO isotope tracer experiment the modeling was kept to the standard formulation of the Richards and advection-dispersion equations. Limitations encountered in the multiresponse performance assessment, from the standpoint of experimental procedure, model formulation, or numerical implementation, will inform follow-up studies at LEO. The simulation results from this tracer experiment, for instance, point to highly complex effects on plume migration of spatially variable water content in the dry soils that characterized the experiment, especially at early times.

The broad results of our study should be quite universal, particularly to deterministic numerical models based on the 3D Richards and advection-dispersion equations. However, any model has its specific features and differs, for example, in the way equations are coded (e.g., choice of numerical solvers) or interface conditions are implemented (e.g.,

free-surface vs boundary condition switching). For insights on the impact of specific model differences in the performance of CATHY-like models, see the intercomparison studies of *Sulis et al.* [2010] and *Maxwell et al.* [2014]. These intercomparison studies have thus far focused only on flow processes, and there is an urgent need to extend the analyses to solute transport phenomena, in order to properly guide our assessment of the physical and numerical correctness of competing models as these models continue to increase in complexity. For instance for this study there are aspects of the CATHY model related to how we implemented evaporation and fractionation that might be expected to negatively impact the generality of our findings, although in terms of isotope tracer mass exiting the seepage face the impact was quite small. But the implementation here was somewhat ad hoc, and more study is needed on the importance and proper representation of fractionation in solute transport models, especially under strongly unsaturated conditions.

4.7 Conclusions

In this study we have used multivariate observations (soil moisture, water and tracer outflow, breakthrough curves, and total water storage) culled from the first isotope tracer experiment at the LEO-1 hillslope of the Biosphere 2 facility to explore some of the challenges in modeling unsaturated flow and transport phenomena. Integrated (first flow and then transport) and distributed (again flow followed by transport) measurements were progressively introduced as response variables with which to assess the results from simulations with CATHY, a 3D numerical model for variably saturated flow and advective-dispersive solute migration. Compared to the first flow experiment at LEO that was successfully modeled with CATHY [*Niu et al.*, 2014b], the modeling task for the tracer experiment was significantly more complicated due to: joint simulation of both flow and transport processes; considerably drier initial conditions and reduced forcing; performance assessment against both system-wide and point-scale measurements; and multiple periods of water/tracer injection compared to a single rainfall episode. In some sense the previous flow study looked at the first order response of the LEO hillslope, whereas the modeling exercise for the tracer experiment represents a first look at higher order responses of the Biosphere 2 landscapes.

There are several findings from this first set of simulations of a LEO isotope tracer

experiment. At the start of the exercise, where integrated flow measurements were used, we were able to obtain good matches for two response variables (total water storage and seepage face outflow) using parameter values and initial and boundary conditions that correspond quite closely to the actual experimental conditions and previous (flow experiment) model implementation [*Niu et al.*, 2014b]. The same soil parameterization was successfully used to reproduce the integrated transport response. When passing to point-scale flow and finally point-scale transport, a refinement of the model setup (augmenting the degree of heterogeneity, mainly) was needed. Moreover, providing more information to the model (for example, the distribution of initial water storage rather than just the initial total volume) generally helped to improve the simulation results.

The effect of saturated hydraulic conductivity (heterogeneity and anisotropy) on the response of subsurface hydrologic models is well known, and was also borne out in this study. Also not surprisingly, the dispersivity parameter had a big impact on the transport simulations, with a clear trend to a better match against measured seepage face concentration as dispersivity was decreased. The spatial distribution of rainfall was not found to have a big impact on simulation results, and there was not much difference, in terms of isotope tracer mass exiting the seepage face, between the zero, partial, and no fractionation cases, suggesting that the injected tracer did not percolate very far into the hillslope, likely due to the very dry initial conditions.

We conclude with a few specific recommendations for alleviating some of the modeling and experimental limitations encountered during this study. On the modeling side, a more sophisticated treatment of solute transport phenomena beyond the standard advection-dispersion equation could start with incorporation of a mobile-immobile conceptualization and/or saturation-dependent dispersivity. Other upgrades to the CATHY model [e.g., *Scudeler et al.*, 2016a] will mitigate the grid Peclet constraint and provide more reliable flow velocity calculations, essential to maintaining low mass balance errors and high accuracy in solute transport. On the experimental side, higher tracer concentrations (including labeled tracers), wetter initial conditions, and more intensive direct or indirect measures of total tracer mass could help address the high sensitivity of solute transport to small scale heterogeneity under dry soil conditions. Any experiments that provide spatially detailed observations of both flow and transport response variables that are then jointly used in estimating, for instance, conductivity and other soil hydraulic parameters (tra-

ditionally identified based solely on flow responses), would be critical to advancing the present state of hydrologic model verification, given the high impact that Darcy velocities, which are directly dependent on such parameters, have on solute mixing processes. Finally, future LEO isotope tracer experiments that also generate some surface runoff would offer valuable benchmark data for improving integrated surface-subsurface models.

Chapter 5

Process-based modeling of surface-subsurface and flow-transport interactions: coupling, boundary conditions, and numerical behavior

5.1 Abstract

Process interactions (for e.g. between streams and aquifers, or between water and solutes) are one of the major controls on the water and solute budgets at the catchment and river basin scales. But their influence is not yet fully understood, and important challenges remain for instance in performing hydrograph separation analysis or deciphering the paths and travel times of water and solutes. In this context, numerical models for integrated hydrological simulations are increasingly used to explore hypotheses, to develop new concepts, and to identify key dynamics. However, their development and application to complex field situations still represents a big challenge, in particular when simulating both flow and transport processes and flow and transport interactions across the land surface. In this study we address this challenge in the framework of an existing physically-based model that couples the Richards and advection-dispersion equations, used to describe subsurface flow and solute transport under variably saturated conditions, with the diffusive wave equations, used to describe surface flow and transport propagation over the land surface. We present the model features and show its performance in a series of test cases of hillslope drainage, rainfall, and runoff generation, and we discuss important modeling issues related to the numerical resolution of the advective-dispersive equation, to the treatment of boundary conditions, and to complex coupling aspects.

5.2 Introduction

In the last decades the growing interest in using an integrated approach to study hydrological processes and their interactions, such as those between surface waters and groundwaters and between flow and transport phenomena, poses new challenges to researchers. The current understanding of the dynamic processes at the surface–subsurface interface is constrained by the strong interplay between heterogeneous topography and geology and the spatio-temporal variability of climate, which controls the spatial patterns of interactions between surface waters and groundwaters. Theoretical studies and significant effort have been devoted to the development of new methods to resolve these issues. Examples include the use of natural tracers or heat to decipher the paths and travel time of solutes and to assess the potential of the groundwater–surface water interface to attenuate polluttants [e.g., *Burns*, 2002; *Constantz*, 2008] and the refinement and use of physically-based numerical models for integrated hydrological simulations [e.g., *Tonina and Buffington*, 2007; *Frei et al.*, 2009, 2010].

Due in part to the lack of adequate techniques to fully measure and observe process interactions, integrated numerical models have become prominent tools for such investigations and are increasingly used to explore surface–subsurface systems. These models are approximations of a very complex reality and require the solution of partial differential equations with complicated coupling. Detailed groundwater models has been linked to existing surface flow models and an entirely new class of fully integrated models has been developed that can simulate coupled systems as a continuum: CATchment HYdrology (CATHY) [*Camporese et al.*, 2010], HydroGeoSphere (HGS) [*Therrien et al.*, 2012], OpenGeoSys (OGS) [*Kolditz et al.*, 2012], Parallel Flow (ParFlow) [*Kollet and Maxwell*, 2006], to name a few. Comparatively fewer models address both flow and transport interactions between the subsurface and the land surface [*Weill et al.*, 2011; *Therrien et al.*, 2012], and the issues associated to their development and testing have not been fully examined to date.

In this study we aim to shed light on important modeling issues related to the development and performance of the CATchment HYdrology Flow-Transport (CATHY_FT) model [*Weill et al.*, 2011]. CATHY_FT is an evolving physically-based model that addresses both flow and transport interactions between the land surface and the subsurface.

The model uses a sequential iterative coupling paradigm [*Delfs et al.*, 2009; *Camporese et al.*, 2010] based on a boundary condition switching algorithm that determines the partitioning of water exchange fluxes between the surface and the subsurface. On the transport side, the solute exchange fluxes across the land surface interface are determined via a mass balance that considers the different states arising from the flow resolution (water storage at the surface, actual water fluxes at the land surface interface, and atmospheric input). Following a general description of the model, we present the time-splitting operator implemented to solve the difficult behavior of the advection-dispersion equation for subsurface solute transport and the solution procedure for the four model components (flow and transport for the surface and subsurface). We then discuss important model features related to the equation-solving algorithm, the treatment of boundary conditions, and coupling aspects, with particular emphasis on details related to mass balances, such as the impact of different interpolation schemes between nodes and elements. The model performance is illustrated for three different scenarios that involve both subsurface-only and coupled surface–subsurface processes for an experimental hillslope at the Landscape Evolution Observatory of the Biosphere 2 facility in Arizona [*Hopp et al.*, 2009].

5.3 Methodology

5.3.1 Governing equations and numerical resolution

The four equations solved by the CATHY_FT model are:

$$\frac{\theta}{n} S_s \frac{\partial \psi}{\partial t} + \frac{\partial \theta}{\partial t} - \nabla \cdot [K_r(\psi) K_s (\nabla \psi + \eta_z)] = q_{sf} + q_s \tag{5.1a}$$

$$\frac{\partial Q}{\partial t} + c_k \frac{\partial Q}{\partial s} - D_h \frac{\partial^2 Q}{\partial s^2} = c_k q_{sb} \tag{5.1b}$$

$$\frac{\partial \theta c}{\partial t} + \nabla \cdot [vc - D \nabla c] = q_{ts} + q_{tsf} \tag{5.1c}$$

$$\frac{\partial Q_m}{\partial t} + c_t \frac{\partial Q_m}{\partial s} - D_c \frac{\partial^2 Q_m}{\partial s^2} = c_t q_{tsb} \tag{5.1d}$$

where in Richards' equation (5.1a) θ [$\mathrm{L^3L^{-3}}$] is the volumetric water content, S_s [$\mathrm{L^{-1}}$] is the aquifer specific storage, ψ [L] is the pressure head, t [T] is time, n [$L^3\mathrm{L^{-3}}$] is the porosity, K_s [$\mathrm{LT^{-1}}$] is the saturated hydraulic conductivity tensor, $K_r(\psi)$ [-] is the relative hydraulic conductivity function, $\eta_z = (0, 0, 1)^T$ with z [L] the vertical coordinate directed upward, q_{sf} [$\mathrm{L^3L^{-3}T^{-1}}$] is the inflow or outflow rate from surface to subsurface, and q_s [$\mathrm{L^3L^{-3}T^{-1}}$]

is a source or sink term. In the surface flow equation (5.1b) Q [L^3T^{-1}] is the discharge along the overland and channel network, c_k [LT^{-1}] is the kinematic celerity, s [L] is the coordinate direction for each segment of the overland and channel network, D_h [L^2T^{-1}] is the hydraulic diffusivity, and q_{sb} [$L^3L^{-1}T^{-1}$] is the inflow or outflow rate from subsurface to surface. In the variably saturated advective-dispersive solute transport equation (5.1c) c [ML^{-3}] is the subsurface solute concentration, v [LT^{-1}] is the Darcy velocity vector, D [L^2T^{-1}] is the tensor accounting for both mechanical dispersion and molecular diffusion, q_{ts} [$ML^{-3}T^{-1}$] is a solute mass source or sink term, and q_{tsf} [$ML^{-3}T^{-1}$] is the solute mass inflow or outflow rate from surface to subsurface. In the surface transport equation (5.1d), which follows the same dynamic of the surface flow equation, Q_m [MT^{-1}] is the solute mass discharge, c_t [LT^{-1}] is the kinematic solute celerity, D_c [L^2T^{-1}] is the surface solute diffusivity, and q_{tsb} [$ML^{-1}T^{-1}$] is the solute mass inflow or outflow from subsurface to surface.

Surface processes are computed using a cell-centered scheme based on the grid digital elevation (DEM) model describing the land surface topography. The surface triangulation $\mathcal{S}$ is derived simply by subdividing each DEM cell into two triangles. Subsurface processes are described using a regular tetrahedral discretization $\mathcal{T}_h(\Omega)$ of the subsurface domain Ω. This produces N nodes and E elements by subdividing each cell $C \in \mathcal{S}$ into triangles, which in turn become the faces of the subsurface boundary elements. The set of nodes and faces of $\mathcal{T}_h(\Omega)$ are defined as $\mathcal{N}$ and $\mathcal{F}$, respectively. Given a tetrahedron $T \in \mathcal{T}_h(\Omega)$, the set of faces that defines T is denoted by $\mathcal{F}_T$.

The solution of the surface equations are obtained numerically using the Muskingum-Cunge method for the variables Q and Q_m for each cell $C \in \mathcal{S}$, and stability is determined by the Courant-Friedrichs-Lewy (CFL) constraint since time integration is explicit. Richards' equation is discretized by means of the linear Galerkin finite element (FE) scheme in space and by the backward Euler finite difference scheme in time, and is linearized by a Picard or Newton iterative scheme. In this case time integration is implicit, thus the scheme is subject only to a convergence constraint related to the non-linear scheme. The equation is solved in its conservative form [*Celia et al.*, 1990a] for the variables pressure head ψ and volumetric water content θ for each node $i \in \mathcal{N}$. The $\mathcal{P}_1$ Galerkin velocity field is post-computed on each element $T \in \mathcal{T}_h$ from the nodal pressure head values. This is reconstructed using the Larson-Niklasson post-processing algorithm

and used as input by the subsurface transport model. The subsurface transport equation is solved by means of a time-splitting technique that adopts appropriate discretizations to solve the advection and dispersion components.

Camporese et al. [2010] and *Weill et al.* [2011] present numerical details related to the solution of the surface equations, *Camporese et al.* [2010], *Paniconi and Putti* [1994], and *Scudeler et al.* [2016a] describe the detailed FE discretization of Richards' equation, and *Scudeler et al.* [2016a] presents the detailed Larson-Niklasson algorithm for velocity field reconstruction. *Mazzia et al.* [2000] develop a time-splitting technique, combining mixed hybrid finite elements (MHFE) and high resolution finite volumes (HRFV), for the solution of the saturated advection-dispersion transport equation. In the next sections we present the time time-splitting technique used to solve the variably saturated advective-dispersive equation in CATHY_FT and the solution procedure for the four equations, and we also discuss important features related to the implementation of the transport boundary conditions and the performance of the surface–subsurface coupling algorithm.

5.3.2 The time-splitting algorithm

The advective-dispersive equation is discretized using the time-splitting algorithm that combines a HRFV scheme for advection and a linear Galerkin FE scheme for dispersion. Integration in time for the former scheme is explicit, whereas it is implicit for the latter. Thus, the stability of the advective step is determined by the CFL constraint, while the dispersive step is not subject to any constraint. A finer advective time step Δt_a together with a coarser dispersive time step Δt_d are employed. For each Δt_d a number $n_a = \Delta t_d / \Delta t_a$ of advective time steps is performed in accordance with the CFL condition that establishes Δt_a.

Denoting with G and F the advective and dispersive fluxes, respectively, equation (5.1c) can be written as:

$$\frac{\partial \theta c}{\partial t} + \nabla \cdot [G + F] = q_{ts} + q_{tsf} \tag{5.2a}$$

$$G = vc \tag{5.2b}$$

$$F = -D \nabla c \tag{5.2c}$$

The time-splitting technique can be viewed as a predictor-corrector approach that, starting from equation (5.2a), solves sequentially two different equations, derived here in

a generic form. Multiplying equation (5.2a) by the test function χ and integrating in space and time, with time-step Δt over the time interval $[t^k,t^{k+1}]$, the following integral is obtained:

$$\int_\Omega \frac{(\theta c)^{k+1}-(\theta c)^k}{\Delta t}\chi d\Omega + \int_\Omega \nabla\cdot(G^k+F^{k+1})\chi d\Omega = \int_\Omega (q_{ts}^k+q_{tsf}^k)\chi d\Omega \tag{5.3}$$

The above equation is split into the following two equations:

$$\int_\Omega \frac{(\theta \hat{c})^{k+1}-(\theta c)^k}{\Delta t}\chi d\Omega + \int_\Omega \nabla\cdot G^k\chi d\Omega = \int_\Omega (q_{ts}^k+q_{tsf}^k)\chi d\Omega \tag{5.4a}$$

$$\int_\Omega \frac{(\theta c)^{k+1}-(\theta \hat{c})^{k+1}}{\Delta t}\chi d\Omega + \int_\Omega \nabla\cdot F^{k+1}\chi d\Omega = 0 \tag{5.4b}$$

First, the advective step solves equation (5.4a) for the variable $\hat{c}^{k+1}$. Second, the dispersive step solves equation (5.4b) for the final concentration c^{k+1}. Note that, the dispersive step uses as initial conditions the total mass of solute obtained at the end of the advective step, i.e., $(\theta\hat{c})^{k+1}$, so that the sum of equations (5.4a) and (5.4b) gives exactly equation (5.3).

The HRFV and FE discretizations of the variably saturated advective equation and the advective-dispersive equation can be found in *Scudeler et al.* [2016b] and *Scudeler et al.* [2016a], respectively. We report here the final fully discretized HRFV equation for the advective flux, which includes also the source/sink term q_{ts} and surface-to-subsurface solute exchange q_{tsf}, and the final fully discretized FE system for the dispersive flux. For each $T\in\mathcal{T}_h$ the HRFV solver applied to the advective flux G with explicit time integration gives:

$$(\theta_T c_T)^{k_a+1} = (\theta_T c_T)^{k_a} - \frac{\Delta t_a}{|T|}\sum_{F\in\mathcal{F}_T}(q_F^T)^{k_a} c_{F,X} A_F + q_{ts,T}^{k_a}\Delta t_a + q_{tsf,T}^{k_a}\Delta t_a \qquad T=1,...,E \tag{5.5}$$

where k_a is the advective time step index, $|T|$ [L^3] indicates the measure (volume) of element T, θ is the volumetric water content obtained from the solution of Richards' equation, q_F^T [L/T] is the Larson-Niklasson post-processed flux associated to face F and oriented outward of element T, $c_{F,X}$ are the concentration values at the right ($c_{F,R}$) or left ($c_{F,L}$) of face F (the distinction between right and left is made with respect to a local counterclockwise reference system defined in accordance to the nodal numbering of face F and which defines also the orientation of q_F), and A_F [L^2] is the area of face F. The term $q_{tsf,T}$ represents the surface-to-subsurface solute exchange associated to element T. Thus, it can assume a non vanishing value only on surface boundary elements. Details on how it is computed in the proposed approach are discussed in section 5.3.5.

The linear Galerkin method applied to the dispersive flux $-D\nabla c$ with implicit time integration gives:

$$(A^{k_d+1} + \frac{1}{\Delta t_d} M^{k_d+1}) c_h^{k_d+1} = \frac{1}{\Delta t_d} M^{k_d} c_h^{k_d} - b^{t,k_d+1} \tag{5.6}$$

where k_d is the dispersive time step index, $c_h = \left\{ c_i \right\}$ is the vector of the numerical approximation for concentration c at each node $i \in \mathcal{N}$, and the coefficients of the, respectively, dispersion and mass matrices and boundary conditions vector are:

$$a_{ij} = \int_\Omega D\nabla\phi_i \nabla\phi_j d\Omega \tag{5.7a}$$

$$m_{ij} = \int_\Omega \theta\phi_i\phi_j d\Omega \tag{5.7b}$$

$$b_i^t = \int_{\Gamma^t} (-D\nabla c)\cdot\nu\phi_i d\Gamma^t = \int_{\Gamma^t} q_n^t \phi_i d\Gamma^t \tag{5.7c}$$

where $i, j = 1, ..., N$, ϕ are the linear basis functions of the Galerkin FE approximation, Γ^t is the domain boundary, D is the dispersion tensor computed by considering the elemental mass-conservative velocity field q recovered from q_F by using lowest order Raviart-Thomas (RT0) interpolation, θ is the volumetric water content obtained from the solution of Richards' equation, q_n^t [M/(L^{2}T)] is the Neumann (dispersive) flux, and ν is the outward normal vector to the boundary.

The time-splitting algorithm solves equation (5.5) n_a times for each $T \in \mathcal{T}_h$ using Δt_a as time step and determining the predictor concentration $c_T^{n_a}$ on each $T \in \mathcal{T}_h$. Since HRFV and FE use different functional spaces for the approximation of the same dependent variable (concentration), an interpolation of $c_T^{n_a}$ between elements and nodes is performed in order to generate the nodal concentration vector $c_h^{n_a} = \hat{c}_h^{k_d+1}$, used as initial condition in the dispersive step. This solves the FE system (5.6) with Δt_d as time step for the final concentration $c_h^{k_d+1}$. Again, an interpolation of the nodal concentration values between nodes and elements is performed in order to generate the elemental concentration field $c_T^{k_d+1}$ for each $T \in \mathcal{T}_h$ used as initial condition in the following step $c_T^{k_d+1} = c_T^{k_a}$. We can express thusly a general form of the time-splitting algorithm used:

For each time step, do:

- advection step, for each $T \in \mathcal{T}_h$

1. $c_T^{(0)} := c_T^{k_a}$

   DO $k_a = 0, n_a - 1$

   $$(\theta_T c_T)^{k_a+1} = (\theta_T c_T)^{k_a} - \frac{\Delta t_a}{|T|} \sum_{F \in \mathcal{F}_T} (q_F^T)^{k_a} c_{F,X} A_F + q_{ts,T}^{k_a} \Delta t_a + q_{tsf,T}^{k_a} \Delta t_a$$

   END DO

2. $c_T^{n_a} \rightarrow c_h^{n_a}$
3. $\hat{c}_h^{k_d+1} := c_h^{n_a}$

- dispersive step for $c_h^{k_d+1}$

  $$(A^{k_d+1} + \frac{1}{\Delta t_d} M^{k_d+1}) c_h^{k_d+1} = \frac{1}{\Delta t_d} M^{k_d+1} \hat{c}_h^{k_d+1} - b^{t,k_d+1}$$

  4. $c_h^{k_d+1} \rightarrow c_T^{k_d+1} \quad \forall T \in \mathcal{T}_h$
  5. $c_T^{k_a} := c_T^{k_d+1} \quad \forall T \in \mathcal{T}_h$

The mass matrix M at the right hand side of the system solved in the dispersive step is computed at time level k_d+1. As noted before for the generic form of the time splitting algorithm, this is done in order to guarantee that the sum of equations (5.4a) and (5.4b) gives equation (5.3).

Compared to the time-splitting approach proposed in *Mazzia et al.* [2000], here the dispersive flux is discretized with the FE scheme instead of with the MHFE scheme. The advantages are that, in contrast to the MHFE method, the FE method is computationally efficient and is not affected by ill-conditioning problems. On the contrary, the new procedure requires concentration interpolation between elements and nodes and vice versa, as represented in steps 2 and 4 of the above algorithm. This interpolation has to be performed carefully in order to maintain mass conservation.

The HRFV and linear FE schemes use different functional spaces for the approximation of the dependent variable, which are the space of element-wise constant functions and the space of linear test functions, respectively. Thus, the HRFV concentration field is element-wise constant while the FE concentration field, computed on each node of the computational domain, is continuous and piecewise linear. When the two techniques are combined in a time-splitting technique, the variable interpolations required to pass information from elements to nodes and vice versa are performed by ensuring that the following equality always holds:

$$\int_\Omega \theta c d\Omega = \sum_{T \in \mathcal{T}_h} \theta_T c_T |T| = \sum_{i \in \mathcal{N}} \theta_i c_i V_i \tag{5.8}$$

where V_i is the volume associated to node i. The above equation states that the total solute mass in the system has to be the same whether it is calculated by summing up each elemental contribution or each nodal contribution. Defining $\mathcal{N}_T$ as the set of nodes of element T and $\mathcal{E}_i$ as the set of tetrahedra sharing node i, the linear mass-conservative element-to-node and node-to-element interpolations satisfying equation (5.8) are:

$$c_i = \Big[\sum_{T \in \mathcal{E}_i} (\theta_T c_T |T|) \Big] / (4 \theta_i V_i) \qquad \forall i \in \mathcal{N} \tag{5.9}$$

$$c_T = \Big[\sum_{i \in \mathcal{N}_T} (\theta_i c_i V_i) \Big] / (4 \theta_T |T|) \qquad \forall T \in \mathcal{T}_h \tag{5.10}$$

where equation (5.9) is used after the advective time step to calculate the nodal concentration field from the elemental concentration field while equation (5.10) is used after the dispersive step to calculate the elemental concentration field from the nodal concentration field.

5.3.3 Boundary conditions

The time-splitting requires careful handling of boundary conditions. To better describe how the boundary conditions are implemented, we distinguish between inflow and outflow boundaries, defined as Γ_I^t and Γ_O^t and characterized by having the normal components of the flow velocity directed into ($v \cdot \nu < 0$) and out of ($v \cdot \nu > 0$) the domain, respectively. A special case occurs when $v \cdot \nu = 0$, as here the advective flux will automatically be zero. The boundary of the domain Γ^t is thus subdivided into inflow boundary, outflow boundary, and zero-advective (or Neumann) boundary Γ_n^t, such that $\Gamma^t = \Gamma_I^t \cup \Gamma_O^t \cup \Gamma_n^t$. Inflow boundaries can be characterized by both advective inflow and dispersive exchanges. For this reason, Cauchy conditions, expressed as $q_c^t = (vc - D\nabla c) \cdot \nu$, are usually of use on Γ_I^t. In CATHY_FT they have been implemented by imposing Dirichlet-type boundary conditions ($c = c_D$) in the advective step and Neumann-type boundary conditions ($q_n^t = -D\nabla c \cdot \nu$) in the dispersive step. However, since the transport module in CATHY_FT at this time does not account for diffusive or dispersive exchange at the boundaries, a zero-Neumann condition is set in the dispersive step. For example, solute inflow from rainfall or infiltration from a source of contaminant are specified as:

$vc \cdot \nu = vc_D \cdot \nu$ on Γ_I^t $\quad \Rightarrow$ Dirichlet boundary condition $c = c_D$ in the advective step

$q_n^t = -D\nabla c \cdot \nu = 0$ on $\Gamma_I^t \Rightarrow$ zero-Neumann condition in the dispersive step

Outflow boundaries Γ_O^t are characterized by outgoing velocities. In the HRFV approach this type of boundary is governed only by the velocity field and it is thus implemented by imposing a zero-Neumann condition ($q_n^t = 0$) in the dispersive step. For example, outflow from a seepage face is modeled as:

$vc \cdot \nu$ on Γ_O^t $\Rightarrow$ Boundary governed by the velocity field in the advective step

$q_n^t = -D\nabla c \cdot \nu = 0$ on $\Gamma_O^t \Rightarrow$ zero-Neumann condition in the dispersive step

For zero-advective boundaries Γ_n^t, the dispersive flux can be either zero, of inflow, or of outflow. Each of these cases has to be implemented in the dispersive step by imposing, for example, a known Neumann dispersive flux q_n^t. However, for the same reasons noted above, zero-advective boundaries in CATHY_FT are also treated with a zero-Neumann condition.

In the time-splitting code implementation of the transport boundary conditions, we define the set of boundary faces of the computational mesh as $\mathcal{F}_B$, which is the union $\mathcal{F}_O \cup \mathcal{F}_I \cup \mathcal{F}_n$, where $\mathcal{F}_O$ is the set of outflow boundary faces, $\mathcal{F}_I$ is the set of inflow boundary faces, and $\mathcal{F}_n$ is the set of zero-advective boundary faces. Boundary elements are characterized by having, at least, one face in $\mathcal{F}_B$. For each face in $\mathcal{F}_T \cap \mathcal{F}_B$ the term $q_F^T c_{F,X}$ of eq. (5.5) represents a boundary advective flux. For boundary faces we consider that $q_F = q_F^T$ (meaning that the flux associated to face F is oriented outward of element T). Consequently, $c_{F,L}$ and $c_{F,R}$ represent, respectively, the subsurface concentration (inside the domain) and the surface concentration (outside the domain and eventually imposed) of face F. Since inflow, outflow, and zero-advective boundary faces are characterized by having, respectively, $q_F < 0$, $q_F > 0$, and $q_F = 0$, boundary conditions on each $F \in \mathcal{F}_B$ are imposed as it follows:

if $q_F < 0 \Rightarrow F \in \mathcal{F}_I$, $q_F c_{F,X} = q_F c_{F,D}$ with $c_{F,R} = c_{F,D}$ Dirichlet boundary condition

if $q_F > 0 \Rightarrow F \in \mathcal{F}_O$, $q_F c_{F,X} = q_F c_{F,L}$ with ouflowing advective flux governed by q_F

if $q_F = 0 \Rightarrow F \in \mathcal{F}_n$, $q_F c_{F,X}$=0

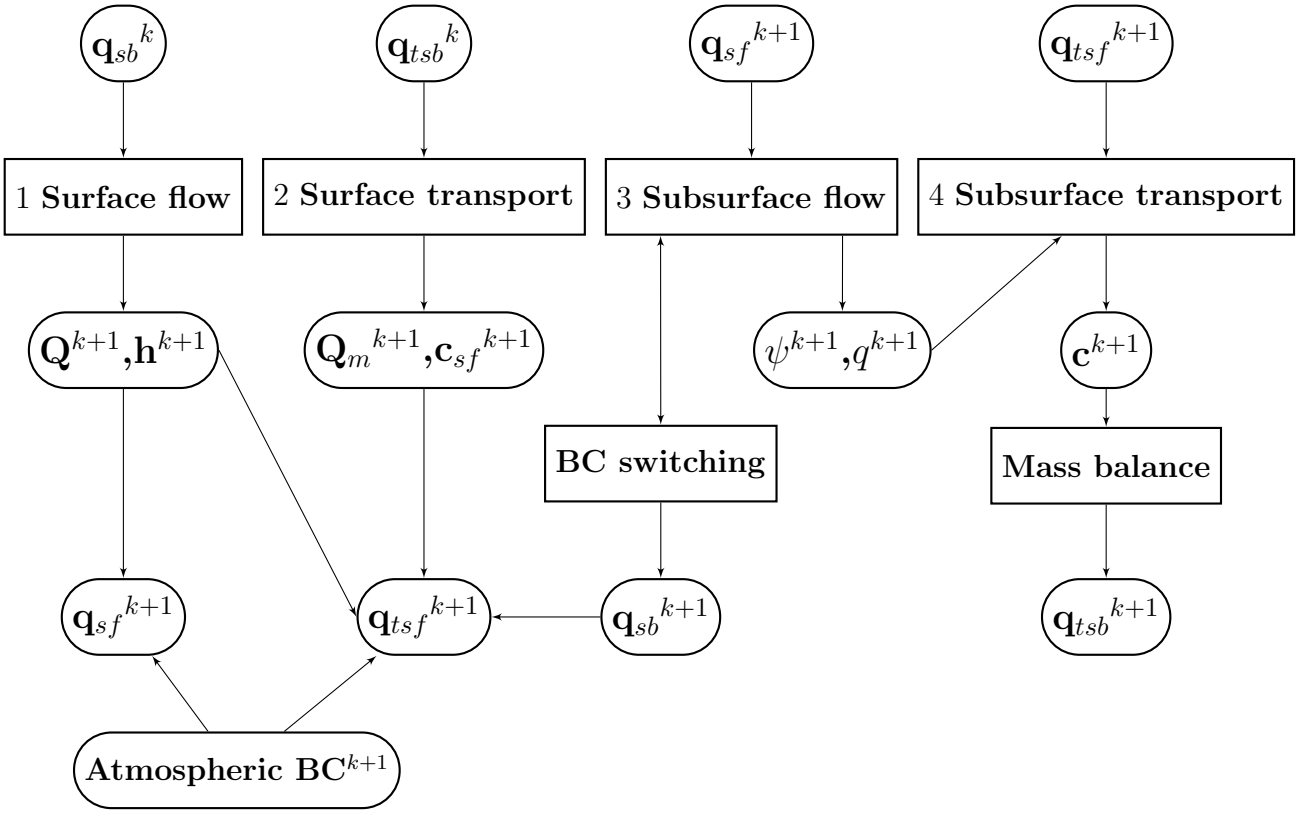

Figure 5.1: *Solution sequence (from 1 to 4 as labeled) for the four governing equations in CATHY_FT. k is the time step counter and the solution is evaluated at t^{k+1}. h [L] is the ponding head relative to Q and c_{sf} [M/L^3] is the surface concentration relative to Q_m. All other variables are as defined in section 5.3.1. The values ${q_{sb}}^{k+1}$ and ${q_{tsb}}^{k+1}$ are used as input at the following time step for, respectively, the surface flow and surface transport equations (so they become the new ${q_{sb}}^{k}$ and ${q_{tsb}}^{k}$).*

5.3.4 Solution procedure

Integration of the surface and subsurface equations is achieved with a sequential iteration procedure and coupling is performed through a boundary condition switching algorithm. Surface-subsurface partitioning is managed by the subsurface module since this is the model component that handles the crucial atmospheric inputs. The solution of the flow and transport equations is seamlessy handled since in the sequential solution procedure the flow modules are solved before their transport counterparts. In the sequential solution procedure, coupling is intrinsically linked to time stepping. The control on the time step evolution of the overall procedure is made by the subsurface flow router, subject only to a convergence constraint related to the nonlinear scheme. By contrast, the stability of the explicit method used to discretize the surface equations requires a CFL restriction on the time step. Thus, for each subsurface time step Δt, multiple surface time steps are performed. The dispersive fluxes of the subsurface transport equation, discretized by means of an implicit method, are not constrained by stability or convergence conditions, thus the dispersive time step Δt_d is synchronized with the subsurface flow time step ($\Delta t_d = \Delta t$). Within this framework, multiple advective explicit time steps are taken per dispersive step, as described earlier.

The procedure to solve the four coupled governing equations is described schematically in the flow chart of Figure 5.1 and in stepwise fashion below. In what follows, we define the set of surface boundary faces as $\mathcal{F}_S$ and the set of surface boundary nodes as $\mathcal{N}_S$. Given the time step Δt, the different steps to evaluate the solution at time t^{k+1} from the solution at time t^k for surface discharge Q, surface mass discharge Q_m, subsurface pressure head ψ, and subsurface concentration c are:

1. solution of the surface flow equation for Q^{k+1} (on each cell $C \in \mathcal{S}$). This requires the subsurface-to-surface water exchange q_{sb}^k (on each cell $C \in \mathcal{S}$) as input, calculated at the end of the previous subsurface flow time step. Ponding heads h^{k+1} (on each cell $C \in \mathcal{S}$) are calculated from the computed Q^{k+1} (on each cell $C \in \mathcal{S}$) values.

2. solution of the surface transport equation for Q_m^{k+1} (on each cell $C \in \mathcal{S}$). The procedure requires the subsurface-to-surface mass exchange q_{tsb}^k (on each cell $C \in \mathcal{S}$) as input, calculated at the end of the previous subsurface transport solution. Surface concentration c_{sf}^{k+1} (on each cell $C \in \mathcal{S}$) is then calculated from the computed mass

discharges Q_m^{k+1} (on each cell $C \in \mathcal{S}$) and flow discharges Q^{k+1} (on each cell $C \in \mathcal{S}$) of the preceding step.

3. update of the subsurface boundary condition on the surface nodes. This is accomplished by considering the ponding head h^{k+1} (on each node $i \in \mathcal{N}_S$) and the atmospheric boundary condition to determine the surface-to-subsurface water exchange q_{sf}^{k+1} (on each node $i \in \mathcal{N}_S$).

4. solution of the subsurface flow equation for the pressure head ψ^{k+1} (on each node $i \in \mathcal{N}$) and moisture content θ^{k+1} (on each node $i \in \mathcal{N}$). The velocity field v^{k+1} (on each element $T \in \mathcal{T}_h$) is post-computed from the pressure head solution.

5. reconstruction of the velocity field v^{k+1} with the mass-conservative Larson–Niklasson post-processing algorithm. The reconstructed velocity fields q_F^{k+1} (on each face $F \in \mathcal{F}$) and q^{k+1} (on each element $T \in \mathcal{T}_h$) are then used, respectively, by the advective and dispersive solvers of the subsurface transport equation.

6. computation of the subsurface-to-surface water exchange fluxes q_{sb}^{k+1} (on each node $i \in \mathcal{N}_S$) based on the pressure head solution ψ^{k+1} (on each node $i \in \mathcal{N}$) and the balance with the atmospheric fluxes. The q_{sb}^{k+1} (on each cell $C \in \mathcal{S}$) is then used as input by the surface flow solver at the next time step, thus becoming q_{sb}^{k} (on each cell $C \in \mathcal{S}$).

7. computation of the surface-to-subsurface mass exchange fluxes q_{tsf}^{k+1} (on each face $F \in \mathcal{F}_S$). This term relies on the velocity field q_F^{k+1} (on each face $F \in \mathcal{F}_S$). In particular, if a Dirichlet condition for concentration is required (in the case of inflow), the concentration value to be imposed is calculated by performing a solute mass balance which considers the concentration c_{sf}^{k+1} (on each face $F \in \mathcal{F}_S$), h^{k+1} (on each face $F \in \mathcal{F}_S$), and the atmospheric input.

8. solution of the subsurface transport equation for c^{k+1} (on each element $T \in \mathcal{T}_h$). Using as initial condition the concentration c^k (on each element $T \in \mathcal{T}_h$), i.e., the solution at the previous time step, the advective step computes $\hat{c}^{k+1}$ (on each element $T \in \mathcal{T}_h$). With a mass-conservative variable interpolation, the concentration values are determined on each node $i \in \mathcal{N}$ and used as initial condition by the dispersive

solver, which computes the final concentration field c^{k+1} (on each node $i \in \mathcal{N}$). The final concentration field on each $T \in \mathcal{T}_h$, required as initial condition for the next time step, is calculated by performing a mass-conservative variable interpolation from the nodal values.

9. computation of the subsurface-to-surface solute mass exchanges q_{tsb}^{k+1} (on each face $F \in \mathcal{F}_S$). This is accomplished by performing a solute mass balance on each face of the surface mesh based on the atmospheric input and the solute mass passed across the surface, governed by the velocity field q_F^{k+1} (on each face $F \in \mathcal{F}_S$). The q_{tsb}^{k+1} (on each cell $C \in \mathcal{S}$) is then used as input by the surface flow solver at the next time step, thus becoming q_{tsb}^{k} (on each cell $C \in \mathcal{S}$).

The 9-step procedure described above shows how the different numerical schemes used require input variables and compute output variables which are defined in different sets of the computational mesh or surface grid. In particular: ponding heads h are calculated in step 1 on each cell $C \in \mathcal{S}$ while they are required as input in step 3 on each node $i \in \mathcal{N}_S$ to compute the nodal surface-to-subsurface exchanges q_{sf} and in step 7 on each face $F \in \mathcal{F}_S$ to compute the surface-to-subsurface solute mass exchanges q_{tss}; the subsurface-to-surface water exchanges q_{sb} are calculated on each node $i \in \mathcal{N}_S$ in step 6 while they are required as input in step 4 on each cell $C \in \mathcal{S}$; surface concentrations c_{sf} are calculated on the surface cell and are required as input in step 7 on each face $F \in \mathcal{F}_S$ to compute the surface-to-subsurface solute mass exchanges q_{tsf}; in step 8 the advective solver requires and computes concentrations c on each element $T \in \mathcal{T}_h$, while the dispersive solver requires and computes concentrations on each node $i \in \mathcal{N}$; and the subsurface-to-surface solute mass exchanges q_{ts} are calculated in step 9 on each face $F \in \mathcal{F}_S$ while they are used as input on each cell $C \in \mathcal{S}$ in step 2. Interpolation algorithms are required to pass information to and from the surface and subsurface domains, the flow and transport components, and the advection and dispersion solvers.

Careful considerations are always required when performing variable interpolations since they can introduce mass balance errors that affect the overall numerical solution [e.g., *Goumiri and Prevost*, 2011]. *Camporese et al.* [2010] and *Weill et al.* [2011] describe in detail the procedure to calculate the terms used to couple the surface and subsurface equations in CATHY and CATHY_FT. Additionally, *Dagès et al.* [2012] and *Fiorentini et al.* [2015] provide an in-depth mass balance analysis of the sources of coupling error in

the CATHY (flow-only) model and propose improvements to coupling related algorithms in the model. In this study we proposed earlier a mass-conservative variable interpolation to reconstruct the nodal concentration field from an elemental concentration field and vice versa (eqs. (5.9) and (5.10)), as required by the time-splitting technique implemented to solve the advective-dispersive equation. We now present a mass-conservative algorithm to compute the surface–subsurface transport coupling terms. We thus focus on steps 7 and 9 of the solution procedure.

5.3.5 Computation of surface–subsurface transport coupling terms

The terms that couple the surface and subsurface transport equations are q_{tsf} and q_{tsb} of equations (5.1c) and (5.1d) and represent the exchange of solute between the surface and subsurface domain. Since solute transport depends on the flow conditions, they mainly rely on the different states arising after the solution of the surface and subsurface flow equations (ponding situation, atmospheric input, and the actual water flux corresponding to infiltration or exfiltration).

The term q_{tsf} represents the surface-to-subsurface solute mass exchange and can assume a non vanishing value only on inflow boundaries, representing an advective mass flux, or on zero-advective boundaries, representing a dispersive mass flux. However, since the coupling in CATHY_FT does not yet explicitly account for diffusive or dispersive exchanges between the surface and the subsurface, q_{tsf} is always zero on zero-advective boundaries. On inflow boundaries it is implemented as a subsurface transport boundary condition, computed by imposing a Dirichlet-type condition in the advective step (and a zero-Neumann flux condition in the dispersive step). With reference to the HRFV equation (5.5), the surface-to-subsurface solute exchange associated to the surface boundary element T and relative to the face $F \in \mathcal{F}_T \cap \mathcal{F}_S$ is computed as:

$$\text{if } q_F < 0 \text{ (infiltration)} \rightarrow F \in \mathcal{F}_I \cap \mathcal{F}_S \cap \mathcal{F}_T \quad q_{tsf,T} = q_F c_{F,D} A_F / |T|$$

$$\text{if } q_F > 0 \text{ (exfiltration)} \rightarrow F \in \mathcal{F}_O \cap \mathcal{F}_S \cap \mathcal{F}_T \quad q_{tsf,T}=0$$

$$\text{if } q_F = 0 \text{ (zero-flux)} \quad \rightarrow F \in \mathcal{F}_n \cap \mathcal{F}_S \cap \mathcal{F}_T \quad q_{tsf,T} = 0$$

where $c_{F,D}$ is the Dirichlet boundary condition for concentration associated to face $F \in \mathcal{F}_I \cap \mathcal{F}_S \cap \mathcal{F}_T$. The Dirichlet concentration $c_{F,D}$ is determined via a local solute mass

balance calculation which considers the atmospheric input, ponding head, and the surface concentration imposed and obtained after the solution of the surface equations. We define the surface concentration and ponding head associated to cell C as $c_{c,sf}$ and h_c, respectively. The set of faces that defines C is denoted by $\mathcal{F}_c$. Since h_c and $c_{c,sf}$ are constant on cell C, for each face $F \in \mathcal{F}_c$ the relative ponding head $h_{F,sf}$ and surface concentration $c_{F,sf}$ are equal to the cell values ($h_{F,sf} = h_c$ and $c_{F,sf} = c_{c,sf}$). To calculate $c_{F,D}$ the surface concentration is updated by performing a mass balance which accounts for any dilution or accretion by rainfall and evaporation. The updated concentration $c_{F,upd}$ associated to face F is computed as:

$$c_{F,upd} = c_{F,D} = \frac{q_{atm} c^* A_F \Delta t + h_{F,sf} c_{F,sf} A_F}{q_{atm} A_F \Delta t + h_{F,sf} A_F} \tag{5.11}$$

where q_{atm} [L/T] is the atmospheric flux given as input and c^* [M/L^3] is a concentration value to be set according to the sign of q_{atm}, which corresponds to rainfall when positive and to evaporation when negative. The three following situations can arise:

$q_{atm} > 0 \rightarrow c^* = c_{atm}$

$q_{atm} < 0 \rightarrow c^* = c_{F,sf}$ if the solute evaporates with water

$q_{atm} < 0 \rightarrow c^* = 0$ if the solute does not evaporate with water

where c_{atm} is the solute concentration associated with the atmospheric input in the case of rainfall. Note that infiltration and evaporation can coexist only if ponding is present. Note also that, if no ponding occurs after the solution of the surface flow equation, the Dirichlet concentration $c_{F,D}$ will be equal to the rainfall concentration c_{atm}.

The term q_{tsb} represents the subsurface-to-surface solute exchange, computed after the solution of the subsurface transport equation for each cell $C \in \mathcal{S}$. It accounts for the solute mass that, subsequent to any source arising from exfiltration and rainfall and any sink arising from evaporation and infiltration, has to be, respectively, added to or removed from the solute mass calculated by the surface transport module (at the previous time step). It is thus calculated as the difference between the incoming mass flux and the mass flux leaving the surface. We distinguish the rainfall case from the evaporation case. In the case of rainfall ($q_{atm} > 0$), the subsurface-to-surface solute exchange $q_{tsb,F}$ associated to face $F \in \mathcal{F}_s$ of cell C is computed as:

$$q_{tsb,F} = \frac{q_{atm} c_{atm} A_F + q_F c_{F,X} A_F}{\Delta s} \tag{5.12}$$

where Δs [L] is the length of the channel segment for the given cell. In the above equation the first term represents the incoming mass flux from rainfall while the second term represents either the incoming mass flux from exfiltration ($q_F > 0$), with the concentration $c_{F,X}$ assuming the subsurface value $c_{F,L}$ associated to face F, or the mass flux leaving the surface through infiltration ($q_F < 0$), with the concentration $c_{F,X}$ assuming the surface or Dirichlet value associated to face F. Complications arise for the evaporation case ($q_{atm} < 0$) as different scenarios have to be carefully considered. In the copresence of evaporation and infiltration, the subsurface-to-surface solute exchange associated to face F is computed as:

$$q_{tsb,F} = \frac{q_{atm} c^* A_F + q_F c_{F,D} A_F}{\Delta s} \tag{5.13}$$

where c^* can be the surface concentration $c_{F,sf}$ if the solute evaporates with water and zero otherwise. The two terms in the above equation represent the mass flux leaving the surface through evaporation and infiltration, respectively. In the case of evaporation and exfiltration from the soil three different situations have to be examined according to the potential surface evaporative flux, defined as $q_{F,ev} = -h_{F,sf}/\Delta t$ for face F. If $q_{F,ev} = 0$ no mass can evaporate from the surface and the mass exfiltrated from the soil flows directly to the atmosphere; if $q_{F,ev} < q_{atm}$ all surface water evaporates, surface mass can either evaporate or not, and the mass exfiltrated from the soil goes directly to the atmosphere; if $q_{F,ev} > q_{atm}$ part of the surface water evaporates, part of the surface mass can either evaporate or not, and the mass exfiltrated from the soil flows to the surface. Thus, for the three different cases the subsurface-to-surface solute exchange $q_{tsb,F}$ associated to face F is computed as:

if $q_{F,ev} = 0 \rightarrow \quad q_{tsb,F} = 0$

if $q_{F,ev} < q_{atm} \rightarrow \quad q_{tsb,F} = q_{F,ev} c^* A_F / \Delta s$

if $q_{F,ev} > 0 \rightarrow \quad q_{tsb,F} = (q_{F,ev} c^* A_F + q_F c_{F,L} A_F)/\Delta s$

where c^* can be either $c_{F,sf}$ or zero. At the end the subsurface-to-surface solute exchange $q_{tsb,c}$, associated to cell C and used directly as input by the surface transport equation in the following time step, is calculated as:

$$q_{tsb,c} = \sum_{F \in \mathcal{F}_c} q_{tsb,F} \tag{5.14}$$

i.e., by summing up the values associated to the two faces defining C.

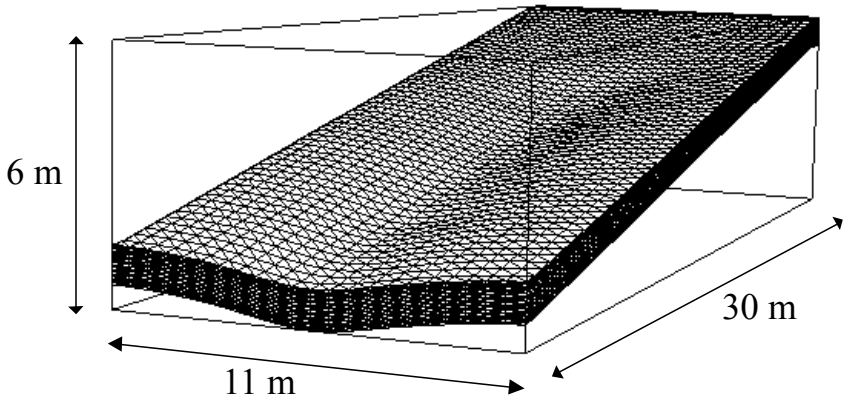

Figure 5.2: *3D numerical grid for the LEO landscape.*

5.4 Results

The model's performance is shown for three different scenarios that involve: 1) variably saturated subsurface flow and advective transport; 2) variably saturated subsurface flow and advective-dispersive transport; and 3) coupled surface-subsurface flow and transport. The test cases are designed to allow analysis of the HRFV model and velocity reconstruction algorithm, of the time-splitting algorithm for a variably saturated case, and of the algorithm which couples the surface and subsurface transport processes. The CATHY_FT model is run at the Landscape Evolution Observatory (LEO) [*Hopp et al.*, 2009].

LEO consists of three identical 30 m long and 11 m wide convergent hillslopes filled with 1 m of basaltic tephra ground to homogeneous loamy sand. The hillslopes are of 10° average slope. The surface of the LEO hillslope is discretized into 60 x 22 grid cells (1403 nodes and 2640 triangular elements). The resulting surface mesh is projected vertically to form a 3D tetrahedral mesh with 18 parallel layers of varying thickness (Figure 5.2). From top to bottom the thickness of the 18 layers is: 0.05 m for the first four layers, 0.06 m from layer 5 to layer 14, and 0.05 m from layer 15 to 18.

The first two scenarios reproduce the isotope tracer (deuterium, ^2H) experiment conducted at LEO in April 2013. A detailed description and a first modeling analysis of the experiment can be found in *Scudeler et al.* [2016b]. With the first scenario we compare the accuracy and quality of the CATHY_FT solution to the solution obtained in *Scudeler et al.* [2016b], where the subsurface transport equation was entirely solved with an FE-based model. It is well known that the FE method is subject to Peclet limitations when

applied to advection-dominated processes. To avoid oscillatory behavior one can impose a local grid Peclet number restriction, achievable by using a fine spatial discretization but at the expense of high computational effort, or apply an upwinding scheme, obtaining a first order accurate stable solution but with numerical diffusion smearing the front. CATHY_FT uses a more sophisticated numerical solver that is also better suited to simulate advective dominated processes and that does not suffer from Peclet limitations as the FE solution does. With the second scenario we compare the FE and CATHY_FT results when simulating both advection and dispersion in order to assess the quality and accuracy of the time-splitting technique implemented. The third scenario simulates a synthetic test case in the presence of water and solute injection and runoff generation, suitable to test the surface–subsurface transport coupling algorithms.

5.4.1 Isotope tracer experiment performed at LEO

During the first tracer experiment performed at LEO three pulses of rain at a rate of 12 mm/h were injected into the system: at the beginning (9.30 am, 13 April 2013) for 5.5 h, after 23.5 h for 6 h, and after 9 d (215.5 h) for 1.25 h + 4 h separated by 3 h with no rain. ^2H was introduced into the system with the second pulse of rain. Before this, the deficit (δ_{H^2}) measured in the system, as in the water of the first and third pulses, is 60‰. Initially the system was very dry since it had not been wetted for 6 weeks prior to the experiment. The estimated total initial volume of water is about 26 m^3 (the total storage capacity of the hillslope is 135 m^3). All the rain water applied infiltrated into the soil and generated seepage face outflow that started after 5 h and was characterized by two outflow peaks. No direct measurements of evaporation were made during the experiment. The estimated rate calculated from water balance calculations, which considered the total water storage and total seepage face flow recorded every 15 minutes, was 5 mm/d during rain pulses and 3.9 mm/d after the third pulse.

The flow solution is obtained with the same model setup and parameterization that in *Scudeler et al.* [2016b] was successfully used to reproduce the integrated flow response: rainfall and evaporation are handled with a Neumann (water flux) boundary condition, the outflow from the downslope vertical plane is modeled with a seepage face boundary, and on the remaining LEO boundaries a zero Neumann (water flux) condition is set; the initial conditions match the soil moisture distribution at each sensor location; spatially variable

rainfall is set according to analysis performed on the engineered rain system; anisotropy is added with vertical saturated hydraulic conductivity $K_v = 1.4 \times 10^{-4}$ m/s and horizontal conductivity $K_h = 6 \times 10^{-4}$ m/s; and heterogeneity is added with a lower conductivity at the seepage face ($K_{sf} = 2.2 \times 10^{-5}$ m/s) on the basis of a clogging hypothesis from accumulation of fine particles [*Niu et al.*, 2014b].

The resulting volumetric water content and velocity field, reconstructed at each time step, are used as input by the transport model, which is run for two different scenarios, the first for pure advection and the second for advection-dispersion with longitudinal dispersivity $\alpha_l = 0.01$ m and transverse dispersivity α_t one order of magnitude smaller than α_l. In the transport analysis the $\delta_2{}_H$ values are expressed in terms of c [-], which is the concentration relative to the minimum deficit 0. Concentration c=0 means that in the water the deficit is maximal (60‰), while c=1 means that in the water there is no deficit. As a consequence, as initial conditions c=0 is set everywhere. The surface boundary is treated as an inflow boundary during rainfall and an outflow boundary during evaporation. Cauchy conditions are used in the first case, with a Dirichlet-type condition implemented in the advective step and a zero-Neumann (dispersive) condition implemented in the dispersive step, when it takes place. In particular the Dirichlet concentration c_D is set to zero for the first and third pulses (during water injection) and to one for the second pulse (during ^2H-enriched water injection). Zero-Neumann (dispersive) conditions are used during evaporation, as solute outflow from the surface is only governed by the velocity field, with all the isotopic mass in solution with the evaporating water leaving the domain by advection. Solute outflow from the seepage face boundary, implemented at the downslope vertical plane boundary, is also governed by the velocity field. On all the other boundaries (the three other lateral boundaries and the base of the hillslope) a zero-Neumann (dispersive) condition is set in the dispersive step and, with the zero water flux condition imposed, solute advective flux is automatically zero as well.

Figures 5.3 and 5.4 compare the results obtained with the FE-based and HRFV-based models when simulating pure advection. For the FE-based model the instabilities arising from the Peclet limitations are controlled by reducing the grid spacing. The model could be run by setting a relatively small longitudinal and transverse dispersivity ($\alpha_l = 0.001$ m and α_t=0.0001 m), but mesh refinement was nonetheless required in order to maintain low Peclet numbers when capturing infiltration/evaporation fluxes and formation of base flow

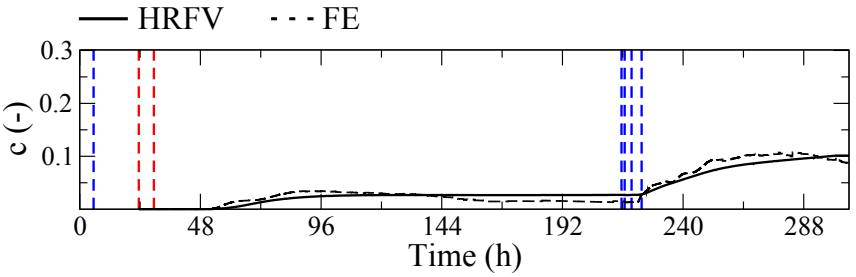

Figure 5.3: *Results for the average concentration at the seepage face obtained for the purely advective case. The vertical dashed lines indicate the timing of the three pulses of rain (red when the water is ^2H-enriched and blue when it is not).*

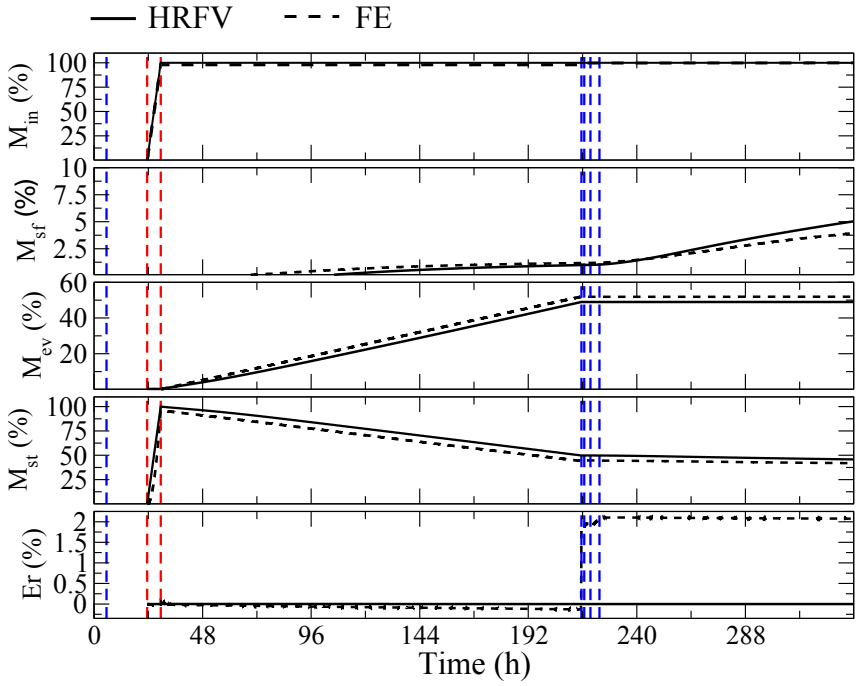

Figure 5.4: *Simulated mass balance results obtained for the purely advective case. From top to bottom: ^2H mass that enters the system, M_{in} (normalized with respect to the total mass added to the system during the simulation); that exits through the seepage face, M_{sf}; that exits through evaporation, M_{ev}; and that remains in storage, M_{st}. The bottom graph shows the cumulative mass balance error $E_r = (M_{in} - M_{sf} - M_{ev} - M_{st})$. The vertical dashed lines indicate the timing of the three pulses of rain (red when the water is ^2H-enriched and blue when it is not).*

and to avoid unbounded oscillatory behavior of the solution yielding failure to converge numerically. The 3D mesh employed for this FE run is formed by 30 layers of varying thickness (compared to 18 for the HRFV run), with the thinnest layers (0.01 m) assigned to the surface and bottom layers.

In Figure 5.3 we report the results for the average concentration at the seepage face. For both the FE and HRFV runs the curves look similar, with ^2H showing up after the second pulse and with the presence of a breakthrough after the third pulse. In contrast to the HRFV solution, the FE curve exhibits slight oscillatory behaviour, in particular towards the end of the simulation. These oscillations could be reduced by subjecting the method to further grid Peclet number restrictions. However, further mesh refining would easily render the computational costs unacceptably high. In contrast, the HRFV method shows robustness to Peclet limitations and potential oscillations are bounded by adapting the advective time-step size according to the CFL constraint. Since smaller time steps are employed only at times when large velocities occur, the computational efficiency is not affected as much as by grid restrictions. Moreover, in the HRFV scheme the algorithm can be easily accelerated by introducing a spatially variable time step size, which performs more advective time steps only where large velocities occur [*Mazzia and Putti*, 2005].

In Figure 5.4 we report the results in terms of a balance between the cumulative mass of deuterium that entered the hillslope (with the second rainfall pulse), that exited the system (through seepage face outflow and evaporation), and that remained in storage. For both the FE and HRFV runs at the end of the simulation a high percentage of the total mass of ^2H injected has been lost through evaporation while only a small percentage has seeped out, in accordance to the low concentration values obtained. The two solutions exhibit different mass balance behavior as at the end the FE cumulated mass balance error is 2% while for HRFV it is negligible and of order 10^{-5}% for the whole simulation. These results are evidence of the high accuracy that can be achieved with an advective transport solver that mimics a mass balance within each cell of the computational domain and that makes use of a mass-conservative velocity field, compared to the solution obtained with a classical FE model.

Figures 5.5 and 5.6 show the average concentration at the seepage face and the mass balance results when both models are run with longitudinal and transverse dispersivity of 0.01 m and 0.001 m, respectively. The results show that while the FE solution is not

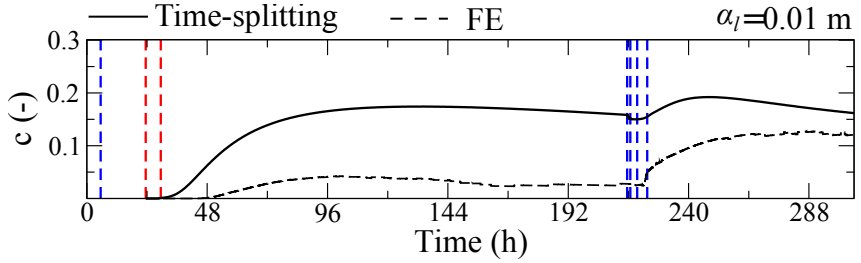

Figure 5.5: *Results for the average concentration at the seepage face obtained for the advective-dispersive case. The vertical dashed lines indicate the timing of the three pulses of rain (red when the water is ^2H-enriched and blue when it is not).*

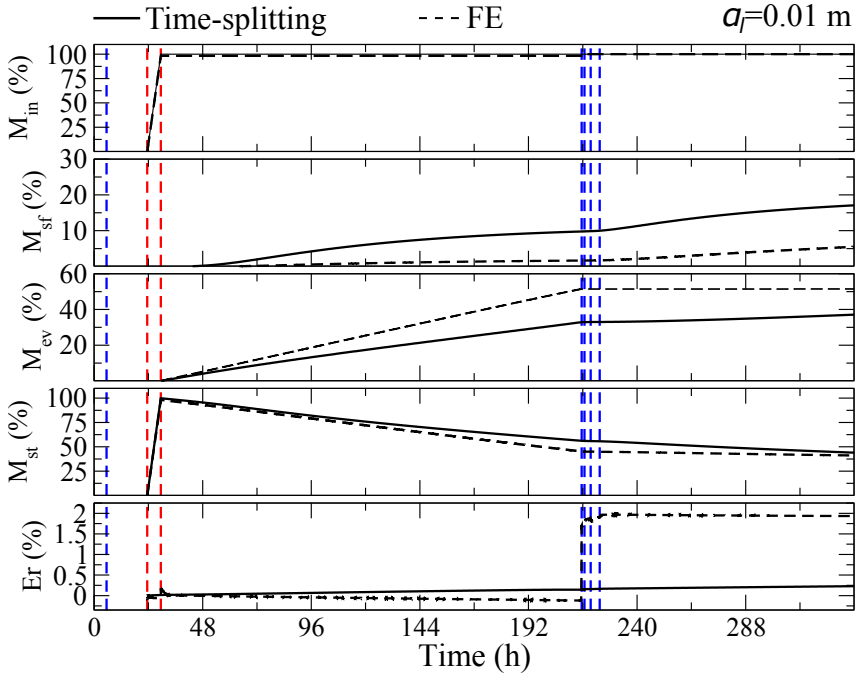

Figure 5.6: *Simulated mass balance results for the advective-dispersive case. From top to bottom: ^2H mass that enters the system, M_{in} (normalized with respect to the total mass added to the system during the simulation); that exits through the seepage face, M_{sf}; that exits through evaporation, M_{ev}; and that remains in storage, M_{st}. The bottom graph shows the cumulative mass balance error E_r=($M_{in} - M_{sf} - M_{ev} - M_{st}$). The vertical dashed lines indicate the timing of the three pulses of rain (red when the water is ^2H-enriched and blue when it is not).*

significantly affected by the increase in dispersivities, for the CATHY_FT (time-splitting) model the mass balances obtained by performing or not the dispersive step are completely different. Even for the relatively small dispersivity values used in this test, the total mass outflow from the seepage face at the end of the simulation as well as the concentration before the third pulse of rain are four times higher compared to the purely advective case. This clearly shows how the time-splitting procedure calculates greater dispersive flux than would occur by physical dispersion alone or would be indicated by an exact solution of the governing equation. This non-physical dispersion, which causes the solute to quickly spread and arrive at the discharge outlet, can be attributed to the node-to-element and element-to-node variable interpolations implemented to combine the node-based FE and element-based HRFV solutions. Thus, in this case the near-perfect mass balance obtained with the time-splitting approach (at the end of the simulation the cumulative mass balance error is 0.2% compared to 2% for the FE case) does not guarantee that a true or accurate solution has been achieved.

5.4.2 Synthetic test case involving surface–subsurface coupled processes

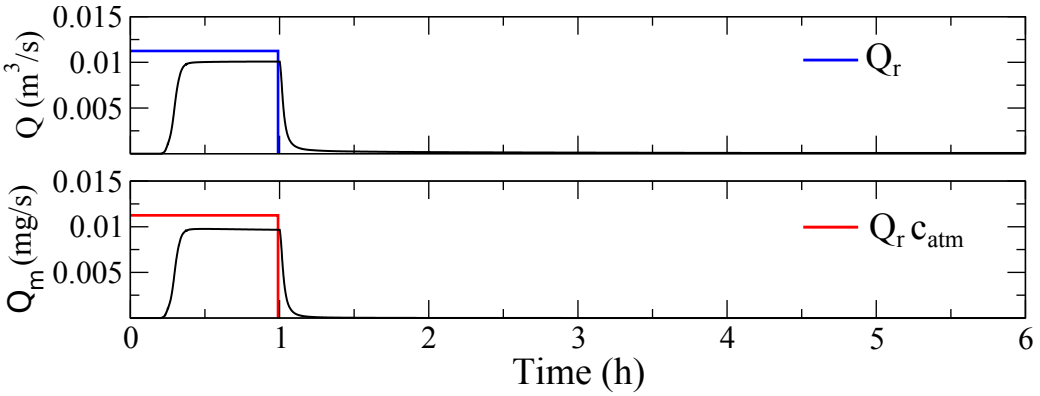

Figure 5.7: *Hydrological response to the synthetic test case involving coupled surface–subsurface processes: rain input pulse Q_r, solute input pulse $Q_r c_{atm}$ (c_{atm}=1 mg/m^3), and discharge Q and solute mass discharge Q_m at the surface outflow cell.*

We test the surface–subsurface coupling algorithm for a synthetic test case on the LEO hillslope (Figure 5.2). Solute mass is injected into the system with a pulse of rain at a rate of 118.8 mm/h for 1 h from the beginning of the simulation (rain input pulse

Q_r=1.125×10^{-2} m^3/s as shown in Figure 5.7 for a total of 40.4 m^3 of water volume injected). The tracer concentration in the rain water is set to c_{atm}=1 mg/m^3 (solute input pulse $Q_r c_{atm}$=1.125×10^{-2} mg/s as shown in Figure 5.7 for a total of 40.4 mg of solute mass injected). After this, zero evaporation is set until the end of the simulation, which is run for 36 h. Initially the water table is set at 0.6 m above the bottom with the pressure head hydrostatically distributed and the soil is solute-free. For the flow model setup we set a seepage face at the downslope vertical plane, atmospheric conditions at the surface (rainfall and evaporation) updated at each nonlinear iteration according to the surface conditions, and zero water flux conditions on all the other boundaries. On the transport side, we treat as an inflow boundary, an outflow boundary, and a zero-advective boundary each portion of the boundary characterized, respectively, by normal velocity components directed inside the domain, by normal velocity components directed outside, and by zero water flux conditions. The flow solution is obtained with a simple homogeneous parameterization: saturated hydraulic conductivity $K_s = 10^{-4}$ m/s, porosity $n = 0.39$, and elastic storage $S_s = 5 \times 10^{-3}$ 1/m. The van Genuchten retention curves are used with parameters $n_{VG} = 2.26$ (van Genuchten fitting parameter), residual moisture content S_{wr}=0.002, and ψ_{sat}=-0.6 m (parameter related to the air entry suction). The transport solution is obtained by performing only the advective step since both dispersivity and diffusion are set to zero.

The hydrological response is characterized by both outflow from the base of the hillslope and surface outflow. Seepage face outflow begins right from the start of the simulation as a direct outcome of the wet initial conditions. The discharge Q at the outlet (shown in Figure 5.7), starts during rainfall, reaches values comparable to the rain pulse rate Q_r, and ends a little bit after rainfall, shows that the surface soil gets quickly saturated and that the saturation mechanism is mainly Dunnian. On the transport side, mass discharge Q_m at the outlet (shown in Figure 5.7) behaves as the flow discharge Q, while solute mass at the seepage face shows up only towards the end of the rainfall event and with reduced rate compared to the flow. This means that seepage face outflow is mainly characterized by old water (water already present in the system before the injection).

In Figures 5.8 and 5.9 we show respectively the water and mass balance results for the simulation. At the end of the simulation (after 36 h), 63.6% of the total volume of water injected has seeped out and 70.58% has exited from the surface outlet. The cumulative

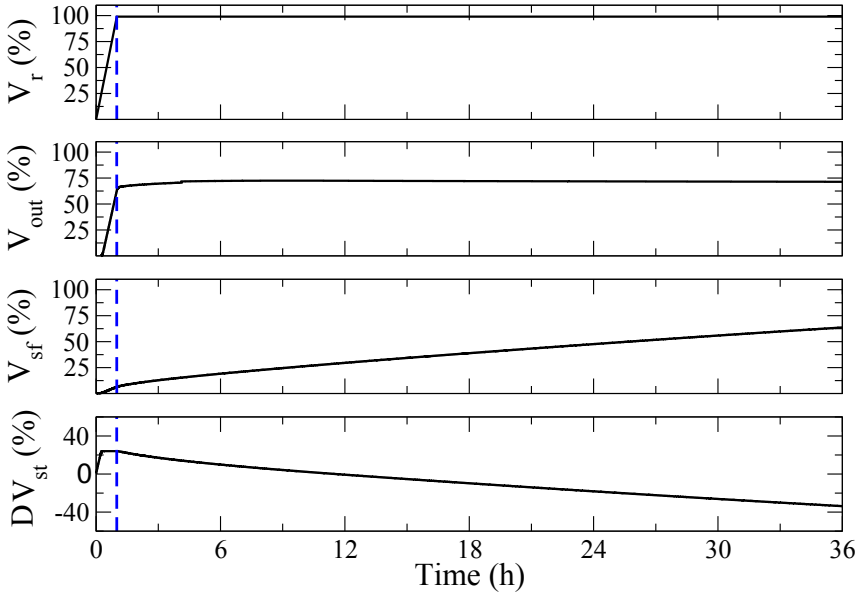

Figure 5.8: *Simulated water balance results. From top to bottom: cumulated volume of water that enters the system, V_r (normalized with respect to the total volume added to the system during the simulation); that flows out through the surface outlet, V_{out}; that exits through the seepage face, V_{sf}; and cumulated change in total water storage, DV_{st}. The blue vertical dashed line indicates the duration of the pulse of rain.*

change in water storage is -34.45% and the negative sign indicates that over the course of the simulation the total water storage decreases. The water balance error, calculated as $Er_v = V_{in} - V_{sf} - V_{out} - DV_{st}$ at the end of the simulation, is 0.27%. A good mass balance is also obtained for the transport. By the end of the simulation 5.95% of the total solute mass injected into the system has seeped out, 64.65% has exited through the surface outlet, and the rest remains in storage, minus a cumulative mass balance error ($Er_m = M_{in} - M_{sf} - M_{out} - M_{st}$) of 0.9%. The negative value of the total change in water storage obtained at the end of the simulation and the small seepage face component computed by the transport model compared to the flow are further evidence that the seepage face outflow is mainly characterized by old water.

5.5 Discussion and conclusions

Integrated modeling of solute transport in surface water and groundwater is a particularly complex problem involving many interacting processes and difficult physics and numer-

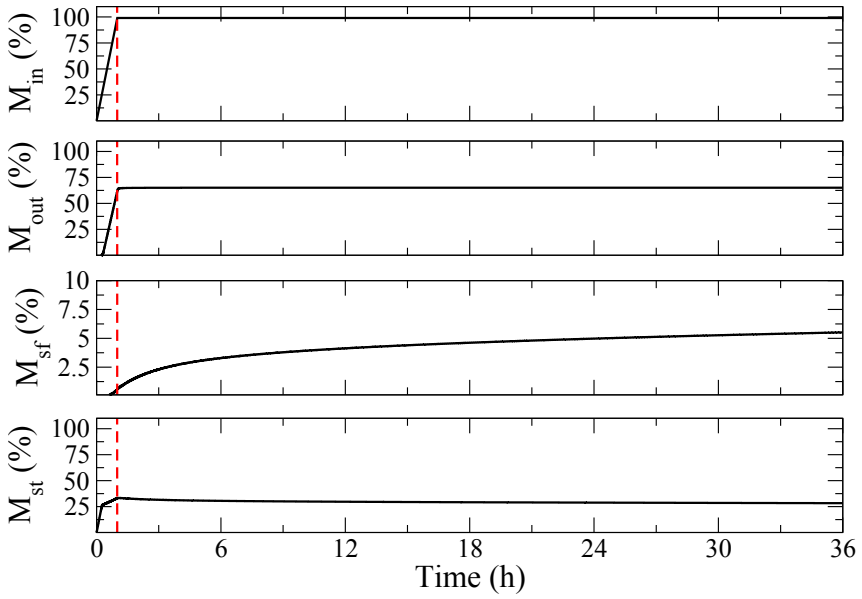

Figure 5.9: *Simulated mass balance results. From top to bottom: mass that enters the system, M_{in} (normalized with respect to the total mass added to the system during the simulation); that exits through the surface outlet, M_{out}; that exits through the seepage face, M_{sf}; and that remains in storage, M_{st}. The red vertical dashed line indicates the duration of the pulse of rain through which the solute was injected.*

ics. Hydrological models that incorporate a detailed description and resolution of solute surface–subsurface interactions are at their early stages and numerous specific improvements are possible, attainable only by performing thorough and rigorous analyses of their physical and numerical behavior. In this study we have addressed this challenge for the CATHY_FT model and we have described some of its features and identified some of the key issues associated to its further development, such as controlling numerical dispersion and mass balance errors, handling complex boundary conditions, and capturing process interactions.

The CATHY_FT model, first introduced by *Weill et al.* [2011], is an evolving physically-based model which couples the 3D Richards equation and advection-dispersion equation, used to describe subsurface flow and transport processes, with the diffusive wave equation, used to describe surface flow and solute transport propagation over the land surface and in stream channels. Its development has faced the challenge of approximating accurately and efficiently the difficult behavior of the advection-dispersion equation. Solving the advection-dispersion equation, in fact, is always very challenging since no numerical

method is optimal for the entire domain of problems, as has also been shown in this study. For example, finite element (FE) methods are ideal for dispersive processes whereas in advection-dominated processes their solution exhibits oscillatory behavior and/or excessive numerical dispersion near steep concentration gradients [*Guddati and Yue*, 2004]. On the other hand, methods which are adequate to preserve the steep gradients with minimal oscillations and numerical diffusion, such as high order Godunov-type finite volumes [e.g., *Dawson*, 1993; *Mazzia and Putti*, 2005] and discontinuous Galerkin finite elements [e.g., *Siegel et al.*, 1997; *Cockburn et al.*, 2000], are not ideal to discretize the dispersive component and are not compatible with finite element based flow models [*Dawson et al.*, 2004a; *Klausen and Russell*, 2004]. Previous studies related to the CATHY_FT model have shown that the use of the time-splitting operator, which adopts an appropriate numerical technique for advection and dispersion (e.g., high order Godunov finite volumes and mixed finite element (MFE) [*Mazzia and Putti*, 2005]), and of locally conservative methods (e.g., MFE [*Putti and Sartoretto*, 2009]) for the discretization of the flow equation give accurate results but at a high computational cost, this last arising from the computational effort required to solve the MFE systems.

To resolve the trade-off between model accuracy and computational cost, and thus avoid the use of MFE discretization, we have proposed a mass-conservative linear interpolation to combine an element-based high resolution (HRFV) scheme for advection and a node-based FE scheme for dispersion with a time-splitting operator, and we have resolved the incompatibility between the finite volume solver and the FE-based Richards' model by restoring the mass-conservation properties of the FE velocities with a post-processing technique [*Scudeler et al.*, 2016a]. The results of the simulations performed have demonstrated how for purely advective processes the new model gives a solution with near-perfect mass balance properties and successfully overcomes the limits associated with FE discretizations and the computational effort of MFE flow solutions. However, when simulating advective-dispersive processes, the numerical solution clearly introduces non-physical dispersion that causes the solute mass to quickly spread within the domain, and thus computational efficiency is gained at the expense of accuracy.

The transport boundary conditions are an additional source of numerical and physical complexity in the development of CATHY_FT. A value-dependent flux (or Cauchy boundary condition) is used to represent the solute inflow and outflow across the bound-

ary of the domain, with the advective exhanges governed by the actual fluxes across the boundaries and the dispersive exchanges governed by the concentration gradient. For numerical consistency, Dirichlet-type conditions are specified in the case of inflow in the advective part of the solution procedure while Neumann-type conditions are imposed in the dispersive step. Thus, a correct representation of the transport processes at the boundaries relies on the accurate resolution of both the water fluxes and concentration values to be eventually imposed. In this study we have shown how these modeling issues represent a particularly difficult problem when boundary conditions are used to represent solute interactions across the land surface. Boundary conditions together with mass balance calculations are accurately combined to resolve the solute exchanges between surface and subsurface. Satisfactory results have been obtained for saturation excess (Dunnian) surface runoff processes. However, additional tests should be conducted to evaluate if the method accurately extends to situations governed by infiltration excess (Hortonian) runoff and in the presence of evaporation. Further studies are also needed to quantify and assess the importance of diffusive exchanges between the surface and subsurface, currently neglected in CATHY_FT.

Numerous specific improvements and extensions are possible for the model. A future challenge will be resolving the efficiency and accuracy of the advection-dispersion numerical solution by using, for example, least squares reconstruction [*Coudière et al.*, 1999; *Manzini and Putti*, 2007] to evaluate nodal variables from cell averages, instead of with the linear interpolation as is currently used. Additional physical and numerical complexities will be introduced by incorporating, as the model continues to evolve, new features such as chemical reactions (e.g., first-order decay and adsorption), density-dependent solute transport (e.g., seawater intrusion phenomena), energy balance (including evapotranspiration and soil–vegetation interactions), and so on.

Chapter 6

Conclusions

This thesis has addressed some of the challenges related to the development and application of complex numerical models for integrated hydrological simulation. The work was performed in the framework of a specific model, the CATchment HYdrology Flow-Transport (CATHY_FT) model, and was elaborated into four specific objectives. In the first three studies, specific aspects related to state-of-the-art models (mass conservation, complex boundary conditions, and model testing and benchmarking) were analyzed, whereas in the final study the disparate elements were brought together into an updated, tested, and documented version of CATHY_FT.

The first study met the challenge of improving the numerical performance of the state-of-the-art hydrological models of both flow and transport phenomena. It was shown that the non mass-conservative nature of the velocity field arising from standard finite element (or $\mathcal{P}_1$ Galerkin) methods can cause problems for advective transport simulations, such as solute mass that easily exits from no-flux boundaries, solute mass that remains permanently entrapped in zones of low hydraulic conducticity, and the generation of artificial solute mass sources or sinks within some elements of the computational domain, eventually causing the simulation to abort. To overcome these issues, a post-processing technique capable of restoring the mass conservation properties starting from the $\mathcal{P}_1$ Galerkin velocity field was proposed. It was shown how this improves the overall accuracy of the companion advective transport model and, as a consequence, how post-processing strategies for velocity reconstruction represent an attractive alternative to the use of locally conservative methods, which require a much higher computational cost.

The second study concerned integrated surface water/groundwater resources modeling. By performing a detailed and novel analysis on the seepage face boundary condition, it

was shown how integrated modeling involves complex dynamic boundaries that require careful consideration. In particular, it was shown that a static condition is not always an adequate stand-in to model the dynamics of the seepage face boundary; that an algorithm capable of dealing with the multiple seepage faces/exit points case is necessary to model seepage faces in the presence of layered heterogeneity; and that a coupled surface-surface model is required to model seepage faces forming at the land surface because ponding, overland routing, re-infiltration, and return flow have a strong impact on the dynamics.

In the context of model testing and benchmarking, in the third study the CATHY_FT model was tested against a very detailed observation dataset obtained from a highly controlled flow and isotope tracer experiment performed at the Landscape Evolution Observatory. This study demonstrated the challenges in validating the new generation of integrated hydrological models and how complex the problem of model parameterization is when dealing with multiple processes and multivariate observations of both integrated and distributed nature.

Based partly on the insights gained from the first three studies, the final study arrived at a current version of the CATHY_FT model which reflects the numerical and physical processes represented. Important modeling issues related to the numerical resolution of the advective-dispersive equation and to complex coupling aspects were discussed. It was shown that, when combining finite volumes with finite elements in a time-splitting technique to solve the advective-dispersive equation, significant artificial spreading of the solution is introduced. On the other hand, the use of mixed finite elements instead of finite elements yields accurate but computationally expensive results. Concerning the coupling aspects, it was demonstrated how the transport boundary conditions are a source of numerical and physical complexity, particularly when they are used to represent solute interactions across the land surface. As of this writing, satisfactory results have been obtained when simulating solute exchanges during rainfall and saturation excess runoff and for advective exchanges, whereas additional analyses should be performed in order to test the model for situations involving evaporation, dispersive exchanges, and infiltration excess runoff.

This thesis demonstrated how accurate and reliable modeling of integrated processes requires continual updating, bringing code improvements such as advanced computational and numerical algorithms and exhaustively testing the model. As integrated hydrological

models continue to evolve, numerous challenges still need to be addressed. To give some examples: the efficiency and accuracy of the advection-dispersion numerical solution still needs to be improved; the importance of solute diffusive exchanges between the surface and subsurface should be assessed and quantified; the reliability of numerical models in performing hydrograph separation analysis or deciphering the paths and travel times of water and solutes needs to be enhanced; validation studies that extend model applications to complex field situations with detailed observation datasets should be performed; and, in the specific case of CATHY_FT, additional physical processes (e.g., chemical reactions, density-dependent solute transport, energy balance, ...) should be incorporated.

Bibliography

Agarwal, N., and T. J. Oden (1993), An unified approach to a posteriori error estimation using element residual methods, *Num. Mat.*, *65*, 23–50, doi:10.1007/BF01385738.

Ainsworth, M., and T. J. Oden (1992), A procedure for a posteriori error estimation for h-p finite element methods, *Comp. Methods App. Mech. Eng.*, *101*, 73–96, doi:10.1016/0045-7825(92)90016-D.

Ainsworth, M., and T. J. Oden (1993), A posteriori error estimation for second order elliptic systems. part 2. an optimal order process for calculating self equilibrating fluxes, *Comput. Math. Appl.*, *26*, 75–87, doi:10.1016/0898-1221(93)90007-I.

Anderman, E. R., and M. C. Hill (1999), A new multistage groundwater transport inverse method: presentation, evaluation, and implications, *Water Resour. Res.*, *35*(4), 1053–1063, doi:10.1029/1998WR900114.

Arbogast, T., C. N. Dawson, P. T. Keenan, M. F. Wheeler, and I. Yotov (1998), Enhanced cell-centered finite differences for elliptic equations on general geometry, *SIAM J. Sci. Comput.*, *19*(2), 404–425, doi:10.1137/S1064827594264545.

Ascher, U. M., S. J. Ruuth, and B. T. Wetton (1995), Implicit-explicit methods for time-dependent partial differential equations, *SIAM J. Num. Anal.*, *32*(3), 797–823, doi:10.1137/0732037.

Bahr, J. M., and J. Rubin (1987), Direct comparison of kinetic and local equilibrium formulations for solute transport affected by surface reactions, *Water Resour. Res.*, *23*(3), 438–452, doi:10.1029/WR023i003p00438.

Barlow, P. M., and E. G. Reichard (2010), Saltwater intrusion in coastal regions of North America, *Hydrogeol. J.*, *18*(1), 247–260, doi:10.1007/s10040-009-0514-3.

Barnes, C. J., and G. B. Allison (1988), Tracing of water movement in the unsaturated zone using stable isotopes of hydrogen and oxygen, *J. Hydrol.*, *100*(1), 143–176, doi: 10.1016/0022-1694(88)90184-9.

Barth, T. J., and D. C. Jespersen (1989), The design and application of upwind schemes on unstructured meshes, NASA Ames Research Center, American Institute of Aeronautics and Astronautics, doi:10.2514/6.1989-366.

Bear, J., and A. H.-D. Cheng (2010), *Modeling Groundwater Flow and Contaminant Transport*, Springer.

Beaugendre, H., A. Ern, T. Esclaffer, E. Gaume, I. Ginzburg, and C. Kao (2006), A seepage face model for the interaction of shallow water tables with the ground surface: Application of the obstacle-type method, *J. Hydrol.*, *329*(1–2), 258–273, doi:10.1016/j.jhydrol.2006.02.019.

Bergamaschi, L., and M. Putti (1999), Mixed finite elements and Newton-type linearizations for the solution of Richards equation, *Int. J. Numer. Methods Eng.*, *45*, 1025–1046, doi:10.1002/(SICI)1097-0207(19990720)45:8$\langle$\$1025::AID-NME615\$\rangle\$3.0.CO;2-G.

Bertolazzi, E., and G. Manzini (2005), A second-order maximum principle preserving finite volume method for steady convection-diffusion problems, *SIAM J. Num. Anal.*, *43*(5), 2172–2199, doi:10.1137/040607071.

Beven, K. (1977), Hillslope hydrographs by the finite element method, *Earth Surf. Process. Landforms*, *2*(1), 13–28, doi:10.1002/esp.3290020103.

Beven, K. (1989), Interflow, in *Unsaturated Flow in Hydrologic Modeling*, pp. 191–219, Springer, Netherlands, doi:10.1007/978-94-009-2352-2\$_\$7.

Beven, K., and E. F. Wood (1983), Catchment geomorphology and the dynamics of runoff contributing areas, *J. Hydrol.*, *65*(1–3), 139–158, doi:10.1016/0022-1694(83)90214-7.

Binley, A., J. Elgy, and K. Beven (1989), A physically based model of heterogeneous hillslopes: 1. Runoff production, *Water Resour. Res.*, *25*(6), 1219–1226, doi:10.1029/WR025i006p01219.

Birkholzer, J., and C.-F. Tsang (1997), Solute channeling in unsaturated heterogeneous porous media, *Water Resour. Res.*, *33*(10), 2221–2238, doi:10.1029/97WR01209.

Bixio, A., G. Gambolati, C. Paniconi, M. Putti, V. Shestopalov, V. Bublias, A. Bohuslavsky, N. Kasteltseva, and Y. Rudenko (2002), Modeling groundwater–surface water interactions including effects of morphogenetic depressions in the Chernobyl exclusion zone, *Environmental Geology*, *42*(2-3), 162–177, doi:10.1007/s00254-001-0486-7.

Boone, A., F. Habets, J. Noilhan, D. Clark, P. Dirmeyer, S. Fox, Y. Gusev, I. Haddeland, R. Koster, D. Lohmann, S. Mahanama, K. Mitchell, O. Nasonova, G.-Y. Niu, A. Pitman, J. Polcher, A. B. Shmakin, K. Tanaka, B. van den Hurk, S. Vrant, D. Verseghy, P. Viterbo, and Z.-L. Yang (2004), The Rhone-Aggregation land surface scheme intercomparison project: An overview, *J. Climate*, *17*(1), 187–208, doi:10.1175/1520-0442.

Botter, G., E. Bertuzzo, and A. Rinaldo (2010), Transport in the hydrologic response: Travel time distributions, soil moisture dynamics, and the old water paradox, *Water Resour. Res.*, *46*(3), doi:10.1029/2009WR008371, W03514.

Boughton, W. C. (1990), Systematic procedure for evaluating partial areas of watershed runoff, *J. Irrig. Drain. Eng.*, *116*(1), 83–98, doi:10.1061/(ASCE)0733-9437(1990)116:1(83).

Braud, I., P. Biron, T. Bariac, P. Richard, L. Canale, J. P. Gaudet, and M. Vauclin (2009), Isotopic composition of bare soil evaporated water vapor. Part i: RUBIC IV experimental setup and results, *J. Hydrol.*, *369*(12), 1–16, doi:10.1016/j.jhydrol.2009.01.034.

Brezzi, F., and M. Fortin (1991), *Mixed and Hybrid Finite Element Methods*, Springer.

Brezzi, F., L. D. Marini, and P. Pietra (1989), Two-dimensional exponential fitting and applications to drift-diffusion models, *SIAM J. Num. Anal.*, *26*(6), 1342–1355.

Bromly, M., and C. Hinz (2004), Non-Fickian transport in homogeneous unsaturated repacked sand, *Water Resour. Res.*, *40*(7), doi:10.1029/2003WR002579, W07402.

Brooks, P. D., J. Chorover, Y. Fan, S. E. Godsey, R. M. Maxwell, J. P. McNamara, and C. Tague (2015), Hydrological partitioning in the critical zone: Recent advances and

opportunities for developing transferable understanding of water cycle dynamics, *Water Resour. Res.*, *51*(9), 6973–6987, doi:10.1002/2015WR017039.

Brunner, P., J. Doherty, and C. T. Simmons (2012), Uncertainty assessment and implications for data acquisition in support of integrated hydrologic models, *Water Resour. Res.*, *48*(7), doi:10.1029/2011WR011342, W07513.

Burns, D. A. (2002), Stormflow-hydrograph separation based on isotopes: the thrill is gone-what's next?, *Hydrol. Proc.*, *16*(7), 1515–1517, doi:10.1002/hyp.5008.

Butters, G. L., W. A. Jury, and F. F. Ernst (1989), Field scale transport of bromide in an unsaturated soil: 1. Experimental methodology and results, *Water Resour. Res.*, *25*(7), 1575–1581, doi:10.1029/WR025i007p01575.

Cainelli, O., A. Bellin, and M. Putti (2012), On the accuracy of classic numerical schemes for modeling flow in saturated heterogeneous formations, *Adv. Water Resour.*, *47*, 43–55, doi:10.1016/j.advwatres.2012.06.016.

Camporese, M., S. Ferraris, M. Putti, P. Salandin, and P. Teatini (2006), Hydrological modeling in swelling/shrinking peat soils, *Water Resour. Res.*, *42*(6), W06,420, doi:10.1029/2005WR004495.

Camporese, M., C. Paniconi, M. Putti, and P. Salandin (2009), Ensemble Kalman filter data assimilation for a process-based catchment scale model of surface and subsurface flow, *Water Resour. Res.*, *45*(10), doi:10.1029/2008WR007031.

Camporese, M., C. Paniconi, M. Putti, and S. Orlandini (2010), Surface-subsurface flow modeling with path-based runoff routing, boundary condition-based coupling, and assimilation of multisource observation data, *Water Resour. Res.*, *46*(2), doi:10.1029/2008WR007536, W02512.

Casagrande, A. (1937), Seepage through dams, *J.-NEWWA*, *51*(2), 131–172.

Celia, M. A., E. T. Bouloutas, and R. L. Zarba (1990a), A general mass-conservative numerical solution for the unsaturated flow equation, *Water Resour. Res.*, *26*(7), 1483–1496, doi:10.1029/WR026i007p01483.

Celia, M. A., T. F. Russell, I. Herrera, and R. E. Ewing (1990b), An Eulerian-Lagrangian localized adjoint method for the advection-diffusion equation, *Adv. Water Resour.*, *13*(4), 187–206, doi:10.1016/0309-1708(90)90041-2.

Cheng, C., H. P. Cheng, M. W. Farthing, and C. E. Kees (2010), *Computing Locally-Mass-Conservative Fluxes from Multi-dimensional Finite Element Flow Simulations*, Technical note (System-Wide Water Resources Program), U.S. Army Engineer Research and Development Center, Vicksburg, MS.

Cheng, R. T., V. Casulli, and S. N. Milford (1984), Eulerian–Lagrangian solution of the convection-dispersion equation in natural coordinates, *Water Resour. Res.*, *20*(7), 944–952, doi:10.1029/WR020i007p00944.

Ciarlet, P. (1970), Discrete maximum principle for finite-difference operators, *Aequationes Math.*, *4*, 338–352.

Clark, I. D., and P. Fritz (1997), *Environmental Isotopes in Hydrogeology*, CRC Press, Boca Raton, Florida.

Cloke, H. L., J.-P. Renaud, A. J. Claxton, J. J. McDonnell, M. G. Anderson, J. R. Blake, and P. D. Bates (2003), The effect of model configuration on modelled hillslope-riparian interactions, *J. Hydrol.*, *279*(1-4), 167–181, doi:10.1016/S0022-1694(03)00177-X.

Cockburn, B., G. E. Karniadakis, and C.-W. Shu (2000), The development of discontinuous Galerkin Methods, in *Discontinuous Galerkin Methods: Theory, Computation and Applications*, chap. 1, pp. 3–50, Springer Berlin, doi:10.1007/978-3-642-59721-3_1.

Constantz, J. (2008), Heat as a tracer to determine streambed water exchanges, *Water Resour. Res.*, *44*(4), doi:10.1029/2008WR006996, W00D10.

Cooley, R. L. (1983), Some new procedures for numerical solution of variably saturated flow problems, *Water Resour. Res.*, *19*(5), 1271–1285, doi:10.1029/WR019i005p01271.

Cordes, C., and M. Putti (2001), Accuracy of Galerkin finite elements for groundwater flow simulations in two and three-dimensional triangulations, *Int. J. Numer. Methods Eng.*, *52*, 371–387, doi:10.1002/nme.194.

Coudière, Y., J.-P. Vila, and P. Villedieu (1999), Convergence rate of a finite volume scheme for a two-dimensional convection-diffusion problem, *Math. Model. Num. Anal.*, *33*(03), 493–516, doi:10.1051/m2an:1999149.

Courant, R., K. Friedrichs, and H. Lewy (1967), On the partial differential equations of mathematical physics, *IBM J. Res. Dev.*, *11*, 215–234, doi:10.1147/rd.112.0215.

Craig, H., and L. I. Gordon (1965), Deuterium and oxygen 18 variations in the ocean and the marine atmosphere. In: Stable Isotopes in Oceanographic Studies and Paleotemperatures, E. Tongiorgi (Ed.), pp. 9–130, Laboratorio di geologia nucleare, Pisa.

Crosta, G., and C. Prisco (1999), On slope instability induced by seepage face erosion, *Can. Geothec. J.*, *36*(6), 1056–1073, doi:10.1139/t99-062.

Dagès, C., C. Paniconi, and M. Sulis (2012), Analysis of coupling errors in a physically-based integrated surface water–groundwater model, *Adv. Water Resour.*, *49*, 86–96, doi:10.1016/j.advwatres.2012.07.019.

Dawson, C. (1993), Godunov-mixed methods for advection-diffusion equations in multidimensions, *SIAM J. Num. Anal.*, *30*(5), 1315–1332, doi:10.1137/0730068.

Dawson, C. (2008), A continuous/discontinuous Galerkin framework for modeling coupled subsurface and surface water flow, *Comput. Geosci.*, *12*, 451–472, doi:10.1007/s10596-008-9085-y.

Dawson, C., S. Sun, and M. F. Wheeler (2004a), Compatible algorithms for coupled flow and transport, *Comp. Methods App. Mech. Eng.*, *193*(23–26), 2565–2580, doi:10.1016/j.cma.2003.12.059.

Dawson, C., S. Sun, and M. F. Wheeler (2004b), Compatible algorithms for coupled flow and transport, *Comp. Methods App. Mech. Eng.*, *193*(23-26), 2565–2580, doi:10.1016/j.cma.2003.12.059.

Dawson, C. W., R. J. Abrahart, and L. M. See (2007), Hydrotest: a web-based toolbox of evaluation metrics for the standardised assessment of hydrological forecasts, *Environ. Model. Softw.*, *22*(7), 1034–1052, doi:10.1016/j.envsoft.2006.06.008.

De Smedt, F., and P. J. Wierenga (1984), Solute transfer through columns of glass beads, *Water Resour. Res.*, *20*(2), 225–232, doi:10.1029/WR020i002p00225.

Delfs, J.-O., C.-H. Park, and O. Kolditz (2009), A sensitivity analysis of Hortonian flow, *Adv. Water Resour.*, *32*(9), 1386–1395, doi:10.1016/j.advwatres.2009.06.005.

Diersch, H.-J. (1988), Finite element modelling of recirculating density-driven saltwater intrusion processes in groundwater, *Adv. Water Resour.*, *11*(1), 25–43, doi:10.1016/0309-1708(88)90019-X.

Durlofsky, L. J. (1994), Accuracy of mixed and control volume finite element approximations to Darcy velocity and related quantities, *Water Resour. Res.*, *30*(4), 965–973, doi:10.1029/94WR00061.

Edwards, M. G., and C. F. Rogers (1998), Finite volume discretization with imposed flux continuity for the general tensor pressure equation, *Comput. Geosci.*, *2*(4), 259–290, doi:10.1023/A:1011510505406.

Edwards, M. G., R. D. Lazarov, and I. Yotov (2002), Introduction to special issue on locally conservative numerical methods for flow in porous media, *Comput. Geosci.*, *6*(3), 225–225, doi:10.1023/A:1021267624044.

Eigenbrod, K. D., and N. R. Morgenstern (1972), A slide in cretaceous bedrock, Devon, Alberta, in *Geotechnical Practice for Stability in Open Pit Mining*, edited by C. O. Brawner and V. Milligan, pp. 223–238, American Institute of Mining Engineers, New York.

Farthing, M. W., C. E. Kees, and C. T. Miller (2002), Mixed finite element methods and higher-order temporal approximations, *Adv. Water Resour.*, *25*(1), 85–101, doi:10.1016/S0309-1708(01)00022-7.

Fenicia, F., H. H. G. Savenije, P. Matgen, and L. Pfister (2007), A comparison of alternative multiobjective calibration strategies for hydrological modeling, *Water Resour. Res.*, *43*, W03,434, doi:10.1029/2006WR005098.

Ferguson, G. P., D. L. Rudolph, and J. F. Barker (2009), Hydrodynamics of a large oil sand tailings impoundment and related environmental implications, *Can. Geothec. J.*, *46*(12), 1446–1460, doi:10.1139/T09-071.

Fiorentini, M., S. Orlandini, and C. Paniconi (2015), Control of coupling mass balance error in a process-based numerical model of surface-subsurface flow interaction, *Water Resour. Res.*, *51*(7), 5698–5716, doi:10.1002/2014WR016816.

Fiori, A., and D. Russo (2008), Travel time distribution in a hillslope: Insight from numerical simulations, *Water Resour. Res.*, *44*(12), W12,426, doi:10.1029/2008WR007135.

Fleckenstein, J. H., S. Krause, D. M. Hannah, and F. Boano (2010), Groundwater-surface water interactions: New methods and models to improve understanding of processes and dynamics, *Adv. Water Resour.*, *33*(11), 1291–1295, doi:10.1016/j.advwatres.2010.09.011.

Forsyth, P. A. (1991), A control volume finite element approach to NAPL groundwater contamination, *SIAM J. Sci. Stat. Comput.*, *12*(5), 1029–1057, doi:10.1137/0912055.

Freer, J., J. J. McDonnell, K. J. Beven, N. E. Peters, D. A. Burns, R. P. Hooper, B. Aulenbach, and C. Kendall (2002), The role of bedrock topography on subsurface storm flow, *Water Resour. Res.*, *38*(12), doi:10.1029/2001WR000872, 1269.

Freeze, R. A. (1971), Three-dimensional, transient, saturated-unsaturated flow in a groundwater basin, *Water Resour. Res.*, *7*(2), 347–366, doi:10.1029/WR007i002p00347.

Freeze, R. A. (1974), Streamflow generation, *Rev. Geophys.*, *12*(4), 627–647, doi:10.1029/RG012i004p00627.

Frei, S., J. H. Fleckenstein, S. J. Kollet, and R. M. Maxwell (2009), Patterns and dynamics of river–aquifer exchange with variably-saturated flow using a fully-coupled model, *J. Hydrol.*, *375*(3), 383–393, doi:10.1016/j.jhydrol.2009.06.038.

Frei, S., G. Lischeid, and J. H. Fleckenstein (2010), Effects of micro-topography on surface–subsurface exchange and runoff generation in a virtual riparian wetland-A modeling study, *Adv. Water Resour.*, *33*(11), 1388–1401, doi:10.1016/j.advwatres.2010.07.006.

Furman, A. (2008), Modeling coupled surface–subsurface flow processes: a review, *Vadose Zone J.*, *7*(2), 741–756, doi:10.2136/vzj2007.0065.

Gambolati, G., M. Putti, and C. Paniconi (1999), Three-dimensional model of coupled density-dependent flow and miscible salt transport, in *Seawater Intrusion in Coastal Aquifers*, chap. 10, Kluwer Academic Publishers, Dordrecht, The Netherlands.

Gauthier, M. J., M. Camporese, C. Rivard, C. Paniconi, and M. Larocque (2009), A modeling study of heterogeneity and surface water-groundwater interactions in the Thomas Brook catchment, Annapolis Valley (Nova Scotia, Canada), *Hydrol. Earth Syst. Sci.*, *13*(9), 1583–1596, doi:10.5194/hess-13-1583-2009.

Gevaert, A. I., A. J. Teuling, R. Uijlenhoet, S. B. DeLong, T. E. Huxman, L. Pangle, D. D. Breshears, J. Chorover, J. D. Pelletier, S. R. Saleska, X. Zeng, and P. A. Troch (2014), Hillslope-scale experiment demonstrates the role of convergence during two-step saturation, *Hydrol. Earth Syst. Sci.*, *18*(9), 3681–3692, doi:10.5194/hess-18-3681-2014.

Ghanbarian-Alavijeh, B., T. E. Skinner, and A. G. Hunt (2012), Saturation dependence of dispersion in porous media, *Phys. Rev. E*, *86*(6), doi:10.1103/PhysRevE.86.066316.

Gorelick, S. M., and C. Zheng (2015), Global change and the groundwater management challenge, *Water Resour. Res.*, *51*(5), 3031–3051, doi:10.1002/2014WR016825.

Goumiri, I. R., and J. H. Prevost (2011), Cell to node projections: An assessment of error, *Int. J. Numer. Anal. Methods Geom.*, *35*(7), 837–845, doi:10.1002/nag.927.

Guddati, M. N., and B. Yue (2004), Modified integration rules for reducing dispersion error in finite element methods, *Comp. Methods App. Mech. Eng.*, *193*(35), 275–287, doi:10.1016/j.cma.2003.09.010.

Gupta, H. V., S. Sorooshian, and O. P. Yapo (1998), Toward improved calibration of hydrologic models: Multiple and noncommensurable measures of information, *Water Resour. Res.*, *34*(4), 751–763, doi:10.1029/97WR03495.

Haggerty, R., C. F. Harvey, C. Freiherr von Schwerin, and L. C. Meigs (2004), What controls the apparent timescale of solute mass transfer in aquifers and soils? A comparison of experimental results, *Water Resour. Res.*, *40*(1), doi:10.1029/2002WR001716, W01510.

Harvey, J. W., and K. E. Bencala (1993), The effect of streambed topography on surface-subsurface water exchange in mountain catchments, *Water Resour. Res.*, *29*(1), 89–98, doi:10.1029/92WR01960.

Hassan, A., K. Pohlmann, and J. Chapman (2001), Uncertainty analysis of radionuclide transport in a fractured coastal aquifer with geothermal effects, *Transp. Porous Media*, *43*(1), 107–136, doi:10.1023/A:1010669711434.

Haverd, V., and M. Cuntz (2010), Soil-Litter-Iso: A one-dimensional model for coupled transport of heat, water and stable isotopes in soil with a litter layer and root extraction, *J. Hydrol.*, *388*(34), 438–455, doi:10.1016/j.jhydrol.2010.05.029.

Havis, R. N., R. E. Smith, and D. D. Adrian (1992), Partitioning solute transport between infiltration and overland flow under rainfall, *Water Resour. Res.*, *28*(10), 2569–2580, doi:10.1029/92WR01366.

Heidbüchel, I., P. A. Troch, and S. W. Lyon (2013), Separating physical and meteorological controls of variable transit times in zero-order catchments, *Water Resour. Res.*, *49*(11), 7644–7657, doi:10.1002/2012WR013149.

Heikkinen, P. M., M. L. Räisänen, and R. H. Johnson (2009), Geochemical characterisation of seepage and drainage water quality from two sulphide mine tailings impoundments: acid mine drainage versus neutral mine drainage, *Mine Water Environ.*, *28*(1), 30–49, doi:10.1007/s10230-008-0056-2.

Henderson-Sellers, A., Z.-L. Yang, and R. E. Dickinson (1993), The Project for Intercomparison of Land-surface Parameterization Schemes, *Bull. Am. Meteorol. Soc.*, *74*(7), 1335–1349, doi:10.1175/1520-0477.

Hess, K. M., S. H. Wolf, and M. A. Celia (1992), Large-scale natural gradient tracer test in sand and gravel, Cape Cod, Massachusetts: 3. Hydraulic conductivity variability and calculated macrodispersivities, *Water Resour. Res.*, *28*(8), 2011–2027, doi:10.1029/92WR00668.

Hill, A. (1990), Ground water flow paths in relation to nitrogen chemistry in the near-stream zone, *Hydrobiologia*, *206*(1), 39–52, doi:10.1007/BF00018968.

Hills, R. G., P. J. Wierenga, D. B. Hudson, and M. R. Kirkland (1991), The second Las Cruces trench experiment: experimental results and two-dimensional flow predictions, *Water Resour. Res.*, *27*(10), 2707–2718, doi:10.1029/91WR01538.

Hirschfeld, R. C., and S. J. Poulos (1973), *Embankment-Dam Engineering*, Wiley, New York.

Hofer, M., P. Lehmann, M. Stähli, S. Seifert, and M. Krafczyk (2012), Two approaches to modeling the initiation and development of rills in a man-made catchment, *Water Resour. Res.*, *48*(1), doi:10.1029/2011WR010719, W01531.

Hopp, L., C. Harman, S. L. E. Desilets, C. B. Graham, J. J. McDonnell, and P. A. Troch (2009), Hillslope hydrology under glass: confronting fundamental questions of soil-water-biota coevolution at Biosphere 2, *Hydrol. Earth Syst. Sci.*, *13*, 2105-2118, doi:10.5194/hess-13-2105-2009.

Horita, J., K. Rozanski, and S. Cohen (2008), Isotope effects in the evaporation of water: a status report of the Craig-Gordon model, *Isotopes Environ. Health Stud.*, *44*(1), 23–49, doi:10.1080/10256010801887174.

Hornberger, G. M., I. Remson, and A. A. Fungaroli (1969), Numeric studies of a composite soil moisture ground-water system, *Water Resour. Res.*, *5*(4), 797–802, doi:10.1029/WR005i004p00797.

Huxman, T., P. A. Troch, J. Chorover, D. D. Breshears, S. Saleska, J. Pelletier, X. Zeng, and J. Espeleta (2009), The hills are alive: interdisciplinary Earth science at Biosphere 2, *EOS Transactions of American Geophysical Union*, *90*, 120.

Huyakorn, P. S., and K. Nilkuha (1979), Solution of transient transport equation using an upstream finite element scheme, *Appl. Math. Model.*, *3*(1), 7–17, doi:10.1016/0307-904X(79)90062-3.

Huyakorn, P. S., J. W. Mercer, and D. S. Ward (1985), Finite element matrix and mass balance computational schemes for transport in variably saturated porous media, *Water Resour. Res.*, *21*(3), 346–358, doi:10.1029/WR021i003p00346.

Huyakorn, P. S., E. P. Springer, V. Guvanasen, and T. D. Wadsworth (1986a), A three-dimensional finite-element model for simulating water flow in variably saturated porous media, *Water Resour. Res.*, *20*(13), 1790–1808, doi:10.1029/WR022i013p01790.

Huyakorn, P. S., B. G. Jones, and P. F. Andersen (1986b), Finite element algorithms for simulating three-dimensional groundwater flow and solute transport in multilayer systems, *Water Resour. Res.*, *22*(3), 361–374, doi:10.1029/WR022i003p00361.

Huyakorn, P. S., P. F. Anderson, J. W. Mercer, and H. O. White (1987), Saltwater intrusion in aquifers: Development and testing of a three-dimensional finite element model, *Water Resour. Res.*, *23*(2), 293–312, doi:10.1029/WR023i002p00293.

Isaacs, L. T. (1980), Location of seepage free surface in finite element analyses, *Civil Eng. Trans., Australia*, *22*(1), 9–16.

Ivanov, V. Y., E. R. Vivoni, R. L. Bras, and D. Entekhabi (2004), Preserving high-resolution surface and rainfall data in operational-scale basin hydrology: a fully-distributed physically-based approach, *J. Hydrol.*, *298*(1), 80–111, doi:10.1016/j.jhydrol.2004.03.041.

Kampf, S. K., and S. J. Burges (2007), Parameter estimation for a physics-based distributed hydrologic model using measured outflow fluxes and internal moisture states, *Water Resour. Res.*, *43*(12), doi:10.1029/2006WR005605, W12414.

Keating, E. H., J. Doherty, J. A. Vrugt, and Q. Kang (2010), Optimization and uncertainty assessment of strongly nonlinear groundwater models with high parameter dimensionality, *Water Resour. Res.*, *46*(10), doi:10.1029/2009WR008584, W10517.

Kees, C. E., M. W. Farthing, and C. N. Dawson (2008), Locally conservative, stabilized finite element methods for variably saturated flow, *Comp. Methods App. Mech. Eng.*, *197*, 4610–4625, doi:10.1016/j.cma.2008.06.005.

Kees, C. E., I. Akkerman, M. W. Farthing, and Y. Bazilevs (2011), A conservative level set method suitable for variable-order approximations and unstructured meshes, *J. Comp. Phys.*, *230*(12), 4536–4558, doi:10.1016/j.jcp.2011.02.030.

Kelly, D. W. (1984), The self-equilibration of residuals and complementary a posteriori error estimates in the finite element method, *Int. J. Numer. Methods Eng.*, *20*, 1491–1506, doi:10.1002/nme.1620200811.

Kershaw, D. (1981), Differencing of the diffusion equation in Lagrangian hydrodynamics codes, *J. Comp. Phys.*, *39*, 375–395.

Klausen, R. A., and T. F. Russell (2004), Relationships among some locally conservative discretization methods which handle discontinuous coefficients, *Comput. Geosci.*, *8*(4), 341–377, doi:10.1007/s10596-005-1815-9.

Knabner, P., and L. Angermann (2003), *Numerical Methods for Elliptic and Parabolic Partial Differential Equations*, Texts in Applied Mathematics, Springer, New York.

Kolditz, O., S. Bauer, L. Bilke, N. Böttcher, J. O. Delfs, T. Fischer, U. Görke, T. Kalbacher, G. Kosakowski, C. McDermott, C. Park, F. Radu, K. Rink, H. Shao, H. B. Shao, F. Sun, Y. Y. Sun, A. K. Singh, J. Taron, M. Walther, W. Wang, N. Watanabe, Y. Wu, M. Xie, W. Xu, and B. Zehner (2012), OpenGeoSys: An open-source initiative for numerical simulation of thermo-hydro-mechanical/chemical processes in porous media, *Environ. Earth Sci.*, *67*(2), 589–599, doi:10.1007/s12665-012-1546-x.

Kollet, S. J., and R. M. Maxwell (2006), Integrated surface-groundwater flow modeling; a free-surface overland flow boundary condition in a parallel groundwater flow model, *Adv. Water Resour.*, *29*(7), 945–958, doi:10.1016/j.advwatres.2005.08.006.

Konikow, L. F. (2001), Use of numerical models to simulate groundwater flow and transport, in *Environmental Isotopes in the Hydrological Cycle: Principles and Applications*, edited by W. G. Mook, chap. 4, pp. 75–116, International Atomic Energy Agency, Vienna.

Konikow, L. F., and J. D. Bredehoeft (1992), Validation of geo-hydrological models part 1. Ground-water models cannot be validated, *Adv. Water Resour.*, *15*(1), 75–83, doi:10.1016/0309-1708(92)90033-X.

Konikow, L. F., W. E. Sanford, and P. J. Campbell (1997a), Constant-concentration boundary condition: Lessons from the HYDROCOIN variable-density groundwater benchmark problem, *Water Resour. Res.*, *33*(10), 2253–2261, doi:10.1029/97WR01926.

Konikow, L. F., W. E. Sanford, and P. J. Campbell (1997b), Constant-concentration boundary condition: lessons from the HYDROCOIN variable-density groundwater benchmark problem, *Water Resour. Res.*, *33*, 2253–2261, doi:10.1029/97WR01926.

Kumar, M., C. J. Duffy, and K. M. Salvage (2009), A second-order accurate, finite volume-based, integrated hydrologic modeling framework for simulation of surface and subsurface flow, *Vadose Zone J.*, *8*(4), 873–890, doi:0.2136/vzj2009.0014.

Kumar, R., L. Samaniego, and S. Attinger (2013), Implications of distributed hydrologic model parameterization on water fluxes at multiple scales and locations, *Water Resour. Res.*, *49*(1), 360–379, doi:10.1029/2012WR012195.

LaBolle, E. M., G. E. Fogg, J. B. Eweis, J. Gravner, and D. G. Leaist (2008), Isotopic fractionation by diffusion in groundwater, *Water Resour. Res.*, *44*(7), doi:10.1029/2006WR005264, W07405.

Lam, L., D. G. Fredlund, and S. L. Barbour (1987), Transient seepage model for saturated-unsaturated soil systems: a geotechnical engineering approach, *Can. Geothec. J.*, *24*(4), 565–580, doi:10.1139/t87-071.

Larson, M. G., and A. J. Niklasson (2004), A conservative flux for the continuous Galerkin method based on discontinuous enrichment, *Calcolo*, *41*(2), 65–76, doi:10.1007/s10092-004-0084-7.

Larsson, A. (1992), The international projects INTRACOIN, HYDROCOIN and INTRAVAL, *Adv. Water Resour.*, *15*(1), 85–87, doi:10.1016/0309-1708(92)90034-Y.

Le Potier, C. (2005), Schéma volumes finis monotone pour des opérateurs de diffusion fortement anisotropes sur des maillages de triangles non structurés, *C. R. Math. Acad. Sci. Paris*, *341*(12), 787–792.

LeBlanc, D. R., S. P. Garabedian, K. M. Hess, L. W. Gelhar, R. D. Quadri, K. G. Stollenwerk, and W. W. Wood (1991), Large-scale natural gradient tracer test in sand and gravel, Cape Cod, Massachusetts: 1. Experimental design and observed tracer movement, *Water Resour. Res.*, *27*(5), 895–910, doi:10.1029/91WR00241.

Lee, Y. S., C. Y. Cheuk, and M. D. Bolton (2008), Instability caused by a seepage impediment in layered fill slopes, *Can. Geothec. J.*, *45*(10), 1410–1425, doi:10.1139/T08-067.

Leij, F. J., T. H. Skaggs, and M. T. Van Genuchten (1991), Analytical solutions for solute transport in three-dimensional semi-infinite porous media, *Water Resour. Res.*, *27*(10), 2719–2733, doi:10.1029/91WR01912.

Mackay, D. M., D. L. Freyberg, P. V. Roberts, and J. A. Cherry (1986), A natural gradient experiment on solute transport in a sand aquifer: 1. Approach and overview of plume movement, *Water Resour. Res.*, *22*(13), 2017–2029, doi:10.1029/WR022i013p02017.

Manoli, G., S. Bonetti, J.-C. Domec, M. Putti, G. Katul, and M. Marani (2014), Tree root systems competing for soil moisture in a 3d soil–plant model, *Adv. Water Resour.*, *66*, 32–42, doi:10.1016/j.advwatres.2014.01.006.

Manzini, G., and M. Putti (2007), Mesh locking effects in the finite volume solution of 2-D anisotropic diffusion equations, *J. Comp. Phys.*, *220*(2), 751–771, doi:10.1016/j.jcp.2006.05.026.

Maxwell, R. M., M. Putti, S. Meyerhoff, O. Delfs, I. M. Ferguson, V. Ivanov, J. Kim, O. Kolditz, S. J. Kollet, M. Kumar, S. Lopez, J. Niu, C. Paniconi, Y. J. Park, M. S. Phanikumar, C. Shen, E. A. Sudicky, and M. Sulis (2014), Surface-subsurface model intercomparison: A first set of benchmark results to diagnose integrated hydrology and feedbacks, *Water Resour. Res.*, *50*(2), 1531–1549, doi:10.1002/2013WR013725.

Mazzia, A. (1999), Mixed finite elements and finite volumes for the solution of density dependent flow and transport of radioactive contaminants in porous media, Ph.D. thesis, University of Padua.

Mazzia, A. (2008), An analysis of monotonicity conditions in the mixed hybrid finite element method on unstructured triangulations, *Int. J. Numer. Meth. Engnrg.*, *76*(3), 351–375.

Mazzia, A., and M. Putti (2005), High order Godunov mixed methods on tetrahedral meshes for density driven flow simulations in porous media, *J. Comp. Phys.*, *208*(1), 154–174, doi:10.1016/j.jcp.2005.01.029.

Mazzia, A., L. Bergamaschi, and M. Putti (2000), A time-splitting technique for advection-dispersion equation in groundwater, *J. Comp. Phys.*, *157*, 181–198, doi: 10.1006/jcph.1999.6370.

Mazzia, A., L. Bergamaschi, and M. Putti (2001), On the reliability of numerical solution of brine transport in groundwater: analysis of infiltration from a salt lake, *Transp. Porous Media*, *43*(1), 65–86, doi:10.1023/A:1010665609617.

Mazzia, A., L. Bergamaschi, C. Dawson, and M. Putti (2002), Godunov mixed methods on triangular grids for advection–dispersion equations, *Comput. Geosci.*, *6*(2), 123–139, doi:10.1023/A:1019963900511.

Mazzia, A., G. Manzini, and P. M. (2011), Bad behavior of Godunov mixed methods for strongly anisotropic advection-dispersion equations, *J. Comp. Phys.*, *230*(23), 8410–8426, doi:10.1016/j.jcp.2011.07.021.

McCord, J. T., D. B. Stephens, and J. L. Wilson (1991), Hysteresis and state-dependent anisotropy in modeling unsaturated hillslope hydrologic processes, *Water Resour. Res.*, *27*(7), 1501–1518, doi:10.1029/91WR00880.

Milligan, V. (2003), Some uncertainties in embankment dam engineering, *J. Geotech. Geoenviron. Eng.*, *129*(9), 785–797, doi:10.1061/(ASCE)1090-0241(2003)129:9-(785).

Mishra, S., and J. C. Parker (1989), Parameter estimation for coupled unsaturated flow and transport, *Water Resour. Res.*, *25*(3), 385–396, doi:10.1029/WR025i003p00385.

Moretti, G., and S. Orlandini (2008), Automatic delineation of drainage basins from contour elevation data using skeleton construction techniques, *Water Resour. Res.*, *44*(5), W05,403, doi:10.1029/2007WR006309.

Naff, R. L. (1990), On the nature of the dispersive flux in saturated heterogeneous porous media, *Water Resour. Res.*, *26*(5), 1013–1026, doi:10.1029/WR026i005p01013.

Neuman, S. P. (1973), Saturated-unsaturated seepage by finite elements, *J. Hydraul. Div. ASCE*, *99*(HY12), 2233–2250.

Neuman, S. P., and P. A. Witherspoon (1970), Finite element method of analyzing steady seepage with a free surface, *Water Resour. Res.*, *6*(3), 889–897, doi: 10.1029/WR006i003p00889.

Neuman, S. P., R. A. Feddes, and E. Bresler (1975), Finite element analysis of two-dimensional flow in soils considering water uptake by roots, *Soil Sci. Soc. Amer. J.*, *39*(2), 224–237, doi:10.2136/sssaj1975.03615995003900020007x.

Neuweiler, I., and O. A. Cirpka (2005), Homogenization of richards equation in permeability fields with different connectivities, *Water Resour. Res.*, *41*(2), doi:10.1029/2004WR003329, W02009.

Niu, G.-Y., C. Paniconi, P. A. Troch, R. L. Scott, M. Durcik, X. Zeng, T. Huxman, and D. C. Goodrich (2014a), An integrated modelling framework of catchment-scale ecohydrological processes: 1. model description and tests over an energy-limited watershed, *Ecohydrology*, *7*(2), 427–439, doi:10.1002/eco.1362.

Niu, G.-Y., D. Pasetto, C. Scudeler, C. Paniconi, M. Putti, P. A. Troch, S. B. DeLong, K. Dontsova, L. Pangle, D. D. Breshears, J. Chorover, T. E. Huxman, J. Pelletier, S. R. Saleska, and X. Zeng (2014b), Incipient subsurface heterogeneity and its effect on overland flow generation–Insight from a modeling study of the first experiment at the Biosphere 2 Landscape Evolution Observatory, *Hydrol. Earth Syst. Sci.*, *18*(5), 1873–2014, doi:10.5194/hess-18-1873-2014.

Ogden, F. L., and B. A. Watts (2000), Saturated area formation on nonconvergent hillslope topography with shallow soils: A numerical investigation, *Water Resour. Res.*, *36*(7), 1795–1804, doi:10.1029/2000WR900091.

Orlandini, S., and R. Rosso (1996), Diffusion wave modeling of distributed catchment dynamics, *J. Hydrologic Engrg. ASCE*, *1*(3), 103–113, doi:10.1061/(ASCE)1084-0699(1996)1:3(103).

Orlandini, S., and R. Rosso (1998), Parametrization of stream channel geometry in the distributed modeling of catchment dynamics, *Water Resour. Res.*, *34*(8), 1971–1985, doi:10.1029/98WR00257.

Packman, A. I., and K. E. Bencala (2000), Modeling surface-subsurface hydrological interactions, in *Streams and Ground Waters*, edited by J. B. J. J. Mulholland, Aquatic Ecology, pp. 45–80, Academic Press, San Diego, doi:10.1016/B978-012389845-6/50003-X.

Padilla, I. Y., T.-C. J. Yeh, and M. H. Conklin (1999), The effect of water content on solute transport in unsaturated porous media, *Water Resour. Res.*, *35*(11), 3303–3313, doi:10.1029/1999WR900171.

Panday, S., and P. S. Huyakorn (2004), A fully coupled physically-based spatially-distributed model for evaluating surface/subsurface flow, *Adv. Water Resour.*, *27*, 361–382, doi:10.1016/j.advwatres.2004.02.016.

Panday, S., P. S. Huyakorn, R. Therrien, and R. L. Nichols (1993), Improved three-dimensional finite-element techniques for field simulation of variably saturated flow and transport, *J. Contam. Hydrol.*, *12*(1), 3–33, doi:10.1016/0169-7722(93)90013-I.

Pangle, L. A., S. B. DeLong, N. Abramson, J. Adams, G. Barron-Gafford, D. D. Breshears, P. Brooks, J. Chorover, W. E. Dietrich, K. Dontsova, M. Durcik, J. Espeleta, T. P. A. Ferre, R. Ferriere, W. Henderson, E. Hunt, T. E. Huxman, D. Millar, B. Murphy, G.-Y. Niu, M. Pavao-Zuckerman, J. D. Pelletier, C. Rasmussen, J. Ruiz, S. Saleska, M. Schaap, M. Sibayan, P. Troch, M. Tuller, J. van Haren, and X. Zeng (2015), Landscape Evolution Observatory: A large-scale controllable infrastructure to study coupled Earth-surface processes, *Geomorphology*, *244*, 190–203, doi:10.1016/j.geomorph.2015.01.020.

Paniconi, C., and M. Putti (1994), A comparison of Picard and Newton iteration in the numerical solution of multidimensional variably saturated flow problems, *Water Resour. Res.*, *30*(12), 3357–3374, doi:10.1029/94WR02046.

Paniconi, C., and M. Putti (2015), Physically based modeling in catchment hydrology at 50: Survey and outlook, *Water Resour. Res.*, *51*(9), 7090–7129, doi:10.1002/2015WR017780.

Paniconi, C., and E. F. Wood (1993), A detailed model for simulation of catchment scale subsurface hydrologic processes, *Water Resour. Res.*, *29*(6), 1601–1620, doi:0.1029/92WR02333.

Paniconi, C., I. Khlaifi, G. Lecca, A. Giacomelli, and J. Tarhouni (2001), Modeling and analysis of seawater intrusion in the coastal aquifer of eastern Cap-Bon, Tunisia, *Transp. Porous Media*, *43*(1), 3–28, doi:10.1023/A:1010600921912.

Paniconi, C., M. Marrocu, M. Putti, and M. Verbunt (2003a), Newtonian nudging for a Richards equation-based distributed hydrological model, *Adv. Water Resour.*, *26*(2), 161–178, doi:10.1016/S0309-1708(02)00099-4.

Paniconi, C., P. A. Troch, E. E. van Loon, and A. G. J. Hilberts (2003b), Hillslope-storage Boussinesq model for subsurface flow and variable source areas along complex hillslopes: 2. Intercomparison with a three-dimensional Richards equation model, *Water Resour. Res.*, *39*(11), doi:10.1029/2002WR001730, 1317.

Parker, J. C., and M. T. van Genuchten (1984), Flux-averaged and volume-averaged concentrations in continuum approaches to solute transport, *Water Resour. Res.*, *20*(7), 866–872, doi:10.1029/WR020i007p00866.

Pasetto, D., M. Camporese, and M. Putti (2012), Ensemble Kalman filter versus particle filter for a physically-based coupled surface–subsurface model, *Adv. Water Resour.*, *47*, 1–13, doi:10.1016/j.advwatres.2012.06.009.

Pasetto, D., G.-Y. Niu, L. Pangle, C. Paniconi, M. Putti, and P. A. Troch (2015), Impact of sensor failure on the observability of flow dynamics at the Biosphere 2 LEO hillslopes, *Adv. Water Resour.*, *86*, 327–339, doi:10.1016/j.advwatres.2015.04.014.

Passadore, G., M. Monego, L. Altissimo, A. Sottani, M. Putti, and A. Rinaldo (2012), Alternative conceptual models and the robustness of groundwater management scenarios in the multi-aquifer system of the Central Veneto Basin, Italy, *Hydrogeol. J.*, *20*(3), 419–433, doi:10.1007/s10040-011-0818-y.

Pinder, G. F., and E. O. Frind (1972), Application of Galerkin's procedure to aquifer analysis, *Water Resour. Res.*, *8*(1), 108–120, doi:10.1029/WR008i001p00108.

Pohlmann, K., A. Hassan, and J. Chapman (2000), Description of hydrogeologic heterogeneity and evaluation of radionuclide transport at an underground nuclear test, *J. Contam. Hydrol.*, *44*(34), 353–386, doi:10.1016/S0169-7722(00)00100-5.

Povich, T. J., C. N. Dawson, M. W. Farthing, and C. E. Kees (2013), Finite element methods for variable density flow and solute transport, *Comput. Geosci.*, *17*(3), 529–549, doi:10.1007/s10596-012-9330-2.

Prommer, H., D. A. Barry, and C. Zheng (2003), MODFLOW/MT3DMS-based reactive multicomponent transport modeling, *Ground Water*, *41*(2), 247–257, doi:10.1111/j.1745-6584.2003.tb02588.x.

Pruess, K., J. Garca, T. Kovscek, C. Oldenburg, J. Rutqvist, C. Steefel, and T. Xu (2004), Code intercomparison builds confidence in numerical simulation models for geologic disposal of CO2, *Energy*, *29*(9–10), 1431–1444, doi:10.1016/j.energy.2004.03.077.

Putti, M., and C. Cordes (1998), Finite element approximation of the diffusion operator on tetrahedra, *SIAM J. Sci. Comput.*, *19*(4), 1154–1168, doi:10.1137/S1064827595290711.

Putti, M., and C. Paniconi (1995), Picard and Newton linearization for the coupled model for saltwater intrusion in aquifers, *Water Resour. Res.*, *18*(3), 159–170, doi:10.1016/0309-1708(95)00006-5.

Putti, M., and F. Sartoretto (2009), Linear Galerkin vs mixed finite element 2D flow fields, *Int. J. Numer. Methods Fluids*, *60*(9), 1011–1031, doi:10.1002/fld.1929.

Raoof, A., and S. M. Hassanizadeh (2013), Saturation-dependent solute dispersivity in porous media: Pore-scale processes, *Water Resour. Res.*, *49*(4), 1943–1951, doi:10.1002/wrcr.20152.

Rathfelder, K., and L. M. Abriola (1994), Mass conservative numerical solutions of the head-based richards equation, *Water Resour. Res.*, *30*(9), 2579–2586, doi:10.1029/94WR01302.

Reed, J. (1980), Type curves for selected problems of flow to wells in confined aquifers, *Techniques of Water-Res. Invests. of the U.S. Geol. Survey (Book 3: Applications of hydraulics; chapter B3)*.

Refsgaard, J. C. (1997), Parameterisation, calibration and validation of distributed hydrological models, *J. Hydrol.*, *198*(14), 69–97, doi:10.1016/S0022-1694(96)03329-X.

Rodriguez-Iturbe, I. (2000), Ecohydrology: A hydrologic perspective of climate-soil-vegetation dynamies, *Water Resour. Res.*, *36*(1), 3–9, doi:10.1029/1999WR900210.

Rubin, J. (1968), Theoretical analysis of two-dimensional, transient flow of water in unsaturated and partly unsaturated soils, *Soil Sci. Soc. Amer. J.*, *32*(5), 607–615, doi:10.2136/sssaj1968.03615995003200050013x.

Rubin, J. (1983), Transport of reacting solutes in porous media: Relation between mathematical nature of problem formulation and chemical nature of reactions, *Water Resour. Res.*, *19*(5), 1231–1252, doi:10.1029/WR019i005p01231.

Rulon, J. J., and A. R. Freeze (1985), Multiple seepage faces on layered slopes and their implications for slope-stability analysis, *Can. Geothec. J.*, *22*(3), 347–356, doi:10.1139/t85-047.

Rulon, J. J., R. Rodway, and R. A. Freeze (1985), The development of multiple seepage faces on layered slopes, *Water Resour. Res.*, *21*(11), 1625–1636, doi:10.1029/WR021i011p01625.

Russo, D., and A. Fiori (2009), Stochastic analysis of transport in a combined heterogeneous vadose zone-groundwater flow system, *Water Resour. Res.*, *45*(3), doi:10.1029/2008WR007157, W03426.

Russo, D., W. A. Jury, and G. L. Butters (1989a), Numerical analysis of solute transport during transient irrigation: 1. The effect of hysteresis and profile heterogeneity, *Water Resour. Res.*, *25*(10), 2109–2118, doi:10.1029/WR025i010p02109.

Russo, D., W. A. Jury, and G. L. Butters (1989b), Numerical analysis of solute transport during transient irrigation: 2. The effect of immobile water, *Water Resour. Res.*, *25*(10), 2119–2127, doi:10.1029/WR025i010p02119.

Russo, D., J. Zaidel, and A. Laufer (1998), Numerical analysis of flow and transport in a three-dimensional partially saturated heterogeneous soil, *Water Resour. Res.*, *34*(6), 1451–1468, doi:10.1029/98WR00435.

Russo, D., A. Laufer, Z. Gerstl, D. Ronen, N. Weisbrod, and E. Zentner (2014), On the mechanism of field-scale solute transport: Insights from numerical simulations and field observations, *Water Resour. Res.*, *50*(9), 7484–7504, doi:10.1002/2014WR015514.

Scanlon, B. R., M. Christman, R. C. Reedy, I. Porro, J. Simunek, and G. N. Flerchinger (2002), Intercode comparisons for simulating water balance of surficial sediments in semiarid regions, *Water Resour. Res.*, *38*(12), doi:10.1029/2001WR001233, 1323.

Schiavazzi, D. (2011), Redundant multiresolution uncertainty propagation, Ph.D. thesis, University of Padua.

Scudeler, C., M. Putti, and C. Paniconi (2016a), Mass-conservative reconstruction of Galerkin velocity fields for transport simulations, *Adv. Water Resour.*, *94*, 470–485, doi:10.1016/j.advwatres.2016.06.011.

Scudeler, C., L. Pangle, D. Pasetto, G.-Y. Niu, T. Volkmann, C. Paniconi, M. Putti, and P. Troch (2016b), Multiresponse modeling of variably saturated flow and isotope tracer transport for a hillslope experiment at the Landscape Evolution Observatory, *Hydrol. Earth Syst. Sci.*, doi:10.5194/hess-20-1-2016.

Scudeler, C., C. Paniconi, D. Pasetto, and M. Putti (2016c), Examination of the seepage face boundary condition in subsurface and coupled surface/subsurface hydrological models, *Submitted to Water Resour. Res.*

Sebben, M. L., A. D. Werner, J. E. Liggett, D. Partington, and C. T. Simmons (2013), On the testing of fully integrated surface-subsurface hydrological models, *Hydrol. Proc.*, *27*(8), 1276–1285, doi:10.1002/hyp.9630.

Shamsai, A., and T. N. Narasimhan (1991), A numerical investigation of free surface-seepage face relationship under steady state flow conditions, *Water Resour. Res.*, *27*(3), 409–421, doi:10.1029/90WR01905.

Shen, C., and M. S. Phanikumar (2010), A process-based, distributed hydrologic model based on a large-scale method for surface-subsurface coupling, *Adv. Water Resour.*, *33*(12), 1524–1541, doi:10.1016/j.advwatres.2010.09.002.

Siegel, P., R. Mosé, P. Ackerer, and J. Jaffre (1997), Solution of the advection–diffusion equation using a combination of discontinuous and mixed finite elements, *Int. J. Numer. Methods Fluids*, *24*(6), 595–613, doi:10.1002/(SICI)1097-0363(19970330)24:6$\langle$$595::AID-FLD512$\rangle$$3.0.CO;2-I.

Simmons, C. T., K. A. Narayan, and R. A. Wooding (1999), On a test case for density-dependent groundwater flow and solute transport models: The Salt Lake Problem, *Water Resour. Res.*, *35*(12), 3607–3620, doi:10.1029/1999WR900254.

Simpson, M. J., and T. P. Clement (2003), Theoretical analysis of the worthiness of Henry and Elder problems as benchmarks of density-dependent groundwater flow models, *Adv. Water Resour.*, *26*(1), 17–31, doi:10.1016/S0309-1708(02)00085-4.

Šimunek, J., and M. T. van Genuchten (2008), Modeling nonequilibrium flow and transport processes using HYDRUS, *Vadose Zone J.*, *7*(2), 782–797, doi:10.2136/vzj2007.0074.

Šimunek, J., M. T. van Genuchten, and M. Šejna (2008), Development and applications of the HYDRUS and STANMOD software packages and related codes, *Vadose Zone J.*, *7*(2), 587–600, doi:10.2136/vzj2007.0077.

Sophocleous, M. (2002), Interactions between groundwater and surface water: the state of the science, *Hydrogeol. J.*, *10*(1), 52–67, doi:10.1007/s10040-001-0170-8.

Sprenger, M., T. H. M. Volkmann, T. Blume, and M. Weiler (2015), Estimating flow and transport parameters in the unsaturated zone with pore water stable isotopes, *Hydrol. Earth Syst. Sci.*, *19*(6), 2617–2635, doi:10.5194/hess-19-2617-2015.

Srivastava, R., and M. L. Brusseau (1995), Darcy velocity computations in the finite element method for multidimensional randomly heterogeneous porous media, *Adv. Water Resour.*, *18*(4), 191–201, doi:10.1016/0309-1708(95)00013-9.

Sterrett, R. J., and T. B. Edil (1982), Ground-water flow systems and stability of a slope, *Ground Water*, *20*(1), 5–11, doi:10.1111/j.1745-6584.1982.tb01324.x.

Sudicky, E. A. (1986), A natural gradient experiment on solute transport in a sand aquifer: Spatial variability of hydraulic conductivity and its role in the dispersion process, *Water Resour. Res.*, *22*(13), 2069–2082, doi:10.1029/WR022i013p02069.

Sulis, M., S. B. Meyerhoff, C. Paniconi, R. M. Maxwell, M. Putti, and S. J. Kollet (2010), A comparison of two physics-based numerical models for simulating surface

water–groundwater interactions, *Adv. Water Resour.*, *33*(4), 456–467, doi:10.1016/j.advwatres.2010.01.010.

Sulis, M., C. Paniconi, and M. Camporese (2011), Impact of grid resolution on the integrated and distributed response of a coupled surface–subsurface hydrological model for the des Anglais catchment, Quebec, *Hydrol. Proc.*, *25*(12), 1853–1865, doi:10.1002/hyp.7941.

Sun, S., and M. F. Wheeler (2006), A posteriori error estimation and dynamic adaptivity for symmetric discontinuous Galerkin approximations of reactive transport problems, *Comp. Methods App. Mech. Eng.*, *195*(7), 632–652, doi:10.1016/j.cma.2005.02.021.

Taylor, G. S., and J. N. Luthin (1969), Computer methods for transient analysis of water-table aquifers, *Water Resour. Res.*, *5*(1), 144–152, doi:10.1029/WR005i001p00144.

Tetzlaff, D., C. Birkel, J. Dick, J. Geris, and C. Soulsby (2014), Storage dynamics in hydropedological units control hillslope connectivity, runoff generation, and the evolution of catchment transit time distributions, *Water Resour. Res.*, *50*(2), 969–985, doi:10.1002/2013WR014147.

Therrien, R. E., E. A. Sudicky, and Y.-J. Park (2012), *HydroGeoSPhere: a three-dimensional numerical model describing fully-integrated subsurface and surface flow and transport*, User Guide, Aquanty Inc, Waterloo, Ontario, Canada.

Thomson, N. R., J. F. Sykes, and W. C. Lennox (1984), A Lagrangian porous media mass transport model, *Water Resour. Res.*, *20*(3), 391–399, doi:10.1029/WR020i003p00391.

Tonina, D., and J. M. Buffington (2007), Hyporheic exchange in gravel bed rivers with pool-riffle morphology: Laboratory experiments and three-dimensional modeling, *Water Resour. Res.*, *43*(1), doi:10.1029/2005WR004328, W01421.

Tracy, J. C., and M. A. Mariño (1987), Seepage into variably saturated porous medium, *J. Irrig. Drain. Eng.*, *113*(2), 198–212, doi:10.1061/(ASCE)0733-9437(1987)113:2(198).

Troch, P. A., A. Berne, P. Bogaart, C. Harman, A. G. J. Hilberts, S. W. Lyon, C. Paniconi, V. R. N. Pauwels, D. E. Rupp, J. S. Selker, A. J. Teuling, R. Uijlenhoet, and N. E. C.

Verhoest (2013), The importance of hydraulic groundwater theory in catchment hydrology: The legacy of Wilfried Brutsaert and Jean-Yves Parlange, *Water Resour. Res.*, *49*(9), 5099–5116, doi:10.1002/wrcr.20407.

Tromp-van Meerveld, H. J., and J. J. McDonnell (2006), Threshold relations in subsurface stormflow: 2. the fill and spill hypothesis, *Water Resour. Res.*, *42*(2), doi:10.1029/2004WR003800, w02411.

Valocchi, A. J., and M. Malmstead (1992), Accuracy of operator splitting for advection-dispersion-reaction problems, *Water Resour. Res.*, *28*(5), 1471–1476, doi:10.1029/92WR00423.

Van Der Knijff, J. M., J. Younis, and A. P. J. De Roo (2010), LISFLOOD: a GIS-based distributed model for river basin scale water balance and flood simulation, *Int. J. Geogr. Inf. Sci.*, *24*(2), 189–212, doi:10.1080/13658810802549154.

van Genuchten, M. T. (1980), A closed-form equation for predicting the hydraulic conductivity of unsaturated soils, *Soil Sci. Soc. Amer. J.*, *44*(5), 892–898, doi:10.2136/sssaj1980.03615995004400050002x.

VanderKwaak, J. E., and K. Loague (2001), Hydrologic-response simulations for the R-5 catchment with a comprehensive physics-based model, *Water Resour. Res.*, *37*, 999–1013, doi:10.1029/2000WR900272.

Wang, H. F., and M. P. Anderson (1995), *Introduction to Groundwater Modeling: Finite Difference and Finite Element Methods*, Academic Press.

Weill, S., A. Mazzia, M. Putti, and C. Paniconi (2011), Coupling water flow and solute transport into a physically-based surface-subsurface hydrological model, *Adv. Water Resour.*, *34*(1), 128–136, doi:10.1016/j.advwatres.2010.10.001.

Wierenga, P. J., R. G. Hills, and D. B. Hudson (1991), The Las Cruces trench site: Characterization, experimental results, and one-dimensional flow predictions, *Water Resour. Res.*, *27*(10), 2695–2705, doi:10.1029/91WR01537.

Willgoose, G., and H. Perera (2001), A simple model of saturation excess runoff generation based on geomorphology, steady state soil moisture, *Water Resour. Res.*, *37*(1), 147–155, doi:10.1029/2000WR900265.

Wilson, J. L., and L. W. Gelhar (1981), Analysis of longitudinal dispersion in unsaturated flow: 1. The analytical method, *Water Resour. Res.*, *17*(1), 122–130, doi:10.1029/WR017i001p00122.

Winter, T. C., J. W. Harvey, O. L. Franke, and W. M. Alley (1998), *Groundwater and surface water: a single resource*, U.S. Geological Survey Circular 1139.

Woolhiser, D. A., R. E. Smith, and J.-V. Giraldez (1996), Effects of spatial variability of saturated hydraulic conductivity on Hortonian overland flow, *Water Resour. Res.*, *32*(3), 671–678, doi:10.1029/95WR03108.

Yeh, G.-T. (1981), On the computation of Darcian velocity and mass balance in the finite element modeling of groundwater flow, *Water Resour. Res.*, *17*(5), 1529–1534, doi:10.1029/WR017i005p01529.

Zacharias, S., H. Bogena, L. Samaniego, M. Mauder, R. Fuß, T. Pütz, M. Frenzel, M. Schwank, C. Baessler, K. Butterbach-Bahl, O. Bens, E. Borg, A. Brauer, P. Dietrich, I. Hajnsek, G. Helle, R. Kiese, H. Kunstmann, S. Klotz, J. C. Munch, H. Papen, E. Priesack, H. P. Schmid, R. Steinbrecher, U. Rosenbaum, G. Teutsch, and H. Vereecken (2011), A network of terrestrial environmental observatories in Germany, *Vadose Zone J.*, *10*, 955–973, doi:10.2136/vzj2010.0139.

Zanello, F., P. Teatini, M. Putti, and G. Gambolati (2011), Long term peatland subsidence: Experimental study and modeling scenarios in the Venice coastland, *J. Geophys. Res. F: Earth Surf.*, *116*(F4), doi:10.1029/2011JF002010.

Zhang, R., K. Huang, and M. T. van Genuchten (1993), An efficient Eulerian-Lagrangian method for solving solute transport problems in steady and transient flow fields, *Water Resour. Res.*, *29*(12), 4131–4138, doi:10.1029/93WR01674.

Zhang, X.-P., Z.-L. Yang, G.-Y. Niu, and X.-Y. Wang (2009), Stable water isotope simulation in different reservoirs of Manaus, Brazil, by Community Land Model incorporating stable isotopic effect, *Int. J. Climatol.*, *29*, 619–628, doi:10.1002/joc.1740.

Zheng, C., M. Bianchi, and S. M. Gorelick (2011), Lessons learned from 25 years of research at the MADE site, *Ground Water*, *49*(5), 649–662, doi:10.1111/j.1745-6584.2010.00753.x.

Zhou, Q., J. Bensabat, and J. Bear (2001), Accurate calculation of specific discharge in heterogeneous porous media, *Water Resour. Res.*, *37*(12), 3057–3069, doi:10.1029/1998WR900105.